# UNIVERSITÀ DEGLI STUDI DELL'AQUILA

**DIPARTIMENTO DI INGEGNERIA INDUSTRIALE E DELL'INFORMAZIONE E DI ECONOMIA**

Dottorato di Ricerca in

INGEGNERIA INDUSTRIALE E DELL'INFORMAZIONE E DI ECONOMIA

XXXII ciclo

Titolo della tesi

*Graphene-like nanoscale gas sensors from material synthesis to applications*

SSD ING-IND/22


Dottorando

Valentina Paolucci

Coordinatore del corso

Prof. Roberto Cipollone

Tutore

Prof. Carlo Cantalini


A.A. 2018/2019

# ABSTRACT

A very widespread area of application for nanomaterials is that of gas sensors. Until now, in fact, the measurement of pollutants in the air or in gaseous currents, a practice made necessary by the restrictive legislation in this field, has always been carried out through the use of traditional techniques, very effective, but long and often complicated. The use of solid-state gas sensors, devices capable of transforming chemical information, such as the concentration of a pollutant, into an electrical signal through the combined action of a receptor and a transducer, is considered the future in the field of environmental monitoring, as it allows simple, immediate measures and involves the use of small, portable or even wearables devices. To improve sensors' features, in recent decades there has been an increased attention for the development of nanomaterials which provide high structural and morphological control, high efficiency and miniaturization of gas sensors.

In the work presented in this Thesis nanomaterials have been used as gas sensors, thus exploiting the properties of these to significantly modify the electrical resistance following exposure to small concentrations of oxidizing and reducing gases.

Material's evolution has been followed from the synthesis to the final application as gas sensors. In particular Transition Metal Dichalcogenides exfoliation process to produce high quality and high quantity of mono to few layer flakes has been set up, and once the final product has been tested, his performances have been optimized by combination with other materials. The design of the exfoliation process has been developed in light of the possibility of massive production and eventually the scalability of the process itself.

Morphological characterization of materials was carried out by means of Electron Microscopy (TEM and SEM), Atomic Force Microscopy (AFM), X-ray Diffraction (XRD) and X-ray Photoelectron Spectroscopy (XPS). The electrical characterizations have been carried out by a laboratory equipment. Target gases such as $H_2$ and $NO_2$ with concentrations like those found in pollute environments were investigated. Fabricated gas sensors have shown excellent results and performances suggesting the use of nanomaterials-based devices for commercial purposes. Moreover, not only two-dimensional materials have been studied, but also 0D-nanomaterials based sensors have been studied, giving the premises for a future work on the engineering of the sensing material with appropriate doping.

This PhD work has developed through relationships with various research groups including the Departments of Physics and Industrial Engineering of the University of L'Aquila, the Department of Industrial Engineering of the University of Padova and the Department of Chemistry of the University of Sassari.

# THESIS OBJECTIVES

The work presented in this thesis is focused on the design and the optimization of the exfoliation process to obtain and mono to few layered 2D Transitional Metal Dichalcogenides (TMDs), Tungsten Disulfide in particular, to be employed as gas sensors for gas sensing applications. Moreover, the testing of gas sensing properties has been extended to other nanomaterials. In particular, this research has been aimed to:

- Exfoliation of mono to few layered 2D Transitional Metal Dichalcogenides (TMDs) by grinding assisted probe sonication technique and optimization of exfoliation process;
- Investigation of the effect of the exfoliation on the surface chemistry of $WS_2$;
- Investigation the thermal stability of exfoliated $WS_2/WO_3$ at elevated temperatures;
- The morphological, microstructural and electrical characterization of synthesized sensing materials to define factors influencing gas sensing properties;
- Investigation on the gas sensing properties of above-mentioned nanostructured semiconductors to target gases such as $H_2$, $NO_2$, and humidity under simulated conditions.
- Synthesis and investigation of gas sensing properties of traditional semiconductor Metal Oxide Sensors (MOS)

# ACHIEVED RESULTS

The main achievements earned during this PhD program have been:

- Design of a reproducible and controllable exfoliation procedure to fabricate pristine mono and few layered $WS_2$, by means of grinding assisted probe sonication yielding suspension of flake of average lateral size of 100 nm and thickness of 6 nm (less than 10 layers per flake)
- Control of the surface oxidation and thermal stability of exfoliated $WS_2$ flakes
- Application of the exfoliated material to produce gas sensors, with complete understanding of the role of $WS_2/WO_3$, able to detect $NO_2$ at concentration of 200 ppb and $H_2$ 5 ppm
- Improvement of the gas sensing performances of $WS_2$ by the combination of graphene oxide to enhance conductivity and improvement of the response/recovery of the sensor by using light irradiation
- Improvement of the gas sensing performances of traditional metal oxide sensors by adding different doping elements during synthesis

# PREFACE

During the PhD Program several papers were published as follows:

**Journal publications:**

1. Resmini, A.; Anselmi-Tamburini, U.; Emamjomeh, S.M.; **Paolucci, V**.; Tredici, I.G.; Cantalini, C. *The influence of the absolute surface area on the $NO_2$ and $H_2$ gas responses of ZnO nanorods prepared by hydrothermal growth*. Thin Solid Films **2016**, *618*, 246–252.

2. Perrozzi, F.; Emamjomeh, S.M.M.; **Paolucci, V**.; Taglieri, G.; Ottaviano, L.; Cantalini, C. *Thermal stability of $WS_2$ flakes and gas sensing properties of $WS_2/WO_3$ composite to H2, NH3 and NO2*. Sensors Actuators, B Chem. **2017**, *243*, 812–822.

3. Rigon, M.; **Paolucci, V**.; Sturaro, M.; Emamjomeh, S.M.; Cantalini, C.; Martucci, A. *Effect of Pt Nanoparticles on the Plasmonic and Chemoresistive Gas Sensing Properties of ZnO:Ga Film*. Proceedings **2018**.

4. **Paolucci, V**.; Emamjomeh, S.M.; Anselmi-Tamburini, U.; Cantalini, C. *The Influence of Temperature and Visible Light Activation on the $NO_2$ Response of $WO_3$ Nanofibers Prepared by Electrospinning*. Proceedings **2019**, *14*, 1.

5. **Paolucci, V**.; Emamjomeh, S.M.; Ottaviano, L.; Cantalini, C. *Near Room Temperature Light-Activated $WS_2$-Decorated rGO as $NO_2$ Gas Sensor*. Sensors (Basel). **2019**, *19*.

6. **Paolucci, V**.; Emamjomeh, S.M.; Nardone, M.; Ottaviano, L.; Cantalini, C. *Two-Step Exfoliation of $WS_2$ for $NO_2$, $H_2$ and Humidity Sensing Applications*. Nanomaterials **2019**, 1–17.

7. **Paolucci, V**.; Rigon, M.; Cantalini, C.; Martucci, A. *Effect of Group III and Group IV dopants on ZnO nanoparticles on the Plasmonic and Chemoresistive Gas Sensing Properties,* in preparation.

8. **Paolucci, V**.; Ottaviano, L.; Cantalini, C., *Optimization of synthesis parameter on TMDs exfoliation and their influence on surface stability*, in preparation.

**Attendance at national and international conferences**

- Chem2Dmat- Strasbourg 22-26 August 2017- Faculté de Chimie, Université de Strasbourg (France): S.M. Emamjomeh, **V. Paolucci**, F. Perrozzi, L. Ottaviano, C. Cantalini "*Controlling microstructure and surface oxidation of WS2 exfoliated by ball milling and sonication for gas sensing applications*"– ORAL CONTRIBUTION

- 17th International Meeting on Chemical Sensors (IMCS 2018), July 15-19, 2018 - University of Vienna, Austria:

  - **V. Paolucci**, S.M. Emamjomeh, L. Ottaviano, C. Cantalini "*$WS_2$-decorated rGO for Quasi-room Temperature Gas Sensing Applications*" - POSTER

  - U.Anselmi-Tamburini, J.M. Tulliani, **V. Paolucci**, S.M. Emamjomeh, C. Cantalini "*Correlation between the $NO_2$ gas sensing properties and surface area of ZnO nanofibers, hyerarchical and thin films structures*" – POSTER

  - S.M. Emamjomeh, L. Lee, G.S. Henshaw, C. Cantalini, **V. Paolucci**, D.E. Williams "*Enhanced $NO_2$ response of surface decorated $WO_3$ low-cost gas sensors"* - POSTER

- 8th GOSPEL Workshop. Gas sensors based on semiconducting metal oxides: basic understanding & application fields, 20-21 June 2019 - University of Ferrara: **V. Paolucci** , S.M. Emamjomeh , and C. Cantalini "*The Influence of Temperature and Visible Light Activation on the $NO_2$ and $H_2$ response of $WO_3$ Electrospun Nanofibers*" – ORAL CONTRIBUTION.
- 105° Congresso Nazionale della Società Italiana di Fisica 23 al 27 september 2019, L'Aquila: **V. Paolucci**, L. Ottaviano, C. Cantalini "Controlling microstructure and chemical stability in TMDs exfoliation and their application for gas sensing" – ORAL CONTRIBUTION

**Attendance at PhD Schools:**

- PhD school "*Introduction to structural crystallography and diffraction*" Dipartimento di Geoscienze, Università di Padova 4-8 June 2018 (3 ECTS)

- Summer school "*6 th ISGS Summer School Frontiers in Hybrid Materials*" 16-19 September 2018, University of Sassari, Alghero (3 ECTS)

# ACKNOWLEDGMENTS

Ho sempre pensato che il Dottorato di Ricerca rappresentasse l'opportunità per tre anni di fare il lavoro che mi è sempre piaciuto, e se tornassi indietro lo rifarei allo stesso modo.

Per prima cosa devo ringraziare il Prof. Cantalini, che mi ha dato questa opportunità facendomi da maestro sempre e in ogni circostanza, offrendomi la possibilità di conoscere un mondo sconfinato e affascinante come quello della ricerca, sia dietro il bancone che in giro per l'Italia e non solo. Grazie per gli insegnamenti continui, il mettersi in gioco e soprattutto per la grande fiducia, devo a lui non solo la mia crescita professionale ma anche e soprattutto quella umana.

Grazie ancora una volta a Fabiola che è e sarà sempre un punto di riferimento, un'insegnante e un'amica, un faro che si muove tra il bancone e la scrivania sempre pronta a condividere, spiegare, discutere e interpretare insieme ogni risultato e ogni idea. Se ho scelto di fare questo lavoro lo devo anche a te.

Un particolare grazie al Prof. Luca Ottaviano che mi ha mostrato il punto di vista dei fisici, insegnandomi a fare ricerca non solo come un ingegnere.

Durante questo dottorato ho avuto la grande opportunità di viaggiare, di conoscere nuove realtà al di fuori di questa meravigliosa ma piccola città. "Emigrando" a Padova prima, e ad Alghero poi ho incontrato persone che mi hanno lasciato tanto, e da ogni viaggio sono tornata con la valigia piena di esperienze e nuove conoscenze e capacità da portare a casa e in laboratorio. Grazie al Prof. Martucci, a Michele e Alessandro per avermi accolta a Padova e ai Prof. Innocenzi e Malfatti, e a Stefania per i mesi ad Alghero.

Il grazie più speciale di tutti va alla mia famiglia, a Mamma e Papà che mi hanno sempre guidata e supportata in ogni momento. Che mi hanno sempre guardata con gli occhi piedi di orgoglio ad ogni traguardo.

Grazie a chi non può vedermi oggi, ma io vi porto sempre con me.

Ancora una volta voglio chiudere al meglio, perché *ultimo ma non meno importante* devo dire un milione di volte grazie a Luigi. Per tutto, per esserci sempre, per sopportarmi, per aver camminato insieme a me per tutti questi anni. E grazie in anticipo per tutto quello che ci aspetta.

E infine grazie anche un po' a me, per essermi buttata nella mischia ed essere diventata la persona che sono ora, e che mai avrei osato desiderare di essere…

Ad maiora semper.

# INDEX

# CHAPTER 1.
# Gas sensing and Nanomaterials: definitions and working principles

## ABSTRACT

Chapter 1 represent a general overview on both gas sensors and nanomaterials. Regarding gas sensors, their traditional working principles are reported together with some features that brought nanomaterials to be suitable for that applications. Moreover, a summary of nanomaterials classification and general synthesis methods is illustrated.

## CONTENT

## 1.1 MOS semiconductors and their surface reaction

Chemoresistive gas sensors were introduced for the first time fifty years ago. At the beginning of the 1960s, Seyama, using ZnO thin film as a sensing layer, was able to demonstrate that gas sensing was possible with simple electrical devices [1]. He used a simple chemoresistive device based on ZnO thin films operating at the temperature of 485°C. The response of the detection system to propane was about 100 times higher compared to the thermal conductivity detector used at that time. In the early 1950s, Brattain and Bardeen, two scientists working at Bell Laboratories, gave the first demonstration that some semiconductor materials such as Ge modify their resistance, depending on the atmosphere they are in contact with [2]. Later, Heiland additionally described [3] that metal oxides such as ZnO modify their semiconducting properties with a change in the partial pressure of oxygen or other gases in the surrounding atmosphere. However, these discoveries were not investigated further.

After Seyama's work, Shaver [4] in 1967 described effects achievable with oxide semiconductors modified by the addition of noble metals (e.g., Pt, Pd, Ir, Rh). Since that time, the sensitivity and selectivity of semiconductor sensing devices have been enhanced significantly, and the research about new formulations for sensing materials has been intensified. At the beginning of the 1970s, Taguchi fabricated and patented the first chemoresistive gas sensor device for practical applications using tin dioxide ($SnO_2$) as the sensitive material [5]. Indeed, after investigating many metal oxides, he found that $SnO_2$ has many advantageous properties such as higher sensitivity, low operating temperature, and a thermal stable structure.

### 1.1.1 Semiconducting metal oxide gas sensors

The semiconducting metal oxide gas sensor is a chemoresistive type gas sensor. It is normally constructed from a semiconducting material on a heated insulating substrate and connected by metal wires. The sensing signals are obtained in the form of resistance changes. This gas sensor has a wide range of gas detection capability that covers the market needs for detecting oxygen, inflammable gases, toxic gases and air pollutants. However, since the invention of $SnO_2$ chemo-resistive metal oxide gas sensors until now, the semiconducting metal oxide type suffers from lack of selectivity. However, the potential advantages, such as the low cost, reliable performance that metal oxide presents, makes it the fastest growing type of material for gas sensors which have been commercially expanded. Figure 1- 1 show an overview of the most studied semiconductors employed for gas sensing [6].

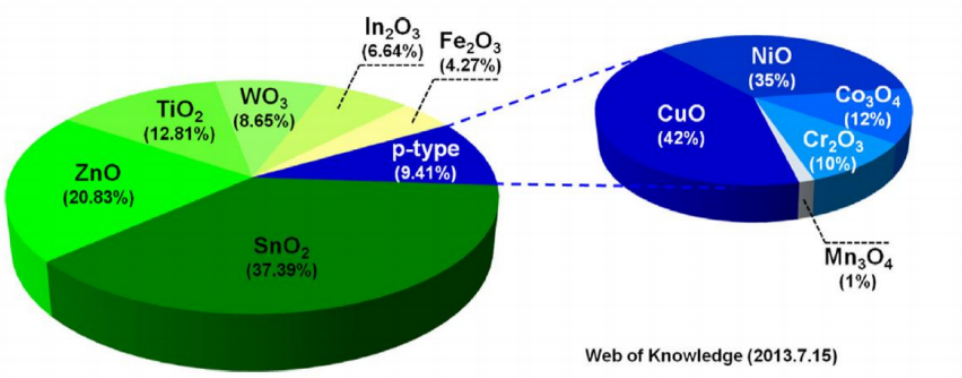


Figure 1- 1. Studies on n-type and p-type semiconductor gas sensors.

### 1.1.2 Chemoresistive gas sensors

Chemiresistors constitute one of the most investigated groups of gas sensor devices; their operating mechanism is based on the gas molecules adsorbed on the surfaces of the gas sensing material inducing a change of its electrical resistance, and by measuring this resistance change, the target gases can be effectively detected. Chemiresistors have their own advantages, such as ease in fabrication, simplicity of operation, cost effectiveness, long term stability, low power consumption, ability to reuse and are also easy in miniaturization [7].

Chemiresistors contain the sensing materials supported by an inert substrate and two metallic electrodes or interdigitated electrodes. It can be used to detect $O_2$, CO, $H_2$, $NO_x$, $SO_x$, $Cl_2$ and some organic vapors [8–10]. The chemoresistive sensors are also included with a back-side heating circuit. The deposited sensor is connected to a volt-amperometric system to measure the resistance changes of deposited semiconductor when exposed to air and different oxidizing and reducing gases [9].

### 1.1.3 MOS Semiconductor surface reaction with oxidizing and reducing gases

In the energy band diagram of the elementary intrinsic semiconductors (e.g. Si or Ge), the valence electrons belonging to the covalently bound crystal, occupy the energy levels in the valence band. Above the valence band there is a forbidden energy range (band gap), in which there are no possible energy states (for silicon for example it is 1.1 eV at 20 ° C), above of this energy range there is a conduction band.

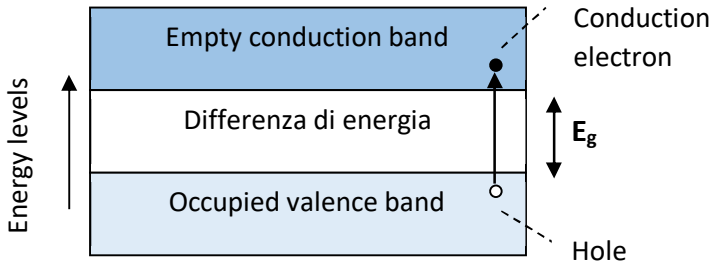


Figure 1- 2- Energy band diagram for an elementary intrinsic semiconductor such as pure silicon. When an electron is excited through the energy range, an electron-hole pair is created.

and germanium, are completely filled, while the conduction bands are completely empty. All valence electrons are permanently engaged in their respective bonds, causing the solid to behave like a perfect crystal. The binding electrons fail to move through the crystal lattice, and therefore to conduct electricity, unless they are given enough energy to excite them from their bonding positions.

At temperatures above 0 K each electron has a small but finite probability of leaving the potential hole corresponding to the covalent bond and being in the lattice, available as a conduction electron. The thermal energy is sufficient to excite the electrons from the valence band to the conduction band, and subsequently the bond electrons can become free conduction electrons and leave vacant sites or electronic holes in the valence band, thus creating two charge carriers, a negatively charged electron and a positive charge gap (Figure 1- 2, Figure 1- 3). In the electrical conduction process of a semiconductor such as pure silicon or germanium, both electrons and electronic gaps are charge carriers and move due to an applied electric field.

The ease with which electrons can be brought from the valence band to the conduction band depends on the energy gap existing between the bands; this size distinguishes the different types of solids: while the semiconductors generally have energy gaps of about 1 electron-volt, the insulators have energy gaps that are many times greater.

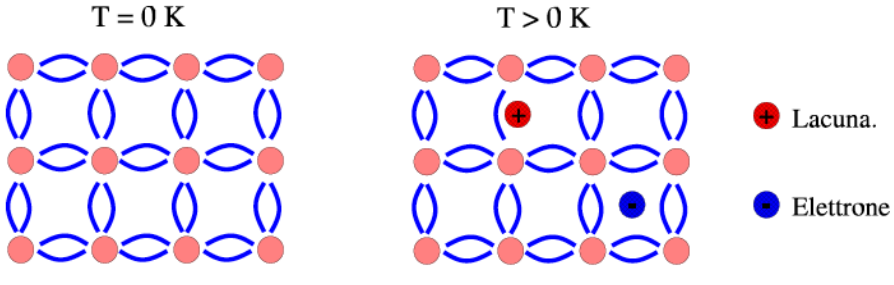


Figure 1- 3. Intrinsic semiconductor, a) at zero absolute there are no available charge carriers in the lattice, b) at temperatures higher than absolute zero some electrons become available as conduction electrons.

Gaps and electrons are continuously generated in pairs following the breakdown of covalent bonds due to thermal agitation and disappear in pairs, when a gap and an electron recombine to reform a covalent bond. Therefore, in the intrinsic semiconductor the hole concentration (p) will always be equal to that of the electrons (n). The value $n_i$ of p and n, called intrinsic concentration, is determined by the dynamic equilibrium between generation and recombination and depends on the characteristics of the semiconductor material and on the temperature T:

$$n_i^2 = n^2 = p^2 = BT^3 e^{-EG/kT} \qquad (1-1)$$

where EG is the breaking energy of a covalent bond, k the Boltzmann constant and B a characteristic constant of the material. The intrinsic concentration $n_i$ increases rapidly with temperature and this increase is the cause of the strong decrease in semiconductor resistivity with heating.

In semiconductors the electric current is generated by the flow of the electrons themselves or the vacancies left by the electrons. It is possible to increase the number of charge carriers of a semiconductor, by substituting atoms of other chemical elements which, depending on the case, can increase the number of conduction electrons (n-type semiconductor, i.e. negative) or holes (semiconductor p type, i.e. positive). This operation is called semiconductor doping.

In n-type semiconductors, free electrons are the majority carriers and holes are minority carriers. To better understand this, for example, if the silicon that has 4 electrons in its valence band is doped with antimony atoms that have 5 electrons in their valence band, 4 electrons of antimony make covalent band with 4 electrons of valence band of silicon and an extra free electron of antimony will be introduced to the valence band. At room temperature, these lightly attached fifth valence electrons of impurity atoms can easily come out from their position due to thermal excitation. Due to this phenomenon there will be a huge number of free electrons, and also breakdowns of covalent bonds in the crystal can occur, due thermal excitation at room temperature, causing further free electron in the material. Moreover, whenever a free electron is created during breakdown of a semiconductor-to-semiconductor covalent bond, there is a vacancy created in the broken bond. These vacancies are referred as holes. Each of these holes is considered as positive equivalent of negative electron as it is created due to lack of one electron. Here electrons are main mobile charge carriers. In an n-type semiconductor there will be both free electrons and holes, but number of holes are quite smaller than that of electrons because holes are created only due to breakdown of semiconductor-to-semiconductor covalent bond whereas free electrons are created both due to loosely bound non-bound fifth valence electron of impurity atoms and break down of semiconductor-to-semiconductor covalent bonds. Hence, number of free electrons is much higher than the number of holes in n-type semiconductor. That is why free electrons are called majority carriers and holes are called minority carriers in the n-type semiconductor. As the negatively charged electrons are mainly involved in charge transferring through this semiconductor it is referred as negative type or n-type semiconductor. Figure 1- 4 clearly show a n-type semiconductor.

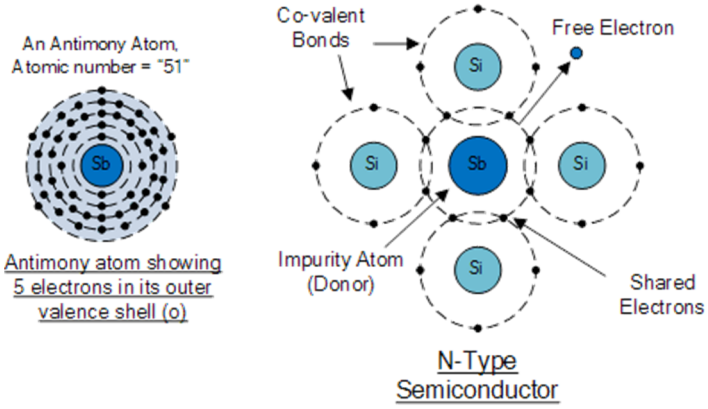


Figure 1- 4. Schematic of a n-type doped semiconductor

In the same way, if the silicon that has four electrons in its valence band is doped with boron atoms that have 3 electrons in their valence band, as Figure 1- 5 shows, three complete covalent bond will be formed but one covalent bond will be left incomplete with one electron. This vacancy is referred as hole. In this case, impurity generates empty energy levels in the valence band and there are many holes in the absence of thermal excitation. Thus, there is an excess of positive charge carriers and the level of Fermi moves down.

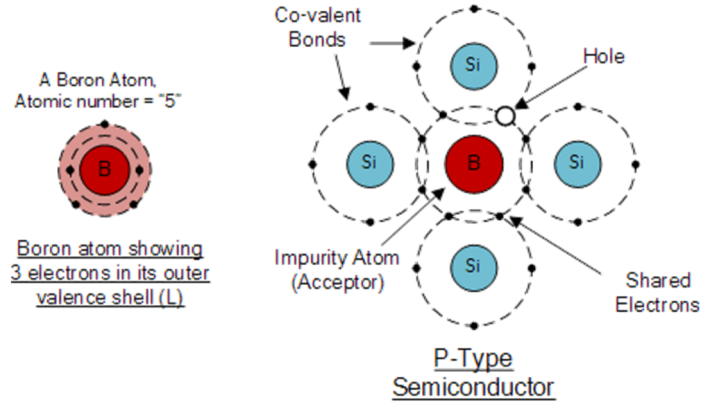


Figure 1- 5. Schematic of a p-type doped semiconductor

Each hole is created from one impurity atom. Beside electron mobility, in a semiconductor crystal, holes can also move like electrons, but the mechanism of their movement is different from that of electrons. When one hole is formed from an incomplete covalent bond, it will not remain incomplete lifelong. Very soon electron of other neighboring covalent bonds breaks out, fills the hole and makes a new covalent bond. In this case, we can say that the hole is moved from its previous position to a new position. The same mechanism will happen for the rest of holes and each hole will further move to another new position. This is how the holes move in a semiconductor crystal. Finally, we can say that a p-type semiconductor has plenty of holes that move randomly inside the crystal. Besides the holes generated from trivalent impurity atoms in the p-type semiconductor crystal, there will also be

thermally generated electron-hole pairs that refers to those electron-hole pairs that are generated due to the breakdown of covalent bond due to thermal excitations at room temperature. These thermally generated electrons contribute free electrons in the p-type semiconductor crystal. Hence, the total number of holes in a p-type semiconductor is a sum of holes due to trivalent impurity atoms and holes generated due to thermal excitation whereas free electrons are only due to thermal excitation. Hence, number of free electrons in a p-type semiconductor is much smaller than number of holes in it and therefore holes are considered as majority carries and electrons are called minority carriers in a p-type semiconductor.

In addition to pure semiconductors, some metal oxides also exhibit semiconducting properties and therefore have found applications as gas sensors. Among them, the most commonly used are non-transition element oxides (such as $SnO_2$, ZnO), but some transition metal oxides (such as $WO_3$, $TiO_2$) have also been studied.

There are two types of semiconductor metal oxides: n-type, in which the majority charge carriers are electrons (as in $SnO_2$, ZnO, $TiO_2$, $WO_3$) and p-type, in which the majority charge carriers are electronic gaps (as in NiO, CuO, $Co_3O_4$). [11]

As seen, majority charge carriers in pure intrinsic semiconductors, such as silicon, can be manipulated with appropriate doping of donors or acceptors. Regarding semiconductor oxides, the main charge carriers are determined by the non-stoichiometric nature of oxygen in the crystalline structure. For example, $SnO_2$ with a stoichiometric oxygen defect shows an n-type behavior as the formation of oxygen vacancies accompanies the generation of electrons. While the p-type behavior of a NiO can be explained by the stoichiometric defect of metal ions in the material. Once the operating temperature and environment have been set, the non-stoichiometry of oxygen cannot be changed, and to control the concentration of charge carriers it is possible to use doping with cations of greater or lesser valence. [6]

The surface gas/semiconductor interactions on which the gas-sensing mechanism of semiconductor oxides is based, occur on the surface of the grains of the polycrystalline oxide film. They generally involve adsorption processes of chemical species (environmental gases) directly on the semiconductor and / or their consequent adsorption with reaction with the pre-adsorbed environmental oxygen on the semiconductor. The effect of these surface phenomena is a reversible and significant change in electrical resistance, which can be easily observed and used to detect the concentration of chemical species in the environment.

Generally, the devices operate in air, at temperatures between 100 ° C and 600 ° C. Under these conditions the oxygen molecules present adsorb onto the surface of the metal oxide grains: due to its high electronegativity, oxygen extracts electrons from the oxide conduction band and therefore there is the formation of $O_2^-$, $O^-$ ions and $O_2^-$ adsorbed, depending on temperature (Figure 1- 6). The possible reactions that can occur are:

$$O_2(gas) \leftrightarrow O_2(adsorbed) \qquad (eq. 1-2)$$

$$O_2(adsorbed) + e^- \leftrightarrow O_2^-$$

$$O_2^- + e^- \leftrightarrow 2O^-$$

$$O^- + e^- \leftrightarrow O^{2-}$$

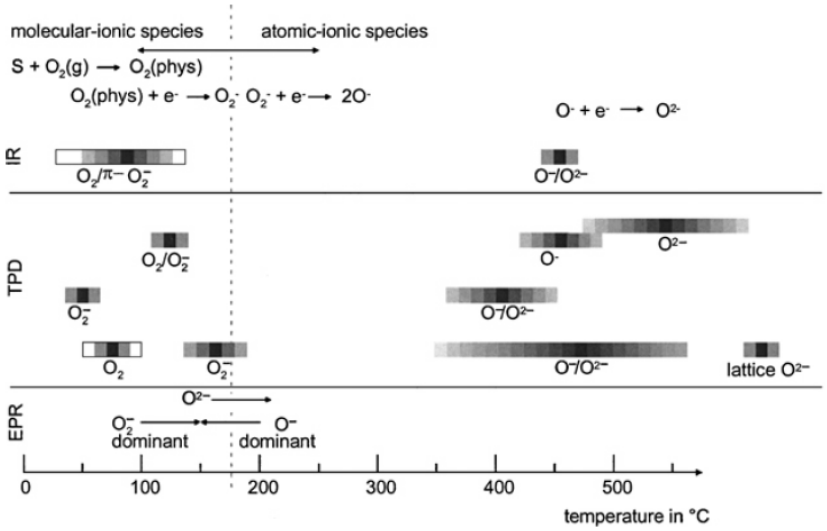


Figure 1- 6. Literature survey of oxygen species detected at different temperatures at $SnO_2$ surfaces with IR (infrared analysis), TPD (temperature programmed desorption), EPR (electron paramagnetic resonance)

The $O_2^{--}$, $O^-$ and $O^{2-}$ ions are stable respectively below 100 ° C, between 100°C and 300°C and above 300°C. Correspondingly, they will desorb from the surface at temperatures of 80, 130 and 250°C respectively.

This phenomenon leads to the formation of a core-shell electronic configuration (Figure 1- 7). As regards n-type oxides, there will therefore be a resistive electronic depletion layer (EDL) in the particle shell and a n-type semiconductive region in the particle center. The adsorption of oxygen anions in p-type semiconductor oxides instead, forms a layer of accumulation of holes (HAL) near the surface of the material, thus establishing an electronic core-shell configuration in which the insulating region is at the center of the particles, while the semiconductor layer is near the surface of the particles.

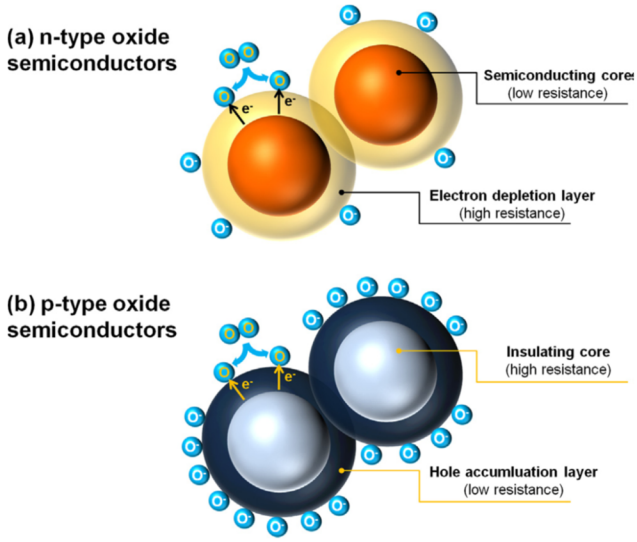


Figure 1- 7. Formation of the core-shell electronic structure in semiconductor oxides (a) n-type and (b) p-type. [21]

The thickness of the depletion layer ($d_{SC}$) can be calculated through Debye's equation as follows;

$$d_{SC} = \frac{Q_S}{N_d e} \qquad (1\text{-}3)$$

$$Q_S = \left(\sum_j N_{S,j} q_j \theta_j\right)$$

where $N_d e$ is the number of donors per volume of the material, $N_{S,j}$ is the number of surface states of j type with unitary electronic charge, $q_j$ ,per unit of surface, $\theta_j$ is the fraction of adsorbed area corresponding to the states surface type j, and is the electric charge of the electron. The surface potential and the height of the Schottky barrier, can be calculated by equation (1-4):

$$\Delta\phi_S = \frac{(Q_S)^2}{2\varepsilon\varepsilon_0 N_d\, e} \qquad (1\text{-}4)$$

where $Q_S$ is the charge associated with surface oxygen coverage, $\varepsilon$ is the dielectric constant of the material, $\varepsilon_0$ is the dielectric constant relative to the vacancy. It should be noted that if $\varepsilon\varepsilon_0 = 10^{-12} F/cm$, $N_d \approx 10^{18} cm^{-3}$ , $\Delta\phi_S \approx 1V$ would have a surface $\sum_j N_{S,j}\theta_j \approx 10^{13} cm^{-2}$ which implies a depletion layer thickness of $d_{SC}$ between 1-100 nm.

The influence of the above-mentioned chemical surface phenomena on the sensor response can be understood on the basis of the charge transfer model (CTM) and of the band model for semiconductor metal oxides.

According to this model, the variations in the electrical resistance of the sensor are consequent to the formation of regions of emptying of space charge on the surface and around the grains; this results in surface energy barriers that electrons must overcome in order to ensure electrical conduction; the height and width of these barriers is variable, depending on the nature of the adsorbed species (oxidizing or reducing). [12]

Through the adsorption of oxygen therefore both in the n-type and p-type semiconductor oxides core-shell configurations of electrical layers are established, and their conductive behavior is however different. The resistance of the n-type oxide sensor is mostly determined by the shell-shell resistive contacts formed between the particles, so an equivalent circuit can be represented as serial connections between semiconductor particle centers ($R_{core}$) and resistive interparticle contacts ($R_{SHELL}$).

Conduction in semiconductor p-type oxides can be explained instead through a competition between parallel paths: on the one hand through the large and resistive particle center ($Rc_{ore}$) and on the other along the narrow shell and semiconductor ($R_{shell}$). Consequently, the global resistance can be described by two resistors in parallel (Figure 1- 8).

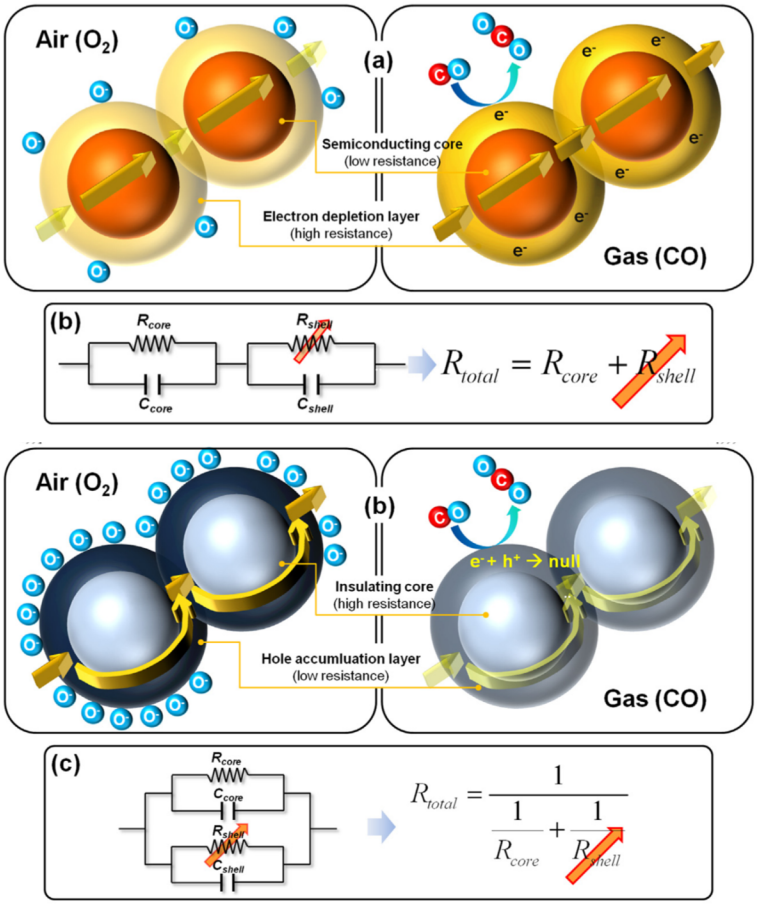


Figure 1- 8. Gas sensing mechanism for reducing gases and equivalent circuits of semiconductor oxides n-type (a, b) and p-type (c,d)

For an assigned configuration of the ion-adsorbed oxygen species, when interfering gases interact with the surface of the semiconductor, the base line resistance ($R_a$ at equilibrium) will change. Based on the type of semiconductor (n-type or p-type) and interfering gas (oxidizing or reducing), such variation in resistance may be an increase or a decrease. For n-type semiconductors the interfering gases can be classified as reducing gases or as oxidizing gases, depending on whether they cause a decrease or an increase of $R_a$ respectively. Following the interactions of reducing and oxidizing gases at the surface of a n-type semiconductor are discussed.

Environmental gases can be divided into two groups, based on oxidizing or reducing effects. For example, $NO_2$, NO, $N_2O$ and $CO_2$ are oxidants, while $H_2S$, CO, $NH_3$, $CH_4$, $SO_2$ and $H_2$ are reducing agents. When the oxide surfaces are exposed to oxidizing gases, they react with O-adsorbed ions and/or they adsorb directly on the surface of the oxide. The reactions between metal oxide and these oxidizing gases take place according to the following paths:

- $NO_2(gas) + e^- \rightarrow NO^{2-}(ads)$ (1-5)
- $NO^{2-}(ads) + O^-(ads) + 2e^- \rightarrow NO(gas) + 2O^{2-}(ads)$
  - $NO(gas) + e^- \rightarrow NO^-(ads)$
  - $2NO^-(ads) \rightarrow N_2(gas) + 2O^-(ads)$
- $N_2O(gas) + e^- \rightarrow N_2O^-(ads)$

- $N_2O^-(ads) \rightarrow N_2(gas) + O^-(ads)$
- $CO_2(gas) + e^- \rightarrow CO^{2-}(ads)$
- $CO^{2-}(ads) + O^-(ads) + 2e^- \rightarrow CO(gas) + 2O^{2-}(ads)$

The adsorption of O- is a crucial step in sensor's operation, because it assists the ions of the adsorbed oxidizing gases to tear the electrons from the surface of the oxide. The concentration of electrons on the surface of the oxide decreases, this increases the width of the depletion layer and the height of the potential barrier, consequently the resistance of the n-type oxide layer grows proportionally to the concentration of the oxidizing gas analyte, assuming a value $R_g > R_a$. In contrast, the surface resistance of the p-type oxide decreases, as the extracted electrons cause a generation of holidays in the valence band (in this case $R_g < R_a$).

When the surface of the metal oxide is exposed to reducing gases, chemiadsorbed oxygen anions are used to oxidize the reducing gas, and the remaining electrons are released into the semiconductor. The global reactions between $H_2S$, CO, $NH_3$, $CH_4$, $SO_2$ and $H_2$ are reducing agents and the adsorbed oxygen ($O^-$ and $O^{2-}$) are the following:

- $2NH_3 + 3O^-(ads) \rightarrow N_2 + 3H_2O + 3e^-$ (1-6)
- $2NH_3 + 3O^{2-}(ads) \rightarrow N_2 + 3H_2O + 6e^-$
- $H_2S + 3O^-(ads) \rightarrow H_2O + SO_2 + 3e^-$
- $H_2S + 3O^{2-}(ads) \rightarrow H_2O + SO_2 + 6e^-$
- $CO + O^-(ads) \rightarrow CO_2 + e^-$
- $CO + O^{2-}(ads) \rightarrow CO_2 + 2e^-$
- $SO_2 + O^-(ads) \rightarrow SO_3 + e^-$
- $SO_2 + O^{2-}(ads) \rightarrow SO_3 + 2e^-$
- $CH_4 + 4O^-(ads) \rightarrow 2H_2O + CO_2 + 4e^-$
- $CH_4 + 4O^{2-}(ads) \rightarrow 2H_2O + CO_2 + 8e^-$
- $H_2 + O^-(ads) \rightarrow H_2O + e^-$
- $H_2 + 2O^{2-}(ads) \rightarrow 2OH^- + 2e^-$

As a result, the concentration of electrons on the surface of the oxide grows, the depletion layer becomes thinner, the potential barrier is lowered and the resistance of the n-type oxide decreases proportionally to the concentration of the reducing analyte gas, assuming a value $R_g < R_a$. On the contrary, the resistance of the p-type oxide increases because the reinjected electrons recombine with the holidays, leading to a decrease in their concentration ($R_g > R_a$).

The change with the temperature of the entity of the adsorption and desorption phenomena of oxygen ions on the surface, causes the dependence of the sensing properties on the operating temperature.

The response of the sensor to gases is relatively high, due to the presence of $O^-$ adsorbed ions, in a temperature range ranging from 250 to 350°C. At higher temperatures, however, the dominant process becomes the adsorption of $O^-$ ions, therefore the response of the sensor decreases. Furthermore, at very high temperatures a progressive desorption of all the species occurs, so the response decreases.

When the interfering gases are removed from the sensor's working environment, the surface of the material tends to desorb the oxidized and / or reduced species, re-establishing the equilibrium conditions of the ionadsorbed species of oxygen.

## 1.2 Factors affecting the characteristics of a sensor

The process of gas sensing by a semiconductor device involves two key functions as illustrated in Figure 1- 9. (i) Recognition of a target gas through a gas–solid interaction which induces an electronic change of the oxide surface (receptor function) and (ii) transduction of the surface phenomenon into an electrical resistance change of the sensor (transducer function) [13]. Accordingly, for a given type of base material, the sensor sensitivity depends on some issues such as the structural features, the presence and state of catalytically active surface dopants, and the working temperature.

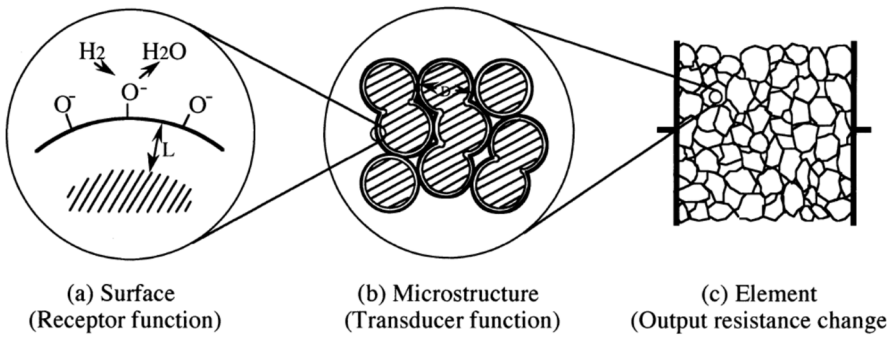


Figure 1- 9. Receptor and transducer function of a semiconductor gas sensor: a) surface, providing the receptor function, b) microstructure of the sensing layer, providing the transducer function, and c) element, enabling the detection of the change in output resistance of the sensing layer, here deposited on an interdigital microelectrode [14].

### 1.2.1 Effect of Particle size

As said, typical values of the depletion layer thickness ($L_s$) are in the range of 1-100 nm. Its dependency on grain size (diameter, D) has been observed empirically [15]. It has been reported that the gas sensitivity of sintered $SnO_2$ changed with a change in D. For D > 20 nm the sensor response barely changed along with the grain size; for D < 20 nm it increased with decreasing grain size; for D < 10 nm, the increase was huge. Some studies revealed that D has a critical value (Dc), 6 nm for $SnO_2$, and corresponds to twice the thickness (Ls) of the surface charge layer [16,17].

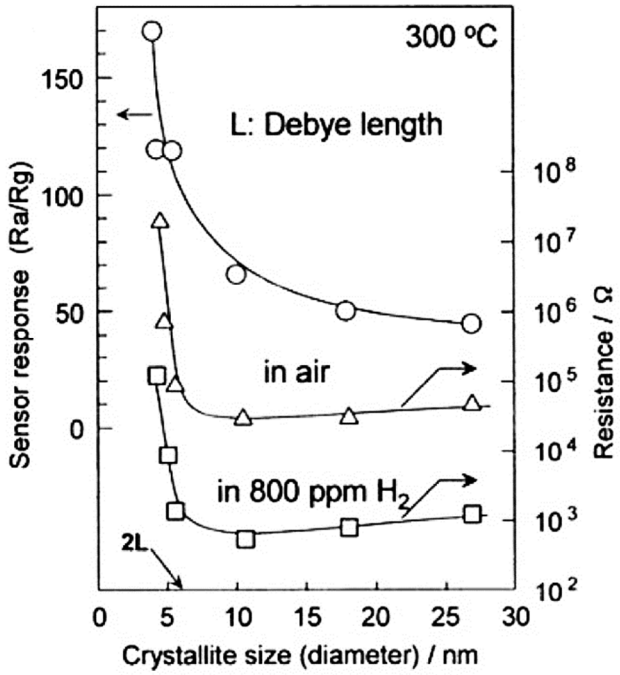


Figure 1- 10. Grain size effect on resistance and sensor response of $SnO_2$ to $H_2$ [16].

For D >> $2L_s$: a small portion of the volume of grains has surface interactions with the analyte gas. The effect on the sensor conductivity is dominated by the grain boundary (GB) barriers to intergrain charge transport from one grain to another. The electrical resistance of a sample with large grains is controlled by Schottky barriers and changes with them exponentially, see Figure 1- 11(a).

For D ≥ $2L_s$: in this case, the grain is somewhat larger or similar in size to the thickness of the depletion layer. The unaffected volume (core region) becomes smaller. When D is approaching $2L_s$, but still larger, the depletion region in each neck of each aggregate makes the conduction channel constricted, see Figure 1- 11(a). Consequently, changes in the total conduction is affected by the GB barriers and the cross-sectional area of constricted channels. From these two factors, the gas sensitivity increases with decreasing grain diameter.

For D < $2L_s$: In this case, the conductivity decreases steeply because the crystallites are almost depleted of mobile charge carriers throughout the entire grain and the conduction channels between the grains have vanished, see Figure 1- 11(b). The energy bands are nearly flat, since intercrystallite charge transfer is not interrupted by

GB barriers and the GB barrier effect is negligible, see Figure 1- 12(b). However, the sensing mechanism of particles in this range is not clear.

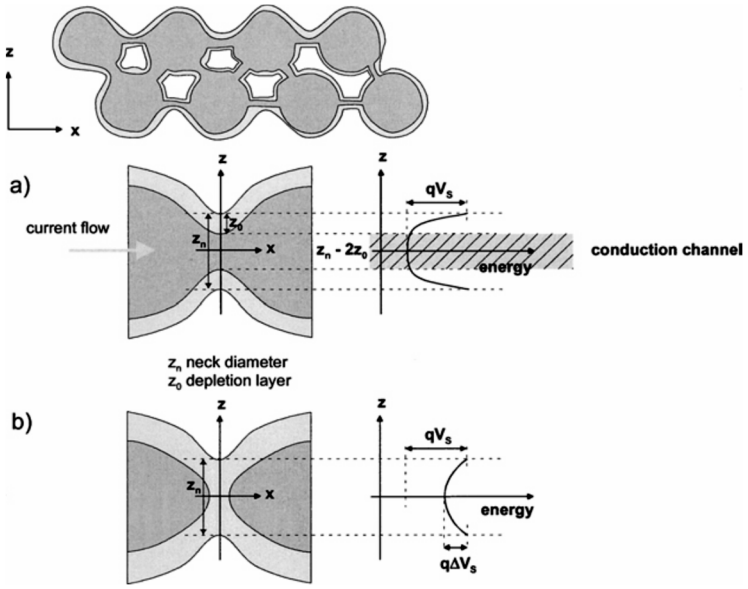


Figure 1- 11. Schematic representation of a porous sensing layer with geometry and surface energy band-case with necks between grains. $Z_n$ is the neck diameter; $Z_0$ is the thickness of the depletion layer. a) represents the case of only partly depleted necks whereas b) represents large grains where the neck contact is completely depleted [18].

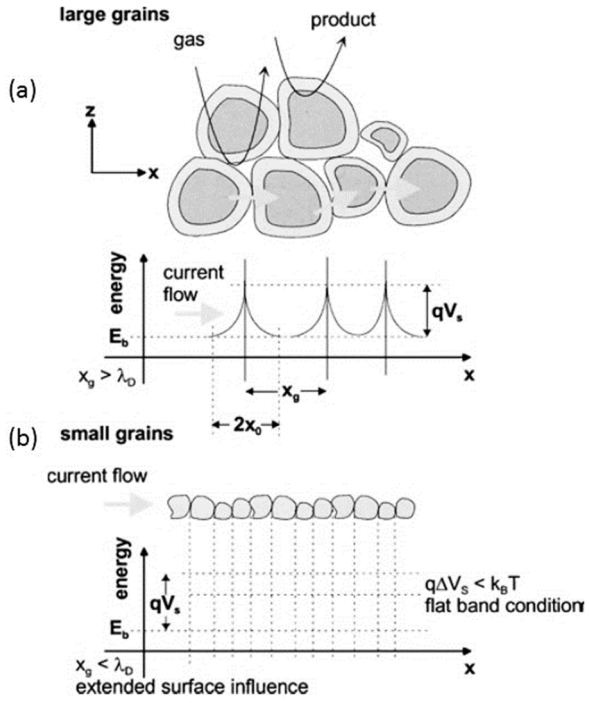


Figure 1- 12. Schematic representation of a porous sensing layer with geometry and energy band. $\lambda_D$ Debye length, $x_g$ grain size [18]

### 1.2.2 Effect of microstructure

Beside the particle size, the influence of the microstructure, that includes the film thickness and its porosity, is an important issue that plays a critical factor on the response time and the sensitivity of sensor and is needed to be discussed. Sensing layers are penetrated by oxygen and analyte molecules so that a concentration gradient is formed, which depends on the equilibrium between the diffusion rates of the reactants and their surface reaction. The rate of reaching the equilibrium condition determines the response time ($\tau_{ads}$) and recovery time ($\tau_{des}$). Therefore, a fast diffusion rate of the analyte and oxygen into the body of sensing material, which depends on its mean pore size and the working temperature, is fundamental. Moreover, maximum sensitivity will be achieved when all percolation paths contribute to the overall change of resistance and are all accessible to the analyte molecules in the ambient. Thus a thinner film together with a higher porosity results in a higher sensitivity and enhanced response time [19,20]. This was verified experimentally by Yamazoe et al., investigating the gas response on $H_2$ and $H_2S$ of thin films of monodisperse $SnO_2$ with particle diameters ranging from 6–16 nm [21,22]. It was found that the sensor response was greatly enhanced with decreasing film thickness but with increasing grain size up to 16 nm. The latter appears to be unexpected but can be understood in terms of an increased porosity, which cannot be achieved with the smallest particles studied. Thus, by controlling the nano and microstructure of the sensing layer, for example, by arranging the primary particles into larger secondary particles, analyte diffusion is facilitated via the larger micropores, whereas the grain size effect on the sensitivity can be maintained.

Historically, metal oxide sensors are polycrystalline materials, which unfortunately present some serious drawbacks such as poor reproducibility and long-term instability due to aging, high cross-sensitivity (cross-sensitivity), sensitivity to humidity, and slow response of the sensor.

To achieve selectivity in these types of gas sensors, the required operating temperature is usually between 300□C and 600□C; at these temperatures, chemisorption becomes more important than physisorption and chemisorption is by far the more selective process. Another important disadvantage is represented by the fact that physiosorbed water converts almost every material operating at low temperature into a humidity sensor [23]. Therefore, the sensing unit must feature a heating element that provides the desired temperature for adsorption and desorption of oxygen gas and for reaction of the analyte gases with those reactive adsorbed oxygen species. The gas-induced resistance changes are influenced by many material-related factors such as the type of semiconductor oxide material, oxide film thickness, grain size, porosity, material sintering temperature and time. In an optimized gas sensor design, the power consumption should be as low as possible and the heat losses owing to convection, conduction or radiation by the heater should thus be minimized. To minimize the power consumption, one needs to reduce the mass of both the heater and the sensor element and optimize the design for uniformity of heating. Both the heater and the sensor material are obviously strongly influenced by miniaturization. Moreover, material microstructure influences the reactivity in light

of diffusion phenomena: a better sensing material is the one that maximize the surface-to-volume ratio, possibly an all-reactive material, with no bulk.

Nanomaterials, with their high specific surface and their peculiar electronic properties, which let them work as low temperature sensors, can represent a solution to overcome traditional metal oxide sensors weaknesses.

## 1.3 Nanomaterials: introduction and classification

The general definition of “Nanotechnology” refers to a multidisciplinary approach to the realization of materials, devices and systems in which at least one of the three spatial dimensions of the components has a measure of the order of nanometres (nm, 1 nm = $10^{-9}$ m).

Some definitions include a reference to molecular nanotechnology systems and devices and purists “argue” that any definition needs to include a reference to “functional systems”. The inaugural issue of the journal Nature Nanotechnology asked 13 researchers from different areas what nanotechnology means to them and the responses, from enthusiastic to sceptical, reflect a variety of perspectives.

Materials in which structural and functional properties depend on the dimensions and at least one of them is on a nanometre scale are called nanostructured materials and such nanometric components are called nanostructures. The physics of nanostructures as a new and well- known scientific discipline is commonly traced back to the intuition of Richard Feynman, who explained the possibility of controlling matter and making devices on a scale atomic atom for the first time in a conference held in December 1959 at the California Institute of Technology. At that conference, remembered also for his title *There's plenty of room at the bottom*, Feynman noted that "the principles of physics do not oppose the possibility of manipulating atomic objects per atom", anticipating a broad spectrum of scientific research fields technical application that at the end of the 20th century already appear well-established.

Possible applications of nanotechnologies are expanding very rapidly and directly or indirectly affect all sectors of economic activity. The ability to produce materials precisely assembling nanostructured blocks with a composite and controlled size to obtain structures of desired shape and size represents a radical change in both production processes and materials properties, other than those so far known. These changes make the application potential of nanostructured materials very high, either in the form of dust, artefacts or thin films, or in special shapes such as nanofibers, unworkable with traditional textile materials.

People are interested in the nanoscale, because it is at this scale that the properties of materials can be very different from those at a larger scale. Nanoscience is defined as the study of phenomena and manipulation of materials at atomic, molecular and macromolecular scales, when properties differ significantly from those at a larger scale. Therefore, nanotechnology is the design, fabrication and application of nanostructures of nanomaterials and the fundamental understanding of the relationships between physical properties of phenomena and materials dimensions.

The bulk properties of materials often change dramatically with nano ingredients. Composites made from particles of nano-size ceramics or metals smaller than 100 nanometers can suddenly become much stronger than predicted by existing materials-science models.

For example, metals with a so-called grain size of around 10 nanometers are as much as seven times harder and tougher than their ordinary counterparts with grain sizes in the hundreds of nanometers. The causes of these drastic changes stem from the weird world of quantum physics. The bulk properties of any material are merely the average of all the quantum forces affecting all the atoms. As you make things smaller and smaller, you eventually reach a point where the averaging no longer works.

The properties of materials can be different at the nanoscale for two main reasons:

First, nanomaterials have a relatively larger surface area when compared to the same mass of material produced in a larger form. This can make materials more chemically reactive (in some cases materials that are inert in their larger form are reactive when produced in their nanoscale form), and affect their strength or electrical properties.

Second, quantum effects can begin to dominate the behavior of matter at the nanoscale – particularly at the lower end – affecting the optical, electrical and magnetic behavior of materials. Materials can be produced that are nanoscale in one dimension (for example, nanowires, nanorods and nanotubes), in two dimensions (plate-like shapes like nanocoatings, nanolayers, and graphene) or in all three dimensions (for example, nanoparticles).

### 1.3.1 Nanomaterials classification

The most important requirement for the nanotechnology definition is that the nano-structure has special properties that are exclusively due to its nanoscale proportions. This definition is based on the number of dimensions of a material, which are outside the nanoscale (<100 nm) range.

Depending on dimensionality, some typical types of nanomaterials are defined (Figure 1- 13 and Table 1-2) such as:

- 0D nanomaterials: All dimensions at the nanoscale
- 1D nanomaterials: Two dimensions at the nanoscale, one dimension at the macroscale
- 2D nanomaterials: One dimension at the nanoscale, two dimensions at the macroscale
- 3D nanomaterials: No dimensions at the nanoscale, all dimension at the macroscale

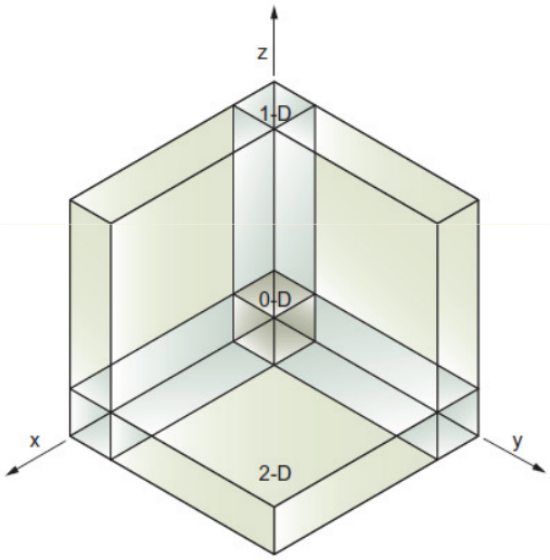


Figure 1- 13. Classification of nanoscale dimensions

Table 1-2 - Classification of nanomaterials based on dimensions

| Type of Nanomaterial | Dimension | Material |
|---|---|---|
| (0-D) nanocrystals and clusters (quantum dot) | Diameter 1-10 nm | Metals, semiconductors, magnetic materials |
| (0-D) Other Nanoparticles | Diameter 1-100 nm | Ceramic Oxides |
| (1-D) Nanowire | Diameter 1-100 nm | Metals, semiconductors, oxides |
| (1-D) Nanotube | Diameter 1-100 nm | Carbon |
| (2-D) Nanoparticles matrix | Several $nm^2$ to several $\mu m^2$ | Metals, Semiconductors, Magnetic Materials |
| (2-D) Thin films | Thicknesses 1-1000 nm | Various materials (organic and inorganic) |
| (3-D) Three-dimensional structures | Several nm in 3 dimensions | Metals, semiconductors, magnetic materials |

### 1.3.2 0D Nanostructures

The term "structure 0D" normally identifies the set of particles formed by atomic or molecular aggregates with a diameter of between 2 and 200 nm. The term is currently used to denote nanoparticles or nanoaggregates, that is, molecular or atomic aggregates with interesting chemical-physical properties that can also be produced and used in nanotechnologies [24].

Special equipment, electronic microscopes (scanning and transmission) or soft and hard X-rays, should be used for their study. Nanoparticles are of great scientific interest as they are in fact a bridge between coarse materials and atomic or molecular structures. Large materials have physical properties consistent with their size, but nanometer scale size dependent properties are often observed. As said, material properties change as soon as they approach the nanometre scale when the percentage of atoms in the surface of the material becomes significant. For materials of more than one micrometre size, the percentage of atoms at the surface level is insignificant in relation to the number of atoms included in the total mass of the material.

The interesting and sometimes unexpected properties of nanoparticles are due more to the large surface area of the material which prevails over the contributions made by the small mass of the material.

An excellent example of this is the absorption of solar radiation by photovoltaic cells, much higher in nanoparticulate composites than in thin layers that constitute continuous pieces of material.

In this case, the smaller particles are the larger the solar absorption. Other size-dependent property changes include quantum confinement in semiconductor, particles or surface plasmon resonance in some metal particles.

Nanoparticles have a very large surface area in relation to volume, thus provide a high propelling force for diffusion, especially at high temperatures. Sintering can take place at lower temperatures, on shorter time scales than larger particles; this theoretically does not affect the density of the final product, although the difficulty of flow and the tendency of nanoparticles to agglomerate complicates the phenomenon. The large surface area in volume ratio also reduces the incipient melting point of nanoparticles [25]. Figure 1- 14 shows the images of different types of 0D nanomaterials.

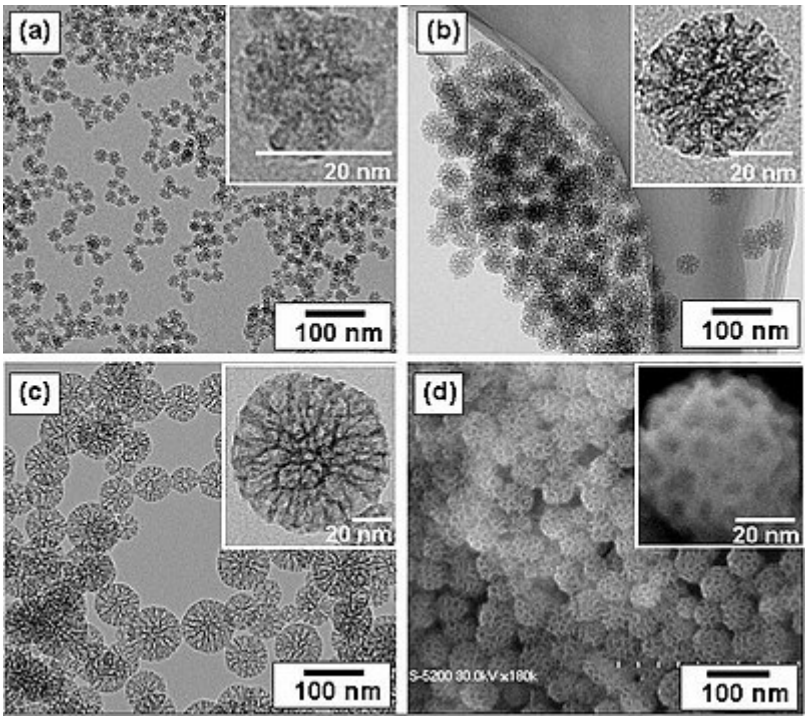


Figure 1- 14. Typical transmission electron microscope (TEM) image of different types of 0D nanomaterials

### 1.3.3 1D nanostructures

One-dimensional (1D) nanostructures, such as nanotubes, nanofibers and nanofibers, have been the focus of intense research activity in the recent years, for their unique application in mesoscopic physics and nanoscale devices. It has been also observed that 1-D nanostructures provide good electrical and thermal transport or mechanical properties by dimensionality and size reduction.

Although 1D nanostructures can be manufactured using many advanced nanolithographic techniques such as electron beam or ion beam lithography, probe scan lithography and X- ray or UV lithography, the further development of these nanostructures Techniques for implementing 1D nanostructures with a diverse range of materials and reasonably low costs still require great effort. Unconventional methods based on chemical synthesis could provide an alternative and intriguing strategy for the generation of 1D nanostructures in terms of material diversity, cost, and high-volume productivity. Figure 1- 15 shows the 1D nanomaterials, such as nanowires, nanorods, nanotubes, nanobelts, nanoribbons, and hierarchical nanostructures.

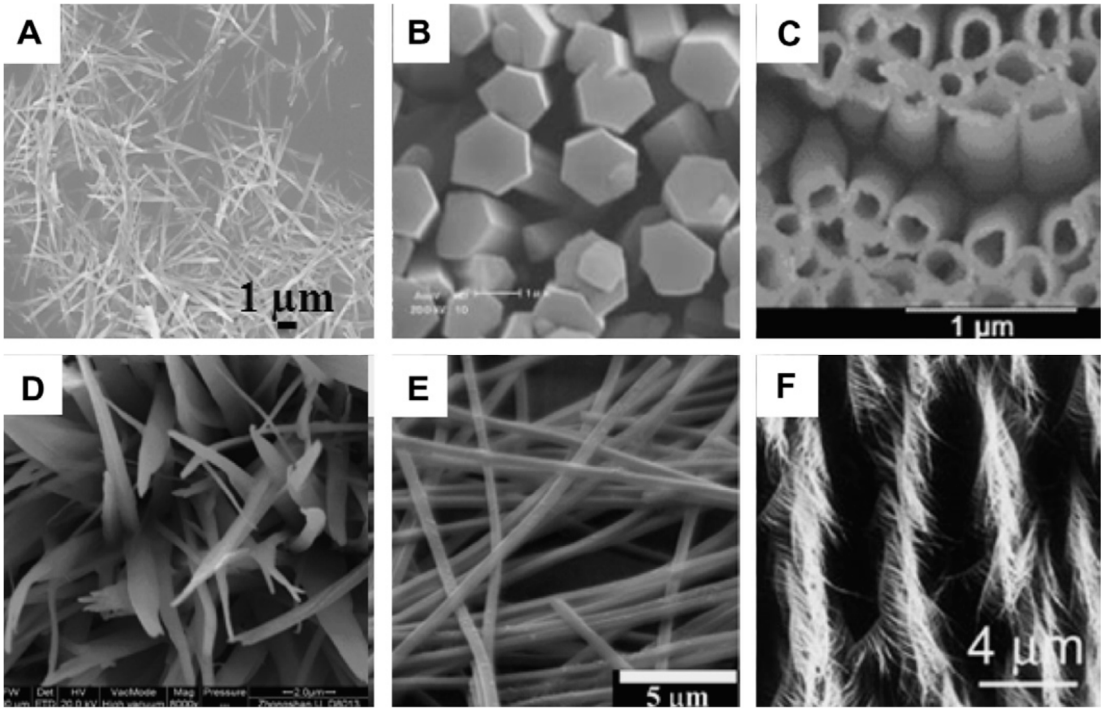


Figure 1- 15. SEM image of different types of 1D NSMs, which is synthesized by several research groups. (A) Nanowires, (B) nanorods, (C) nanotubes, (D) nanobelts, (E) nanoribbons, and (F) hierarchical nanostructures [35].

**Nanotubes**

The carbon nanotubes (CNTs) were discovered in 1991 by S. Iijima in Japan. Since that time, there has been intense research activity related to the synthesis, structure, properties and applications of CNTs. The discovery of carbon nanotubes has also led to many researches into other unidimensional nanostructures such as nanotubes and nanorods both organic and inorganic [26]. It is extremely difficult to give a precise definition of carbon nanotubes, especially because of the huge variety of sizes and conformations they may have. The CNTs have an elongated cylindrical structure with diameters of the order of the nanometers and the lengths of the micron order; they are made up of one or more sheets of graphite coiled on themselves to form a tube. Generally, their terminal part is closed by a fullerene hemispherical structure [27]. In general, nanotubes can be divided into two large families: single-walled nanotubes (SWNTs) and multi-walled nanotubes (MWNTs).

SWNTs can be considered for conformation and structure as belonging to the fullerenes family, while MWNTs are closer to the nanofilament family, which they represent a particular case. MWNTs are nanotubes formed by several concentric SWNTs and are therefore called "multi-walled nanotubes".

**Nanofibers**

Nanofibers are defined as fibers having a diameter of the order of the nanometers. It is important to point out that while the academic community has approved the criterion

of taking nanotechnology less than 100 nm, the business sector has allowed greater flexibility while also accepting values up to 500 nm.

It is obvious that nanofibers geometrically fall into the category 1D which also includes nanotubes and nanorods. Nanofiber production techniques are diverse and include both top-down and bottom-up. Specifically, polymeric nanofibers can be elaborated by a number of techniques such as interfacing polymerization, phase separation, self-assembly and electrospinning.

Inorganic nanofibers (sometimes called ceramic nanofibers) can be prepared with various types of inorganic substances by means of the electrophilic technique. The most frequently mentioned ceramic materials with nanofibrate morphology are titanium dioxide ($TiO_2$), silicon dioxide ($SiO_2$), zirconium dioxide ($ZrO_2$), aluminum oxide ($Al_2O_3$), titanium titanate ($Li_4Ti_5O_{12}$), titanium nitride TiN) or platinum (Pt). Synthesis usually consists of two main phases: in the first phase, the nanofibers of the polymer (organic) are created by the conventional electrophilic technique; In the second phase, the polymeric nanofibers formed of inorganic salts or organometallic compounds are stratified into ceramics by heat treatment. In the formation of nanofibers from the solution, a very high surface/volume ratio is obtained which in a few tens of milliseconds allows complete evaporation of the solvent [28].

**Nanorods**

In the field of nanotechnologies, nanorods are a morphology of nanometric objects. Each of them varies from 1-100 nm. They can be synthesized by metals or semiconductor materials. Standard proportions (length / width) are 3-5. Nanorods are produced by direct chemical synthesis, a combination of ligands acts as a form control agent and as a bond of different facets of the nanorod with different strength. This allows the different nanorod faces to grow in a different way, producing an elongated object.

### 1.3.4 2D nanostructures

Bi-dimensional structures are structures that have two macroscopic and one nanoscopic dimensions, so commonly referred to as thin films, which are often used as protective layers for optical and electrical applications and also for sensing applications.

There are many layered materials with strong in-plane chemical bonds and weak coupling between the layers. These layered structures provide the opportunity to be cleaved into individual freestanding atomic layers. These layers with one dimension strictly restricted to a single layer are called two-dimensional (2D) material (Figure 1-16).

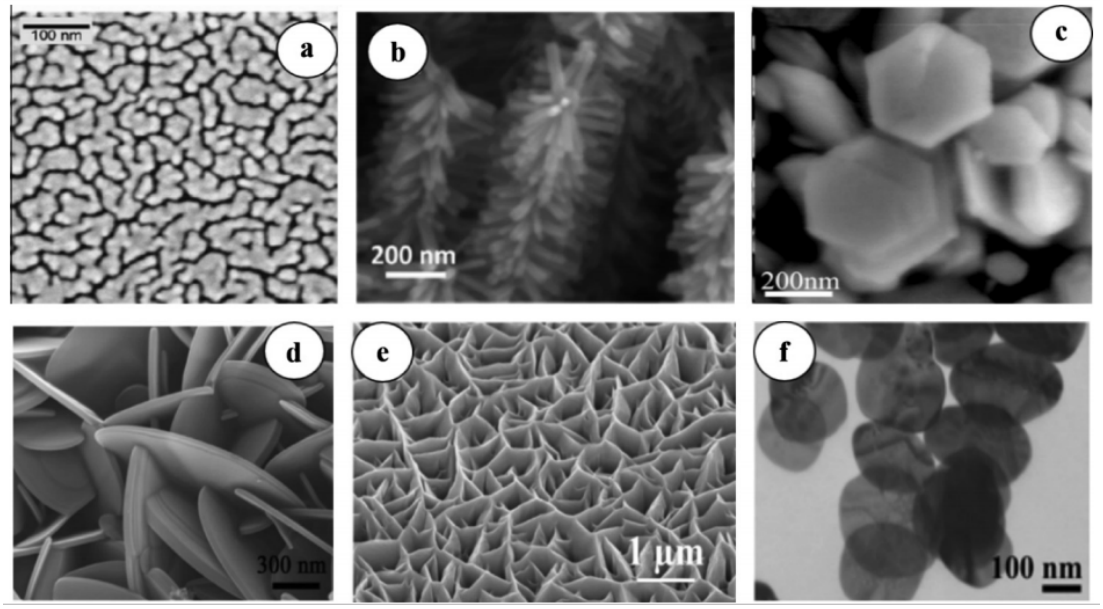


Figure 1- 16. Electron microscope image of different types of 2D NSMs. (a) Nano island structure, (b) branched nanostructures, (C) nanoplates, (D) nanosheets, (E) nanowalls, and (F) nanodisks [29]

### 1.3.5 3D nanostructures

Owing to the large specific surface area and other superior properties over their bulk counterparts arising from quantum size effect, 3D nanomaterials have attracted considerable research interest and many 3D nanomaterials have been synthesized in the past 10 years. It is well known that the behaviour strongly depends on the sizes, shapes, dimensionality and morphologies, which are thus the key factors to their ultimate performance and applications. Therefore, it is of great interest to synthesize 3D nanomaterials with a controlled structure and morphology. In addition, 3D nanostructures are an important material due to its wide range of applications in the area of catalysis, magnetic material and electrode material for batteries. Moreover, the 3D nanomaterials have recently attracted intensive research interests because the nanostructures have higher surface area and supply enough absorption sites for all involved molecules in a small space. On the other hand, such materials with porosity in three dimensions could lead to a better transport of the molecules. In Figure 1- 17 the typical 3D nanomaterial is shown.

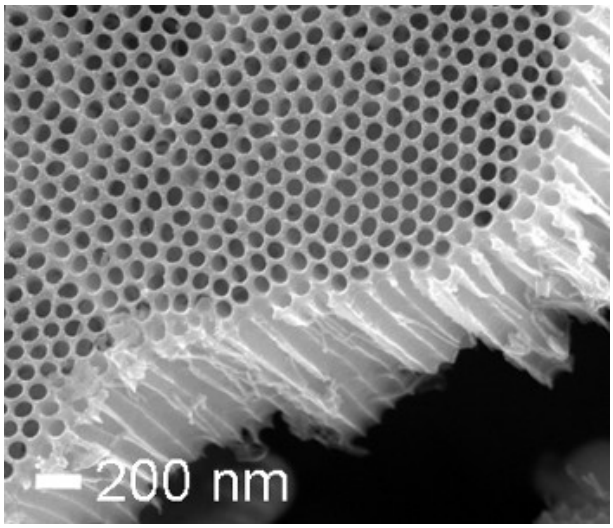


Figure 1- 17. Typical 3D nanomaterial: all dimensions are in the macrometer scale, nanotruscture is related to pore dimension

An example of a material which is well-known to exist in all the mentioned nano-categories is carbon, as shown in Figure 1- 18.

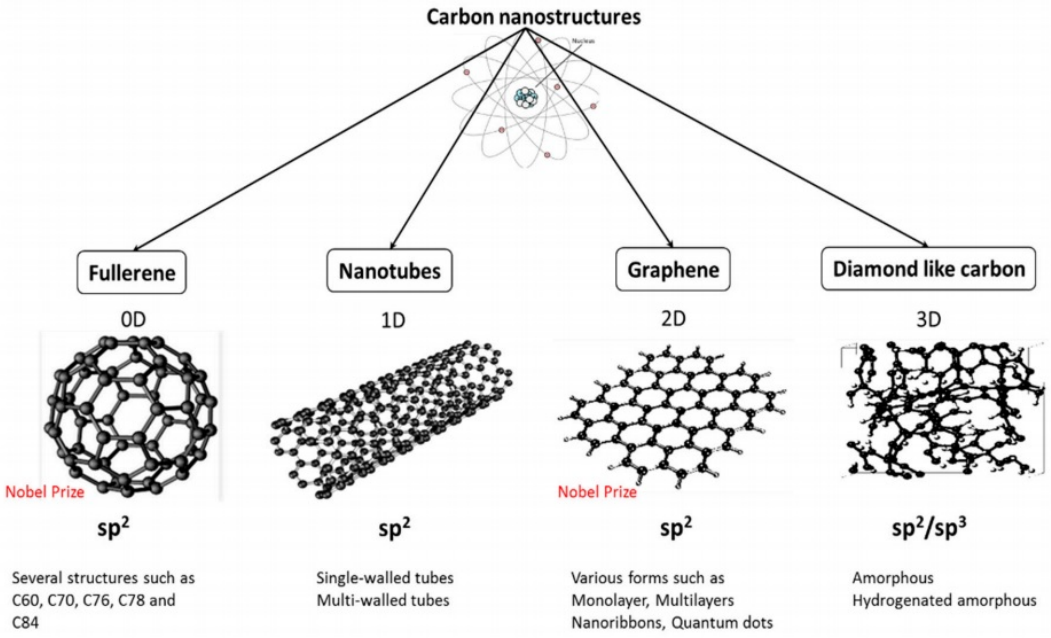


Figure 1- 18. Several forms of carbon nanostructures [30].

### 1.3.6 Hierarchical structures

Hierarchical nanostructures are top-of-the-range structures that are constructed from nano-sized structures such as nanoparticles (0D), nanowires, nanotubes (1D) and nanosheets (2D). Hierarchical nanostructures show well-aligned porous structures without sacrificing the high surface area, and are extremely difficult to achieve these structures due to agglomeration difficulties of oxide nanoparticles. Various hierarchical structures are classified considering the size of the nano-building blocks

and the resulting hierarchical structures, referring to the dimensions of the nano-building blocks and assembled hierarchical structures respectively (Figure 1- 19).

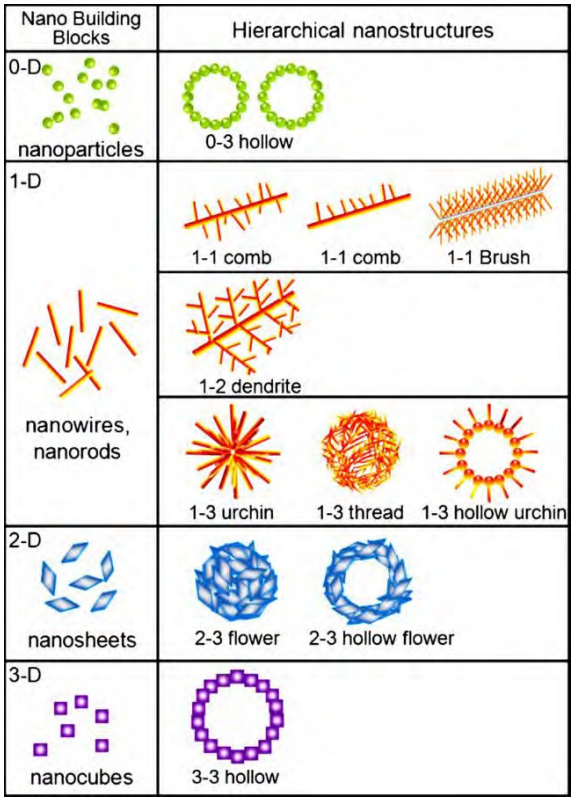


Figure 1- 19. Schematic of diverse 0D, 1D, 2D and 3D hierarchical structures.

For example, “1-3 urchin” describes a structure that includes nanowires / nanorods (1D) with a secondary construction to form a spherical spider (3D) curve and “2-3 flower” indicates a flower type 3D structure consisting of a hierarchical structure assembled from nanosheets (2D). Under this picture, the spherical spheres can be considered as assembling nanoparticles (1D) in a spherical spherical shape (3D). Therefore, based on what has been said, “0-3 hollowspheres” should be considered as a type of hierarchical structure [31].

## 1.4 Nanomaterials synthesis

There are two general approaches to the synthesis of nanomaterials and the fabrication of nanostructures: the bottom-up approach and the top-down approach, schematically described in Figure 1- 20.

The first one includes the miniaturization of materials components (up to atomic level) with further self-assembly process leading to the formation of nanostructures. During self-assembly the physical forces operating at nanoscale are used to combine basic units into larger stable structures. Typical examples are quantum dot formation during epitaxial growth and formation of nanoparticles from colloidal dispersion.

The second one makes use of larger (macroscopic) initial structures, which can be externally-controlled in the processing of nanostructures. Typical examples are etching through the mask, ball milling, and application of severe plastic deformation.

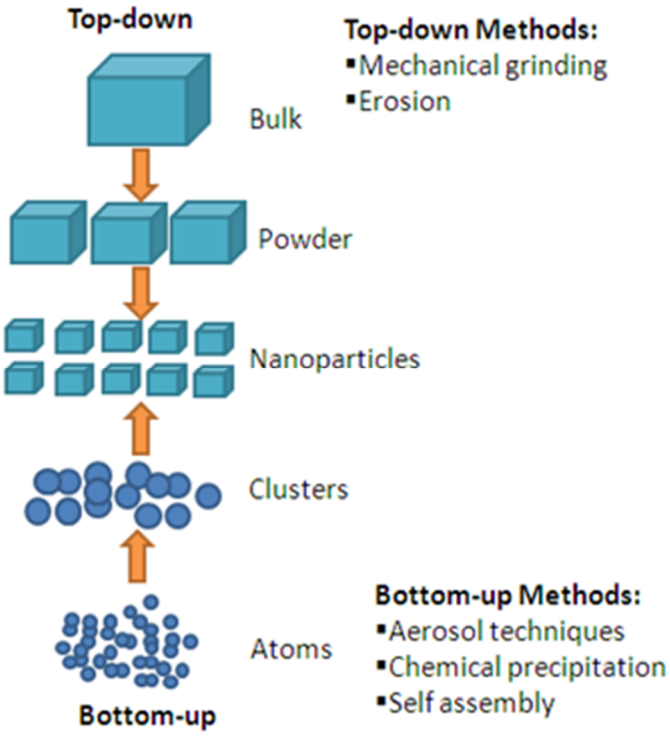


Figure 1- 20. Top down and bottom up approaches for nanomaterials synthesis

### 1.4.1 0-D Preparation techniques

Either top-down or bottom up techniques can be used to produce nanoparticles. For example, sol-gel method is widely used for synthesizing metal oxides, ceramics or glass materials. Sol-gel method normally involves the use of metal alkoxides or organometallic inorganic salts as precursors. In this process, the precursors undergo a series of hydrolysis and polycondensation reaction to form a colloidal suspension or a sol. The sol-gel process involves the transition of a system from a liquid “sol”

(mostly colloidal) into a solid "gel" phase. The drying of the gel followed by calcination at different temperatures lead to the final nano powder.

Another technique widely used to produce nanoparticles is Hydrothermal method. Hydrothermal synthesis is typically carried out in a pressurized vessel called an autoclave with the reaction in aqueous solution [32]. The temperature in the autoclave can be raised above the boiling point of water, reaching the pressure of vapour saturation. Hydrothermal synthesis is widely used for the preparation of metal oxide nanoparticles. The hydrothermal method can be useful to control grain size, particle morphology, crystalline phase and surface chemistry through regulation of the solution composition, reaction temperature, pressure, solvent properties, additives and aging time.

### 1.4.2 1D structure preparation techniques

In recent years, a wide variety of 1D structures of organic and inorganic materials have been synthesized and characterized. These structures have been realized using various techniques. One of the most important factors in the synthesis of 1D structures is controlling the composition, size and crystallinity.

The formation of a solid starting from a liquid, steam or solid phase involves two fundamental steps: nucleation and growth. Since the concentration of the constituent elements (atoms, ions, molecules) of a solid becomes sufficiently high, they aggregate into small clusters (or nuclei) through homogeneous nucleation. With the continuous supply of constituent elements, these nuclei can serve as seeds for further growth in order to form larger structures. Various strategies for 1D structures have been developed with different levels of control over growth parameters including the use of solid anisotropic crystal structure to facilitate the growth of single-dimensional structures; the introduction of a solid liquid interface to reduce the precursor symmetry, the use of different models with 1D morphologies to direct the formation of single-dimensional structures, the use of an over-saturation controller to modify the growth of the structure, using appropriate reagents for kinetically controlling the growth rate of the various precursor facets, the self-assembly of 0D nanostructures, and finally the reduction in the size of 1D microstructures [33,34].

### 1.4.3 2D structures preparation techniques

Bi-dimensional structures are structures that have two macroscopic and one nanoscopic dimensions, so commonly referred to as thin films, which are often used as protective layers for optical and electrical applications and also for sensing applications.

The most popular processes for thin film preparation can be divided into two categories: physical methods and chemical methods. Physical methods are those that a material is physically transferred from a medium to a substrate to form the

film and on the other hand, chemical methods are those which suitable chemical precursors are carried on a substrate where a chemical reaction within film formation occurs [35]. In Figure 1- 21 the most common preparation processes of 2D nanomaterials are reported.

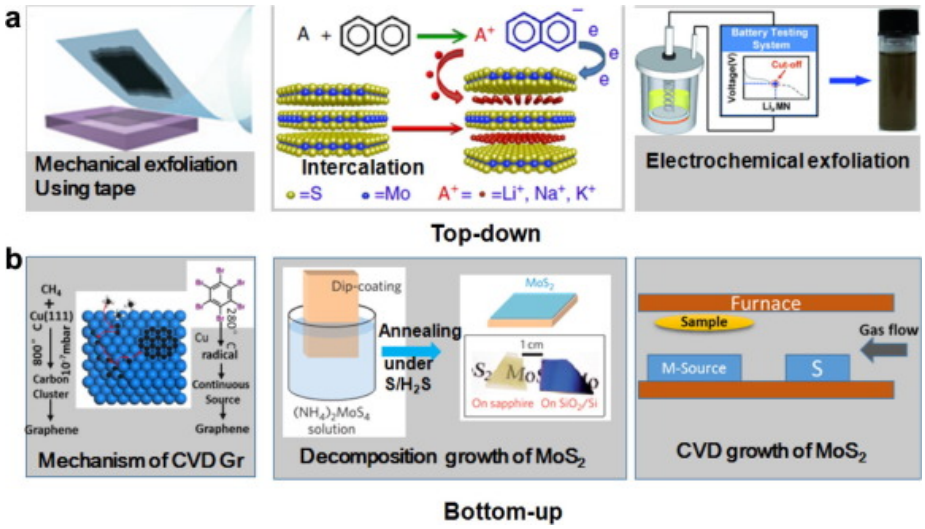


Figure 1- 21. The main 2D-materials preparation routes

### 1.4.4 3D structures preparation techniques

Owing to the large specific surface area and other superior properties over their bulk counterparts arising from quantum size effect, 3D NSMs have attracted considerable research interest and many 3D NSMs have been synthesized in the past 10 years. It is well known that the behaviours of NSMs strongly depend on the sizes, shapes, dimensionality and morphologies, which are thus the key factors to their ultimate performance and applications. Therefore, it is of great interest to synthesize 3D NSMs with a controlled structure and morphology. In addition, 3D nanostructures are an important material due to its wide range of applications in the area of catalysis, magnetic material and electrode material for batteries. Moreover, the 3D NSMs have recently attracted intensive research interests because the nanostructures have higher surface area and supply enough absorption sites for all involved molecules in a small space. On the other hand, such materials with porosity in three dimensions could lead to a better transport of the molecules.

## 1.5 Sensing applications of nanomaterials

Nano-structuring of materials result in changes in the conduction, magnetic, optical, thermal, mechanical properties of issues related to scale phenomena. On the other hand, nano-structuring has a significant effect on sensors performance and increase the sensitivity and selectivity of sensors through reduction in dimensions.

As previously pointed out, an important parameter of a semiconductor material is the width of the "energy gap" that separates the conduction and valance bands. In macroscopic semiconductors, the width of this gap is a fixed parameter determined by the nature of the material. However, the situation changes in the case of nanostructured semiconductor particles, smaller than 10 nm (Figure 1- 22).

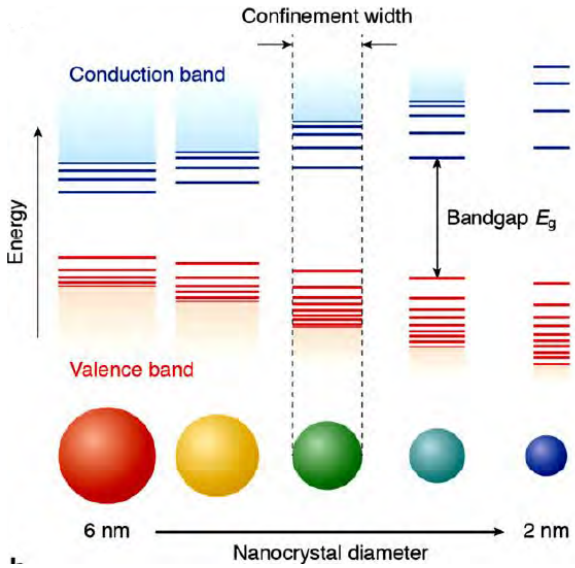


Figure 1- 22. Schematic representation of the quantum confinement effects: the bandgap (or HOMO–LUMO gap) of the semiconductor nanocrystal increases with decreasing size, while discrete energy levels arise at the band-edges. The energy separation between the band-edge levels also increases with decreasing size [38].

This range of dimensions corresponds to the quantum confinement regime, where electronic excitations "feel" the presence of particle bounds and respond to changes in grain size by adjusting their energy spectrum. This phenomenon is known as quantum size effect, while the nanometric particles that exhibit it are often referred to as quantum dots (QD).

As the QD size decreases, the energy gap increases, leading, in particular, to a blue shift in the emission spectrum. At first approximation, this effect can be described by a simple quantum box model. For a spherical R-ray QD, this model assumes that the dependence on the energy gap dimension is simply proportional to 1 / R2. In addition to the growing energy gap, quantum confinement leads to a collapse of massive energy bands of massive material in discrete, or 'atomic' energy levels [36].

### 1.5.1 Nano Effect of Small Size of Metal Oxide Nanoparticles

In addition to the quantum size effect, the reduction in the size of nano crystals results in a so-called "small size effect": when the grain size (D) is twice as small as the thickness of the electronic emptying layer (L) then the resistance of the sensor can be quickly modulated by changing the extent of the impoverishment, obtainable through interactions with the sample gas.

As previously said and now shown in Figure 1- 23, a sensor is considered to be composed of partially sintered crystallites that are connected to their neighbours by necks. Those interconnected grains form larger aggregates that are connected to their neighbours by grain boundaries. On the surface of the grains, adsorbed oxygen molecules extract electrons from the conduction band and trap the electrons at the surface in the form of ions, which produces a band bending and an electron depleted region called the space-charge layer. When the particle size of the sensing film is close to or less than double the thickness of the space-charge layer, the sensitivity of the sensor will increase remarkably. Sun et al. [37] explained the phenomena by a semi quantitative model. Three different cases can be distinguished according to the relationship between the particle size (D) and the width of the space- charge layer (L) that is produced around the surface of the crystallites due to chemisorbed ions and the size of L is about 3 nm for pure $SnO_2$ material in literatures. When $D >> 2L$, the conductivity of the whole structure depends on the inner mobile charge carriers and the electrical conductivity depends exponentially on the barrier height. It is not so sensitive to the charges acquired from surface reactions. When $D \geq 2L$, the space-charge layer region around each neck forms a constricted conduction channel within each aggregate. Consequently, the conductivity not only depends on the particle boundaries barriers, but also on the cross-section area of those channels and so it is sensitive to reaction charges. Therefore, the particles are sensitive to the ambient gas composition. When $D < 2L$, the space-charge layer region dominates the whole particle and the crystallites are almost fully depleted of mobile charge carriers. The energy bands are nearly flat throughout the whole structure of the interconnected grains and there are no significant barriers for intercrystallite charge transport and then the conductivity is essentially controlled by the intercrystallite conductivity [37]. Few charges acquired from surface reactions will cause large changes of conductivity of the whole structure, so the crystalline $SnO_2$ becomes highly sensitive to ambient gas molecules when its particle size is small enough.

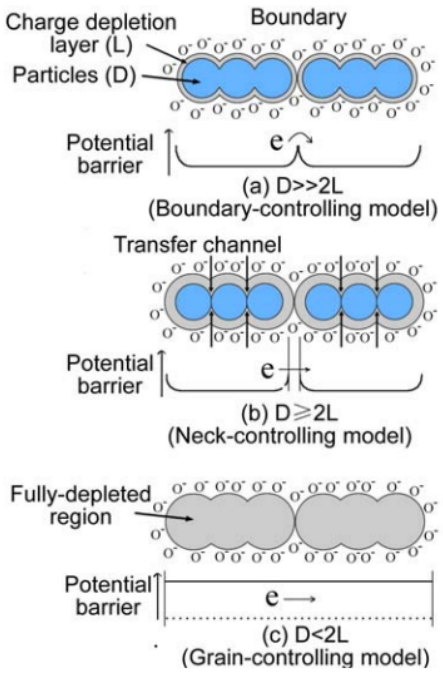


Figure 1- 23. Schematic model of the effect of the crystallite size on the sensitivity of metal-oxide gas sensors: (a) D >> 2L; (b) D ≥ 2L; (c) D < 2L [39].

Based on Xu's model, many new sensing materials are developed to achieve high gas sensing properties. Typically, the nanocomposite of $SnO_2$ and multiwall carbon nanotube (MWCNT) was exploited to detect persistent organic pollutants (POPs) which possess stable chemical properties and are ordinarily difficult to detected with metal oxides. The preparation of materials with size and porosity in the nanometre range is of technological importance for a wide range of sensing applications.

In addition to those just described, another great variety of physical properties such as mechanical strength, plasticity, sintering and alloy capacity, diffusivity and chemical reactivity, as well as crystal growth patterns (self-assembling), are dependent on the particle size. Among the modulating properties there are also thermodynamic properties (critical temperatures for phase transitions such as liquefaction, evaporation), reticular dynamics (optical and acoustic vibration modes of the lattice), optics (photoemission and absorption), electronic (work function, positions of energy levels, electron-phonon coupling), magnetic (magnetization enhancement) and dielectric performance.

## 1.6 Bibliography Chapter 1


1. Neri, G. First Fifty Years of Chemoresistive Gas Sensors. *Chemosensors* **2015**, *3*, 1–20.
2. Brattain, W.H.; Bardeen, J. Surface Properties of Germanium. *Bell Syst. Tech. J.* **1953**, *32*, 1–41.
3. Heiland, G. Zum Einfluß von Wasserstoff auf die elektrische Leitfähigkeit an der Oberfläche von Zinkoxydkristallen. *Zeitschrift für Phys.* **1957**, *148*, 15–27.
4. Shaver, P.J.; J., P. Activated Tungsten Oxide Gas Detector. *Appl. Phys. Lett.* **1967**, *11*, 255–257.
5. Taguchi, N. Gas-detecting device 1970.
6. Kim, H.-J.; Lee, J.-H. Highly sensitive and selective gas sensors using p-type oxide semiconductors: Overview. *Sensors Actuators B Chem.* **2014**, *192*, 607–627.
7. Raguse, B.; Chow, E.; Barton, C.S.; Wieczorek, L. Gold Nanoparticle Chemiresistor Sensors:~ Direct Sensing of Organics in Aqueous Electrolyte Solution. *Anal. Chem.* **2007**, *79*, 7333–7339.
8. Liu, Y.; Parisi, J.; Sun, X.; Lei, Y. Solid-state gas sensors for high temperature applications {\textendash} a review. *J. Mater. Chem. A* **2014**, *2*, 9919–9943.
9. Giancaterini, L.; Emamjomeh, S.M.; De Marcellis, A.; Palange, E.; Resmini, A.; Anselmi-Tamburini, U.; Cantalini, C. The influence of thermal and visible light activation modes on the NO2 response of WO3 nanofibers prepared by electrospinning. *Sensors Actuators, B Chem.* **2016**, *229*, 387–395.
10. Perrozzi, F.; Emamjomeh, S.M.M.; Paolucci, V.; Taglieri, G.; Ottaviano, L.; Cantalini, C. Thermal stability of WS2 flakes and gas sensing properties of WS2/WO3 composite to H2, NH3 and NO2. *Sensors Actuators, B Chem.* **2017**, *243*, 812–822.
11. Wetchakun, K.; Samerjai, T.; Tamaekong, N.; Liewhiran, C.; Siriwong, C.; Kruefu, V.; Wisitsoraat, A.; Tuantranont, A.; Phanichphant, S. Semiconducting metal oxides as sensors for environmentally hazardous gases. *Sensors Actuators B Chem.* **2011**, *160*, 580–591.
12. Capone, S.; Forleo, A.; Francioso, L.; Rella, R.; Siciliano, P.; Spadavecchia, J.; Presicce, D.S.; Taurino, A.M. Solid State Gas Sensors: State of the Art and Future Activities. *ChemInform* **2004**, *35*.
13. Yamazoe, N.; Sakai, G.; Shimanoe, K. Oxide semiconductor gas sensors. *Catal. Surv. from Asia* **2003**, *7*, 63–75.
14. Franke, M. 25emE. E.; Koplin, T. 25emJ. J.; Simon, U. Metal and Metal Oxide Nanoparticles in Chemiresistors: Does the Nanoscale Matter? *Small* **2006**, *2*, 36–50.
15. Bochenkov, V.E.; Sergeev, G.B. Preparation and chemiresistive properties of nanostructured materials. *Adv. Colloid Interface Sci.* **2005**, *116*, 245–254.
16. Xu, C.; Tamaki, J.; Miura, N.; Yamazoe, N. Grain size effects on gas sensitivity

of porous {SnO}2-based elements. *Sensors Actuators B Chem.* **1991**, *3*, 147–155.

17. Xu, C.; Tamaki, J.; Miura, N.; Yamazoe, N. Correlation between Gas Sensitivity and Crystallite Size in Porous {SnO}2-Based Sensors. *Chem. Lett.* **1990**, *19*, 441–444.

18. Barsan, N.; Weimar, U. Conduction model of metal oxide gas sensors. *J. Electroceramics* **2001**, *7*, 143–167.

19. Sakai, G.; Matsunaga, N.; Shimanoe, K.; Yamazoe, N. Theory of gas-diffusion controlled sensitivity for thin film semiconductor gas sensor. *Sensors Actuators B Chem.* **2001**, *80*, 125–131.

20. Matsunaga, N.; Sakai, G.; Shimanoe, K.; Yamazoe, N. Formulation of gas diffusion dynamics for thin film semiconductor gas sensor based on simple reaction{\textendash}diffusion equation. *Sensors Actuators B Chem.* **2003**, *96*, 226–233.

21. Vuong, D.D.; Sakai, G.; Shimanoe, K.; Yamazoe, N. Preparation of grain size-controlled tin oxide sols by hydrothermal treatment for thin film sensor application. *Sensors Actuators B Chem.* **2004**, *103*, 386–391.

22. Vuong, D.D.; Sakai, G.; Shimanoe, K.; Yamazoe, N. Hydrogen sulfide gas sensing properties of thin films derived from {SnO}2 sols different in grain size. *Sensors Actuators B Chem.* **2005**, *105*, 437–442.

23. Sharma, S.; Madou, M. A new approach to gas sensing with nanotechnology. *Philos. Trans. R. Soc. A Math. Phys. Eng. Sci.* **2012**, *370*, 2448–2473.

24. Kim, Y.-T.; Han, J.H.; Hong, B.H.; Kwon, Y.-U. Electrochemical Synthesis of {CdSe} Quantum-Dot Arrays on a Graphene Basal Plane Using Mesoporous Silica Thin-Film Templates. *Adv. Mater.* **2010**, *22*, 515–518.

25. Buffat, P.; Borel, J.-P. Size effect on the melting temperature of gold particles. *Phys. Rev. A* **1976**, *13*, 2287–2298.

26. Iijima, S. Helical microtubules of graphitic carbon. *Nature* **1991**, *354*, 56–58.

27. Dresselhaus, M.S.; Dresselhaus, G.; Eklund, P.C. Science of Fullerenes and Carbon Nanotubes. *Prog. Mater. Sci.* **1996**, 739–755.

28. Wang, C.; Li, X.; Cai, Z.; Huang, J.; Fan, X.; Liu, H.; Xu, W.; Fang, D. A Review on the Electrospun Oxide Nanofibers for Anode Electrodes in Lithium-Ion Batteries. *Curr. Nanosci.* **2017**, *13*.

29. Gupta, A.; Sakthivel, T.; Seal, S. Recent development in 2D materials beyond graphene. *Prog. Mater. Sci.* **2015**, *73*, 44–126.

30. Al-Jumaili, A.; Alancherry, S.; Bazaka, K.; Jacob, M. Review on the Antimicrobial Properties of Carbon Nanostructures. *Materials (Basel).* **2017**, *10*, 1066.

31. Ding, B.; Wang, M.; Yu, J.; Sun, G. Gas Sensors Based on Electrospun Nanofibers. *Sensors* **2009**, *9*, 1609–1624.

32. Pan, Z.; Wang, Y.; Huang, H.; Ling, Z.; Dai, Y.; Ke, S. Recent development on preparation of ceramic inks in ink-jet printing. *Ceram. Int.* **2015**, *41*, 12515–12528.

33. Wagner, R.S.; Ellis, W.C. Vapor-Liquid-Solid Mechanism of single crystal growth. *Appl. Phys. Lett.* **1964**, *4*, 89–90.

34. Sen, S.; Kanitkar, P.; Sharma, A.; Muthe, K.P.; Rath, A.; Deshpande, S.K.; Kaur, M.; Aiyer, R.C.; Gupta, S.K.; Yakhmi, J. V Growth of {SnO}2/W18O49 nanowire hierarchical heterostructure and their application as chemical sensor. *Sensors Actuators B Chem.* **2010**, *147*, 453–460.

35. Tiwari, J.N.; Tiwari, R.N.; Kim, K.S. Zero-dimensional, one-dimensional, two-dimensional and three-dimensional nanostructured materials for advanced electrochemical energy devices. *Prog. Mater. Sci.* **2012**, *57*, 724–803.

36. Rabouw, F.T.; de Mello Donega, C. Excited-State Dynamics in Colloidal Semiconductor Nanocrystals. *Top. Curr. Chem.* **2016**, *374*.

37. Sun, Y.-F.; Liu, S.-B.; Meng, F.-L.; Liu, J.-Y.J.-H.; Jin, Z.; Kong, L.-T.; Liu, J.-Y.J.-H. Metal Oxide Nanostructures and Their Gas Sensing Properties: A Review. *Sensors* **2012**, *12*, 2610–2631.

# CHAPTER 2.
# Transition metal dichalcogenides as promising high performances gas sensors

## ABSTRACT

This chapter represent an in-depth analysis of the use of layered materials as gas sensors. In particular it is focused on Transition metal dichalcogenides, the mechanisms involved in gas sensing, their synthesis methods and properties in light of practical applications.

## CONTENT

## 2.1 2D semiconductors for gas sensing applications

Among the sensing materials, metal oxides generally show advantages of high sensitivities and low cost; however, high operating temperature (OT), large power requirement, and low selectivity have been their serious drawbacks. Thus, this is important to explore novel sensing materials with high sensitivity and low operating temperature. Graphene is one of those 2-dimensional type of materials which is highly studied for gas sensing applications. Graphene is an atomic-thin layered carbon nanomaterial with a large surface-to-volume ratio, that provides large adsorbing capacity of gas molecules and strong surface activities.

Recently, layered inorganic analogues of graphene, such as transition metal dichalcogenides (TMDs) including $MoS_2$, $WS_2$, $MoSe_2$, $WSe_2$, $ReS_2$, and $ReSe_2$, as well as layered metal oxides ($MoO_3$ and $SnO_2$), layered group III–VI semiconductors (GaS, GaSe, and $SnS_2$), phosphorene, h-BN, etc., have also raised attention due to their thickness-dependent physical and chemical properties. In addition to having a large surface-to-volume ratio like graphene, these layered inorganic analogues also have semiconducting properties with an appropriate bandgap, which is attractive for modulating the transport characteristics to enhance the sensing performance [1].

### 2.1.1 Oxygen ions surface adsorption mechanism in 2D materials

As previously explained in detail in Chapter 1, in conventional metal oxide-based gas sensors like $SnO_2$, the sensing mechanism is related adsorbed oxygen ions on their surface. In the normal operating temperature range (200 ˚C-500 ˚C), oxygen negative ions such as $O_2^-$, $O^-$ and $O^{2-}$ are adsorbed on the surface of metal oxides and charge them negatively. Different gases adsorbing on metal oxides will interact with the oxygen negative ions, and change the conductivity of the metal oxides. After exposing to a reducing gas, it releases a negative charge due to the oxidation, and results in increasing the conductivity of metal oxides.

Apart from the conventional metal oxides, the gas sensing of graphene and related layered inorganic analogues like Transition Metal Dichalcogenides (TMDs) is mainly based on the charge transfer processes, in which the sensing materials act as charge acceptors or donors. When layered materials are exposed to various gases, the charge transfer reaction happens between the sensing materials and the adsorbed gases, accompanied by different charge transfer directions and quantities, which results in different changes of the material resistance. If the sensing materials are re-exposed to air, desorption of gas molecules takes place, causing the resistance of the sensing material to return to the initial state. Taking n-type $MoS_2$ as an example, Yue et al. [2] reported the charge transfer between different gas molecules and monolayer MoS2, and the adsorbed gas molecules include $O_2$, $H_2O$, $NH_3$, NO, $NO_2$. Figure 2- 1 shows the charge density difference for the above gases interacting with monolayer

$MoS_2$, where the red region shows the charge accumulation, while the green region shows the charge depletion.

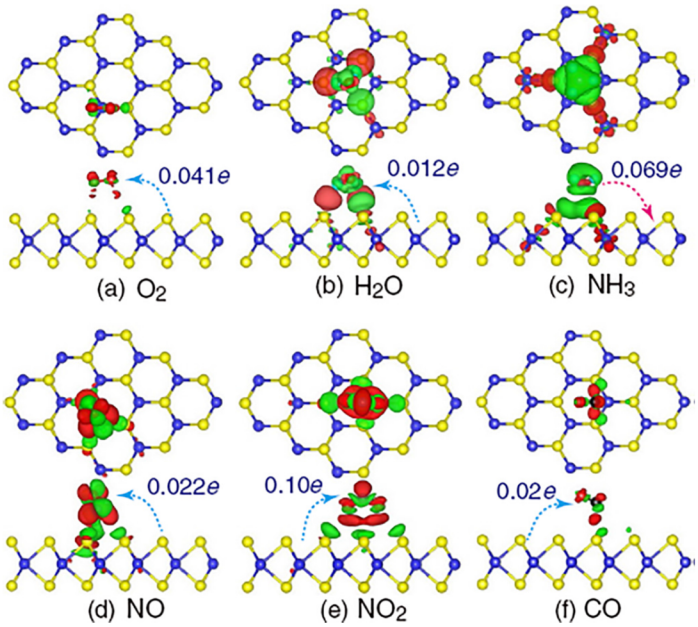


Figure 2- 1. Charge transfer process and density difference plots for (a) $O_2$, (b) $H_2O$, (c) $NH_3$, (d) NO, (e) $NO_2$, and (f) CO interacting with monolayer $MoS_2$ [2]

Before gas adsorption, some electrons have already present in the conduction band (CB) of the n-type $MoS_2$ monolayer. When n-type $MoS_2$ is exposed to these electron-acceptor gases such as $O_2$, $H_2O$, NO, $NO_2$, and CO, the electron charges are transferred from $MoS_2$ to the sensitive gases, resulting in a decrease of carrier density in $MoS_2$ and therefore, leading to an increase of $MoS_2$ resistance. On the other hand, $NH_3$ molecules adsorbed on the $MoS_2$ act as charge donors and transfer electrons to the $MoS_2$ monolayer, and result in increasing the electron carrier density of the n-type $MoS_2$ monolayer, reducing its resistance [2].

## 2.2 Generalities of TMDs

Graphene, while being fundamentally and technologically interesting for a variety of applications, has some important drawbacks regarding its gas sensing properties. As it has not a right bandgap, it can work as gas sensor only if used together with other materials or in its more reactive form, the Graphene Oxide [3]. In contrast, single-layered 2D TMDs whose generalized formula is $MX_2$, where M is a transition metal of groups 4-10 and X is a chalcogen (Figure 2- 2), exhibit versatile chemistry. This offers opportunities for fundamental and technological research in a variety of fields

including catalysis, energy storage, sensing and electronic devices such as field-effect transistors and logic circuits.

The properties of bulk TMDs are diverse, ranging from insulators such as $HfS_2$, semiconductors such as $MoS_2$ and $WS_2$, semimetals such as $WTe_2$ and $TiSe_2$, to true metals such as $NbS_2$ and $VSe_2$. A few bulk TMDs such as $NbSe_2$ and $TaS_2$ exhibit low-temperature phenomena including superconductivity, charge density wave (CDW, a periodic distortion of the crystal lattice) and Mott transition (metal to non-metal transition). Exfoliation of these materials into mono- or few-layers largely preserves their properties, and leads to additional characteristics due to confinement effects. The chemistry of $MX_2$ compounds thus offers opportunities for going beyond graphene and opening up new fundamental and technological pathways for inorganic 2D materials [4].

### 2.2.1 Composition and crystal structure of TMDs

Typical TMDs form is a graphite-like layered structure that leads to strong anisotropy in their electrical, chemical, mechanical and thermal properties. Group 4-7 TMDs in Figure 2- 2 (a) are predominantly layered, whereas some of group 8-10 TMDs are commonly found in non-layered structures. In layered structures, each layer typically has a thickness of 6~7 Å, which consists of a hexagonally packed layer of metal atoms sandwiched between two layers of chalcogen atoms. The intra-layer M-X bonds are predominantly covalent in nature, whereas the sandwich layers are coupled by weak van der Waals forces thus allowing the crystal to readily cleave along the layer surface. Several studies have shown that the single layers are stabilized by development of a ripple structure as in the case of graphene [5,6]. The metal atoms provide four electrons to fill the bonding states of TMDs such that the oxidation states of the metal (M) and chalcogen (X) atoms are +4 and –2, respectively. The lone-pair electrons of the chalcogen atoms terminate the surfaces of the layers, and the absence of dangling bonds makes those layers stable against reactions with environmental species. The M–M bond length varies between 3.15 Å and 4.03 Å, depending on the size of the metal and chalcogen ions. These values are 15-25% greater than the bond lengths found in elemental transition metal solids, indicating limited energetic and spatial overlap of the d orbitals in TMD compounds. The metal coordination of layered TMDs can be either trigonal prismatic or octahedral (typically distorted and sometimes referred to as trigonal-antiprismatic) as shown in Figure 2- 2 b and c, respectively. Depending on the combination of the metal and chalcogen elements, one of the two coordination modes is thermodynamically preferred. In contrast to graphite, bulk TMDs exhibit a wide variety of polymorphs and stacking polytypes (a specific case of polymorphism) because an individual $MX_2$ monolayer, which itself contains three layers of atoms (X-M-X), can be in either one of the two phases. Most commonly encountered polymorphs are 1T, 2H and 3R where the letters stand for trigonal, hexagonal and rhombohedral, respectively, and the digit indicates the number of X-M-X units in the unit cell (that is, the number of layers in the stacking sequence).

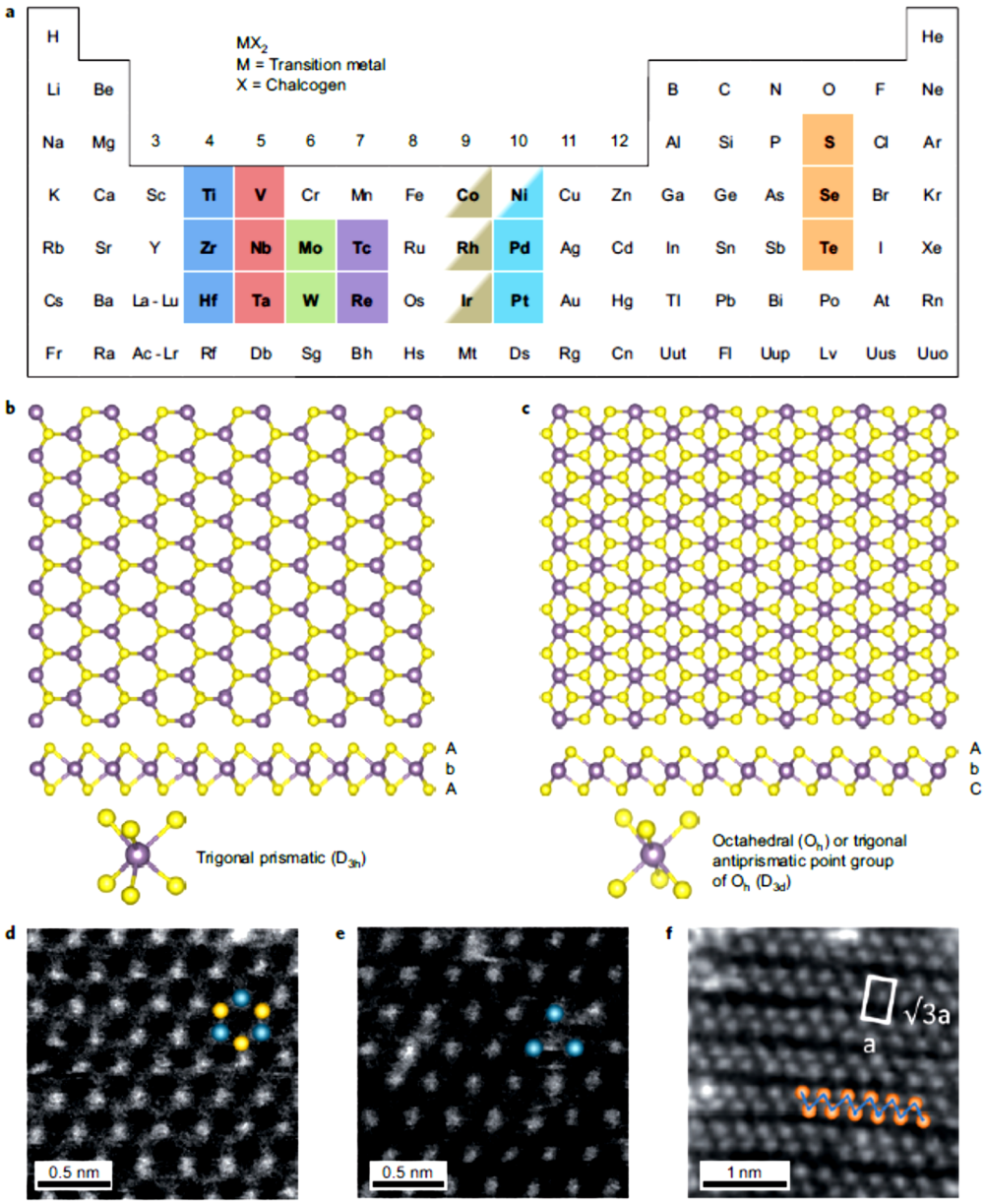


Figure 2- 2. Structure of monolayered TMDs. a) Partial highlights for Co, Rh, Ir and Ni indicate that only some of the dichalcogenides form layered structures. For example, $NiS_2$ is found to have pyrite structure but $NiTe_2$ is a layered compound. b and c) c-Axis and section view of single-layer TMD with trigonal prismatic (b) and octahedral (c) coordinations. Atom colour code: purple, metal; yellow, chalcogen. The labels AbA and AbC represent the stacking sequence where the upper- and lower-case letters represent chalcogen and metal elements, respectively. d and e) Dark-field scanning transmission electron microscopy image of single-layer $MoS_2$ showing the contrast variation of 1H (d) and 1T (e) phases. Blue and yellow balls indicate Mo and S atoms, respectively. f) Zigzag chain clusterization of W atoms due to Jahn–Teller distortion in single layer $WS_2$. The clustered W atoms are represented by orange balls. The √3a x a unit cell of the superstructure is indicated with a white rectangle [7].

### 2.2.2 Electronic properties

From a practical point of view, the electronic properties of TMDs change with composition, and in particular arise from the progressive filling of the non-bonding d-bands from group 4 to group 10 species, according to Table 2-1.

| Group | M | X | Properties |
|---|---|---|---|
| **4** | Ti, Hf, Zr | S, Se, Te | Semiconducting ($E_g$= 0.2 ~ 2 eV). |
| **5** | V, Nb, Ta | S, Se, Te | Narrow band metals (ρ~$10^{-4}$ Ω.Cm) or semimetals. Superconducting. Charge density wave (CDW). Paramagnetic, antiferromagnetic, or diamagnetic. |
| **6** | Mo, W | S, Se, Te | Sulfides and selenides are semiconducting ($E_g$= 1 eV). Tellurides are semimetallic (ρ~$10^{-3}$ Ω.Cm). Diamagnetic |
| **7** | Tc, Re | S, Se, Te | Small-Gap semiconductors. Diamagnetic. |
| **10** | Pd, Pt | S, Se, Te | Sulfides and selenides are semiconducting ($E_g$= 0.4 eV) and diamagnetic. Tellurides are metallic and paramagnetic. $PdTe_2$ is superconducting |

Table 2-2. Electronic character of different layered TMDs [8]

## 2.3 TMDs Exfoliation techniques

As previously reported, the various techniques to obtain nanomaterials can be classified in two main categories: top-down and bottom-up approaches. Similarly, this organization can be applied also to the various exfoliation process developed to obtain 2D-materials.

In particular, the top down exfoliation procedures are the most widespread, and consist in the exfoliation starting from the bulk material. They include techniques such as mechanical exfoliation, chemical intercalation exfoliation, liquid and mixed exfoliation. On the other hand, bottom up techniques generate single or few layer structures by joining different blocks of molecules or compounds, as happens for example in chemical vapor deposition.

### 2.3.1 Top-Down Approaches

#### Mechanical exfoliation

Mechanical exfoliation is one of the earliest and most common top-down approach to obtain ultrathin 2D TMD nanosheets. The resistance in the exfoliation of layered materials like TMDs is the van der Waals attraction between the adjacent layers. The process to overcome this force and obtain mono few layers from the bulk TMD is a mechanical phenomenom. In general, there are two kinds of mechanical routes to exfoliate bulk TMDs into mono-few layered TMDs, normal force and lateral force. One applies normal force to overcome the van der Waals forces when peeling two layers apart, and the other one can also exert lateral force to promote the relative motion between the two layers. These two mechanical routes are illustrated in Figure 2- 3. In the following sections, in terms of the above two mechanical routes, ball milling and sonication mechanical exfoliation routes are discussed [17].

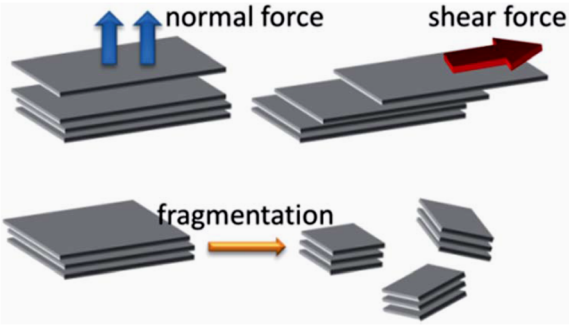


Figure 2- 3. Two kinds of mechanical routes for mechanical exfoliation of van der Waals layered material into mono-few layers and the auxiliary route for fragmentation.

#### Mechanical exfoliation: Micromechanical cleavage

The general idea of this method is the cleavage of graphene or TMD layers from the bulk Highly oriented pyrolytic graphite (HOPG) surface. The procedure is presented in Figure 2- 4. The exfoliation mechanics of this method are that the Scotch tape is applied to the HOPG surface and thus exerts a normal force. If one takes great pains to repeat this normal force numerous times, the TMD layer becomes thinner and thinner and finally it will become single-layer TMD. The exfoliation mechanics are dominated by a normal force. This method can be used to prepare high-quality and large-area TMD flakes. However, this method is extremely labour-intensive and time-consuming. It is limited to laboratory research and seems impossible to scale up for industrial production [17].

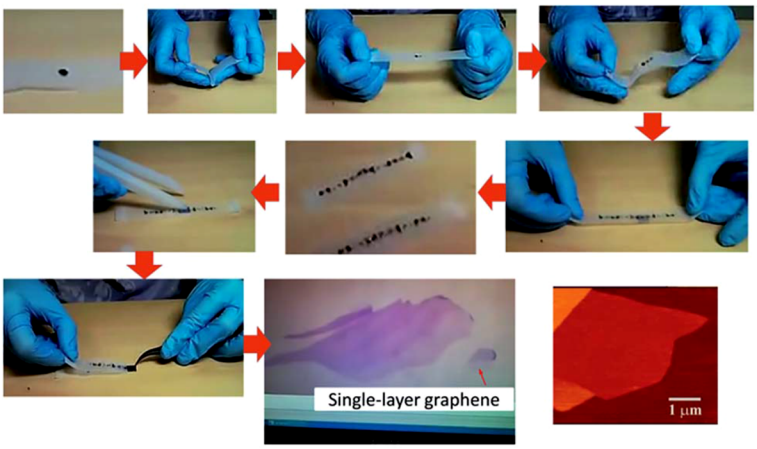


Figure 2- 4. An illustrative procedure of the Scotch-tape based micromechanical cleavage of HOPG.

**Mechanical exfoliation: Ball milling**

Besides the sonication-based exfoliation method which is a normal-force-dominated way, shear force can also be utilized to laterally exfoliate bulk TMD into mono-few layers TMD flakes, as schematized in Figure 2- 5. Ball milling, a common technique in the powder production industry, is a good candidate for generating shear force. The mechanical mechanism of ball milling in exfoliating mono-few layers TMDs can be illustrated in Figure 2- 5.

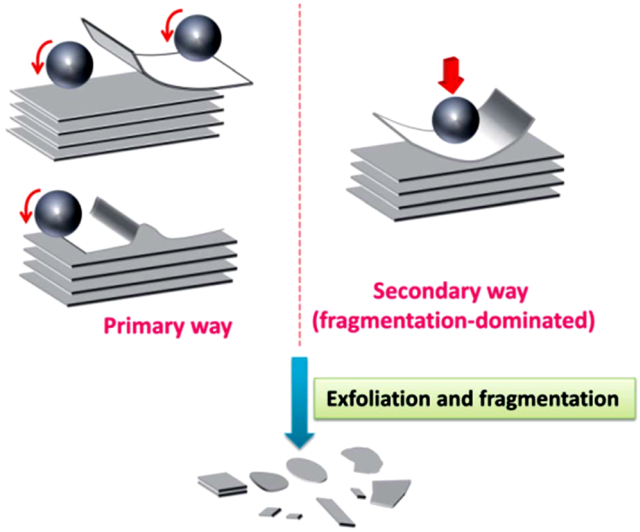


Figure 2- 5. Illustration of the mechanical mechanism for exfoliation via ball milling.

In most ball milling apparatus, there are two possible ways responsible for the exfoliation and fragmentation effects. The primary one is the shear force, which is thought to be an excellent mechanical route for exfoliation. This way is highly desired for achieving large-sized TMD flakes. The secondary one is the collisions or vertical

impacts applied by the balls during rolling actions. In this way, large flakes can fragment into small ones, and some-times even destroy the crystalline nature of structures to form amorphous or non-equilibrium phases. Therefore, it is expected that to attain high-quality and large-sized graphene, the secondary effect should be minimized.

Generally, two types of ball milling techniques, i.e. planetary ball mills and stirred media mills, are widely used. Besides, ball milling techniques are being used in wet and dry modes. Initially, ball milling was adopted to reduce the size of graphite, and it was found that graphitic flakes with a thickness down to 10 nm could be obtained. But this milling scheme was not further continued to obtain graphene. Until 2010, following the same idea as the sonication-based liquid-phase exfoliation of graphene, Knieke et al., Zhao et al., modified the milling technique to produce graphene. So far variety of studies has done to investigate the effect of different solvents with diverse surface tension energy during wet ball miling such DMF, NMP, tethramethylura etc [17].

**Chemical and Liquid phase Exfoliation (LPE)**

In chemistry, the intercalation process consists in the inclusion or reversible insertion of a molecule or an ion in compounds that have a stratified structure. This technique therefore constitutes the basis of another typical exfoliation method of graphite and TMDs. In fact, the intercalation of ionic species increases the spacing between the layers, weakening the interlayer adhesion and consequently reducing the energy barrier for exfoliation [18].

The main step of this process is certainly the formation of the $LiXS_2$ complex, and this reaction can be controlled to manage the yield in terms of monolayer production. These techniques can be carried out at high temperatures and for a long time, even days. In literature there are other methods that directly use galvanic cells containing lithium ions, allowing a better control of the process and therefore the yield [4,19].

The importance of being able to control the formation of these complexes lies not only in the regulation of yield but also in the prevention of the formation and precipitation of compounds such as $Li_2S$ [4]. In fact, an important limitation of this technology consists in the effect, not yet fully clarified, that the presence of lithium ions can have on the final structure and on the properties of the product obtained. In particular these can influence the nature of the final layers, which in some cases exhibit a behaviour different from the semiconductors due to the formation of a metallic phase [12].

The solvents most commonly used to promote interleaving are n-butyllithium, t-butyllithium and Methyl-butyllithium [20–23], always used dispersed in a solvent, generally hexane. Each compound has a different exfoliation efficiency.

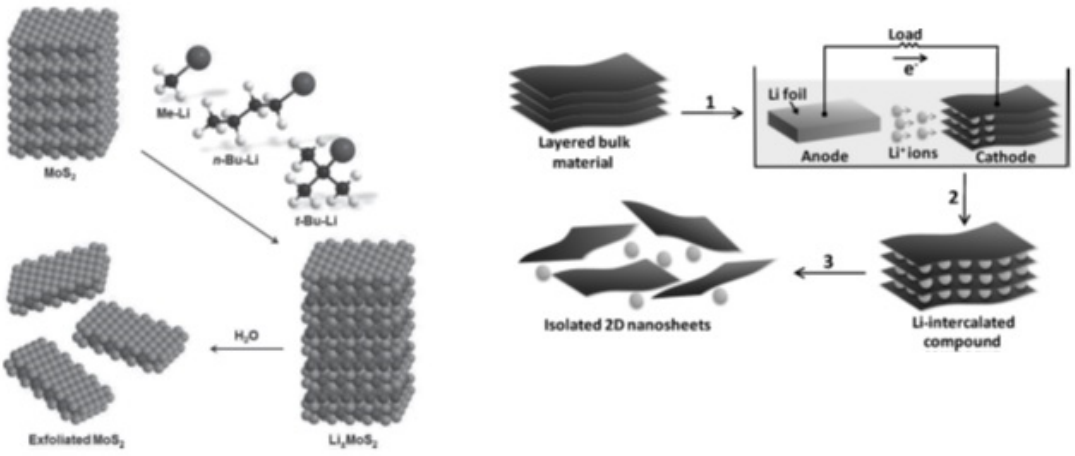


Figure 2- 6. Example of a technique of intercalation with lithium ions for MoS2

Obviously, the intercalation it must be followed by a subsequent treatment to complete the exfoliation process. This treatment can consist in a simple prolonged agitation with following centrifugation and collection of the supernatant [9], or in a sonication step, generally in water, always followed by appropriate separation by centrifugation [8] [12].

Studies concerning this type of process have allowed us to establish a hierarchy of efficiency for the solvents used, in particular A. Ambrosi, Z. Sofer et al. [11], have shown that among the organolithic reagents, the best are n-butyllithium, t-butyllithium. These compounds in fact give rise to a production of larger flakes in terms of surface and smaller in terms of thickness (number of layers). Moreover, subjected to electrical tests, the exfoliated flakes with these reagents provide better answers.

**Liquid Exfoliation via Ultrasonication**

The exfoliation methods discussed so far have been tested but have several disadvantages such as duration, sensitivity to environmental conditions and, as far as TMDs are concerned, they are not very efficient in the case of selenides and tellurides [24]. A more recent exfoliation technique consists in using the material placed in a specific solvent and exposing it to the effect of ultrasound. When the liquid is subjected to this treatment, the waves propagate through it causing an alternation of high and low pressure depending on the frequency of the electric generator. The rapid movement of the probe creates an effect called cavitation. Cavitation occurs when vibrations generate a series of microscopic bubbles in the solution, pockets of space wedged between the molecules that form and then still collapse under the weight of the solution, sending small shock waves into the surrounding substance. Thousands of these bubbles that form and collapse constantly, create powerful waves of vibration. The resulting hydrodynamic forces are able to break up the agglomerates, overcoming the van der Waals forces. As a result, the exfoliation of the stratified materials is obtained, showing single or few layers as shown in Figure 2- 7 [25].

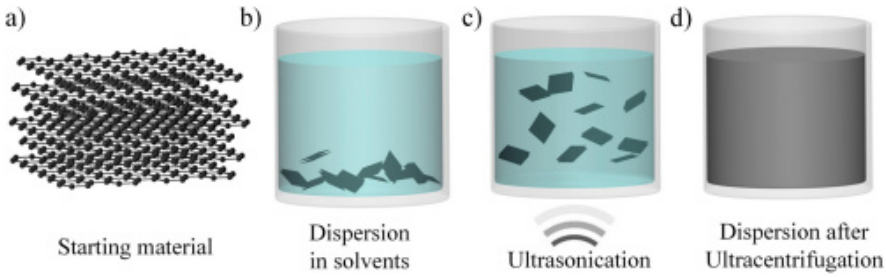


Figure 2- 7. Schematic representation of the liquid exfoliation process

The sonication operation is followed by a centrifugation operation, after which the supernatant containing the material in the form of a layer is collected. The sonication energy, the centrifugation speed and the duration of both these steps are important parameters to adjust in order to improve the efficiency of the whole process.

The choice of solvent is very important. This must:

- Being able to disperse the material to be exfoliated avoiding as much as possible re-agglomeration phenomena;
- Ensure an adequate degree of exfoliation.

A data that allows, in the first instance, to identify the family of solvents that can be used for the process is the surface tension. In fact, in the literature, the substances used for this type of exfoliation have a surface energy of between 25 and 40 mJ / $m^2$ [26]. The most commonly used solvents are N-methyl pyrrolidone (NMP), di-methyl formamide (DMF), acetonitrile (ACN) and water-ethanol mixtures, generally around 50% by weight [18].

It has been demonstrated that such a kind of liquid-phase exfoliation of graphite is attributed to the small net energetic cost during the exfoliation process. This energy balance for the graphene and solvent system can be expressed as the enthalpy of mixing per unit volume in equation (2-1)

$$\frac{\Delta H_{mix}}{V_{mix}} = \frac{2}{T_{flake}}(\delta_G - \delta_{sol})^2 \phi \qquad (2\text{-}1)$$

in which $T_{flake}$ is the thickness of a TMD flake, □ is the TMD volume fraction, and $\delta_i$ is the square root of the surface energy of phase i (i denotes TMD or solvent) which is denoned as the energy per unit area required to overcome the van der Waals forces when peeling two sheets apart. It is obvious that when the graphene and solvent surface energies are close, the mixing enthalpy will be smaller, and the exfoliation occurs more easily. Therefore, the surface energy of a solvent is imperative for such a kind of exfoliation. By using a range of solvents with different surface energies and measuring the corresponding concentration of the resultant graphene dispersions, the

optimal surface energy of the solvents can be roughly estimated. The good solvents tend to have a surface energy of 70-80 $mJm^{-2}$, or a surface tension energy of 40-50 $mJ\ m^{-2}$ at room temperature.[18]

If the sonication time is long or sonication is intensive, the solvents would suffer from degradation and their properties will also be changed. These may make the large-scale production of graphene by sonication fail. Therefore, in these conditions, the above-mentioned model should be modified. In the sonication method, the exfoliation mechanics originate from the liquid cavitation, as illustrated in Figure 2- 8. The cavitation-induced bubbles distribute around the layered TMDs.

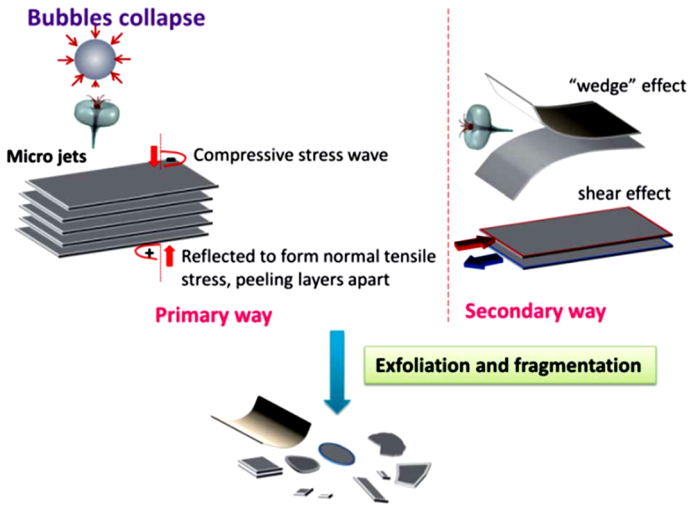


Figure 2- 8. Illustration of the mechanical mechanism for exfoliation via sonication.

When these bubbles collapse, micro-jets and shock waves will act on the TMD surfaces instantly, resulting in compressive stress waves which propagate throughout the TMD body. According to the theory of stress waves, once the compressive wave spreads to the free interface of TMD, a tensile stress wave will be reflected back to the body. As such, collapses of numerous micro-bubbles will lead to intensive tensile stress in the TMD flakes; just as intensive "sucking discs" exfoliate the flakes. In addition, a secondary process is possible in that the unbalanced lateral compressive stress can also separate two adjacent flakes by a shear effect. Also, the micro-jets may split the TMD flakes just as a wedge is driven into the interlayer. In a word, it is the tensile stress that effectively exfoliates TMDs into mono-few layers TMD flakes, resulting in a normal force dominated way [17].

### Two-stage exfoliation: grinding and sonication technique

Chemical exfoliation of TMDs bulk crystals is an attractive alternative to obtain large scale synthesis of 2D nanostructures. Layers within bulk TMDs crystals were first intercalated with *n*-butyl lithium in hexane. Subsequently, water is added and the reaction with n-butyl lithium produced $H_2$ gases, which expand and exert internal pressure to push the layers apart. Zhang's group developed another simple yet high

yield and efficient strategy to obtain TMDs nanosheets based on a controlled electrochemical lithiation process (Figure 2- 9). Liquid-phase exfoliation, first proposed by Coleman and co-workers, is another great top-down approach for 2D TMDs preparation, using sonication to exfoliate the bulk crystals in liquid solvents (Figure 2- 9b). This approach is very simple and scalable to obtain quantities of TMDs exfoliates. In addition, liquid-phase exfoliation of TMDs crystals can also be achieved by exposing those materials to shear treatments [27].

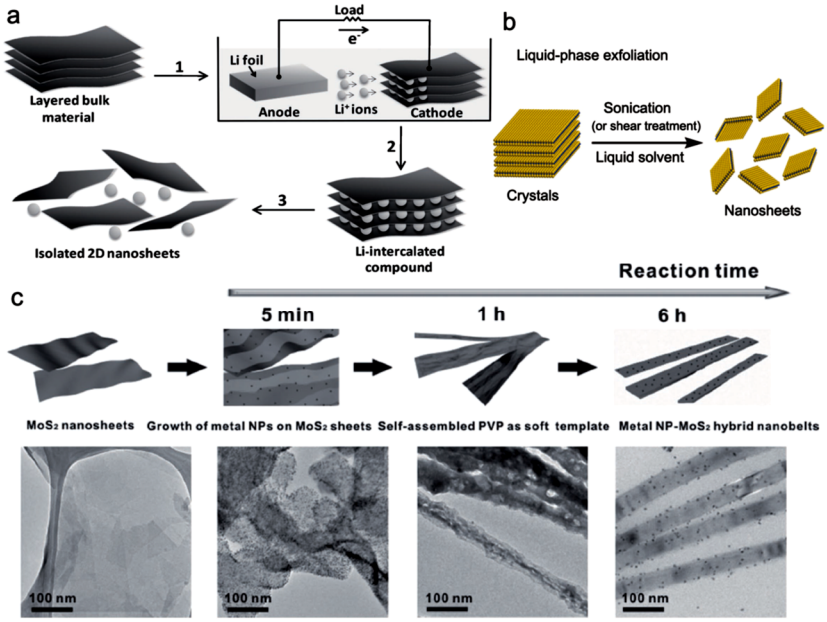


Figure 2- 9. Top-down approaches for the preparation of 2D and 1D TMDs nanostructures. a) Electrochemical lithiation process for preparing 2D MoS2 nanosheets. b) Liquid-phase exfoliation route for the preparation of 2D TMDs nanosheets from their bulk crystals. c) Schematic illustration of the synthesis process of 1D MoS2 nanobelts from their 2D-related morphologies [27].

### 2.3.2 Bottom-Up Approaches

Gas phase methods are ideal for the production of thin films. Gas phase synthesis can be carried out chemically or physically. Chemical vapour deposition (CVD) is a widely used industrial technique that can coat large areas in a short space of time. During the procedure, metal oxide is formed from a chemical reaction or decomposition of a precursor in the gas phase [19,23]. Physical vapour deposition (PVD) is another thin film deposition technique. The process is similar to chemical vapour deposition (CVD) except that the raw materials/precursors, i.e. the material that is going to be deposited starts out in solid form, whereas in CVD, the precursors are introduced to the reaction chamber in the gaseous state. The process proceeds atomistically and mostly involves no chemical reactions.

In general, chemical vapor deposition (CVD) is a chemical process often used in the semiconductor industry to obtain solids in the form of thin films. Typically, a solid substrate is exposed to precursors in gaseous form in other temperature environments. These react or decompose on the surface of the same, generating the

desired compound. The presence of by-products in gaseous form is frequent, which are suitably eliminated through a flow of inert gas in the reaction chamber. The process temperatures vary between 200 and 1600 ° C, and the pressure range is equally wide, being able to operate under vacuum up to pressures above the atmospheric one [28]. The CVD process can therefore be summarized in 4 phases:

1. Introduction of reagent gases into the chamber and transport to the substrate

2. Absorption of reagents on the substrate

3. Diffusion and decomposition of molecules

4. Desorption of reaction products

With regard to TMDs, CVD processes for the production of thin films can be grouped into 3 categories [4]:

• Vaporization of the metal and the dichalcogenide precursor and their decomposition, followed by the deposition of the TMD on a substrate [29];

• Direct sulfurization (or selenization) of the metal film [30];

• Conversion of metal oxide to sulphide (or dichalcogenide in general) by sulfurization [3,31].

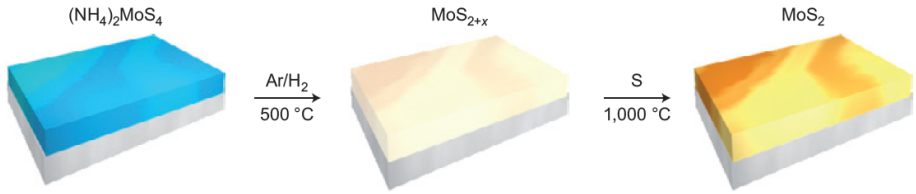


Figure 2- 10. Example of CVD

## 2.4 Defects in 2D TMDs

### Classification of defects in 2D mono-few layered TMDs

Before discussing structural defects, the polytype structure of defect-free (or pristine) TMDs crystals will be introduced (see Figure 2- 11) [32]. A single molecular layer of $MX_2$ is formed by an atomic tri-layer which consists of two adjacent layers of chalcogen atoms (X) covalently bonded by a layer of transition metal atoms (M) forming an X-M-X layer configuration. Two possible structural polytypes have been reported for a monolayer $MX_2$: the semiconducting trigonal prismatic phase (we adopt the notation 1H for monolayers; see Figure 2- 11a; the 2H phase refers to bulk crystals), and the metallic octahedral prismatic phase (the 1T phase; see Figure 2- 11b) [8]. In certain cases, the 1T phase is not thermodynamically stable, and its structurally distorted derivative, denominated as 1T can be observed instead (see Figure 2- 11c). When TMD crystals have more than one atomic chalcogen–metal–chalcogen (X-M-X) layer of the 1H phase bonded by van der Waals (vdW) forces, additional polytypes appear in account for variations in stacking orders. A Bernal

stacking (AbA BaB) yields the 2H phase (see Figure 2- 11d), while an AbA CaC BcB stacking yields a rhombohedral phase denominated as the 3R phase (see Figure 2- 11 e).

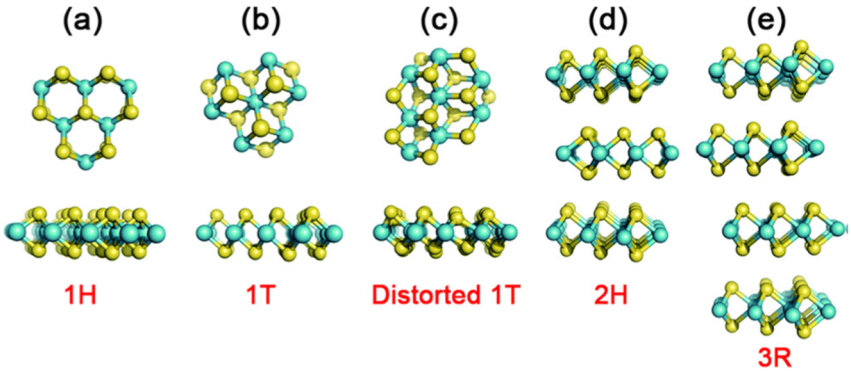


Figure 2- 11. Structural polytypes of pristine TMD layers. Chalcogen atoms are shown in yellow, and transition metal atoms are shown in blue. (a) The 1H phase, (b) the 1T phase, (c) the distorted 1T, or 1T′ phase, (d) the 2H phase, (e) the 3R phase.

After introducing pristine crystal structures, the structural defects in mono-few layered TMDs (intrinsic and extrinsic defects in CVD grown and mechanically exfoliated nanosheets) are classified as follows. By definition, 2D TMDs could be infinitely large within their basal planes, but are only atomically thin perpendicular to the planes. Consequently, defects residing in these 2D crystals could be classified according to their dimensionality as zero-dimensional (point defects, dopants or non-hexagonal rings; see Figure 2- 12a), one-dimensional (grain boundaries, edges, and in-3 plane heterojunctions; see Figure 2- 12b) and two-dimensional (layer stacking of different layers or vdW solids, wrinkling, folding, and scrolling; see Figure 2- 12c).

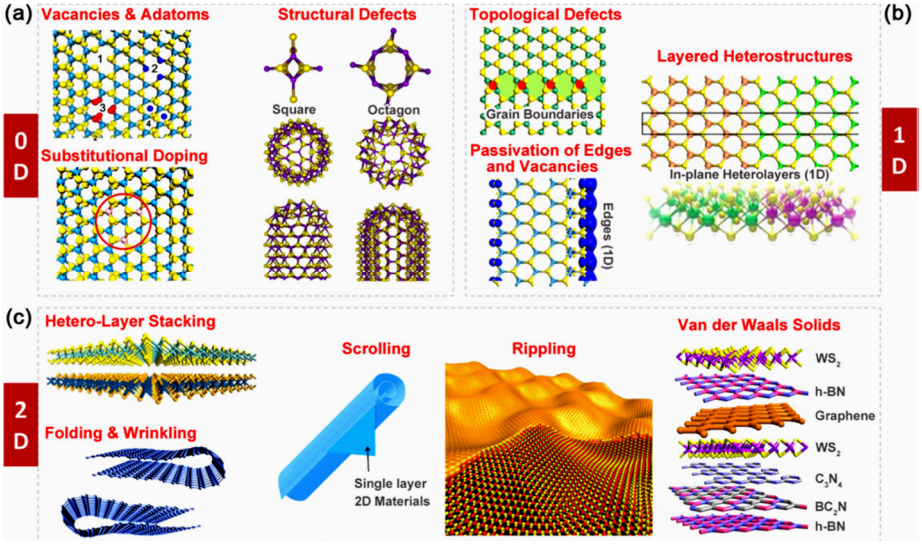


Figure 2- 12. An overview of defects in 2D TMDs. (a) Typical zero-dimensional defects such as vacancies, adatoms, dopants, squares, and octagons [33,34] (b) Typical one-dimensional defects such as grain boundaries, edges, and phase interfaces. (c) Typical two-dimensional defects such as folding, wrinkling, scrolling, rippling, and vertically stacked hetero-layers [35–37].

### 2.4.1 Zero-dimensional defects in TMDs

The simplest and most abundant defects in TMDs are vacancies, and the anti-sites that form on them (see Figure 2- 13a). In synthetic TMD samples, six varieties of intrinsic point defects are observed with regularity (see Figure 2- 13a): single sulfur vacancies ($V_S$), double sulfur vacancies ($V_{S2}$), a vacancy of a Mo atom and a triad of its bonded S within one plane ($V_{MoS3}$), a vacancy of a Mo atom and all six of its nearest neighbors ($V_{MoS6}$), an antisite, with Mo occupying a$V_{S2}$ ($Mo_{S2}$), and a pair of S atoms occupying a Mo position ($S2_{Mo}$). The notable absence of $V_{Mo}$ from this list is likely due to its tendency to complex with sulfur vacancies. With the exception of $Mo_{S2}$, reconstruction of the structure is minimal upon forming vacancies, and the defects retain trigonal symmetries [38,39].

It is also possible for other atomic species to replace lattice atoms by substituting elements. When considering the extent to which a foreign atom may substitute onto a crystal lattice, the ion's relative size, electronegativity, valence, and end member crystal structure are all relevant factors. The lanthanide contraction is a fortuitous periodic trend, which results in comparable radii for the 4d and 5d transition metals. This makes possible a wide variety of dopants from across the transition metal block. Notably, the similarity of W and Mo based on the criteria enumerated above allows for the formation of complete solid solutions in monolayer crystals [40].

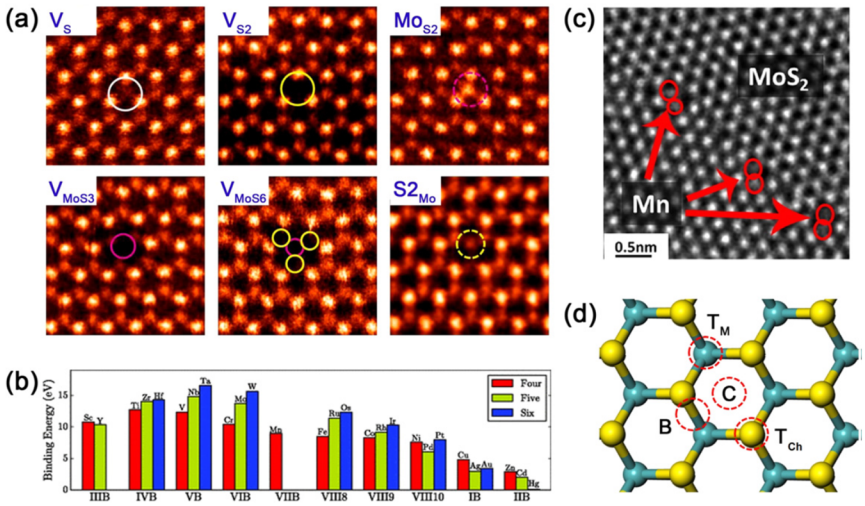


Figure 2- 13. Zero-dimensional defects. (a) Atomic-resolution annular dark field (ADF) images showing different types of vacancy and vacancy complexes in $MoS_2$ monolayers. (b) Comparison of binding energies for $MoS_2$ monolayers doped with transition metal atoms. Red, green and blue symbols correspond to dopants in group four, five and six, respectively. (c) TEM image showing $MoS_2$ monolayers substitutionally doped by Mnatoms, (d) A schematic diagram showing four sites of adatoms adsorbed ontoTMD lattices [41].

### 2.4.2 One-dimensional defects inTMDs

Extrinsic sulfur line vacancies result from the agglomeration of sulfur vacancies which are usually produced by electron bombardment. Single- and double line vacancies

are observed experimentally, both aligned along the zig-zag direction (see Figure 2-14a and b). This experimental result agrees with calculations which determine the formation energy of sulfur line vacancies in the zig-zag direction exhibit lower formation energies than those along the armchair direction. In all cases, the formation energies of line vacancies are a function of the number of vacancies, in the range of 5-6 eV per vacancy for lengths of 6-16. When the freestanding edge regions are imaged by TEM, the orientation of line defects also depends on the strain. Thus, strain may serve as a means to select line vacancy orientations for tuning electronic properties [42,43].

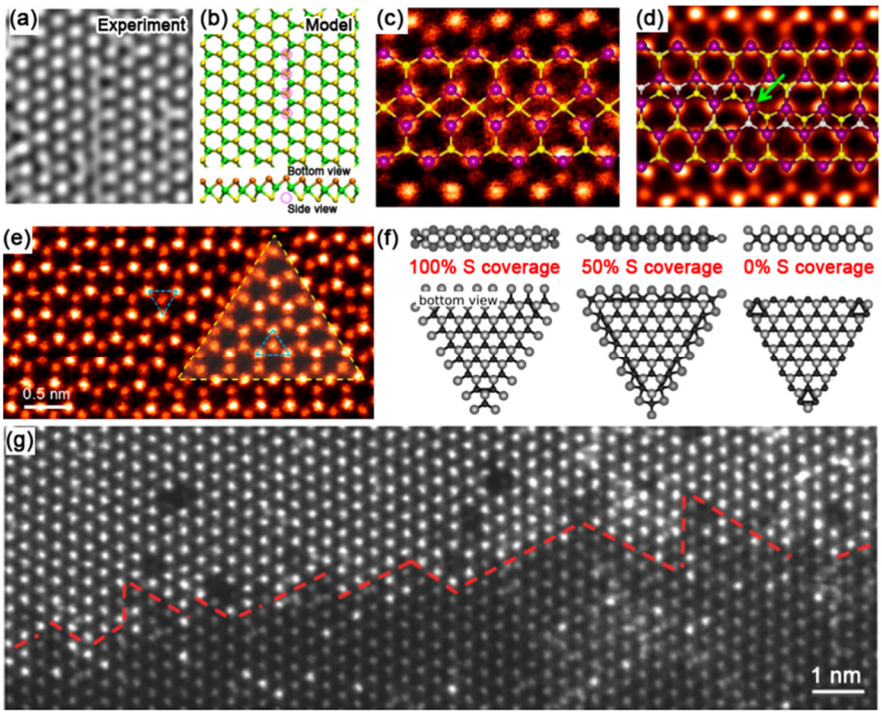


Figure 2- 14. One-dimensional defects. (a) High-resolution transmission electron microscopy (HRTEM) image and (b) structural model showing a single vacancy line in $MoS_2$ monolayers. (c) and (d) ADF images of 4l4P and 4l4E 60° grain boundaries in CVD $MoS_2$ monolayers. Structural models are overlaid on ADF images. (e) ADF image showing an inversion domain in monolayer $MoSe_2$. (f) Structural models showing Mo-terminated $MoS_2$ domains edges with different percentages of sulfur coverage. (g) ADF image showing a 1Dinterface between monolayer $MoS_2$ and $WS_2$ [34].

In addition to sulfur line vacancies, grain boundaries are often observed in TMD monolayers. In comparison to one-atom-thick materials, TMD grain boundaries and the dislocation cores they are comprised of are quite complex. This is because three atomic layers compose TMD monolayers (i.e. chalcogen-metal-chalcogen). As atoms are removed, the structure relaxes in three dimensions, to form dreidel shaped dislocations with a variety of ringed motifs that are dependent on the grain boundary angle [44].

5 Patterns of two point-sharing four member rings (4l-4P) form mirror twin grain boundaries in synthetic $MoS_2$ and $MoSe_2$, when grains meet at 60° angles along the zig-zag direction (see Figure 2- 14c and d).4l4E metallic edge-sharing line defects are another possible 60° grain boundary morphology, which can result in triangular

inversion domains with metallic edges (see Figure 2- 14e). The situation becomes more complex for smaller angles, with 4l6, 4l8, 5l7, and 6l8 motifs appearing. HAADF-STEM shows that on these low angle, and high strain (up to 58%) grain boundaries, sulfur atoms are quite mobile, even under low accelerating voltages, resulting in dislocation movement [38,45,46].

We can now turn our attention to the most prominent defects in TMD flakes, their edges. Synthetic TMD single-crystalline islands most often adopt triangular shapes with edges that appear sharp in microscopic images. The triangular morphology of these flakes can be explained through the 2D application of the Wulff construction, which simply states that low energy edges will be preferred. These surface energies are a function of the $\mu^S$ (the chemical potential), or the sulfur vapor potential. When $\mu^S$ is low (i.e., under low sulfur vapor pressures), $MoS_2$ will adopt distorted hexagonal shapes rather than triangles. Nanoscale calculations predict that under the sulfur rich conditions prevalent during TMD growth, (1010) Mo edges with either 50% or 100% S (see Figure 2- 14f) are the most thermodynamically stable. Nevertheless, in CVD grown samples the Mo-terminated edges with both 0% and 50% S coverage have been observed, suggesting that CVD is a process away from equilibrium. Lateral hetero-interfaces constitute another form of 1D defect. Lateral (inner/outer) heterostructures of $MoS_2/WS_2$, $MoSe_2/WSe_2$, $MoS_2/MoSe_2$, and $WS_2/WSe_2$ have been reported recently. Structurally coherent sharp interfaces (see Figure 2- 14g) have been observed as a result of covalent epitaxy between two dissimilar TMD layers with similar lattice constants [34,38,47].

### 2.4.3 Two-dimensional defects in TMDs

Perfect 2D materials have been predicted by theories as unstable upon thermal fluctuation, but after the discovery of graphene, it has gradually become clear that suspended graphene could be stabilized by the formation of ripples, i.e., finite surface roughness and deformation. Similarly, ripples with a typical height on the order of nm have been observed in as-synthesized $MoS_2$ monolayers (see Figure 2- 15c) and can be generated deliberately by scanning a laser beam over $MoS_2$ monolayers. Ripples introduce strain into the materials and could well affect their electronic properties. In few-layered TMDs, adjacent layers are coupled by vdW forces. The magnitude of vdW forces depends sensitively on the interlayer spacing, which is correlated to stacking configuration. Most synthetic few-layered TMDs exhibit a Bernal stacking (AbA BaBK), but derivations from this stacking configuration are also possible, especially when TMD layers are stacked manually via transfer techniques. Due to the handling of TMDs, it is also possible for flakes to fold over onto themselves. For those that assume the 1H phase, folding produces a structure distinct from the 2H phase. The vdW interface has strong impact on the electronic and optical properties of few-layered TMDs, therefore the interface associated with a stacking and layer orientation can be viewed as a 2D defect (see Figure 2- 15c) [5,48,49].

There is a large family of known 2D materials, such as graphene, hBN, TMDs, and layered oxides. Given the similarity in their interlayer ‘bonding’, 2D materials of different kinds can be placed one on top of another, forming vertical heterostructures

or vdW solids. When the top layer (e.g. $MoS_2$) has a crystal structural similar to the bottom layer (e.g. graphene) (see Figure 2- 15b), their stacking occurs via vdW epitaxy. Compared to covalent epitaxy where adjacent layers are covalently bonded, vdW epitaxy is more tolerant to lattice mismatch between layers, thereby allowing a variety of 2D materials to be stacked in this way. The interfaces between vertical hetero-layers can also be viewed as 2D defects which generate new properties in the materials (see Figure 2- 14c).

The structure and electronic properties of TMD have been predicted for a wide number of TMD materials: the semiconducting TMDs of Mo and W become semi-metallic, while metallic $NbS_2$ and $NbSe_2$ become small gap semiconductors. Therefore, achieving defect control in these 2D systems is very important in order to tailor their electronic properties [50,51].

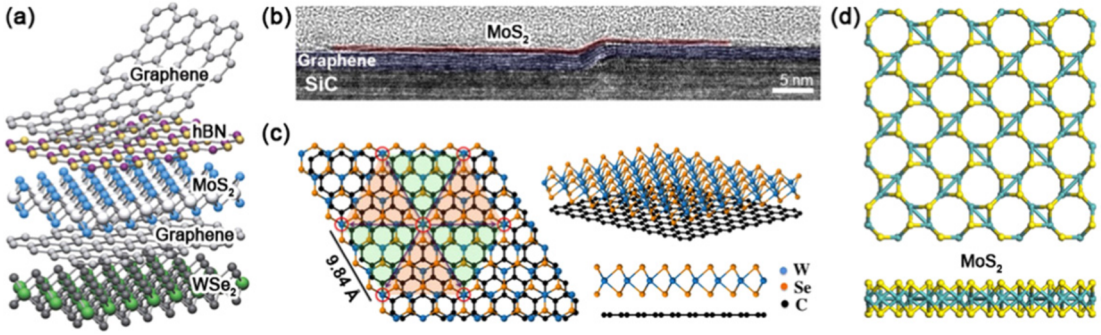


Figure 2- 15. Two-dimensional defects. a) Schematic representation of vdW heterostructures made by stacking different 2D materials. b) Cross-sectional transmission electron microscopy (TEM) image showing a 2D interface between $MoS_2$ and graphene layers. (c) Structural model showing a Moiré pattern in vertically stacked monolayer $WSe_2$ and graphene. (d) Relaxed structural models showing 8–4 MoS2 Haeckelites[51].

### 2.4.4 Chemical air stability and Ageing of 2D TMDs

It is well understood that a monolayer of trigonal prismatic semiconducting TMDs exhibits a direct band gap (in the range 1.52 eV) that it is not present in few-layered systems. This direct band gap is what differentiates monolayer TMDs from other 2D materials such as graphene, which is a zero-band gap semimetal.

Oxidation and degradation can alter the electronic properties of $MX_2$ TMD monolayers, with the corresponding impact on the electrical performance of any TMD-based device. Studies show the degradation of TMDs at elevated temperatures higher than 250 ˚C, or under UV and heat and moisture. Unlike the fast degradation of black phosphorus in air, TMDs have been considered as air-stable semiconductors under ambient conditions. but Koratkar and his group investigated the long-time air stability of mono layer $WS_2$ and $MoS_2$ and showed the susceptibility and large scale structural and morphological changes to the sheets and intense degradation of TMDs to ambient degradation. Their study indicates that the generally accepted view that monolayer TMDs are air-stable materials under ambient conditions is incorrect and

adsorption of organic materials from the ambient and the gradual oxidation of TMDs occur along grain boundaries over a period of months.

Figure 2- 16b shows $WS_2$ monolayer after being stored at room temperature (~25°C) in a container with desiccant for 1 year, that cracks formed in all the $WS_2$ sheets, especially along the grain boundaries. $WS_2$ monolayers that were exposed to moisture-rich conditions (i.e., without drying desiccant) at room temperature went through even more severe structural and morphological changes over the 1-year period, as shown in Figure 2- 16c (almost the entire $WS_2$ sheet exhibits visible degradation). Figure 2- 16b and c indicate that high-humidity conditions severely accelerate the degradation of $WS_2$. Additionally, $MoS_2$ showed similar graduation deterioration, with the grain boundaries and edges first being oxidized in 6 months and almost the whole crystal in 1 year (Figure 2- 16d–f) [52].

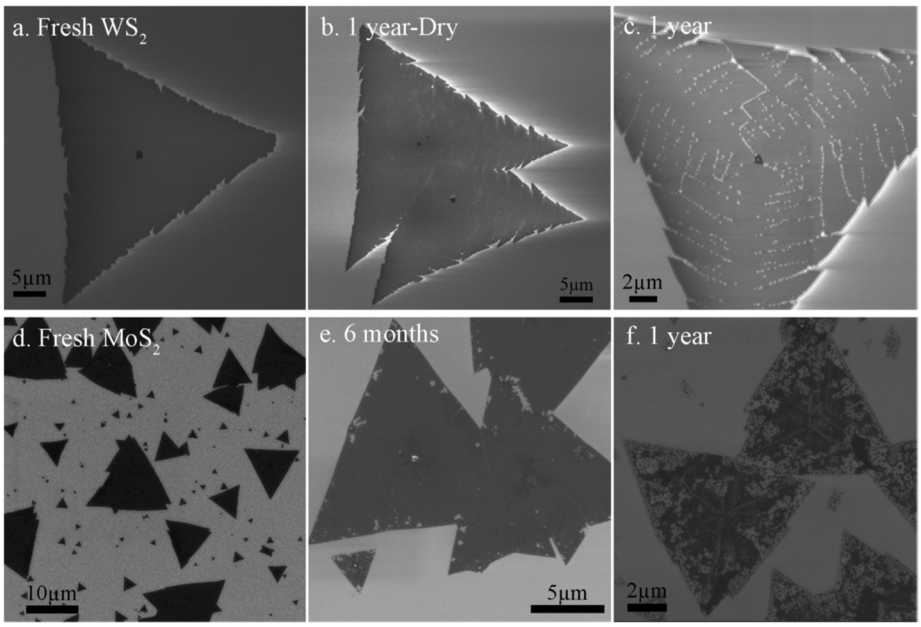


Figure 2- 16. Scanning electron microscopy (SEM) images of (a) fresh $WS_2$, aged $WS_2$ after 1 year in a container (b) with and (c) without desiccant, (d) fresh $MoS_2$, and (e) aged $MoS_2$ after 6 months without desiccant and (f) after 1 year without desiccant. All the samples were stored in Class 100 cleanroom conditions [52]

Figure 2- 17 illustrate the integrated PL intensity map of a typical fresh $WS_2$ sheet (the optical image of the flake is shown in the inset image). Figure 2- 17b shows the corresponding PL mapping and the optical image (inset) of typical 1-year-old $WS_2$ sheets. There is significant spatial variation in the PL intensities in Figure 2- 17b, with certain regions exhibiting severe PL quenching indicative of extensive damage to the samples.

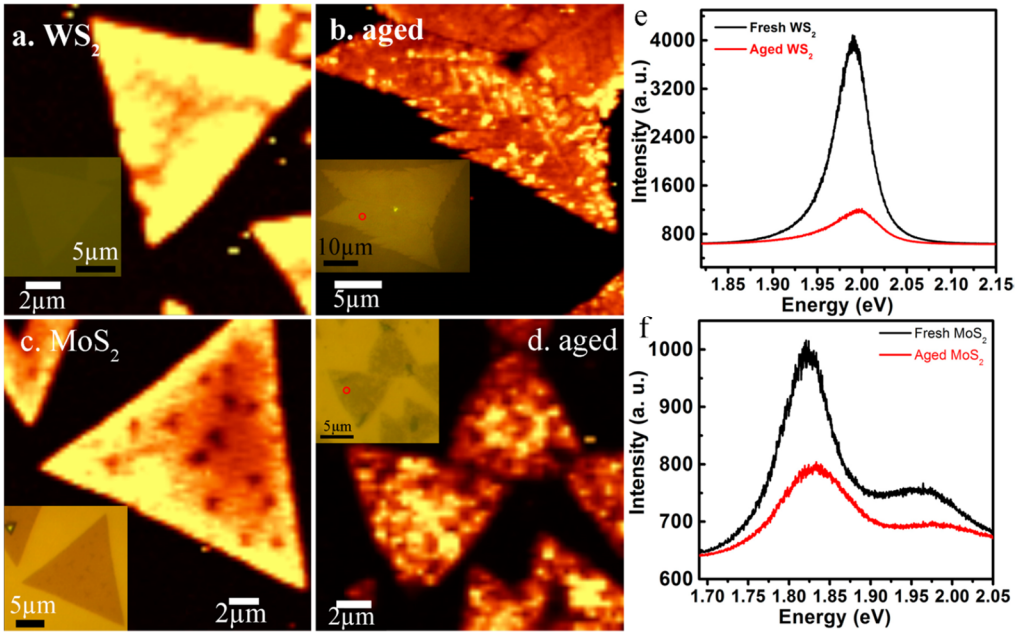


Figure 2- 17. Photoluminescence spectra of fresh and aged TMDs. PL intensity map (centered at the A exciton) of fresh $WS_2$ (a), $WS_2$ aged for 1 year under ambient conditions (b), fresh $MoS_2$ (c), and $MoS_2$ aged for 1 year under ambient conditions (d). The inset optical images show the $WS_2$ and $MoS_2$ flakes from which the data were taken. (e, f) Representative PL spectra of the fresh and 1-year-aged $WS_2$ (e) and fresh and 1-year-aged $MoS_2$ (f). Both the monolayer $WS_2$ and $MoS_2$ films were aged for 1 year under ambient conditions (i.e., room temperature and atmospheric pressure).

An important observation from the measured PL spectra (Figure 2- 17e) is that the PL intensity of the 1-year-aged $WS_2$ sample is almost 6 times smaller than the fresh $WS_2$, that indicates intensive PL quenching due to the oxidation of the $WS_2$ nanosheet.

Figure 2- 17c shows PL mapping and the optical image (inset) of a typical freshly grown $MoS_2$ sheet, while Figure 2- 17d shows the PL mapping of a typical 1-year-old $MoS_2$ sample showing significant PL quenching and spatial variation in the PL intensity. The PL spectrum (Figure 2- 17f) of $MoS_2$ is mainly dominated by neutral A-exciton emission, along with B-exciton emission arising from the spin-orbital splitting of the valence band, ~150 meV away from the A peak.

To study the chemical nature of the aging process, J. Gao et al., studied the room temperature XPS measurement of fresh and 1-year aged $WS_2$ and $MoS_2$, see Figure 2- 18.

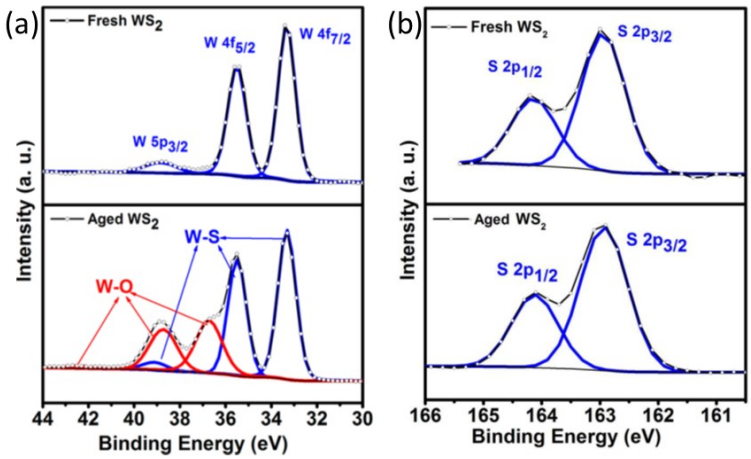


Figure 2- 18. XPS spectra (calibrated using the adventitious carbon C 1s peak) of fresh and 1-year-aged WS2 (a) and fresh and 1-year aged MoS2 (b) showing W 4f (a), Mo 3d (b), with Gaussian-Lorentzian fitting of each peak. The W 4f (Mo 3d) contributions exhibit two distinct sets of peaks after 1 year.

In fresh $WS_2$, the W:S ratio is ~1:2, with only one chemical state doublet in the W 4f core-level spectra (with W 4f7/2 at 33.4 eV and W 4f5/2 at 35.5 eV). However, the W:S ratio after one year is reduced to 1:1 in the aged $WS_2$, indicating intense sulfur loss (Figure 2- 18a). Furthermore, the W 4f core-level spectra recorded from the aged $WS_2$ samples show an additional doublet feature at higher binding energies (~3.1 eV), indicating the presence of tungsten in a higher oxidation state than pristine $WS_2$. The three new peaks (red curves) with higher binding energy originate from the oxidized W (W-O), and the remaining three peaks (blue curves) are corresponding to the S-bound W (W-S). It should be noted that the sulfur is still bound exclusively to W without exhibiting any extra chemical states, as shown in the figure Figure 2- 18b.

This result suggests that, in addition to the “oxidation” of the transition metal, oxygen is also present in the aged sample in the form of “organic contaminants” that are adsorbed onto the aged sheets. The XPS analysis did not indicate the formation of any sulfur oxide (SOx) under ambient conditions for the aged TMD samples, which indicates that S atoms are being displaced by oxygen in these films. J. Gao et al., concluded that the S loss mechanism during aging is not clear and suggested that one possibility for S loss is that O is first bonded to S, followed by breaking of the S-metal bond, followed by substitution of the S by O or OH radicals. Such processes are likely initiated or catalyzed at regions with S deficiency (such as defects and grain boundaries) and then gradually propagated throughout the entire TMD sheet [52].

## 2.5 Transition metal dichalcogenide sensors

In the recent years the isolation of 2D TMDs has raised the interest in this field. 2D layered TMDs consist of a plane of metal atoms covalently bonded to the chalcogen atoms. 2D TMDs have superior molecular sensing capability due to their unique physical and chemical properties as mentioned above, such as semiconducting property, high surface-to volume ratio (impact ratio), sizable bandgaps, high

absorption coefficient, and availability of reactive sites for redox reactions. Following the gas sensing of two of most studied TMDs, $MoS_2$ and $WS_2$ will be discussed.

### 2.5.1 $MoS_2$ sensors

The bulk $MoS_2$ possesses an indirect bandgap (1.2 eV), while the bandgap of monolayer $MoS_2$ becomes direct and wider (1.8 eV). The $MoS_2$ monolayer consists of one layer of Mo atoms sandwiched between two layers of S atoms, and the adjacent S-Mo-S sheets are held together by van der Waals interactions. Micromechanically exfoliated $MoS_2$ flakes have been used to fabricate gas sensors, which demonstrate excellent sensing characteristics. Zhang et al. fabricated $MoS_2$ films with different thicknesses using the micromechanical exfoliation, and the obtained single- and multilayer $MoS_2$ films were used in field-effect transistors (FETs) for the detection of NO; the obtained sensor was an n-type semiconductor. On the contrary, the FET sensors based on bilayer (2L), trilayer (3L), and quadrilayer (4L) $MoS_2$ films exhibited both stable and sensitive responses to NO with a detection limit of 0.8 ppm.

Figure 2- 19c and d show the sensing behavior of the two FETs upon exposure to $NH_3$ and $NO_2$. It can be seen that the resistance of both FETs decreases when exposed to $NH_3$ but increases upon exposure to $NO_2$. For n-type semiconducting $MoS_2$, $NH_3$ acts as an electron donor while NO2 acts as an electron donor, which confirms the charge transfer mechanism. The five-layer $MoS_2$ sensor shows better sensitivity than that of the two-layer device, due to the different electronic structure in samples with dissimilar thickness [53].

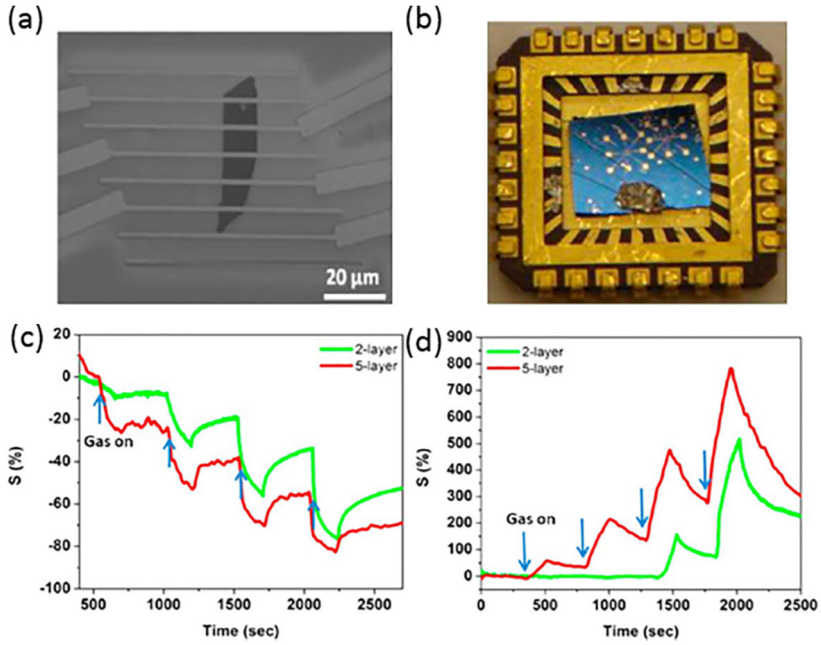


Figure 2- 19. (a) SEM image of a two-layer $MoS_2$ transistor. (b) Optical image of the $MoS_2$ sensor on the chip. Comparison of cyclic sensing performances between two-layer and five-layer $MoS_2$ devices to (c) $NH_3$ and (d) $NO_2$ (for 100, 200, 500, 1000 ppm).

Donarelli et al. reported on $MoS_2$ based resistive-type gas sensors which exhibited sensing response to both oxidative ($NO_2$) and reducing (relative humidity and $H_2$) gases. Two types of gas sensors were fabricated by depositing liquid-chemically exfoliated $MoS_2$ flakes on prepatterned $Si_3N_4$ substrates and then annealing in air at 150˚C and 250˚C, respectively. The "150˚C annealed" $MoS_2$-based device showed a p-type conductivity in the whole 25-200˚C operating temperature (OT) range when exposing to $NO_2$ and 50% relative humidity, ascribing to nitrogen substitutional doping of S vacancies on the $MoS_2$ surface. This device was not sensitive to 1 ppm $NO_2$ at room temperature, while it showed significant resistive changes at higher OTs; in particular, it exhibited good $NO_2$ response at 150˚C or 200˚C. Alternatively, the 250˚C annealed" $MoS_2$-based device showed an n-type behavior to $NO_2$, $H_2$, as well as relative humidity, attributing to the increase in S vacancy concentrations and the occurrence of partial surface oxidation of $MoS_2$ into $MoO_3$. This device showed outstanding sensing performances to $NO_2$ at 200˚C, with a detection limit of 20 ppb and response intensity equal to 5.80 at 1 ppm concentration. Also, it showed good electrical response to $H_2$. In addition, both p- and n-type sensors were sensitive to relative humidity [54].

$MoS_2$ is usually used as a good gas-sensing material due to its various active sites (sulfur defect, vacancy, and edge sties of $MoS_2$) for selective molecular adsorption, together with the semiconducting behaviors and large surface- to-volume ratio. For example, Jung et al. synthesized three distinct $MoS_2$ films with different alignment directions to compare the effect of the $MoS_2$ alignments on their gas adsorption properties. Various $MoS_2$ alignments were prepared by using rapid sulfurization of pre-deposited Mo seed layers with different thicknesses during CVD process, including (1) horizontally aligned $MoS_2$, (2) mixture of horizontally and vertically aligned $MoS_2$ layers, and (3) vertically aligned $MoS_2$. The vertically aligned $MoS_2$ had superior sensing performance to $NO_2$ gas molecules (about 5-fold enhanced sensitivity) compared to the horizontally aligned $MoS_2$ (Figure 2- 20). The electrical response to $NO_2$ molecules correlated directly with the density of exposed edge sites of $MoS_2$, due to the high gas adsorption onto the edge sites of vertically aligned $MoS_2$. DFT calculations showed that multiple configurations were along the edge sites of $MoS_2$ with stronger $NO_2$ binding energies, verifying the experimental results. These results provided clear comparison of gas adsorption properties between the edge and the terrace sites of $MoS_2$ and significantly enhanced $MoS_2$ based gas-sensing performance [53].

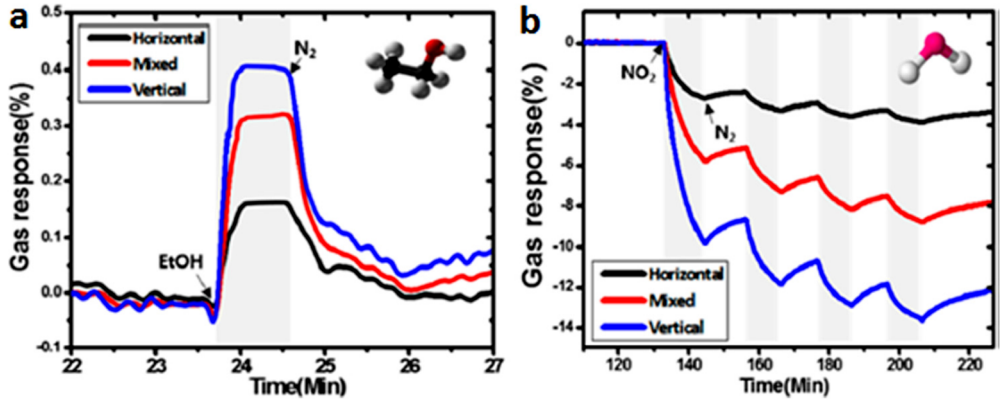


Figure 2- 20. Resistance changes of distinct MoS2 films upon adsorption of (a) 1000 ppm ethanol ($C_2H_5OH$) and (b) 100 ppm of $NO_2$.

The large surface-to-volume ratio of the layered $MoS_2$ film offers unique opportunities for surface functionalization to enable efficient charge transfer between $MoS_2$ and gas molecules. In particular, the incorporation of functional nanomaterials, such as noble metals, and metal oxides can be an effective way of enhancing the sensing performances of $MoS_2$ [53].

### 2.5.2 $WS_2$ sensors

Monolayer $WS_2$ comprises a tungsten layer sandwiched between two sulfur layers in a trigonal prismatic arrangement forming a S-W-S structure. Due to its excellent optical, electrical, and mechanical properties, combined with appreciable bandgap and high surface-to-volume ratio, $WS_2$ has been reported in various applications including field emission, FETs, sensors, etc. The multilayer $WS_2$ FETs could respond to various gas molecules, including reducing gas of ethanol and $NH_3$, as well as oxidizing gas of $O_2$. When exposed to ethanol and $NH_3$, the source-drain current of the FET increased, whereas it decreased in $O_2$ and air, attributing to the different charge transfer between multilayer WS2 and the adsorbed gas molecules. Moreover, this FET was more sensitive to the reducing $NH_3$ molecules rather than other gases (Figure 2- 21 b). $NH_3$ served as electron donors, increasing the electron concentration of n-type $WS_2$ nanoflakes; however, $O_2$ acted as electron acceptors to withdraw electrons from the $WS_2$ nanoflakes, thus reducing their conductivity. however, $O_2$ acted as electron acceptors to withdraw electrons from the $WS_2$ nanoflakes, thus reducing their conductivity. As shown in Figure 2- 21c, more gas molecules would be adsorbed under light illumination, and then the sensitivity of multilayer $WS_2$ FET was increased for $O_2$ but decreased for ethanol and $NH_3$. However, ethanol and $NH_3$ molecules acting as “n-dopants” significantly enhanced the photo-responsivity ($R_k$) and external quantum efficiency (EQE) of the FET, while the $O_2$ molecules acting as “p-dopants” reduced the $R_k$ and EQE. Importantly, the maximum $R_k$ and EQE of the $WS_2$ FETs were 884A/W and 1.73%, respectively, in the $NH_3$ atmosphere under light illumination (Figure 2- 21d) [53].

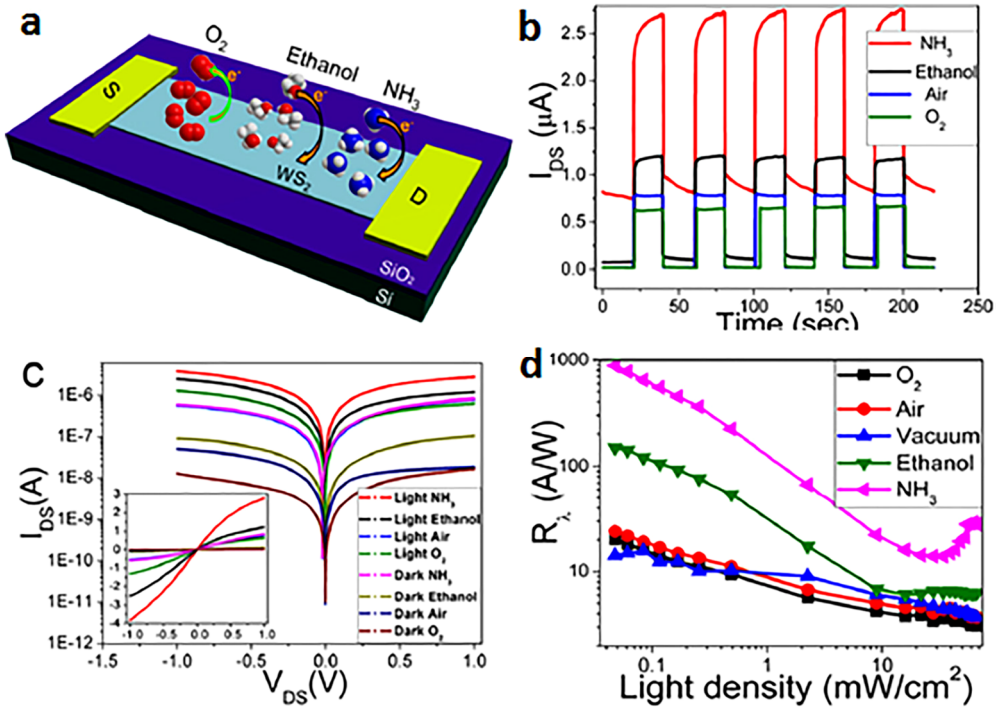


Figure 2- 21. (a) Schematic diagram of the multilayer $WS_2$ nanoflakes transistor. (b) Time-dependent photocurrent response under various gas atmospheres.

## 2.6 Bibliography Chapter 2


1. Yang, W.; Gan, L.; Li, H.; Zhai, T. Two-dimensional layered nanomaterials for gas-sensing applications. *Inorg. Chem. Front.* **2016**, *3*, 433–451.
2. Yue, Q.; Shao, Z.; Chang, S.; Li, J. Adsorption of gas molecules on monolayer MoS2 and effect of applied electric field. *Nanoscale Res. Lett.* **2013**, *8*, 425.
3. Lee, Y.H.; Zhang, X.Q.; Zhang, W.; Chang, M.T.; Lin, C. Te; Chang, K. Di; Yu, Y.C.; Wang, J.T.W.; Chang, C.S.; Li, L.J.; et al. Synthesis of large-area MoS 2 atomic layers with chemical vapor deposition. *Adv. Mater.* **2012**.
4. Chhowalla, M.; Shin, H.S.; Eda, G.; Li, L.-J.; Loh, K.P.; Zhang, H. The chemistry of two-dimensional layered transition metal dichalcogenide nanosheets. *Nat. Chem.* **2013**, *5*, 263–275.
5. Meyer, J.C.; Geim, A.K.; Katsnelson, M.I.; Novoselov, K.S.; Booth, T.J.; Roth, S. The structure of suspended graphene sheets. *Nature* **2007**, *446*, 60–63.
6. Bertolazzi, S.; Brivio, J.; Kis, A. Stretching and Breaking of Ultrathin {MoS}2. *{ACS} Nano* **2011**, *5*, 9703–9709.
7. Eda, G.; Fujita, T.; Yamaguchi, H.; Voiry, D.; Chen, M.; Chhowalla, M. Coherent Atomic and Electronic Heterostructures of Single-Layer {MoS}2. *{ACS} Nano* **2012**, *6*, 7311–7317.
8. Wilson, J.A.; Yoffe, A.D. The transition metal dichalcogenides discussion and interpretation of the observed optical, electrical and structural properties. *Adv. Phys.* **1969**, *18*, 193–335.
9. Neto, A.H.C. Charge Density Wave, Superconductivity, and Anomalous Metallic Behavior in 2D Transition Metal Dichalcogenides. *Phys. Rev. Lett.* **2001**, *86*, 4382–4385.
10. Wang, Q.H.; Kalantar-Zadeh, K.; Kis, A.; Coleman, J.N.; Strano, M.S. Electronics and optoelectronics of two-dimensional transition metal dichalcogenides. *Nat. Nanotechnol.* **2012**, *7*, 699–712.
11. Splendiani, A.; Sun, L.; Zhang, Y.; Li, T.; Kim, J.; Chim, C.-Y.; Galli, G.; Wang, F. Emerging Photoluminescence in Monolayer {MoS}2. *Nano Lett.* **2010**, *10*, 1271–1275.
12. M, C. Photoluminescence from Chemically Exfoliated MoS2. *Nano Lett.* **2012**, *12*, 526.
13. Mak, K.F.; Lee, C.; Hone, J.; Shan, J.; Heinz, T.F. Atomically {ThinMoS}2: A New Direct-Gap Semiconductor. *Phys. Rev. Lett.* **2010**, *105*.
14. Tongay, S.; Zhou, J.; Ataca, C.; Lo, K.; Matthews, T.S.; Li, J.; Grossman, J.C.; Wu, J. Thermally Driven Crossover from Indirect toward Direct Bandgap in 2D Semiconductors: {MoSe}2 versus {MoS}2. *Nano Lett.* **2012**, *12*, 5576–5580.
15. Zhao, W.; Ghorannevis, Z.; Chu, L.; Toh, M.; Kloc, C.; Tan, P.-H.; Eda, G. Evolution of Electronic Structure in Atomically Thin Sheets of $WS_2$ and $WSe_2$. *ACS Nano* **2013**, *7*, 791–797.
16. Xiao, D.; Liu, G.-B.; Feng, W.; Xu, X.; Yao, W. Coupled Spin and Valley Physics

in Monolayers {ofMoS}2and Other Group-{VI} Dichalcogenides. *Phys. Rev. Lett.* **2012**, *108*.

17. Yi, M.; Shen, Z. A review on mechanical exfoliation for the scalable production of graphene. *J. Mater. Chem. A* **2015**, *3*, 11700–11715.

18. Nicolosi, V.; Chhowalla, M.; Kanatzidis, M.G.; Strano, M.S.; Coleman, J.N. Liquid Exfoliation of Layered Materials. *Science (80-. ).* **2013**, *340*, 1226419–1226419.

19. Zeng, Z.; Yin, Z.; Huang, X.; Li, H.; He, Q.; Lu, G.; Boey, F.; Zhang, H. Single-layer semiconducting nanosheets: High-yield preparation and device fabrication. *Angew. Chemie - Int. Ed.* **2011**, *50*, 11093–11097.

20. Eng, A.Y.S.; Ambrosi, A.; Sofer, Z.; Šimek, P.; Pumera, M. Electrochemistry of transition metal dichalcogenides: Strong dependence on the metal-to-chalcogen composition and exfoliation method. *ACS Nano* **2014**, *8*, 12185–12198.

21. Lv, R.; Robinson, J.A.; Schaak, R.E.; Sun, D.; Sun, Y.; Mallouk, T.E.; Terrones, M. Transition metal dichalcogenides and beyond: Synthesis, properties, and applications of single- and few-layer nanosheets. *Acc. Chem. Res.* **2015**, *48*, 56–64.

22. Ambrosi, A.; Sofer, Z.; Pumera, M. Lithium intercalation compound dramatically influences the electrochemical properties of exfoliated MoS<inf>2</inf>. *Small* **2015**, *11*, 605–612.

23. Fan, X.; Xu, P.; Zhou, D.; Sun, Y.; Li, Y.C.; Nguyen, M.A.T.; Terrones, M.; Mallouk, T.E. Fast and Efficient Preparation of Exfoliated 2H MoS<inf>2</inf> Nanosheets by Sonication-Assisted Lithium Intercalation and Infrared Laser-Induced 1T to 2H Phase Reversion. *Nano Lett.* **2015**, *15*, 5956–5960.

24. O'Neill, A.; Khan, U.; Coleman, J.N. Preparation of High Concentration Dispersions of Exfoliated $MoS_2$ with Increased Flake Size. *Chem. Mater.* **2012**, *24*, 2414–2421.

25. Štengl, V.; Henych, J.; Slušná, M.; Ecorchard, P. Ultrasound exfoliation of inorganic analogues of graphene. *Nanoscale Res. Lett.* **2014**, *9*, 167.

26. Coleman, J.N.; Lotya, M.; O'Neill, A.; Bergin, S.D.; King, P.J.; Khan, U.; Young, K.; Gaucher, A.; De, S.; Smith, R.J.; et al. Two-Dimensional Nanosheets Produced by Liquid Exfoliation of Layered Materials. *Science (80-. ).* **2011**, *331*, 568–571.

27. Li, B.L.; Wang, J.; Zou, H.L.; Garaj, S.; Lim, C.T.; Xie, J.; Li, N.B.; Leong, D.T. Low-Dimensional Transition Metal Dichalcogenide Nanostructures Based Sensors. *Adv. Funct. Mater.* **2016**, *26*, 7034–7056.

28. Ji, Q.; Zhang, Y.; Zhang, Y.; Liu, Z. Chemical vapour deposition of group-VIB metal dichalcogenide monolayers: engineered substrates from amorphous to single crystalline. *Chem. Soc. Rev.* **2015**, *44*, 2587–2602.

29. Liu, K.-K.; Zhang, W.; Lee, Y.-H.; Lin, Y.-C.; Chang, M.-T.; Su, C.-Y.; Chang, C.-S.; Li, H.; Shi, Y.; Zhang, H.; et al. Growth of Large-Area and Highly Crystalline $MoS_2$ Thin Layers on Insulating Substrates. *Nano Lett.* **2012**, *12*, 1538–1544.

30. Zhan, Y.; Liu, Z.; Najmaei, S.; Ajayan, P.M.; Lou, J. Large-area vapor-phase

growth and characterization of MoS 2 atomic layers on a SiO 2 substrate. *Small* **2012**, *8*, 966–971.

31. Lin, Y.-C.; Zhang, W.; Huang, J.-K.; Liu, K.-K.; Lee, Y.-H.; Liang, C.-T.; Chu, C.-W.; Li, L.-J. Wafer-scale MoS2 thin layers prepared by MoO3 sulfurization. *Nanoscale* **2012**, *4*, 6637.

32. Voiry, D.; Mohite, A.; Chhowalla, M. Phase engineering of transition metal dichalcogenides. *Chem. Soc. Rev.* **2015**, *44*, 2702–2712.

33. Seifert, G.; Terrones, H.; Terrones, M.; Jungnickel, G.; Frauenheim, T. Structure and Electronic Properties {ofMoS}2Nanotubes. *Phys. Rev. Lett.* **2000**, *85*, 146–149.

34. Gong, Y.; Lin, J.; Wang, X.; Shi, G.; Lei, S.; Lin, Z.; Zou, X.; Ye, G.; Vajtai, R.; Yakobson, B.I.; et al. Vertical and in-plane heterostructures from {WS}2/{MoS}2 monolayers. *Nat. Mater.* **2014**, *13*, 1135–1142.

35. Miró, P.; Ghorbani-Asl, M.; Heine, T. Transition Metal Monolayers: Spontaneous Ripple Formation in {MoS}2Monolayers: Electronic Structure and Transport Effects (Adv. Mater. 38/2013). *Adv. Mater.* **2013**, *25*, 5366.

36. Podila, R.; Rao, R.; Tsuchikawa, R.; Ishigami, M.; Rao, A.M. Raman Spectroscopy of Folded and Scrolled Graphene. *{ACS} Nano* **2012**, *6*, 5784–5790.

37. Terrones, H.; López-Ur\'\ias, F.; Terrones, M. Novel hetero-layered materials with tunable direct band gaps by sandwiching different metal disulfides and diselenides. *Sci. Rep.* **2013**, *3*.

38. Zhou, W.; Zou, X.; Najmaei, S.; Liu, Z.; Shi, Y.; Kong, J.; Lou, J.; Ajayan, P.M.; Yakobson, B.I.; Idrobo, J.-C.C. Intrinsic Structural Defects in Monolayer Molybdenum Disulfide. *Nano Lett.* **2013**, *13*, 2615–2622.

39. Komsa, H.-P.; Krasheninnikov, A. V Native defects in bulk and {monolayerMoS}2from first principles. *Phys. Rev. B* **2015**, *91*.

40. Chen, Y.; Xi, J.; Dumcenco, D.O.; Liu, Z.; Suenaga, K.; Wang, D.; Shuai, Z.; Huang, Y.-S.; Xie, L. Tunable Band Gap Photoluminescence from Atomically Thin Transition-Metal Dichalcogenide Alloys. *{ACS} Nano* **2013**, *7*, 4610–4616.

41. Zhang, K.; Feng, S.; Wang, J.; Azcatl, A.; Lu, N.; Addou, R.; Wang, N.; Zhou, C.; Lerach, J.; Bojan, V.; et al. Manganese Doping of Monolayer {MoS}2: The Substrate Is Critical. *Nano Lett.* **2015**, *15*, 6586–6591.

42. Komsa, H.-P.; Kurasch, S.; Lehtinen, O.; Kaiser, U.; Krasheninnikov, A. V From point to extended defects in two-dimensional {MoS}2: Evolution of atomic structure under electron irradiation. *Phys. Rev. B* **2013**, *88*.

43. Han, Y.; Hu, T.; Li, R.; Zhou, J.; Dong, J. Stabilities and electronic properties of monolayer {MoS}2 with one or two sulfur line vacancy defects. *Phys. Chem. Chem. Phys.* **2015**, *17*, 3813–3819.

44. Cheng, Y.C.; Zhu, Z.Y.; Mi, W.B.; Guo, Z.B.; Schwingenschlögl, U. Prediction of two-dimensional diluted magnetic semiconductors: Doped monolayer {MoS}2systems. *Phys. Rev. B* **2013**, *87*.

45. Lin, J.; Pantelides, S.T.; Zhou, W. Vacancy-Induced Formation and Growth of Inversion Domains in Transition-Metal Dichalcogenide Monolayer. *{ACS} Nano*

**2015**, *9*, 5189–5197.

46. Azizi, A.; Zou, X.; Ercius, P.; Zhang, Z.; El\'\ias, A.L.; Perea-López, N.; Stone, G.; Terrones, M.; Yakobson, B.I.; Alem, N. Dislocation motion and grain boundary migration in two-dimensional tungsten disulphide. *Nat. Commun.* **2014**, *5*.

47. Schweiger, H.; Raybaud, P.; Kresse, G.; Toulhoat, H. Shape and Edge Sites Modifications of {MoS}2 Catalytic Nanoparticles Induced by Working Conditions: A Theoretical Study. *J. Catal.* **2002**, *207*, 76–87.

48. Crowne, F.J.; Amani, M.; Birdwell, A.G.; Chin, M.L.; O'Regan, T.P.; Najmaei, S.; Liu, Z.; Ajayan, P.M.; Lou, J.; Dubey, M. Blueshift of {theA}-exciton peak in folded monolayer1H-{MoS}2. *Phys. Rev. B* **2013**, *88*.

49. Liu, H.; Chi, D. Dispersive growth and laser-induced rippling of large-area singlelayer {MoS}2 nanosheets by {CVD} on c-plane sapphire substrate. *Sci. Rep.* **2015**, *5*.

50. Geim, A.K.; Grigorieva, I. V. Van der Waals heterostructures. *Nature* **2013**, *499*, 419–425.

51. Terrones, H.; Terrones, M. Electronic and vibrational properties of defective transition metal dichalcogenide Haeckelites: new 2D semi-metallic systems. *2D Mater.* **2014**, *1*, 11003.

52. Gao, J.; Li, B.; Tan, J.; Chow, P.; Lu, T.-M.M.; Koratkar, N. Aging of Transition Metal Dichalcogenide Monolayers. *{ACS} Nano* **2016**, *10*, 2628–2635.

53. Yang, S.; Jiang, C.; Wei, S. Gas sensing in 2D materials. *Appl. Phys. Rev.* **2017**, *4*, 21304.

54. Donarelli, M.; Prezioso, S.; Perrozzi, F.; Bisti, F.; Nardone, M.; Giancaterini, L.; Cantalini, C.; Ottaviano, L. Response to NO2 and other gases of resistive chemically exfoliated MoS2-based gas sensors. *Sensors Actuators, B Chem.* **2015**, *207*, 602–613.

# CHAPTER 3.
# Materials characterization and electrical measurement techniques

## ABSTRACT

Aim of this chapter is to give a short overview of the characterization techniques used in this PhD project and how the gas sensing measurement are designed, executed and the results analysed.

## CONTENT

## 3.1 Microstructure and chemical characterization techniques

Dealing with nanomaterials synthesis means to find the good way to characterize the final product from a microstructural, chemical and practical point of view.

Many and different are the techniques commonly employed to characterize the obtained nanostructures and evaluate synthesis methods. This chapter is devoted to the description of some of the techniques used during this research project and how they have been used to evaluate the synthesised nanomaterials and their properties as gas sensors.

### 3.1.1 Atomic Force Microscopy (AFM)

The AFM consists of a cantilever with a sharp tip (probe) at its end that is used to scan the specimen surface. The cantilever is typically silicon or silicon nitride with a tip radius of curvature on the order of nanometers. When the tip is brought into proximity of a sample surface, forces between the tip and the sample lead to a deflection of the cantilever according to Hooke's law. Depending on the situation, forces that are measured in AFM include mechanical contact force, van der Waals forces, capillary forces, chemical bonding, electrostatic forces, magnetic forces, etc. Along with force, additional quantities may simultaneously be measured through the use of specialized types of probes (i.e. scanning thermal microscopy, scanning joule expansion microscopy, photothermal microspectroscopy, etc.). The AFM can be operated in a number of modes, depending on the application. In general, possible imaging modes are divided into static (also called contact) modes and a variety of dynamic (non-contact or "tapping") modes where the cantilever is vibrated or oscillated at a given frequency.

### 3.1.2 Transmission Electron Microscopy (TEM), HR-TEM and STEM

One of the most powerful tools for the structure analysis is Transmission Electronic microscopy (TEM). An electron beam from a gun penetrates materials, creating images and patterns on a fluorescent screen or a digital screen. As the electrons have to pass through the sample, this, therefore, has to have an extremely reduced thickness, between 50 and 500 nm. This technique is used to identify the internal structure of materials or determine unknown materials or structural modifications.

In particular, High Resolution Transmission Electron microscopy (HRTEM) and Selected Area Electron Diffraction (SAED) have been extensively used in this thesis to evaluate the exfoliation process and exfoliated mono or few layered materials and optimize the process parameters. Besides, Scanning Transmission Electron Microscopy (STEM) was used to evaluate purity and surface chemistry of the nanosheets.

### 3.1.3 Scanning Electron Microscopy (SEM)

Scanning electron microscopy (SEM) has become a powerful and versatile tool for material characterization. SEM is a type of electron microscope that produces images of a sample by scanning the surface with a focused beam of electrons. The electrons interact with atoms in the sample, producing various signals containing information about the surface topography and composition of the sample. The electron beam is scanned in a raster scan pattern, and the position of the beam is combined with the intensity of the detected signal to produce an image. In the most common SEM mode, secondary electrons emitted by atoms excited by the electron beam are detected and the number of secondary electrons that can be detected, and thus the signal intensity, depends, among other things, on specimen topography.

In this thesis, this technique has been used to characterize microstructure of exfoliated materials and to prove the effectiveness of the synthesis method.

### 3.1.4 X-Ray Diffraction (XRD)

X-ray diffraction is the most widely used powerful technique to identify the crystal structure and the atomic array of materials. It is based on constructive interference of monochromatic X-rays and a crystalline sample. The interaction of the incident X rays with the sample produces constructive interference when conditions satisfy Bragg's Law (Equation 3-1). This law relates the wavelength of electromagnetic radiation to the diffraction angle and the lattice spacing in a crystalline sample.

$$n\lambda = 2d \cdot \sin\theta \qquad (3\text{-}1)$$

In this thesis, crystalline phases evolution of $WO_3$ in exfoliated $WS_2$ and $WS_2$ commercial powder, annealed at different temperatures was monitored by grazing incidence XRD (PAN Analytical X'PERT Pro) using Cu $K_{\alpha 1}$ radiation ($\lambda$= 0.154 nm) and 0.02° angle step.

The crystallite size was calculated using the Scherrer equation, 3-2

$$\tau = \frac{k\lambda \cos\theta}{\beta} \qquad (3\text{-}2)$$

where τ is the mean crystallite dimension, K is the shape factor (0.89), λ is the X-ray wavelength (Cu Kα = 1.5418Å), β is the line broadening at full width half maximum intensity (FWHM) in radians, and θ is the Bragg angle

### 3.1.5 X-Ray Photoelectron Spectroscopy

The X-Ray Photoelectron Spectroscopy (XPS) is a surface analysis through which, by measuring the kinetic energy of photo-emitted electrons, it is possible to trace their binding energy, thus uniquely identifying the chemical species of the atoms present

in the sample. If the incident radiation is given by X-rays (hv is in this case the order of thousands of eV), the energy supplied is sufficient to free the electrons of the deepest atomic (orbital) energy levels (i.e. those which, being more near the atomic nucleus, they are more strongly linked to it).

For each atomic species, the binding energy of electrons of deep atomic levels (core levels) has very specific values, characteristic of each element, and constitutes a sort of identity card. Thus, an ejected electron has kinetic energy equal to the energy of the incident photon minus the bond energy of the electron in the previous state.

$$KE = hv - BE - \Phi \qquad (3\text{-}3)$$

BE (Binding Energy) is a direct measure of the energy needed to move the electron from its initial level to the vacuum. It is unique for each atom and an orbital datum. Φ is the working function of the spectrometer. Photo-emitted electrons are collected by an electron analyzer, an instrument capable of measuring the energy and the number of electrons that come out of the surface of the sample. The spectrum consists of several peaks with very precise energies: each of them corresponds to an energy level and therefore to a chemical element. X-rays penetrate deep into the sample, but the electrons that come out are only those that start a few nanometers from the surface (1-10 nm).

The information obtainable from the XPS is:

• qualitative analysis of a surface

• identification of surface contaminants and composition

• study of the composition as a function of depth

• heterogeneous catalysis

• differences between surface structure and bulk sample

.

### 3.1.6 Raman Spectroscopy

Raman vibrational spectroscopy is a molecular and structural characterization technique. The operating principle is the diffusion of a monochromatic radiation that affects the sample; a detector at 90 ° and one at 180 ° record the diffuse radiation and, knowing the frequency and intensity of the original wave, it is possible to measure the diffuse radiation. In general, the radiation can be diffused in three ways: Stokes, anti-Stokes and Rayleigh, the Stokes lines are linked to the functional groups of the molecules of the samples and to their modes of vibration and are therefore suitable for spectroscopy. As XPS, it gives, even if in a different way, compositional information about the sample and, in some cases for 2D-material it can give information about sample thickness.

The difference with XPS is given by the depth of measurement. In fact, if XPS gives superficial information (several nanometers), Raman spectroscopy has a penetration depth up to several microns, giving “bulk” information of the sample.

### 3.1.7 Thermogravimetric and Differential Thermal Analysis (TG-DTA)

The analysis of the change in the mass of a sample on heating is known as Thermogravimetric analysis (TG). TG measures mass changes in a material as a function of temperature (or time) under a controlled atmosphere. Its principal uses include measurement of a material's thermal stability and composition. TG is most useful for dehydration, decomposition, desorption, and oxidation processes. The most widely used thermal method of analysis is Differential thermal analysis (DTA). In DTA, the temperature of a sample is compared with that of an inert reference material during a programmed change of temperature. The temperature should be the same until thermal event occurs, such as melting, decomposition or change in the crystal structure. In an endothermic event takes place within the sample, the temperature of the sample will lag behind that of the reference and a minimum will be observed on the curve. On the contrary, if an exothermal event takes place, then the temperature of the sample will exceed that of the reference and a maximum will be observed on the curve. The area under the endotherm or exotherm is related to the enthalpy of the thermal event, $\Delta H$.

In this thesis, TG-DTA analyses have been carried out to follow the oxidation process in TMDs, in light of understanding thermal stability of these materials.

### 3.1.8 Dynamic Light Scattering (DLS)

Particle size distribution was determined by Dynamic Light Scattering (DLS) Malvern Mastersizer 2000. DLS was used to elucidate the overall dimension exfoliated $WS_2$ within a dispersion and evaluate the exfoliation yield and optimize the exfoliation process parameters.

Dynamic Light Scattering is a non-invasive method for measuring the size of suspended particles in a liquid. During the measurement a laser radiation excites the sample, and an appropriate autocorrelation function describes the changes in time of the intensity of the radiation diffused by the excited sample. These fluctuations are related to the Brownian motion of the suspended particles which continuously enter and exit from the measurement volume, causing oscillations of intensity. On the basis of the speed of the fluctuations, the diffusion coefficient of these particles is determined and in the approximation that they have a spherical shape the hydrodynamic radius (Rh) is calculated applying the Stokes-Einstein relation. The universally accepted theory for accurately predicting the diffusion of light of all materials under all conditions is known as the Mie theory, that start form the assumption that the observed material has a spherical shape. Indeed, it is not actually the right technique to be applied on 2D materials, but it has been used to have a general overview of the exfoliation process.

## 3.2 Electrical characterization of sensors

After synthesizing the nanostructured semiconducting sensing materials that will be further explained in detail, the sensing material will be deposited onto the sensing electrodes and will be subjected to electrical tests to investigate their electrical properties in presence of certain target gases and then evaluate their performance in terms of sensitivity, selectivity and stability.

Below is a flow chart that describes the electrical characterization. The process consists of the following phases and blocks:

- deposition of the material on special interdigitated substrates;

- welding of the substrate on T0-12 pins and housing in the measuring cell;

- gas fluxing system;

- power supply, control and data acquisition system.

Figure 3- 1 shows the global scheme for the electrical characterization of the manufactured devices.

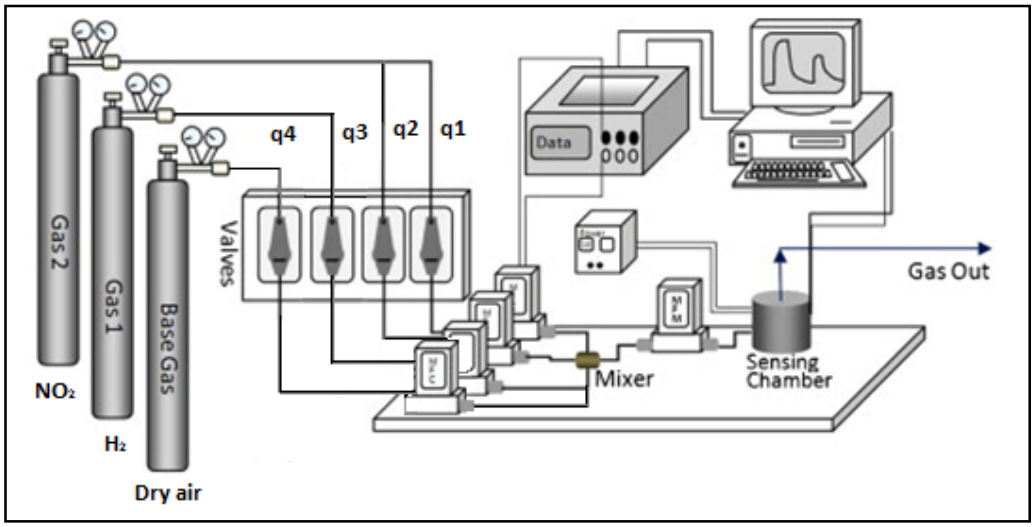


Figure 3- 1. Electrical characterization of the sensors: overall scheme.

# FLOW CHART OF THE ELECTRICAL CHARACTERIZATION PROCESS

| Depositing of sensing maerial onto the interdigitated sensor | Substrate welding and measuring cell housing | Electrical gas sensing system | Power supply system, Control and data acquisition | Testing protocol and electrical responses |
|---|---|---|---|---|
| 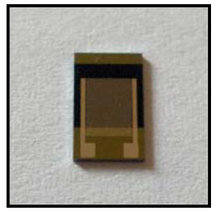 | 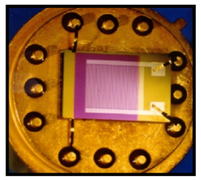 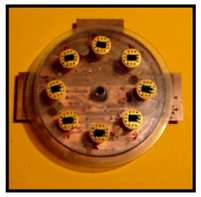 | 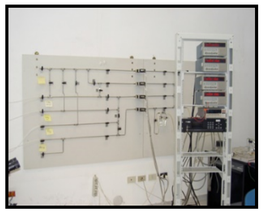 | 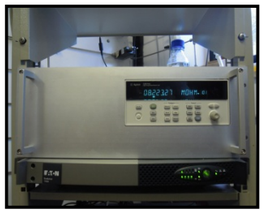 | 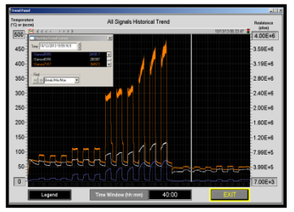 |
| **GENERAL DESCRIPTION** | | | | |
| The material is deposited on a special interdigitated substrate with platinum electrodes on the "front" side. The substrate is heated by a heating circuit on the "back" side. | The substrate is welded with appropriate gold strips on a 12-pin T0 support. Each sensor is housed in the measuring chamber capable of holding 8 devices simultaneously. | The measuring system is able to set the sensor with different target gases at different concentrations. | The control and acquisition system are able to automate the electrical tests, control all the variables involved (temperatures, flows, acquisition times) in real time and record the electrical responses. | Electrical responses are obtained in terms of change in resistance of sensing materials when expose to different gases at different concentrations that are processed and visualized through the Origin environment. |

### 3.2.1 Sensor substrate

The substrates used for the deposition of sensing material and for the subsequent electrical characterization are rectangular supports made of polycrystalline silicon (Si). A very thin amorphous layer of $Si_3N_4$ (200 nm) is deposited on the surface of this support by Chemical Vapor Deposition (CVD) technique.

The system of electrodes on the front side and the back side of the substrate shown in Figure 3- 2 b is obtained by the photolithographic technique. The sensing material will be deposited on the "front side" that two overlapping metallic platinum finger combs make up the electric signal circuit. The "Back side" consists of a heating circuit that is used to heat up the sensing material to the defined operating temperature of sensor, and the thermistor circuit is used to control the temperature of the substrate, see Figure 3- 2.

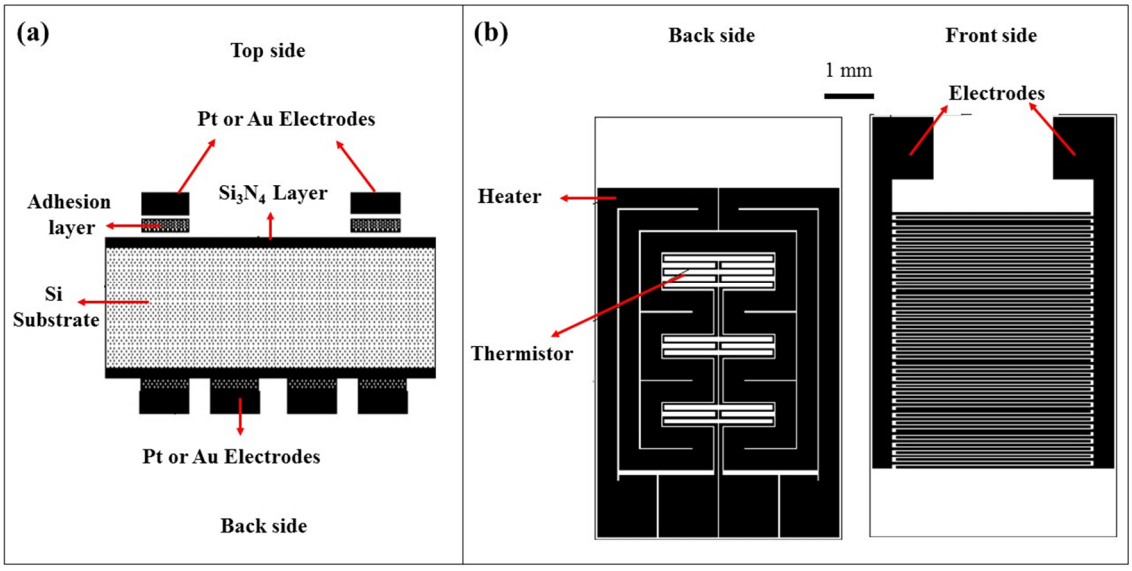


Figure 3- 2. Schematic illustration of interdigitated sensor substrate a) cross section of sensor substrate, b) front and back side circuits of sensor substrate

These substrates represent the second generation of supports family, called "Eurochip", that were previously designed and manufactured in Holland by the group of prof. De Roj on sapphire substrates. This generation of substrates differs from the previous one as regards only the nature of the support materials (in this case $Si_3N_4$). The geometry, the size of the electrodes and the circuits present is the original one.

Silicon Nitride substrates were made on 4" wafers with photolithographic technology at the company MICROSENS, world leader in the field of thin film commercial sensors manufacturing.

### 3.2.2 Substrate welding and housing in measuring cell

After depositing the sensing material onto the two-overlapping metallic platinum finger combs electrodes, the front side electrodes and the back-side electrodes will be welded to the 12-pin support (T0-12) by means of gold strips to ensure the electrical contact of the substrate to the support, see Figure 3- 3. These contacts provide the continuity of the signal between the substrate and the supply and acquisition and control system.

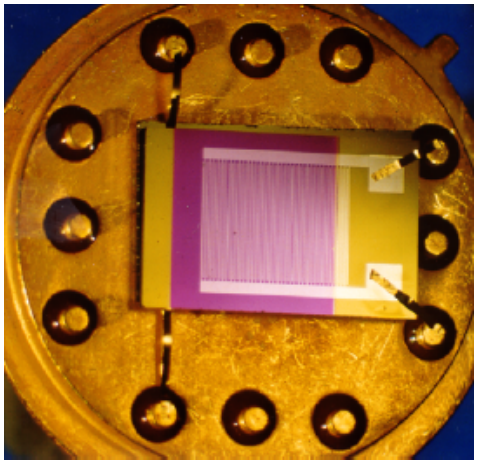

Figure 3- 3. Detail of a sensor welded on a T0-12 support.

The devices connected to the T0-12 are housed inside the measuring cell that contains up to 8 sensors simultaneously with the possibility of independent current supply of the substrates. During the sensing measurements, sensors and sensing materials could be activated by two different modes, one is thermal activation modes that is provides by the heating circuit on the back side of the sensor substrates, and the other is light illumination mode that is provided by the four-color LED lamps placed on top of the sensors at an specific distance, see Figure 3- 4.

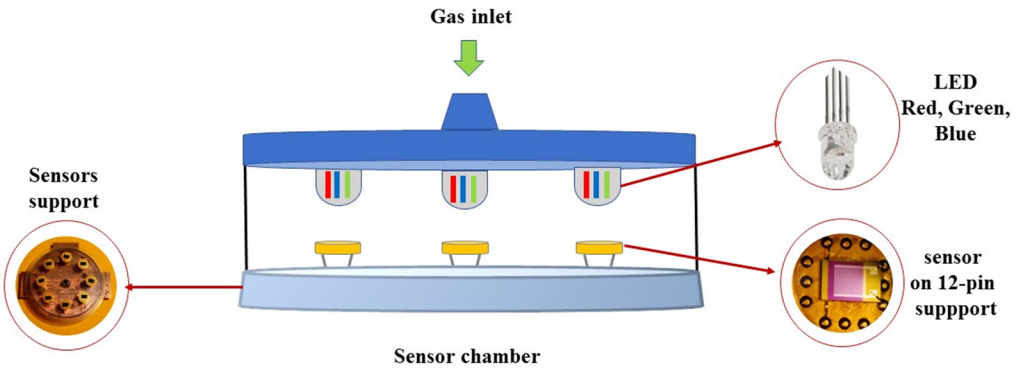


Figure 3- 4. - Measurement chamber with details of the plate on which the eight sensor supports are housed.

Each LED that is placed right on top of each sensor consists of three different colors; Red (RD), Green (GR) and Purple Blue (PB). The gas response of semiconductor gas sensors activated by visible light sources is known to be dependent from both the emission wavelengths and the irradiance. The characterization of the LED sources has been carried out before any gas response evaluation. Figure 3- 5 reports the LED emission spectrum showing the normalized light power as a function of the wavelength. The measurements identify the peak wavelengths located at λ= 430 nm (PB), at λ= 570 nm (GR) and at λ= 630 nm (RD) and the resulting emission spectra present negligible overlapping. The evaluation of the light irradiance has been obtained by integrating each spectral response curve of Figure 3- 5 at four different distances (0.5 cm, 1 cm, 2 cm and 3 cm) between the LED and the photodetector of the power-meter. The corresponding LEDs light irradiance conditions are reported in Table 3-1.

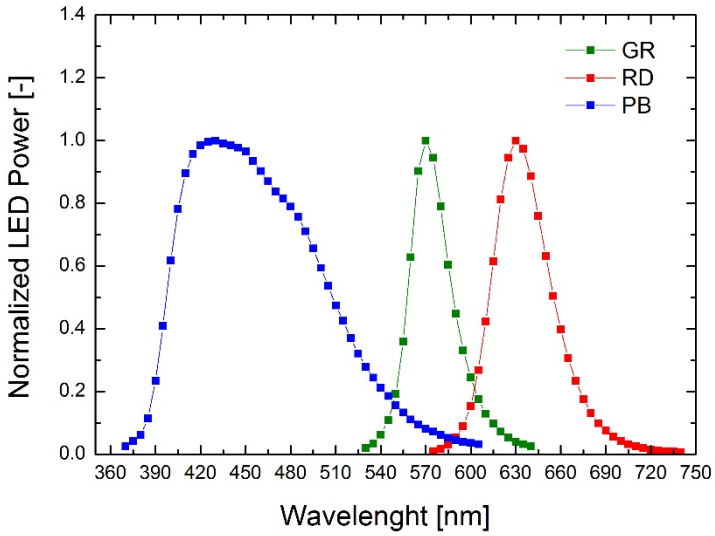


Figure 3- 5. Light emission spectra of the employed LED: normalised light power as a function of the wavelength.

Table 3-1- LED light intensity as a function of the distance from the power-meter photodetector.

| LED colour | Light intensity at 0.5cm [μW/cm²] | Light intensity at 1cm [μW/cm²] | Light intensity at 2cm [μW/cm²] | Light intensity at 3cm [μW/cm²] |
|---|---|---|---|---|
| **RD (λ=630nm)** | 95 | 89 | 59 | 30 |
| **GR (λ=570nm)** | 40 | 38 | 27 | 15 |
| **PB (λ=430nm)** | 770 | 668 | 468 | 270 |

### 3.2.3 Gas fluxing system

The system shown in Figure 3- 6 shows the test bench used for gas flushing.

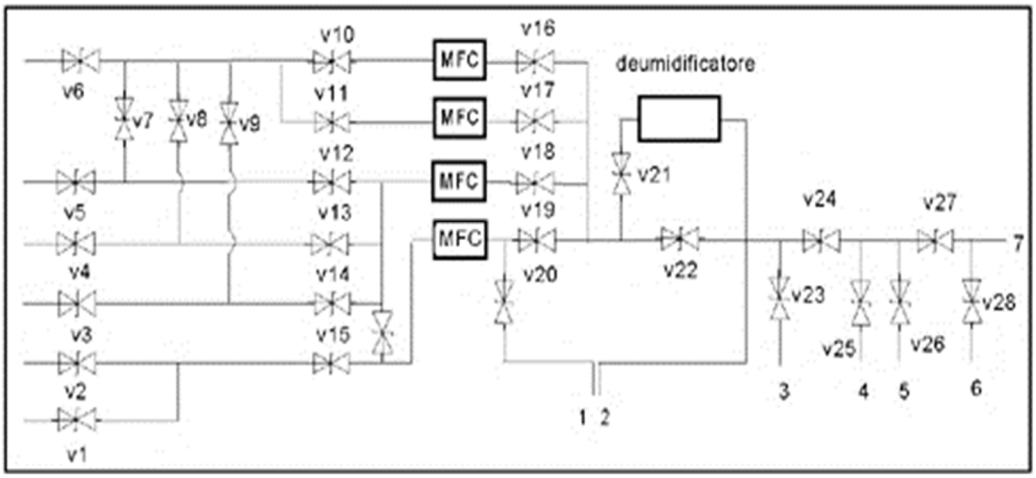


Figure 3- 6. Schematic of the gas fluxing system.

The system is able to flow up to 4 different gases at different flow rates into the measuring cell. The system is provided with the certified storage cylinders for gaseous mixtures with specific concentration. The system is also equipped with a calibrated dehumidifier capable of supplying specific relative humidity deriving from the humidification of the incoming dry air.

The following gases or gas mixtures were used in this thesis:

- Dry air;
- Wet air (0-95% U.R.);
- Mixture of $NO_2$ in dry air (10 ppm);
- Mixture of $H_2S$ in dry air (20 ppm);
- Mixture of $H_2$ in dry air (500 ppm);
- Mixtures of $NH_3$ in dry air (500 ppm)

The flow rates of the four output channels are regulated by four Texas Instruments solenoid valves connected to the control system. Below are the different full scale and therefore the maximum flow rates that can be provided by each of solenoid valves.

- Valve 1: 500 sccm
- Valve 2: 500 sccm
- Valve 3: 100 sccm
- Valve 4: 20 sccm

The concentration of the sample gas entering the chamber (C) is determined by the degree of dilution of the initial air/gas mixture (C0), (characteristic or initial concentration of each cylinder), according to the equation 3-4:

$$C = \frac{C_0 \cdot (q_1 + q_2)}{Q} \qquad (3\text{-}4)$$

where $q_1$ and $q_2$ are the flow rates of the lines that feed the air/gas mixture, while Q is the resulting flow rate, which always assumes the value of 500 sccm (for standardization of the tests).

### 3.2.4 Power supply, control and data acquisition

The power supply, control and data acquisition system consist of the following modules:

“National Instruments NI 9472 8-Channel 24 V Logic, 100 µs module, Sourcing Digital Output Module", which supplies the heating circuit in the "Back" side of the device with a certain current.

"Agilent 34970A Data Acquisition Unit. Modul 34901 Multiplexer", capable of displaying and recording 15 data channels in real time (resistances, temperatures, flows). It measures the passing current and then processes the data supplying of resistance values through the Ohm's law.

The software for the acquisition system is based on an Instrument Server architecture (developed with LabVIEW and resident in NI cRIO) connected to a supervision and control client (developed in WinXP with the SCADA NI Lookout package). Through a remote connection software, it is possible to manage and control the gas sensing tests in real time and to act on some important parameters during construction.

### 3.2.5 Testing protocol for electrical tests

Each of the manufactured sensor device (made of MOx or exfoliated TMD) has been subjected to a standard protocol for a better electrical and conductometric characterization of the sensing material.

The system can interrogate the devices by managing material working temperatures, gas flows in the measuring cell and, as previously described, the "Agilent" module, applies a specific voltage to the electrode/sensitive layer circuit, and measures the passing current and then, calculate the output resistance values by Ohm's law.

The standard characterization protocol consists of various tests which are subdivided into various sub-tests depending on the chosen parameters (temperatures, times, flow rates).

Each test is performed to determine and derive some parameters or characteristics of the material. Table 3-2 shows the various tests and their characteristics that can be obtained from the answers obtained.

Table 3-2- Type of tests carried out according to the testing protocol and various obtainable parameters and characteristics according to the obtained test results.

| Type of Test | Obtained Characteristics and Parameters |
|---|---|
| Test at different temperatures with target gas step | - Ideal operating temperatures<br>- Adsorption and desorption times at various temperatures |
| Test at different concentrations of target gas | - Detection limit of target gas<br>- Recovery of the baseline<br>- Sensitivity line<br>- Adsorption and desorption times |
| Test at different concentrations of target gas - cumulative test | - Recovery of the baseline<br>- Sensor stability<br>- Sensitivity line |
| Cross sensitivity<br>(Target gas - Humidity) | - Influence of humidity on the response to a target gas |
| Cross sensitivity<br>(Target gas - interfering gas) | - Influence of an interfering gas on the response to a target gas. |

### 3.2.6 Gas sensor characteristics

The following figures of merit have been introduced to address these “gas response properties” (Figure 3- 7):

- base line resistance (BLR): the resistance in dry air at equilibrium before a gas exposure;
- relative response (RR): the ratio ($R_G/R_A$) or ($R_A/R_G$) for a given concentration of oxidizing or reducing gas, respectively;
- adsorption/desorption time ($\tau_{ads/des}$): the time required to reach 90% of the full response at equilibrium, during both gas adsorption and desorption;

- recovery percentage (RP): the percentage ratio ($\Delta_D/\Delta_A$) x 100, where $\Delta_D$ and $\Delta_A$ are the variations of the electrical resistance during gas adsorption and desorption, respectively, calculated within the time scale of the sensing cycle. (see Figure 5 for its graphical representation).
- Long-term stability: Stability is an important criterion required for gas sensors. This is because gas sensors should operate consistently under repeated conditions, experiencing response and recovery by detecting a gas at various concentrations and sometimes in harsh environments. Stable performance without showing a drift is another important measure to evaluate the performance of gas sensors.

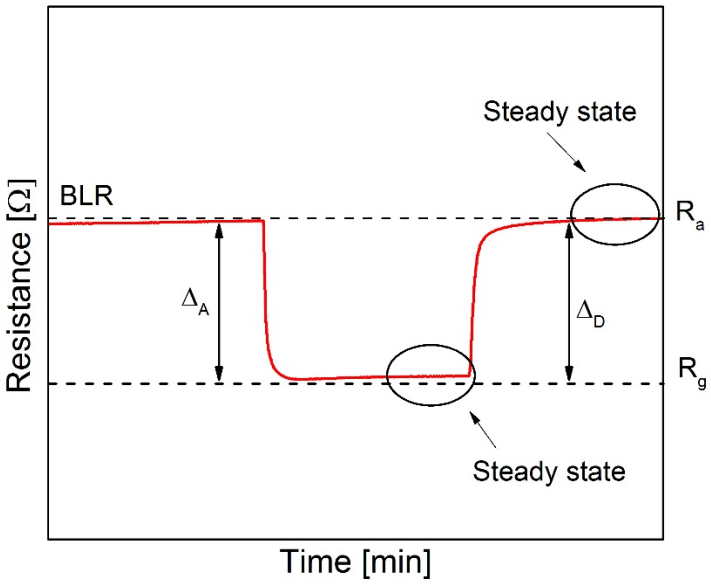


Figure 3- 7. Example of the explained figures of merit in the case of a n-type semiconductor responding to reducing gas

Regarding these points it must firstly be pointed out that, given the time scale of a sensing cycle, gas adsorption/desorption times can be eventually numerically quantified only if the equilibrium conditions are achieved. Secondly, the recovery percentage (RP) is a measure of the sensor ability to recover, after degassing, its BLR. Under these circumstances it could happen that by desorbing in air, equilibrium conditions are achieved (i.e. $\tau_{ads/des}$ can be quantified) but the sensor resistance fails to regain its original base line value. This occurs in the case of irreversible adsorption, when gas molecules are bound so strongly to the surface that they never desorbs, regardless the time scale of a sensing cycle. Lastly, it may be the case that no equilibrium conditions are achieved during desorption so that neither base line recovery is achieved nor $\tau_{ads/des}$ times can be quantified.

# CHAPTER 4
# Exfoliation of 2D materials: optimization, microstructure and chemical characterization of few layered $WS_2$

## ABSTRACT

This chapter reports the experimental results achieved with the optimization of the exfoliation process made of ball milling and sonication steps. Parameters such as duration of ball milling and temperature control have been studied in light of microstructures and surface chemistry of the exfoliated flakes

## CONTENTS

## 4.1 Introduction

In recent years layered materials such as, 2D transition metal dichalcogenides (TMDs) have attracted a high level of interest due to their peculiar properties, which make them appealing for potential applications in gas sensing,[1,2] photo-electro-catalytic hydrogen evolution,[3,4] optical and electronic devices[5,6] and energy storage.[7,8]

As previously shown, Few layer 2D TMDs can be produced through different methodologies like mechanical and liquid phase exfoliation of bulk crystals, classified as top-down routes, or via direct bottom-up routes like chemical vapor deposition.[9,10] High yield liquid exfoliation methods comprising ion intercalation[11,12] and ultrasonic cleavage[13,14] have also been widely employed to exfoliate bulk-layered materials. Besides liquid phase exfoliation, ball milling as a newly explored high yield mechanical exfoliation method has been utilized for scalable production of mono and few layer graphene[15,16] and TMDs nano-sheets.[17,18] More recently, enhanced mixed methods comprising assisted grinding and sonication have been shown to produce higher concentrations of TMDs nano-sheets and reduced amount of defects.[19] All the above-mentioned preparations have devoted to optimization of the exfoliation procedure, or have focused on morphological aspects, rather than investigating the influence of the preparation methods on the evolution of surface defects (i.e. sulfur vacancies) and/or the occurrence of oxidation phenomena.[20,21] Spontaneous oxidation in air represents, indeed, the “Achilles’ heel” of TMDs, which may strongly influence their properties over time. To this extent we demonstrated that both exfoliated $MoS_2$[22] and $WS_2$[23] easily oxidize to their metal oxides counterparts, and that temperature plays the major role when controlling the surface oxidation phenomena.

One of the main goals of this thesis is to set up a simple, efficient and scalable exfoliation process to produce from mono to few layers TMDs, eventually applicable to other layered materials.

## 4.2 Two-step exfoliation of $WS_2$

The studied exfoliation process started from two literature references [24,25], in which $MoS_2$ and $WS_2$ were exfoliated by hand grinding and subsequent sonication. The procedure, described in the flowchart which follows, can be summarized in the following steps:

- Reagent mixing for grinding
- Grinding in automatic ball milling machine
- Drying and first-solvent removal
- Mixing of the ground powder with the second solvent
- Tip-sonication of the dispersion
- Centrifugation and supernatant collection
- Deposition for further analysis

Specifically, 2 g of $WS_2$ commercial powder (Sigma-Aldrich 243639-50G) was dispersed in 2ml Acetonitrile (ACN -VWR 83639.320) in a 45 ml stainless steel jar equipped with 12 balls (D=12 mm) with a ball to powder weight ratio of 24, and automatically grinded in a planetary milling machine (Fritsch – Planetary Micro Mill Pulverisette 7) at 400 rpm, for 2 h in ambient air.

To evaporate ACN residuals after milling, the collected slurry was left overnight at 23±2 °C temperature and 40±3% Relative Humidity (RH). After ACN evaporation, 0.05 g of the dried powder was dispersed in 100 ml of pure ethanol (99.94% VWR 20821.330) and probe into the sonicated (Sonics VC 505 ultrasonic processor) at 250 W for 90 min in a thermostat bath to prevent temperature rise (T 25 °C). Finally, the solution was centrifuged at 2500 rpm for 40 min in a refrigerated (20±2 °C) micro-centrifuge (Eppendorf 5417R) and the supernatant collected.

# FLOW CHART OF THE EXFOLIATION PROCESS

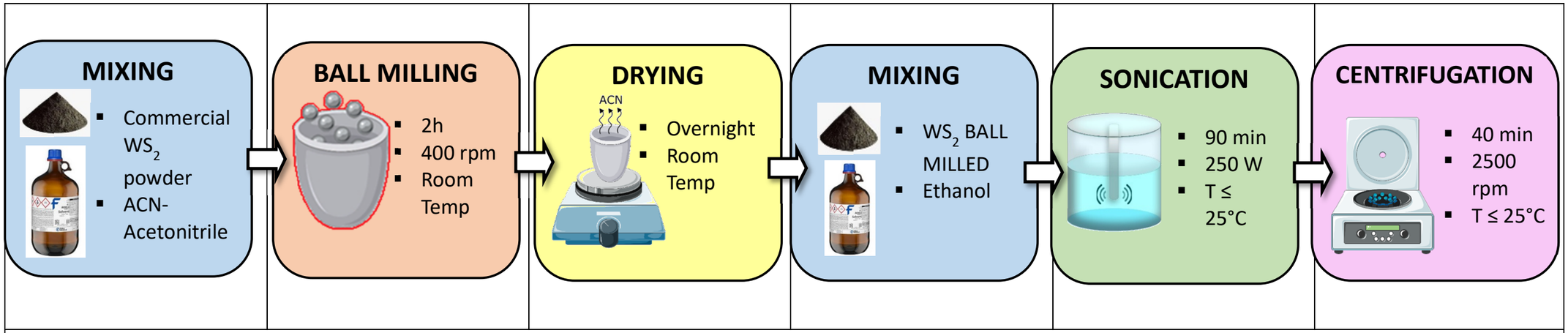


| GENERAL DESCRIPTION OF PROCESS SET UP | | | | |
|---|---|---|---|---|
| Appropriate solvent (Acetonitrile) with low evaporation temperature is chosen for ball milling. | $WS_2$ dispersed in acetonitrile is ball milled for 2 hours at room temperature. The ball/powder weight ratio was 24. | After ball milling the ball milled $WS_2$ was left at room temperature over night to evaporate the residual of Acetonitrile. | After evaporating ACN, dried $WS_2$ were dispersed in pure ethanol and probe sonicated for 90 min at 250 W. To prevent the Oxidation of exfoliated flakes, the temperature should be maintained less than 25˚C. | After 90 mins of probe sonication in pure ethanol, the dispersion is centrifuged to precipitate the unexfoliated flakes and the supernatant is collected by pipette. 5 µL of the supernatant is drop cast and spin coated on the electrode pattern of the sensor. |
| **CRITICAL PARAMETERS AND CONTROL OF PROCESS STEPS** | | | | |
| Surface tension energy of solvent;<br>Evaporation temperature of solvent. | 1. Ball-powder weight ratio;<br>2. Speed;<br>3. Ball milling time;<br>4. Energy. | 1. Evaporation temperature. | 1. Concentration of dispersion (mg. $mL^{-1}$);<br>2. Sonication time;<br>3. Sonication power;<br>4. Sonication temperature. | Centrifugation:<br>1. Speed;<br>2. Time;<br>3. Temperature |

Reagents Mixing, Milling and Evaporation

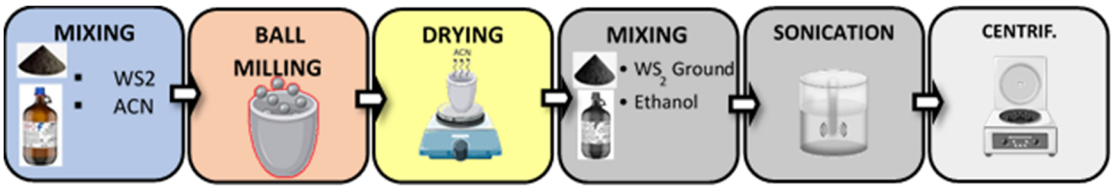


For preparation of exfoliated mono-few layers $WS_2$, 2 g of $WS_2$ commercial powder (Sigma-Aldrich 243639-50G) with 99% purity and average particle size of 2 µm were dispersed in 2 mL of acetonitrile (ACN - VWR 83639.320) and ball milled in a planetary milling machine at 400 rpm with 12 stainless steel balls (D=12 mm) and ball/powder weight ratio of 24 for 2 hours (steps of 15 min milling and 5 min idle to avoid excessive warming).

Low energy ball milling exfoliation mechanism and its associated forces is illustrated and discussed in Chapter 2. Also, a schematic of exfoliation comprising low energy ball milling and the associated shear and compression forces from balls during ball milling is illustrated in Figure 4-1.

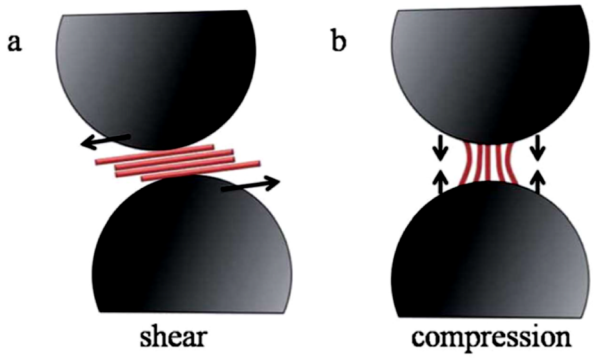


Figure 4- 1. The illustration of the thinning and exfoliation effects of combined low-energy ball milling and sonication. (A) and (B) 2D nanosheet exfoliation by low-energy ball milling. (A) Shear force-induced exfoliation. (B) Compression force-induced exfoliation.

The ball milling machine utilized in this work for exfoliation was planetary type and is illustrated in Figure 4- 2.

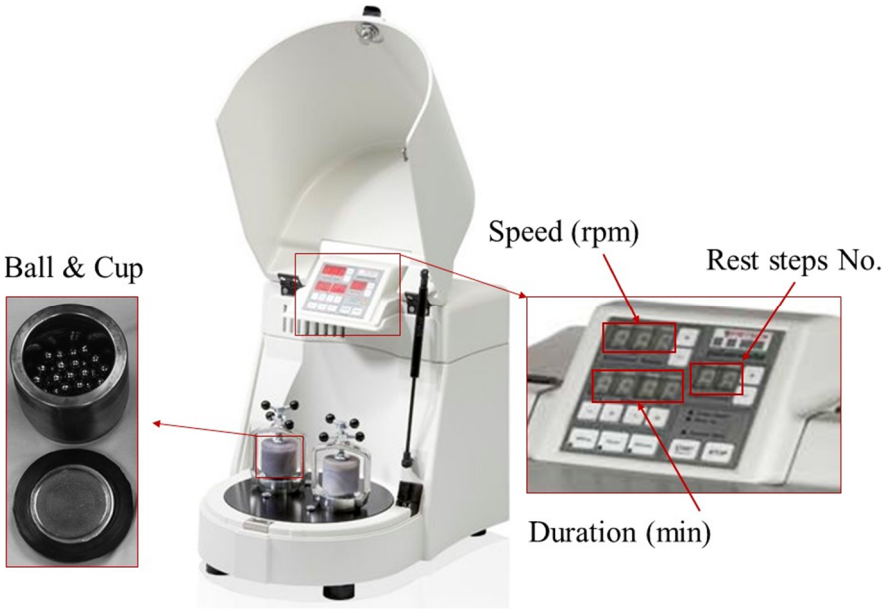


Figure 4- 2. Planetary ball milling machine.

**Operating principles of ball milling**

Figure 4- 3 shows the schematic of the ball milling operation, rotation directions and axes, and induced forces to the powder during milling procedure.

The powder is crushed and ground by induced forces from balls in a grinding bowl. The centrifugal forces from the rotation of the grinding bowls around their own axis and from the rotating support disc act on the contents of the grinding bowl which consists of powder and balls. The bowl and the support disc have opposite directions of rotation so that the centrifugal forces alternate in the same direction and in the opposite direction. The result is that the grinding balls run down the inside of the bowl's wall providing a friction effect and the grinding balls hit the opposite wall of the grinding bowl providing an impact effect. The impact effect is amplified by the impact of the grinding balls against each other.

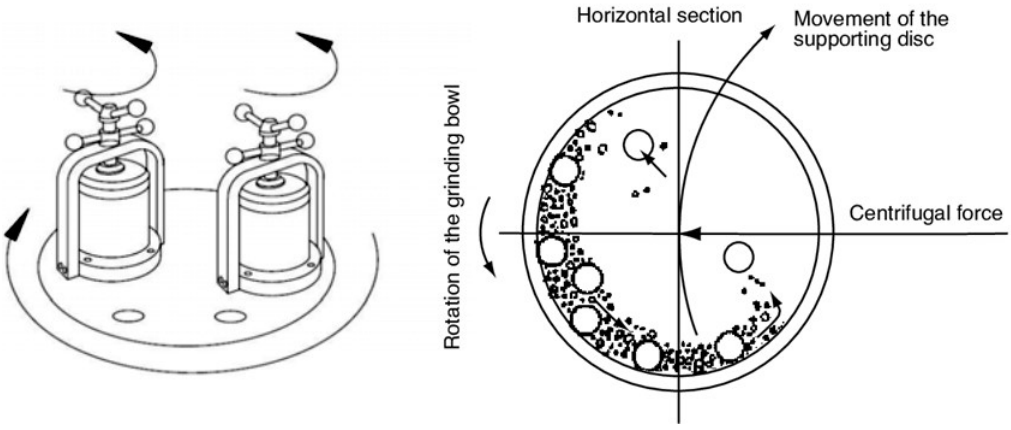


Figure 4- 3. Schematic of the ball milling operation, rotation directions and associated forces

## Ball milling: Influential Parameters

### Ball-to-powder ratio effect

One of the milling parameters that directly changes the amount of induced forces and energies to the layered material is the weight of balls versus powder. The objective is to dominate the shear force due to the rolling of the balls and depress the impact forces of the balls. Ball weight ratio has shown significant influence on dominating these energies so that by increasing the ball weight ratio the shearing forces increase while the impact forces increase as well. This means that the adjacent layers are exfoliated while their lateral dimension is decreasing too.

Deepika et al., showed that compared to the results from the ball-to-powder ratio of 10:1, a similar amount of BN nanosheets were produced when the ratio increased to 20:1. However, the 20:1 ratio produced more BN nanosheets less than 200 nm in diameter. When the 50:1 ratio was applied, many small particles instead of sheets were found. The formation of these particles is due to damage to the BN nanosheets. This indicates that the increase of ball-to-powder ratio can result in higher yields of sheets, but at the cost of more structural damage owing to higher chance of ball-to-vial or ball-to-ball collision and possibly stronger collision see.

They obtained the ball powder ratio of 10:1 for exfoliation of BN utilizing 1 mm stainless steel balls [26].

### Milling speed effect

Studies have shown that the shear force during ball milling increases by increasing the ball milling speed, hence the exfoliation increases. Deepika et al., showed that increasing the milling speed from 600 rpm to 800 rpm results in more exfoliation and exfoliated nanosheets with higher aspect ratio [26].

### Ball size effect

It is reported that the bigger balls provide larger surface area that increases the probability for ball to ball or ball to wall interaction and impact and thus more shearing forces. The other issue is the weight of balls of different sizes, the lighter weight of balls makes the shear forces gentler and minimize the crystal damage comprising from the impact force [26].

### Milling Time

Milling time has been reported as the most significant processing parameter in several studies. It is shown that by increasing the milling time the induced power increases. Deng et al. [27], showed that the concentration of exfoliated graphite milled supernatant increases non-linearly with increasing the milling time. They showed that when the milling time is less than 10 hours the concentration of supernatant increases slowly but over 10 hours of ball milling the concentration significantly increases. In other words, they obtained 10 hours of ball milling as the turning point of ball milling where under this duration shear force is dominant. The conclusion is that up to the turning point (10 hours in their study) the initial large graphite bulk sheets are broken

to smaller pieces under compression forces from balls, see Figure 4- 4, and the size of graphite decreases and concentration of the supernatant increases slowly at the beginning, as shown in Figure 4- 4 the gradient of the concentration up to 7 hours. After that, since smaller graphite flakes are easier to exfoliate as the collective van der Waals force between layers is lower in them, shear force becomes dominant up to the turning point. By exceeding the turning point the impact point becomes dominant and the exfoliated layers are broken on lateral dimensions [27].

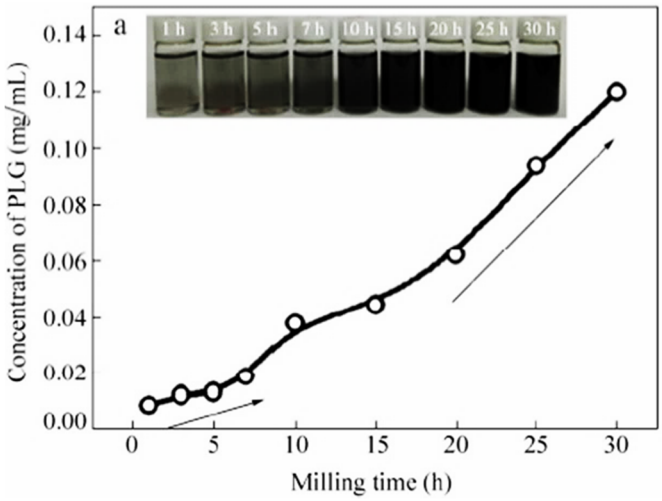


Figure 4- 4. Concentration of FLG as a function of milling time (0.4 g of EG, milling speed: 500 r/min, centrifugation speed: 4000 r/min) [27].

**Milling solvent**

Wet milling is widely used and studied to make sure that the shearing effect is dominant during ball milling. A good solvent for ball milling exfoliation of van der Waals layered materials is the one that has a matched surface energy for overcoming the van der Waals forces of adjacent flakes, such as DMF, NMP, tetramethylurea. Different kind of organic solvents with appropriate surface tension energy has been used in planetary milling machine to fabricate graphene and few layer TMDs. This scheme depends on milling time and rotational speed of milling to dominate the sheering force.

Besides, although organic solvents with appropriate range of surface tension energies have shown good solvents for ball milling exfoliation, their residuals usually remain on the surface of exfoliated flakes due to their high boiling point and do not evaporate even by mild annealing.

For these reasons an appropriate solvent for high yield ball milling exfoliation to obtain pristine mono-few layers flake is a kind of solvent with surface energy of 70 - 80 mJ·m$^{-2}$, or a surface tension energy of 40-50 mJ·m$^{-2}$ at room temperature and can be easily evaporated at low annealing temperature to prevent the oxidation and drawbacks due to elevating temperature [15,24].

Considering the above-mentioned influential parameters in ball milling process, Acetonitrile was chosen as milling solvent in this work, due to its low evaporation temperature to fabricate pristine exfoliated mono-few layers $WS_2$. Besides, ball size and milling speed are kept constant and effect of milling time on exfoliation procedure is extensively studied that will be discussed after explaining the sonication process.

After ball milling of $WS_2$ to evaporate ACN residuals after milling, the collected slurry was left overnight at 23±2°C and 40±3% Relative Humidity (RH).

**Mixing, Probe Sonication and Centrifugation**

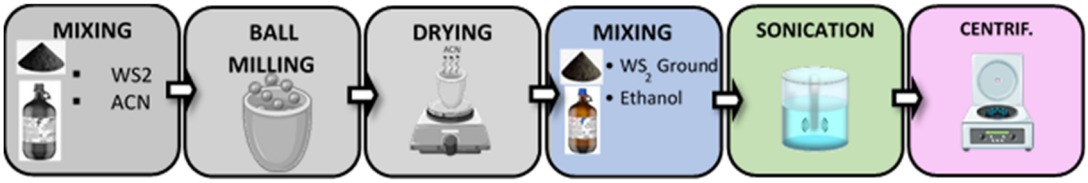


After ACN evaporation at room temperature, 0.05 g of the ball milled powder dispersed in 100 mL of pure ethanol and probe sonicated for 90 minutes in a cool bath (T ≤ 25°C). Finally, the sonicated dispersion was centrifuged at 2500 rpm for 40 min at 20°C and the supernatant collected, and spin coated on a $Si_3N_4$ substrate.

The mechanism of sonication assisted liquid-phase exfoliation method and its associated forces, as a large-scale production technique to fabricate mono-few layer TMDs from their bulk form was extensively discussed in Chapter 2.

The sonicator machine used in this work is a simple probe sonicator machine that is a part of dynamic light scattering machine, Figure 4- 5 (a). To control the temperature during the sonication process, $WS_2$ dispersion beaker was placed inside a bath comprising a cooled water circulating coil, Figure 4- 5 (b), and the coil was connected to a lab chiller, Figure 4- 5 (d).

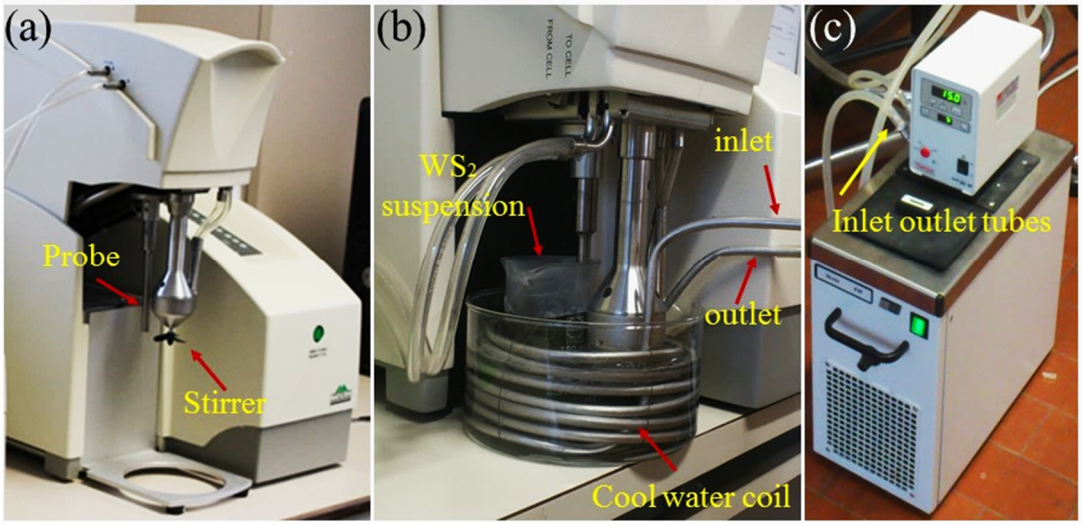


Figure 4- 5. Sonication process set up; (a) probe sonicator, (b) water cooled coil and bath, (c) Chiller.

**Sonication: Influential Parameters**

Studies showed that sonication conditions and parameters can critically influence the exfoliation process and thickness, sizes and other properties of the mono-few layered TMDs formed from their bulk format.

When ultrasonic treatment occurs in a solvent, acoustic waves passing through the fluid create progressive compressions and decompressions in it, with rate depending on the frequency. If the intensity of ultrasound is high enough, the expansion cycle can create bubbles or voids in the liquid. Formation, growth, pulsation and collapse of bubbles in a liquid constitute the phenomenon of cavitation.

Based on the observations, two main consequences of $MX_2$ sonication are (i) exfoliation into $MX_2$ nanosheets, that means the detachment of layers from the bulk, that were only bonded by van der Waals forces (Figure 4- 6d); and (ii) scission into particles with smaller dimensions, down to nanoparticles, by breaking covalent bonds (Figure 4- 6 d).

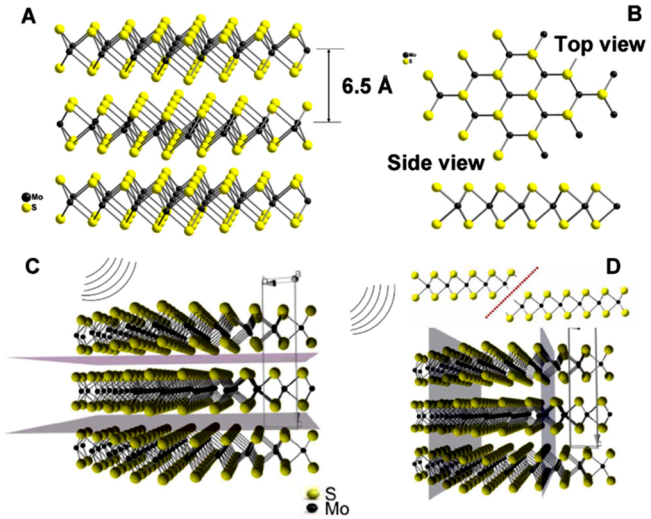


Figure 4- 6. Structure of $MoS_2$ and effects of the strong sonication on $MoS_2$ flakes dispersed in a solvent. (a) Bulk $MoS_2$ crystal, where single layers are separated by a 6.5 Å distance (center to center); (b) $MoS_2$ monolayer: top and side views; (c) Exfoliation into nanosheets: breaking van der Waals bonds between layers; (d) Fragmentation of lamellae: breaking covalent bonds within layers. Yellow and black spheres correspond to sulfur and molybdenum, respectively and D.

Important parameters affecting the sonication assisted liquid exfoliation process are sonotrode shape, sonication time, pressure and temperature of the reaction, ultrasound intensity, solvent density etc.

**Sonication power**

One of the most effective parameters in sonication is the power of sonication. Authors studied the influence of the ultrasound power in the range of 100-500 W on the properties of the $MoS_2$ dispersions forming in NMP, chloroform and acetonitrile or in water/surfactant solutions. It was shown that increase in sonication power from 350 to 500 W decreased nanosheet lateral dimensions almost twice from 200 nm, while thicknesses of 6-12 nm stayed unchanged, and the yield of the dispersed product increased maximum up to 0.43 mg/mL. The expected rise in concentration with increasing ultrasound power was also noted in the paper for $MoS_2$ ($WS_2$)/water/ surfactant combinations. In this work these effects were studied in more detail, and it was demonstrated that at first, the increase in the ultrasound power led to higher concentrations and lower lateral sizes, however, as the power exceeded 320 W, concentrations started to fall, while the nanosheets areas became somewhat larger. This phenomenon is due to the cavitation shielding effect. Two types of cavitation in liquids are discussed (Figure 4- 7a). At lower acoustic fields, stable (no inertial) cavitation takes place, that is, the bubbles have a relatively long growth cycle and oscillate around an equilibrium position over many acoustic cycles. In contrast to stable cavitation, inertial cavitation takes over at higher ultrasound powers. During several acoustic wave cycles, oscillating bubbles or voids rapidly grow, reach their resonant sizes, expand and collapse abruptly, producing high speed liquid jets. When the power is within 100-200 W, stable cavitation is realized. In this case, stably oscillating bubbles colliding against $MoS_2$ basal planes are not able to break covalent

S-Mo-S bonds but can easily overcome van der Waals bonds interlinking $MoS_2$ layers. Thus, in this range of powers, larger $MoS_2$ nanosheets are produced (150×75 nm, 3-7 nm thick, Figure 4- 7, e). When the transmitted power rises to about 320 W, inertial cavitation becomes effective. As a result, high-intensity bubble knocks cleave covalent Mo-S bonds and, thus, generate surface defects in $MoS_2$ basal planes, leading to nanosheet scission into numerous smaller parts (Figure 4- 7d, Figure 4- 7c). This effect is most pronounced at 200-250 W, giving smallest nanosheets with narrow size distributions (72 ×33 nm) and thicknesses of 1-5 nm (Figure 4- 7.b, e). However, at 285 W and, especially, at 400 W, ultrasonic cavitation shielding effect commences. This phenomenon consists in the accumulation of many bubbles around the sonotrode, which hinders the transmission of acoustic waves and development of inertial cavitation (Figure 4- 7d). As a consequence, lateral sizes of the exfoliating sheets increase up to 207× 112 nm with thicknesses of 2-10 nm (Figure 4- 7b, e) [28].

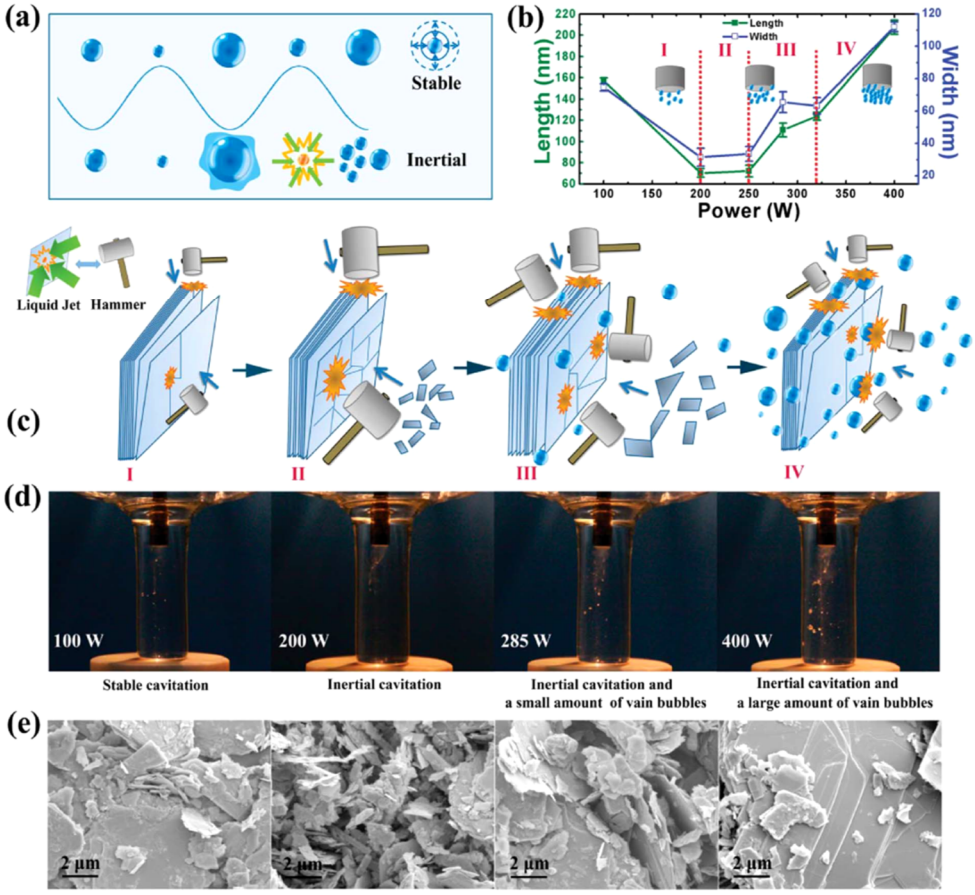


Figure 4- 7. Illustration of the two types of cavitation mechanism; (b) Mean flake length and width (based on> 300 randomly selected nanoflakes for each sample) obtained at different ultrasonic power intensities; (c) Schematic representation of the exfoliation procedure to obtain $MoS_2$ nanoflakes in four distinct regions (I to IV); (d) Images of the acoustic cavitationbubbles in NMP solvent at different input powers; (e) SEM images of the sediment after centrifugation of 100, 200, 285 and 400 W samples.

**Sonication solvent**

Many studies have been done to investigate the effect of sonication solvent on exfoliation properties from various points of view.

On one hand, many studies consider intermolecular $MX_2$-solvent interactions, which may be strong enough to overcome interlayer attraction forces, but do not lead to the formation of covalent bonds. On the other hand, recent research shows that interactions of the solvents with $MX_2$ surfaces may be of a more complex chemical nature, which is due, in particular, to the ability of the solvents to form chemically active particles upon sonolysis. Following, both aspects are discussed.

J. Coleman and co-authors as well as Ajayan and co-authors have symmetrically investigated the exfoliation of numerous dichalcogenides ($MoS_2$, $WS_2$, $MoSe_2$, $MoTe_2$, $TaS_2$, $TaSe_2$, $NbSe_2$, $NiTe_2$, $Bi_2Te_3$) in various solvents under ultrasonication.

Many of these works investigate the appropriateness of various solubility parameters, that is, quantitative characteristics of a solvent and $MX_2$ that should have similar values to minimize the exfoliation energy (enthalpy of mixing) and to form a colloidal dispersion. As such, solvent's surface energy was considered as a solubility parameter. It was noticed that all “successful” solvents had a common value of surface tension σ around 40 $mJ.m^{-2}$ which corresponds to the surface energies γ ~ 70 $mJ{\cdot}m^{-2}$, as these parameters correlate as the equation 4-1

$$\gamma = (\sigma + TS) \qquad 4\text{-}1$$

where S is the surface entropy, and TS ~ 29 $mJ.m^{-2}$ for most liquids at room temperature. This value of surface energy is very close to that of the dichalcogenide nanosheets (75 $mJ{\cdot}m^{-2}$, as measured by inverse gas chromatography. The best solvent for both $MoS_2$ and $WS_2$ were N-vinyl-pyrrolidinone, DMSO, N-dodecyl-pyrrolidone, cyclohexyl-pyrrolidinone, dimethyl-imidazolidinone and DMF. Highest concentrations achieved in NMP were 0.30 $mg{\cdot}mL^{-1}$ for $MoS_2$ and 0.15 $mg{\cdot}mL^{-1}$ for $WS_2$ (Figure 4- 8) by optimizing sonication conditions and centrifugation time, J. Coleman's group succeeded in preparation of $MoS_2$/NMP colloids with very high concentrations of 40 $mg.mL^{-1}$ and yields reaching 40%.

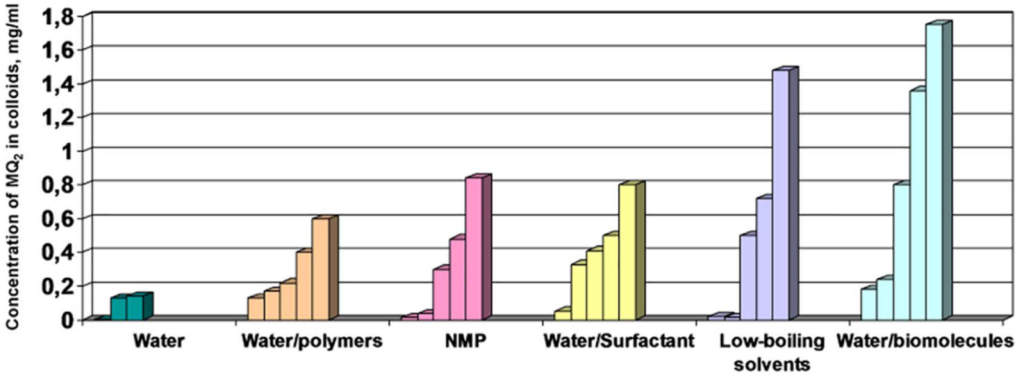


Figure 4- 8. Concentrations of colloidal $MX_2$ nanosheets in different media, produced by direct sonication, mg/mL (summarized from data reported by different authors).

This chart gives a general impression of average achievable numbers, however, in some cases, much higher concentrations are reported: $MoS_2$/NMP after 140 h- long sonication: 40 mg/mL, $MoS_2$/ethanol/water derived from grinding-assisted process: 26 mg/mL; $MoS_2$/water/surfactant Pluronic P-123: 12 mg/mL. For comparison, intercalation-exfoliation methods often yield much more concentrated $MX_2$ colloids: $MoS_2$/organic solvents: 30-55 mg/mL; $WS_2$/DMF: 19 mg/mL; $MoS_2$/ethanol+ water: 1.6-2.2 mg/mL. It should be noted that (i) results may vary depending on the method used for estimation of the colloidal concentration (weighing method or UV data), and (ii) characteristics of the dispersions with similar concentrations may vary (thickness of the nanosheets, their lateral sizes, stability, etc.).

However, it is not rare that solvents with close surface tensions σ disperse $MX_2$ to different extents. For example, this happens with NMP and pyridine. The explanation may lie in the fact that σ describes interactions in general, while intermolecular interactions may have different nature. Full surface tension may be represented by two components accounting for polar (σp) and dispersion (σd) interactions. If one interaction differs strongly in solvent and $MX_2$, even at similar σ, then no colloid formation takes place. While precise values of those components for different solvents are not known, σp/σd ratio may be obtained by measuring contact angles of $MX_2$ with liquids. This method allowed the authors to identify different $MX_2$ dispersing media with matching values of σp/σd ratios by simply varying proportions of the solvents in their binary mixtures. Colloidal dispersions are produced in isopropanol/water mixtures (Table 4-1), acetone/water mixtures (3:2, σp/σd= 0.479) and THF/water (1:1, σp/σd= 0.476). As illustrated in Table 4-1, matching the ratio of surface tension components σp/σd of $MX_2$ and of a solvent mixture is even more important than matching their full surface tensions [28].

Table 4-1- Full surface tension σ and the ratio of its polar and dispersive components $\sigma_p/\sigma_d$ for layered dichalcogenides $MX_2$ and water-isopropanol mixtures best suitable to stabilize $MX_2$ colloids.

| **Material** | **σ, mJ.M$^{-2}$** | **$\sigma^p/\sigma^d$** |
|---|---|---|
| **$MoS_2$** | ~ 40 | 0.449 |
| **Isopropanol: water (4:1)** | 23.4 | 0.450 |
| **$WS_2$** | ~ 40 | 0.563 |
| **Isopropanol: water (1:1)** | 25.1 | 0.482 |

**Sonication time**

Lengthening of the sonication time does not bring about any noticeable changes to hexagonal structures of dispersed $MX_2$ nanosheets, but lowers their lateral sizes due to cutting effects (Figure 4- 6. d) and increases concentrations of the colloids.

**Spin Coating and heat treatment**

After probe sonication, the obtained dispersion has been centrifuged to precipitate non-exfoliated $WS_2$ flakes and collect the supernatant containing exfoliated mono-few layered $WS_2$. After obtaining the supernatant, one drop of it (8 µL) will be spin coated on $Si_3N_4$ substrate for material characterization or on sensor substrate for gas sensing measurements.

Considering the above-mentioned influential parameters in ball milling assisted sonication process, $WS_2$ exfoliation parameters are presented in table Table 4-2.

After spin coating of $WS_2$ solution, the substrates will be annealed at 180˚C.

Table 4-2- Ball milling assisted sonication exfoliation parameters.

| Sample | Grinding parameters | | | | | | Sonication parameters | | | Centrif. parameters | |
|---|---|---|---|---|---|---|---|---|---|---|---|
| | $WS_2$-ACN | Speed [rpm] | Milling time [h] | Nbr. of balls | Weight of each ball [g] | Ball/ Powder weight ratio | $WS_2$-EtOH | Duration [min] | Temperature [°C] | Duration [min] | Speed [rpm] |
| 1 | 2 g-2 mL | 400 | 72 | 12 | 4 | 24 | 0.05 g-100 mL | 90 | 25 | 40 | 2500 |
| 2 | 2 g-2 mL | 400 | 24 | 12 | 4 | 24 | 0.05 g-100 mL | 90 | 25 | 40 | 2500 |
| 3 | 2 g-2 mL | 400 | 2 | 12 | 4 | 24 | 0.05 g-100 mL | 90 | 25 | 40 | 2500 |
| 4 | 2 g-2 mL | 400 | 2 | 12 | 4 | 24 | 0.05 g-100 mL | 120 | 25 | 40 | 2500 |

## 4.3 Microstructural properties of exfoliated $WS_2$

Microstructure and surface oxidation of exfoliated $WS_2$ by milling and sonication are affected by a large number of variables, mainly: solvents' composition, grinding and sonication methods, duration times and operating temperatures. We found that the microstructural features of the exfoliated $WS_2$ are mostly affected by the duration of the milling and sonication steps, whereas surface oxidation depends on the combined action of sonication and temperature.

The evolution of the microstructure was investigated at each step of the exfoliation process as shown in Figure 4- 9. Regarding the ball milling process a key role is represented by the solvent. Considering that TMDs surface energies range between 70-80 mJ $m^{-2}$, solvents with surface tension values of 40-50 mJ $m^{-2}$ are suitable for exfoliation of layered materials.[13,24,25] Although solvents like N-Methyl Pyrolidone (NMP) and Dimethyl Formamide (DMF) with surface tension values of 40.8 mJ $m^{-2}$ and 37.1 mJ $m^{-2}$ respectively represent a solution for high yield exfoliation[29], their high boiling point and the remaining residues after drying, may restrict their applications when pure surfaces are needed.[24,25] In our case acetonitrile (ACN) as a milling solvent, with surface tension of 29.5 mJ $m^{-2}$ [24], has been selected as a trade-off between surface tension and moderate boiling point, enabling complete removal of the solvent at room temperature after grinding.

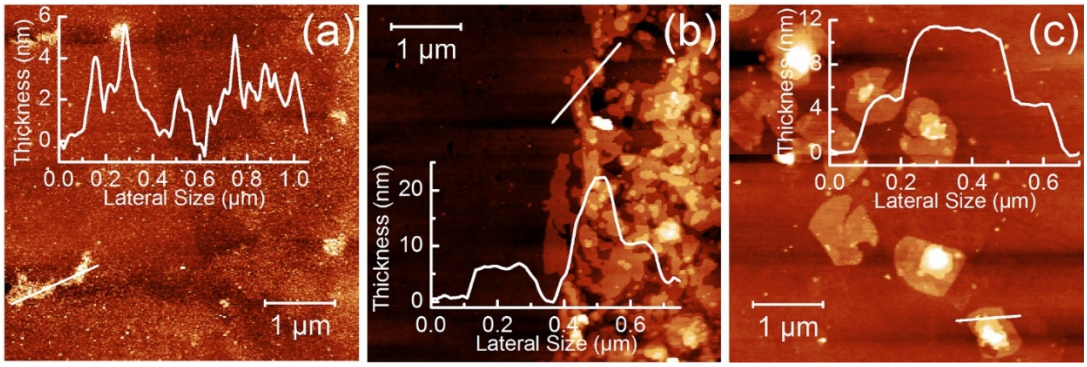


Figure 4- 9**.** AFM pictures of exfoliated WS2 flakes: (a) 72 h ball milled and 90 min sonicated; (b) 24 h ball milled and 90 min sonicated; (c) 2 h ball milled and 90 min sonicated. The inset of each picture shows the thickness profile along the white lines.

Figure 4- 9 shows the AFM pictures of exfoliated $WS_2$ flakes and the relevant thickness profile, in which the ball milling duration is gradually decreased from 72 to 2 h and sonication time fixed at 90 mins. 72 h ball milled $WS_2$ shown in Figure S3a depicts aggregated nano-dots where the rough thickness profile along the line testifies that the intensive impact forces of ball milling has led to fragmentation of $WS_2$ flakes into nano dots.[15,30] Therefore, the ball milling duration was gradually decreased up to 24 h. Figure 4- 9 depicts small flakes of $WS_2$ stacked together confirming the impact forces of 24 h ball milling is still dominant versus the shear force. To minimize this effect, the ball milling duration was decreased till achieving flat thin sheets at high aspect ratios. Figure 4- 9 illustrates large flat flakes of around 1μm obtained after 2 h of ball milling. A thickness profile taken along the white line on one of the flakes is also shown.

With the aim to maximize the "aspect ratio" of lateral dimension to the thickness of the stacked flakes, which may well represent the 2D character of an exfoliated structure, we investigated both the influence of the grinding and sonication times. We prepared several suspensions with constant $WS_2$/ACN ratio decreasing the duration from 72 h, to 24 h and 2 h while increasing the sonication time from 90 min to 120 min.

Regarding the influence of the grinding time, particles' size distribution of the starting $WS_2$ powder (blue plot), determined by DLS technique (see experimental) and shown in Figure 4- 10a, downshifts towards smaller average sizes after 72 h grinding (red plot) and slightly further after 90 min sonication (green plot). The particle size distribution of the $WS_2$ starting powder displays an average particle size of ≈8μm (blue plot) whereas the 72 h ball milled shows a bimodal distribution (red plot), with larger aggregates centered at ≈20 μm and smaller ones at ≈0.7 μm. After 90 min sonication, the bimodal distribution of the grinded powder disappears (green plot) and the average particle dimension places at ≈0.6 μm.

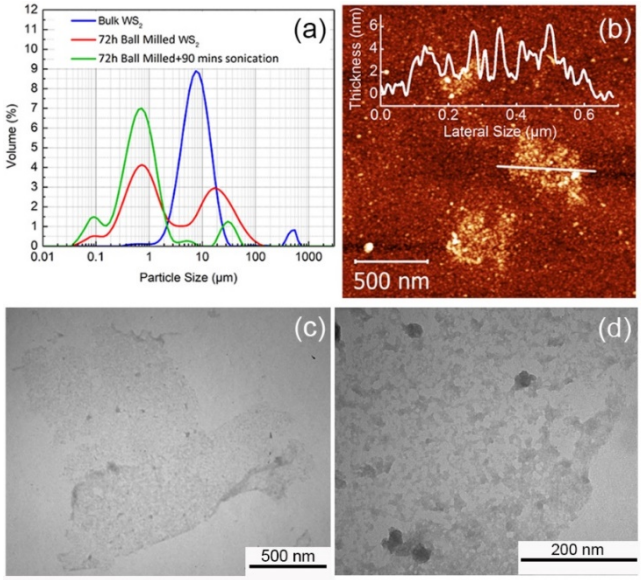


Figure 4- 10. (a) Comparison of the particle size distribution of the starting $WS_2$ commercial powder (blue), 72h ball milled (red) and 72h ball milled and 90 min sonicated (green); (b) AFM picture of 72h ball milled and 90 min sonicated and associated thickness profile along the white line; (c) low magnification and (d) high magnification TEM pictures of the 72h ball milled and 90 min sonicated $WS_2$.

It may be concluded, that grinding has an effective influence to reduce the particle size, while sonication, beside its effectiveness to suppress the bimodal distribution (presumably by separating agglomerated $WS_2$ particles), shows only minor effects to further decrease the particle size of the grinded powder, confirming the dominant role of the milling step. Figure 4- 10b shows the AFM image of the 72 h ball milled and 90 min sonicated $WS_2$ sample. The inset of this image depicts a rough thickness profile along the selected line, with an average height from the substrate of 2 nm. Low and high magnification TEM images illustrated in Figure 4- 10c and Figure 4- 10d, show that long term ball milling for 72 h results in a fragmented structure, which eventually revealed to be amorphous by fast Fourier electron diffraction measurements. These features can be explained considering the two main forces induced by ball milling. The primary force is the shear force provided by rolling of balls on the surface of layers, which causes the removal and the exfoliation of surface layers. The secondary force is the vertical impact from the balls which combined with longer grinding times can fragment the larger exfoliated sheets into smaller ones, eventually collapsing of the crystal structure.[15,30]

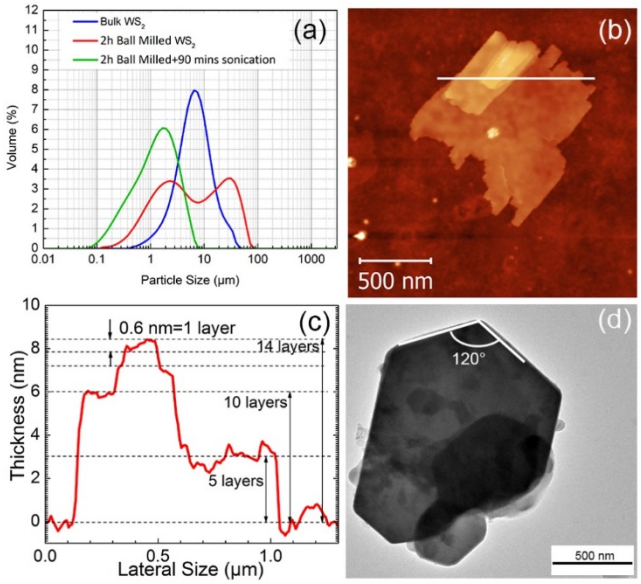


Figure 4- 11. (a) comparison of the particle size distribution of the starting $WS_2$ commercial powder (blue), 2h ball milled (red) and 2h ball milled and 90 min sonicated (green); (b) AFM picture of 2h ball milled and 90 min sonicated; (c) thickness profile of the stacked flake along the white line of Figure (b); (d) TEM picture of exfoliated $WS_2$ flakes.

Figure 4- 11 shows the main microstructural features of the 2 h grinded and 90 min sonicated $WS_2$ powders. Aside from particle size distribution of the starting $WS_2$ powder (Blue plot), Figure 4- 11a shows, as in the previous case, the occurrence of a bimodal particle size distribution after 2 h grinding (red plot), but with larger average particles' with respect to the 72 h grinded (i.e. ≈25 μm vs ≈20 μm and ≈2 μm vs ≈0.7 μm), confirming the indirect relationship between the decrease of the grinding time and the increase of the lateral particles' dimension. Sonication for 90 min results, again, in removing the bimodal distribution with no particular effect on decreasing particles' average size, which maintains at ≈2 μm. Figure 4- 11b shows, as opposite to Figure 4- 10b, the formation of a well-shaped 2D-flake with a large flat surface of 1 μm length. The corresponding thickness profile drawn in Figure 4- 11c highlights a clear formation of a stacked structure comprising a 3 nm thick basal plane, 6 nm thick secondary plane and a third one at the top. Considering that the slight step on top of the profile, 0.6 nm high, corresponds to 1 layer thickness $WS_2$[31], it is shown that the first step is made of 5 layers and the second one of 10 layers respectively. The 2D character of the actual stacked structure shown in Figure 4- 11b, as defined by the "aspect ratio" is high, with an associated value of 250, attesting to the successful optimization of the grinding time for exfoliation. The TEM image depicted in Figure 2d illustrates also a well-shaped exfoliated flake with edge angles of 120°. Comparing Figure 4- 10c with Figure 4- 11d it is shown that by reducing the grinding time to 2 h, the crystalline hexagonal structure of the $WS_2$ nano-sheet is maintained with respect to the 72 h grinded.

Figure 4- 12 and Figure 4- 13 show HRTEM images of both edges and surfaces of the flakes. Figure 4- 12b exhibits two layers with associated interlayer distance of ≈0.63 nm which is in good agreement with the AFM thickness measurements

illustrated in Figure 4- 11c. This interlayer displacement could be also observed at the flake's edges depicted in Figure 4- 12d and Figure 4- 13b, where almost 11 layers can be clearly counted on the 7nm thick edge. The atoms arrangement displayed in Figure 4- 12b and Figure 4- 13c exhibit the hexagonal atomic structure, with lattice spacing of 0.27 nm and 0.25 nm, that are characteristics of (100) and (101) crystal planes of 2H-$WS_2$ flakes, respectively.[29,32] Moreover, the Fast Fourier Transforms (FFTs) shown as the inset of Figure 4- 12d, further confirms the hexagonal crystalline structure of the flake.

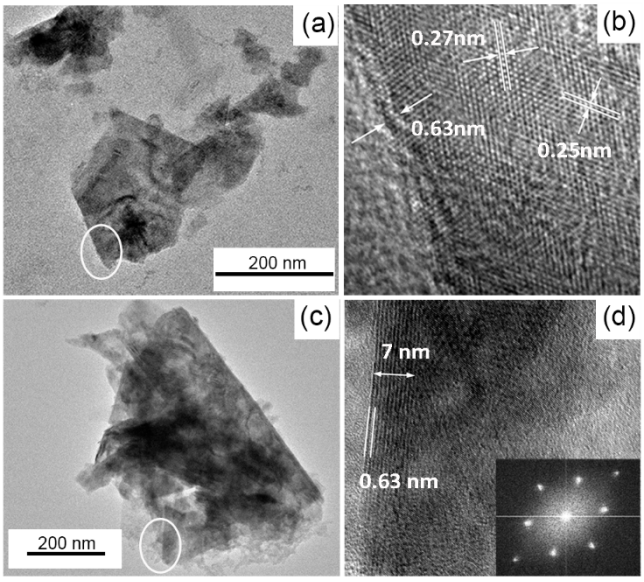


Figure 4- 12. (a) & (c) TEM of 2 h ball milled and 90 min sonicated $WS_2$; (b) HRTEM corresponding to the circled area shown in Figure (a) with highlighted the interlayer distance (0.63 nm) and lattice spacing (0.27 nm and 0.25 nm), corresponding to (100) and (101) planes of $WS_2$ respectively; (d) HRTEM of the edge of the flake corresponding to the circled area shown in figure (c) with highlighted the 7 nm thick edge corresponding to 11 layers. The inset shows the Fast Fourier Transform of the flake.

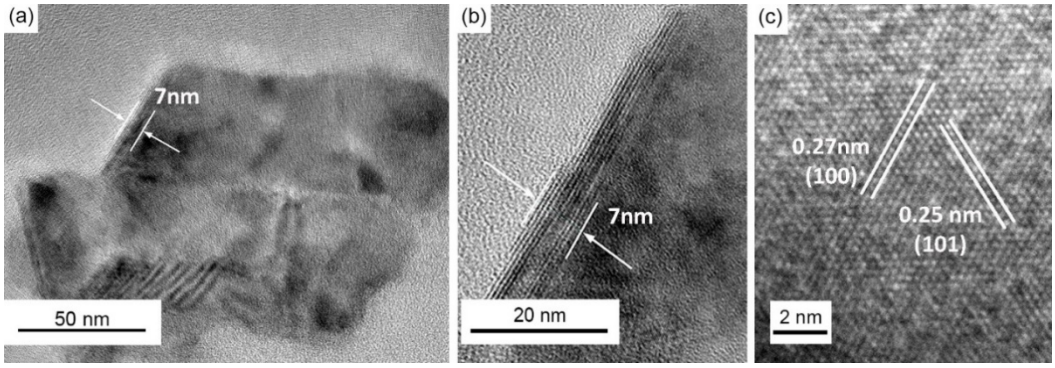


Figure 4- 13. HRTEM pictures of (a) 2 h ball milled and 90 mins sonicated $WS_2$ flake; (b) Edge thickness and number of layers corresponding to the area shown in (a); (c) Lattice spacing and crystal planes of exfoliated $WS_2$.

To give a statistical insight of the reproducibility of the preparation, four different suspensions were prepared after 2 h milling and 90 min sonication and the

corresponding centrifuged suspensions collected and spin coated on $Si_3N_4$ substrates (see experimental). Figure 4- 14a-d shows the AFM images of each prepared sample covering an area of 10x10 $\mu m^2$ and corresponding to a total population of ≈220 flakes. Overall flakes' thickness follows a log-normal distribution as shown in Figure 4- 14e, indicating that almost 30% of the flakes are ≤ 3.0 nm thick (i.e. ≈ 5 layers) and that about 75% are ≤ 6 nm (i.e. ≈ 10 layers). Moreover, as displayed in Figure 4- 14f, average flake lateral dimensions are approximately ≈110 nm yielding a surface coverage of ≈6% as shown in Figure 4- 14g. The overall calculated "aspect ratio" is 27.5, which is comparable to the ones previously reported for $MoS_2$ and $WS_2$, given the same preparation methodology.[24,25] The reduced standard deviations shown in Figure 4- 14f and Figure 4- 14g attest to the high reproducibility of the exfoliation process.

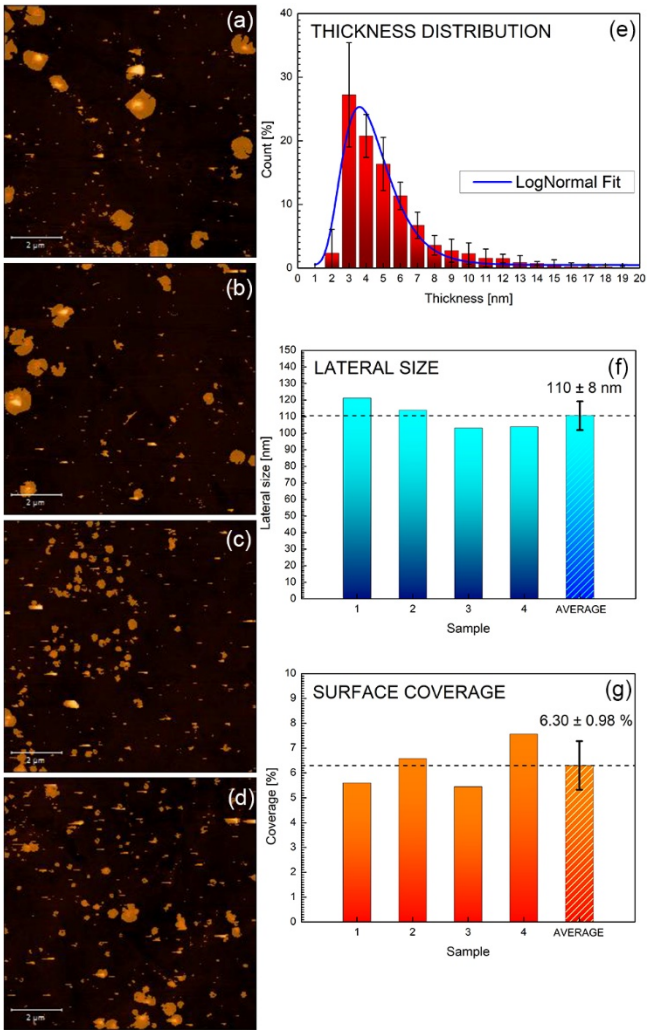


Figure 4- 14. **(**a-d) AFM pictures of $WS_2$ exfoliated corresponding to four different samples prepared under the same conditions (i.e. 2 h ball milling and 90 min sonication). Statistical analysis corresponding to thickness distribution (e), Lateral dimensions (f) and surface area coverage (g).

Lastly, the influence of the sonication time on microstructure by increasing the duration from 90 min to 120 min, has been investigated as shown in Figure 4- 15. Comparing Figure 4- 14 and Figure 4- 15, it is shown that the percentage of flakes with thicknesses ≤ 3.0 nm and ≤ 6 nm increases to 55% and 90% respectively. By contrast, lateral flakes' dimensions drop from 110 nm to 64 nm, surface coverage decreases from 6.3% to 4.1% and the "aspect ratio" turns down from 27.5 to 21.2. Given these results and in light of its final application, 90 min sonication time has been selected, which corresponds to both improved surface coverage and bigger lateral flake dimensions, to enhance percolation paths of charge carriers between interconnected flakes.

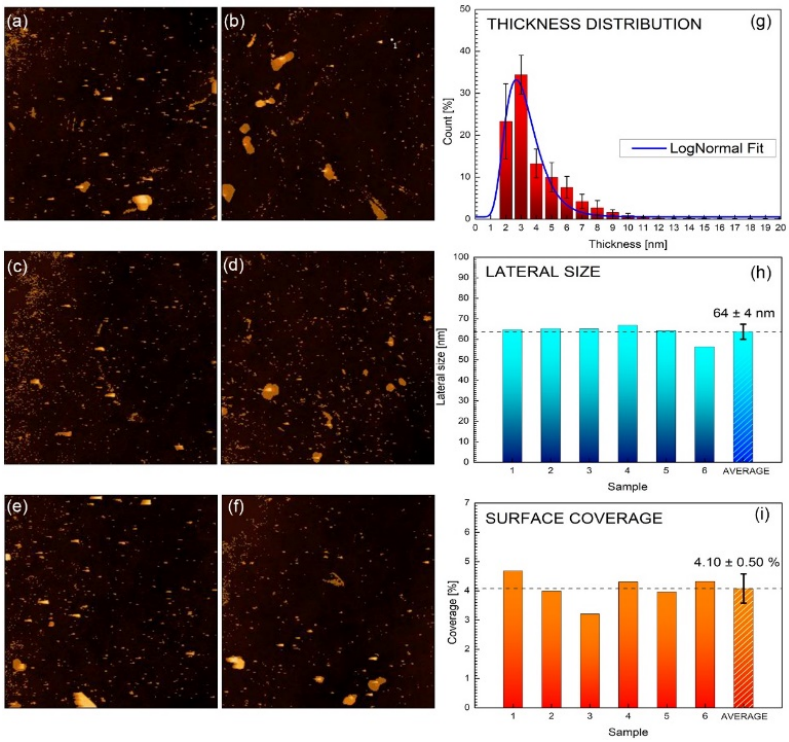


Figure 4- 15. (a-f) AFM pictures of $WS_2$ exfoliated corresponding to six different samples prepared under the same conditions (i.e. 2 h ball milling and 120 min sonication). Statistical analysis corresponding to thickness distribution (g), Lateral dimensions (h) and surface area coverage (i).

## 4.4 Chemical composition of the exfoliated $WS_2$

Chemical issues related to both the evolution of point defects and oxidation phenomena of TMDs highlight important challenges associated with the practical utilization of TMDs monolayers in electronic and optoelectronic devices. Sulfur vacancy is one of the most typical point defect in 2D $MoS_2$ and $WS_2$ monolayers[33], leading to active sites for gas adsorption. On the other hand, spontaneous oxidation of metal sulphides into their metal oxide counterparts[21], may result in poor reproducibility of the gas-sensing response over the long-term. In the discussion which follows possible strategies to control ambient oxidation of 2 h grinded and 90

min sonicated $WS_2$ are highlighted, demonstrating the major role played by the combined action of sonication and temperature.

Figure 4-16 shows the thermo-gravimetric (TG) plot of the $WS_2$ powder heated at 5°C/min from 25°C to 800°C in static air. A cumulative weight loss of -9.4% is shown in the whole temperature investigated range, comprising a primary loss of around -3.2% (25-200°C range) and a secondary of -6.2% (380°C-630°C range).

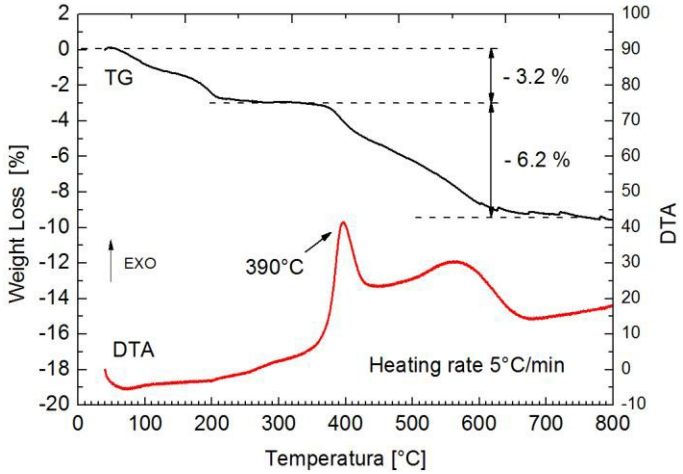


Figure 4- 16. Comparison of the thermogravimetric and Differential Thermal Analysis plots of $WS_2$ commercial powder heated at 5°C/min to 800°C in static air.

The first weight loss may be ascribed to the evaporation of chemisorbed water, the second one to the oxidation of $WS_2$, leading to the formation of $WO_3$ oxides. According to literature [43] the oxidation of $WS_2$ to $WO_3$ is confirmed by both the evolution of a strong exothermic peak around 390°C, as shown by the differential thermal analysis (DTA) plot, and by the occurrence of a weight loss of approximately -6.2%, as displayed by the TG signal, which is reasonably close to the theoretical weight loss expected for the oxidation of $WS_2$ to $WO_3$ (-6.4%). Notably, at temperatures higher than 600°C no further weight loss is shown, attesting the complete oxidation of $WS_2$.

The formation of $WS_2/WO_3$ composite has been divided into different steps, each of them related to the annealing temperature and discussed in light of the XPS, SEM, XRD and STA analysis and published works. As a first issue, thermodynamic calculations [44,45] reveal favourable conditions (i.e. $\Delta G < 0$) for direct oxidation of $WS_2$ in air oxygen, as to reaction 4-2, for all the investigated annealing temperatures.

$$2WS_2(S) + 7\ O_2(G) = 2\ WO_3(S) + 4SO_2\ (G) \qquad (4\text{-}2)$$

$\Delta G$ (150°C) = -1642.8 kJ/mol
$\Delta G$ (250°C) = -1447 kJ/mol
$\Delta G$ (350°C) = -1246 kJ/mol

Beside these preliminary thermodynamic computations, kinetics issues involving diffusion phenomena within the layers, direct sulfur atoms replacement by air oxygen, nucleation and growth of new crystalline structures, play a major role. As a first consideration density functional theory (DFT) simulations on $MoS_2$ single layer demonstrated that the substitution of an S atom by an O atom is energetically favorable, even at room temperature, suggesting a high susceptibility of $MoS_2$ defective layers to be oxidized [46,47].

By heating in the temperature range 25°C-150°C in ambient air (45% ± 5 relative humidity) oxygen atoms rapidly exchange with sulfur as to reaction 4-2, forming an oxide layer, possibly located on superficial or edge defects of $WS_2$ flakes. $WS_2$ interlayer channels provide a path for inward- oxygen and backward-sulfur diffusion, resulting in the formation of amorphous $WO_3$, which propagates over time into the TMD flakes. This mechanism is likely to occur considering, as previously reported, the oxidation kinetic of monolayer $WS_2$ in ambient air [33], and the reverse sulphidization process of bulk $WO_3$ to yield inorganic fullerene-like $WS_2$ nanotubes [48,49].

Figure 4- 17a reports the W 4f core level XPS spectra of the pristine commercial $WS_2$ powder (PWD). The two doublets corresponding to $4f_{7/2}$ peaks are assigned, according to literature, to $WS_2$ and $WO_3$ respectively.[34,35] Notably the pristine powder is already oxidized, with a $WO_3$ content of ≈18%. This phenomenon, most likely due to a surface oxidation, as confirmed by the absence of $WO_3$ peaks in the Raman spectrum in Figure 4- 19, is not surprising considering that surface oxidation at room temperature after 6-12 months has been already reported in literature, demonstrating poor-long term stability of $MoS_2$ and $WS_2$ monolayers.[23] Figure 4- 17b shows that after grinding at room temperature ($G_{25°}$) and subsequent drying (D) to evaporate ACN solvent at 25 °C, i.e. ($G_{25°}$ + $D_{25°}$), the $WO_3$ content decreases to ≈13%. This could be reasonably explained considering that by grinding $WS_2$ powders, newly not-yet-oxidized surfaces are formed, resulting in a smaller content of $WO_3$ as evidenced by XPS measurements. Conversely, as shown in Figure 4- 17c, by grinding at 25 °C and drying at 100 °C, i.e. ($G_{25°}$ + $D_{100°}$), the $WO_3$ content increases to ≈21%. This result implies that, although the positive action of grinding leads to an increase in the $WS_2$ surface area, drying at 100 °C moderately enhances the oxidation process. By grinding and drying at 25 °C followed by 90 min sonication at 60 °C, i.e. ($G_{25°}$ + $D_{25°}$ + $S_{60°}$), as reported in Figure 4- 17d, $WS_2$ is almost fully oxidized to ≈99% $WO_3$. Conversely by grinding, drying and sonicating at 25 °C, i.e. ($G_{25°}$ + $D_{25°}$ + $S_{25°}$), only ≈16% of $WO_3$ is formed, as shown in Figure 4- 17e. This behavior can be clarified considering the combined action of sonication and temperature on the oxidation kinetics of $WS_2$. Literature reports demonstrated that the oxidation of bulk TMDs comprises two parallel steps. Oxygen atoms rapidly exchange with surface sulfur forming an oxide layer, whilst $WS_2$ interlayer channels provide a path for inward-oxygen and backward-sulfur diffusion, resulting in the formation of amorphous $WO_3$, which propagates over time into the TMD flakes.[36,37] Sonication has the positive effect of exfoliating the grinded $WS_2$, removing the coarser particles in the bimodal distribution of Figure 4- 11. Under these circumstances the oxygen/sulfur atoms

counter diffusion mechanism between the layers can be excluded. The fast surface oxidation of $WS_2$ flakes of the early exfoliated samples is driven by temperature, which boosts the substitution of sulfur operated by oxygen atoms. The combined action of sonication and temperature is further confirmed considering the $WO_3$ content of the ($G_{25°}$ + $D_{100°}$) and ($G_{25°}$ + $D_{25°}$ + $S_{60°}$). Despite a drying temperature of 100°C the final $WO_3$ content of the ($G_{25°}$ + $D_{100°}$) is only ≈21% as compared to ≈99% of the ($G_{25°}$ + $D_{25°}$ + $S_{60°}$). Compared to sonicated samples, the grinded samples are comprised of a microstructure of coarser, not yet fully-exfoliated aggregates. Under these circumstances the counter diffusion of S and O atoms between packed layers may be regarded as the controlling step of the whole oxidation process. It shows that surface oxidation is not enhanced by increasing the drying temperature to 100 °C, except for a minor effect.

As discussed in the next chapter, considering the gas sensing as one of the practical application for such material and given the optimum operating temperature for gas sensing at 150 °C, exfoliated $WS_2$ suspensions of ($G_{25°}$ + $D_{25°}$ + $S_{25°}$), were therefore drop cast and air annealed at 180 °C for 1 h, i.e. ($G_{25°}$ + $D_{25°}$ + $S_{25°}$ + $A_{180°}$) to stabilize the oxidation levels. As shown in Figure 5f the $WO_3$ content increased to ≈58%.

In order to give a complete report on the XPS analysis, the S 2p core level spectra are reported in Figure 4- 18. The spectra show the presence of several chemically shifted components, composed of the $2p_{3/2}$ and $2p_{1/2}$ doublets. These components are very likely a consequence of the high reactivity and oxidation states number of sulfur. The spectra are characterized by three main components, assigned to $WS_2$ (component 1, at 162.3 eV), to $SO_4$ (component 2, at 168.8 eV) and to non-metallic disulfide compounds $(S_2)^{2-}$ (component 3, at 163.7 eV). The presence of $SO_4$ and $(S_2)^{2-}$ on the surface of the pristine powder is due to air oxidation processes. The ball milling procedure removes the $SO_4$ and $(S_2)^{2-}$ components partially and completely respectively, while a new component, assigned to $S^{2-}$ ions (component 4, at 161.3 eV) appears. This is most likely due to the exfoliation procedure, which exposes new and not oxidized $WS_2$ but brings some sulfur residuals in the process. Furthermore, if the sonication process is performed at 60 °C, a new sulfur component assigned to $SO_3$ (component 5, at 167.1 eV) is emerged, while the $WS_2$ component is no longer visible. This phenomenon is in agreement with the corresponding W 4f spectrum reported in Figure 4- 17, were it can be seen that the $WS_2$ is almost completely oxidized. Furthermore, all the assignments of the S 2p components are in line with literature.[23,38] Lastly, considering 1% the detection limit of the XPS measurement, we found no clear evidence of defects or sulfur vacancies related components (typically at binding energies of ≈36.1) in the W 4f core level XPS spectra of Figure 5. The analysis of the S 2p core level XPS spectra, reported in Figure 4- 18 is in line with the analysis reported for the W 4f. Notably the analysis of the S 2p spectra confirms the strong oxidative action produced by the combined action of sonication and temperature as previously discussed.

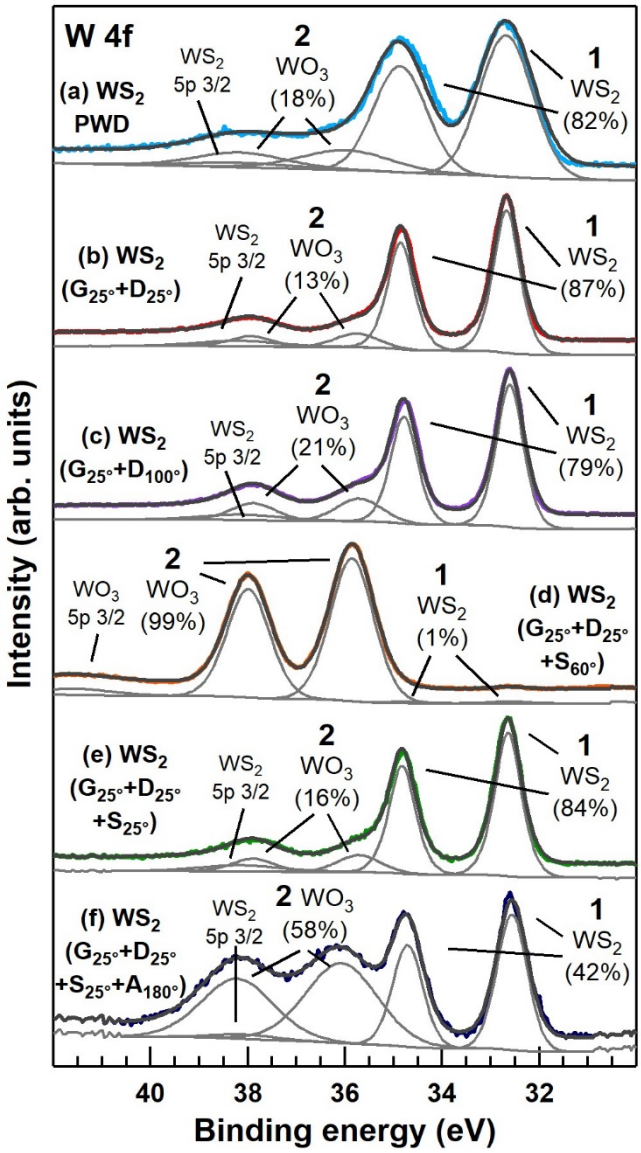


Figure 4- 17. XPS spectra of W 4f core level acquired respectively on (a) pristine $WS_2$ commercial powder ($WS_2$ PWD); (b) ball milled and dried $WS_2$ at 25 °C ($G_{25°}+D_{25°}$); (c) ball milled at 25 °C and dried at 100 °C ($G_{25°}+D_{100°}$); (d) ball milled and dried at 25 °C, and sonicated at 60°C ($G_{25°}+D_{25°}+ S_{60°}$); (e) ball milled, dried and sonicated at 25 °C, ($G_{25°}+D_{25°}+ S_{25°}$); (f) ball milled, dried and sonicated at 25°C and post-annealed at 180°C ($G_{25°}+D_{25°}+ S_{25°}+ A_{180°}$). All the components and their relative atomic percentages are labeled in the figure.

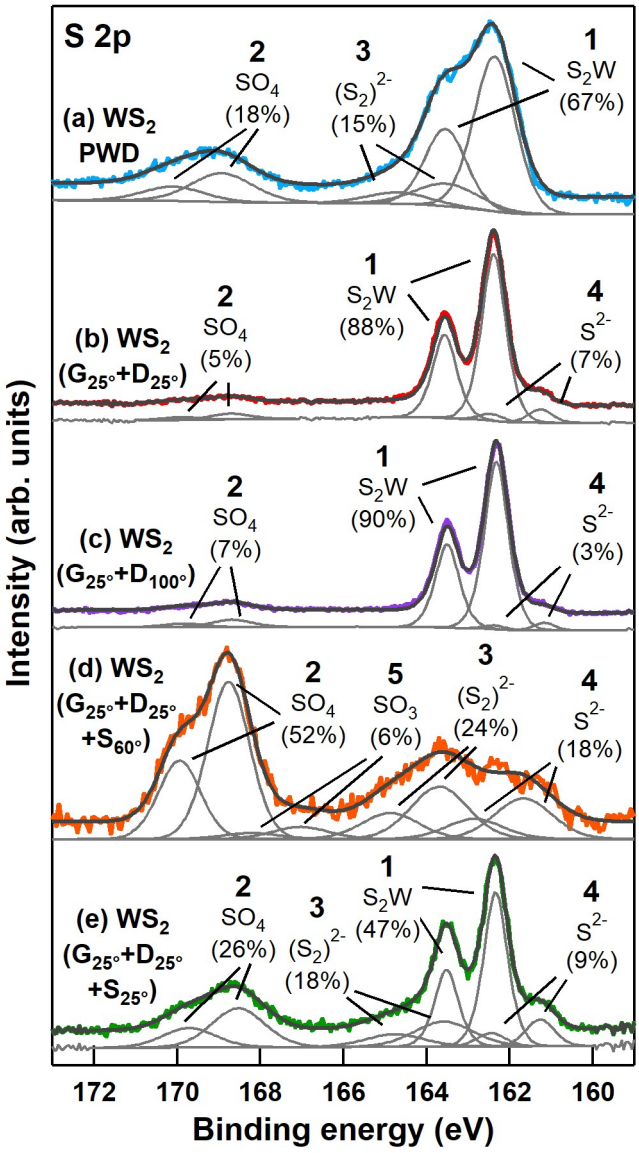


Figure 4- 18. XPS spectra of S 2p core level acquired respectively on (a) pristine $WS_2$ commercial powder ($WS_2$ PWD); (b) ball milled and dried $WS_2$ at 25 °C ($G_{25°}+D_{25°}$); (c) ball milled at 25 °C and dried at 100 °C ($G_{25°}+D_{100°}$); (d) ball milled and dried at 25 °C, and sonicated at 60°C ($G_{25°}+D_{25°}+ S_{60°}$); (e) ball milled, dried and sonicated at 25 °C, ($G_{25°}+D_{25°}+ S_{25°}$)

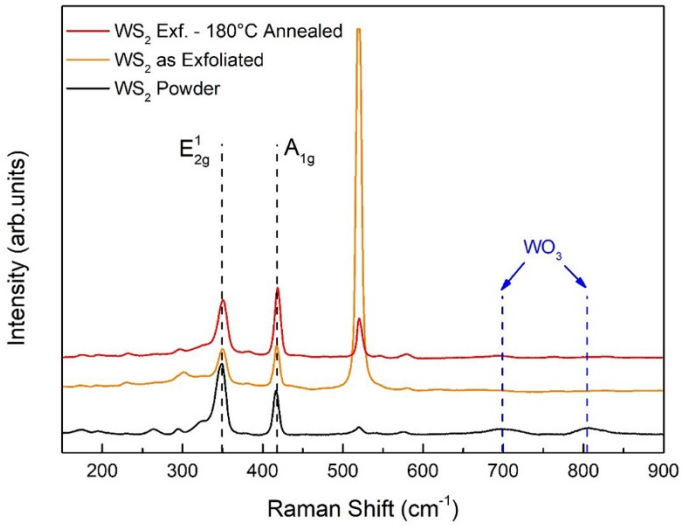


Figure 4- 19. Raman spectra of $WS_2$ bulk powder, $WS_2$ as-exfoliated and $WS_2$ flakes post-annealed at 180°C.

Figure 4- 19 displays the Raman spectra of bulk powder, exfoliated flakes and 180°C annealed film. Peaks located at 350 and 419 $cm^{-1}$ refer to crystalline $WS_2$. Peak at 520 $cm^{-1}$ corresponds to the substrate (i.e. crystalline $SiO_2$). Raman spectra reveal that neither crystalline nor amorphous $WO_3$ are formed. According to literature [39] the displacement of crystalline $WO_3$ is excluded considering that no peaks corresponding to the dashed lines at 719 and 807 $cm^{-1}$ are observed. No signals of amorphous $WO_3$ are also shown as attested by the absence of a broad peak between 600 and 900 $cm^{-1}$, attributed to the W-O stretching vibration of amorphous $WO_3$. The lack from the Raman spectra of any $WO_3$ signal, as opposite to XPS, can be explained considering that Raman spectroscopy penetrates more deeply inside the material, suggesting that the overall amount of $WO_3$ throughout the whole flakes is negligible.

In order to have a better understanding where the as formed $WO_3$ is located, firstly we have to consider that both XPS and Raman techniques give information on the chemical bonding of the elements, secondly that XPS information comes from photoelectrons escaping maximum up to 10 nm below the material surface, lastly that Raman spectroscopy, compared to XPS, is a "bulk" technique (given the negligible attenuation of visible light at the length scale of microns). It turns out that the $WS_2/WO_3$ percentage content measured by XPS and shown in Figure 4- 17 (i.e. ≈ 58%), represents the average chemical compositions of a portion of the material confined within at last 10 nm from the material surface. This region, for simplicity, can be referred as a "surface layer", which represents the reacting surface to interfering gases.

The STEM-EDX image shown in Figure 4- 20 highlights also that W, S and O atoms are homogeneously distributed within the $WS_2$ flakes, and that no domains pertaining to secondary phases are detectable. In light of the practical use of the exfoliated material, the presence of superficial oxide is an issue that should not be underestimated.

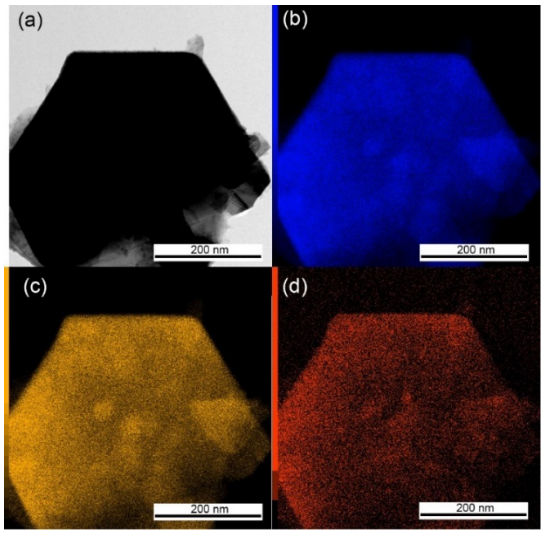


Figure 4- 20. STEM pictures of an exfoliated $WS_2$ flake annealed at 180°C (a) and corresponding elemental mapping of (b) Tungsten, (c) Sulfur and (d) Oxygen.

In light of the practical use of the exfoliated $WS_2$, the presence of the superficial oxide is an issue that should not be underestimated. High Resolution-TEM shown in Figure 4- 21 and Figure 4- 22 reports a high magnification of a $WS_2$ flake from the synthesis named $G_{25}+D_{25}+S_{60}$, the one revealing 99% $WO_3$ on the surface. The images display the occurrence of a complex surface patchwork comprising amorphous $WO_3$ regions (located inside the green square of Figure 4- 21b), possibly rearranging as not-connected, amorphous, isolated-clusters which are eventually embedded in crystalline $WS_2$ phase (located inside the red square of Figure 4- 21b), suggesting the conclusion that oxide grows not only on flake's edges but also in "islands" on the surfaces.

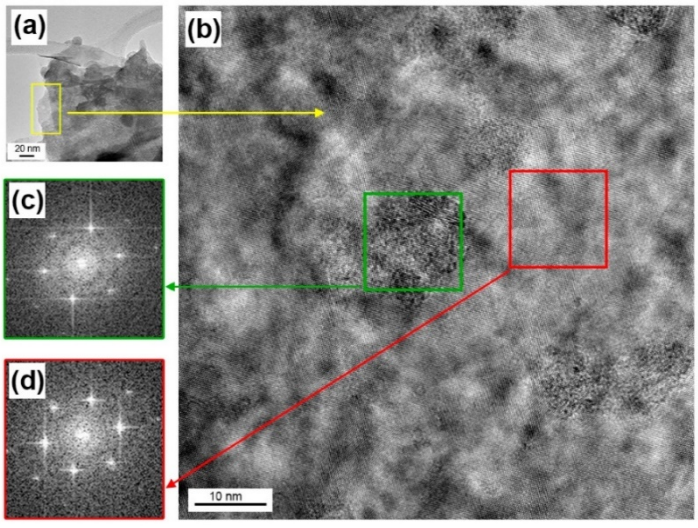


Figure 4- 21. HRTEM images of a $WS_2$ flake exfoliated without temperature control (**b**) Magnification of the yellow area of Figure 4-21(**a**) displaying the presence of ordered structures (i.e., inside the red square) referred to crystalline $WS_2$ and the presence of disordered ones (i.e., inside the green square) attributed to amorphous $WO_3$. Related Selected Area Electron Diffraction (SAED) patterns are shown in (**c**) and (**d**), highlighting the occurrence of sharper reflections (**d**) associated to crystalline $WS_2$.

To confirm, EDX-STEM analysis reported in Figure 4- 22 confirm that the discontinuous area corresponds to an increasing amount of oxygen, meaning the presence of oxide grown on flake surface.

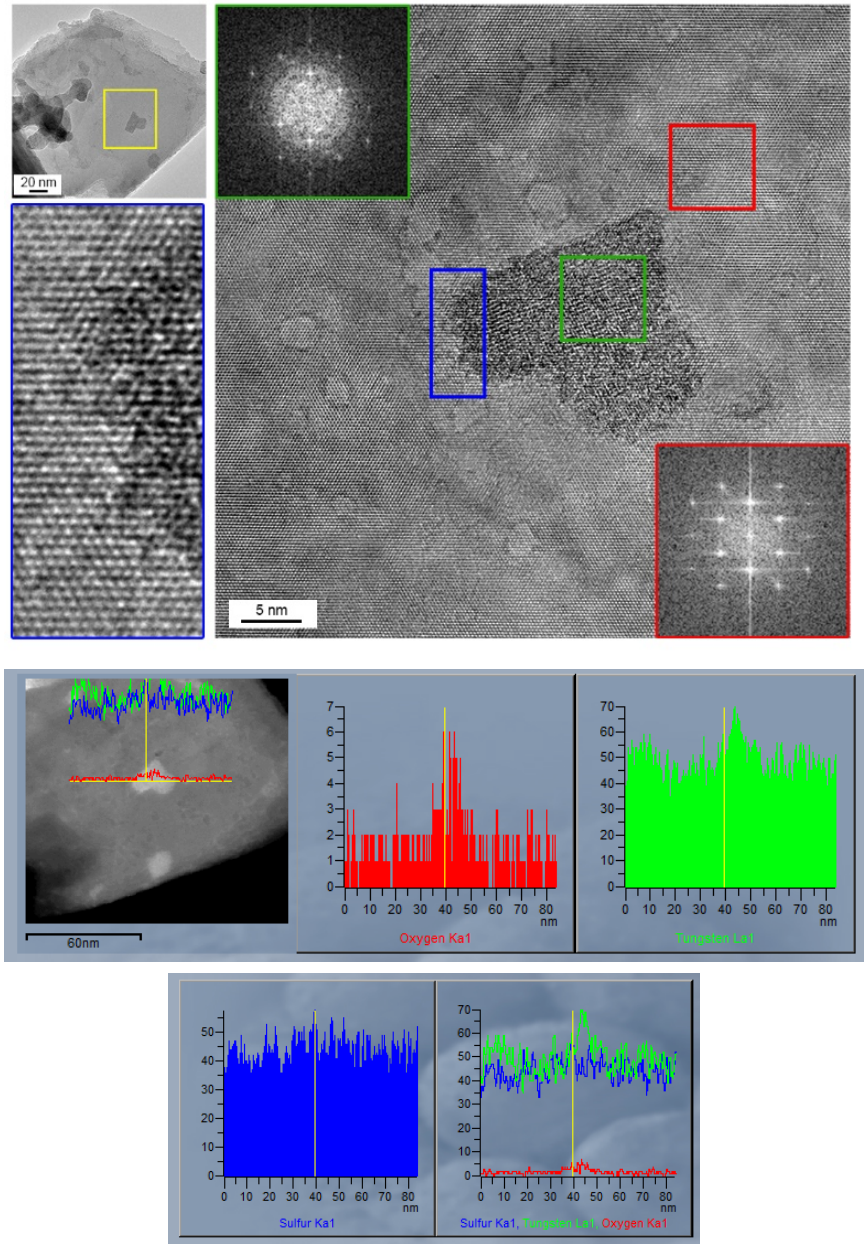


Figure 4- 22. STEM-EDX analysis of partially oxidized WS2 flake.

Finally, in order to complete the characterization of $WS_2$ flakes produced by ball milling and sonication techniques, grazing incidence XRD has been performed on products coming from both controlled and uncontrolled synthesis (i.e. temperatures of 25°C and >60°C during sonication, respectively), and the results are reported in Figure 4-23. The spectra show the absolute absence of any crystalline form of $WO_3$, whose contribute in gas sensing performances will be discussed in the next chapter.

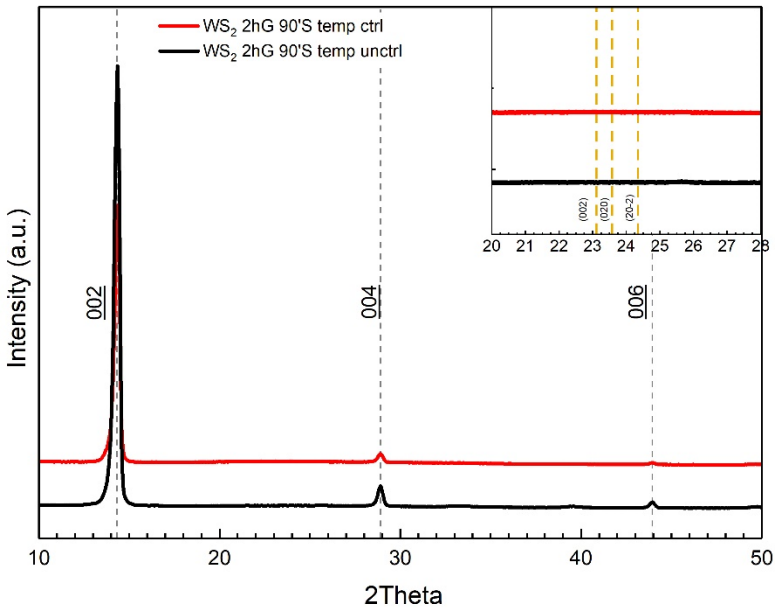


Figure 4- 23. XRD grazing incidence spectra of the samples $G_{25}+D_{25}+S_{25}$ (controlled, ctrl) and $G_{25}+D_{25}+S_{60}$ (uncontrolled, unctrl) . Top right inset shows the close up of the 2θ region characteristic of crystalline WO3 (corresponding peaks of crystalline WO3, according to ICDS 98-001-7003, are highlighted by dashed green lines)

## 4.5 Chapter summary and conclusion

In conclusion, it has been demonstrated that the microstructure of exfoliated $WS_2$ commercial powders produced by an enhanced ball milling and sonication process is mostly affected by the duration of the milling steps, whereas surface oxidation depends on the combined action of sonication and temperature. Specifically, the optimization of the grinding and sonication process followed by drop casting the centrifuged exfoliated suspension leads to the deposition of thin films of well packed and interconnected $WS_2$ flakes with controlled and reproducible microstructure over large areas, thus representing a fast, simple and scalable method, compatible with standard microelectronic fabrication techniques. The influence of the combined action of sonication and temperature upon oxidation of $WS_2$ demonstrating the formation of amorphous $WO_3$ is investigated which resulted in homogeneously distributed over the $WS_2$ flakes, thus addressing the crucial role of surface oxidation upon the long-term response of TMDs monolayers in electronic applications.

## 4.6 Bibliography Chapter 4


1. Yang, W.; Gan, L.; Li, H.; Zhai, T. Two-dimensional layered nanomaterials for gas-sensing applications. *Inorg. Chem. Front.* **2016**, *3*, 433–451.
2. Late, D.J.; Huang, Y.K.; Liu, B.; Acharya, J.; Shirodkar, S.N.; Luo, J.; Yan, A.; Charles, D.; Waghmare, U. V.; Dravid, V.P.; et al. Sensing behavior of atomically thin-layered MoS2 transistors. *ACS Nano* **2013**, *7*, 4879–4891.
3. Voiry, D.; Yamaguchi, H.; Li, J.; Silva, R.; Alves, D.C.B.; Fujita, T.; Chen, M.; Asefa, T.; Shenoy, V.B.; Eda, G.; et al. Enhanced catalytic activity in strained chemically exfoliated {WS}2 nanosheets for hydrogen evolution. *Nat. Mater.* **2013**, *12*, 850–855.
4. Voiry, D.; Yang, J.; Chhowalla, M. Recent Strategies for Improving the Catalytic Activity of 2D TMD Nanosheets Toward the Hydrogen Evolution Reaction. *Adv. Mater.* **2016**, 6197–6206.
5. Mak, K.F.; Shan, J. Photonics and optoelectronics of 2D semiconductor transition metal dichalcogenides. *Nat. Photonics* **2016**, *10*, 216–226.
6. Shim, J.; Park, H.-Y.; Kang, D.-H.; Kim, J.-O.; Jo, S.-H.; Park, Y.; Park, J.-H. Electronic and Optoelectronic Devices based on Two-Dimensional Materials: From Fabrication to Application. *Adv. Electron. Mater.* **2017**, *3*, 1600364.
7. Pumera, M.; Sofer, Z.; Ambrosi, A. Layered transition metal dichalcogenides for electrochemical energy generation and storage. *J. Mater. Chem. A* **2014**, *2*, 8981–8987.
8. Wang, H.; Feng, H.; Li, J. Graphene and graphene-like layered transition metal dichalcogenides in energy conversion and storage. *Small* **2014**, *10*, 2165–2181.
9. Gupta, A.; Sakthivel, T.; Seal, S. Recent development in 2D materials beyond graphene. *Prog. Mater. Sci.* **2015**, *73*, 44–126.
10. Bhimanapati, G.R.; Lin, Z.; Meunier, V.; Jung, Y.; Cha, J.; Das, S.; Xiao, D.; Son, Y.; Strano, M.S.; Cooper, V.R.; et al. Recent Advances in Two-Dimensional Materials beyond Graphene. *ACS Nano* **2015**, *9*, 11509–11539.
11. Yang, D.; Frindt, R.F. Li-intercalation and exfoliation of WS2. *J. Phys. Chem. Solids* **1996**, *57*, 1113–1116.
12. Ambrosi, A.; Sofer, Z.; Pumera, M. Lithium intercalation compound dramatically influences the electrochemical properties of exfoliated MoS<inf>2</inf>. *Small* **2015**, *11*, 605–612.
13. Nicolosi, V.; Chhowalla, M.; Kanatzidis, M.G.; Strano, M.S.; Coleman, J.N. Liquid Exfoliation of Layered Materials. *Science (80-. ).* **2013**, *340*, 1226419–1226419.
14. Niu, L.; Coleman, J.N.; Zhang, H.; Shin, H.; Chhowalla, M.; Zheng, Z. Production of Two-Dimensional Nanomaterials via Liquid-Based Direct Exfoliation. *Small* **2016**, *12*, 272–293.
15. Yi, M.; Shen, Z. A review on mechanical exfoliation for the scalable production

of graphene. *J. Mater. Chem. A* **2015**, *3*, 11700–11715.

16. Kumar, G.R.; Jayasankar, K.; Das, S.K.; Dash, T.; Dash, A.; Jena, B.K.; Mishra, B.K. Shear-force-dominated dual-drive planetary ball milling for the scalable production of graphene and its electrocatalytic application with Pd nanostructures. *RSC Adv.* **2016**, *6*, 20067–20073.

17. Abdelkader, A.M.; Kinloch, I.A. Mechanochemical Exfoliation of 2D Crystals in Deep Eutectic Solvents. *{ACS} Sustain. Chem. Eng.* **2016**, *4*, 4465–4472.

18. Krishnamoorthy, K.; Pazhamalai, P.; Veerasubramani, G.K.; Kim, S.J. Mechanically delaminated few layered MoS2 nanosheets based high performance wire type solid-state symmetric supercapacitors. *J. Power Sources* **2016**, *321*, 112–119.

19. Yao, Y.; Tolentino, L.; Yang, Z.; Song, X.; Zhang, W.; Chen, Y.; Wong, C.P. High-concentration aqueous dispersions of MoS2. *Adv. Funct. Mater.* **2013**, *23*, 3577–3583.

20. Jawaid, A.; Nepal, D.; Park, K.; Jespersen, M.; Qualley, A.; Mirau, P.; Drummy, L.F.; Vaia, R.A. Mechanism for Liquid Phase Exfoliation of {MoS}2. *Chem. Mater.* **2015**, *28*, 337–348.

21. Gao, J.; Li, B.; Tan, J.; Chow, P.; Lu, T.-M.M.; Koratkar, N. Aging of Transition Metal Dichalcogenide Monolayers. *{ACS} Nano* **2016**, *10*, 2628–2635.

22. Donarelli, M.; Prezioso, S.; Perrozzi, F.; Bisti, F.; Nardone, M.; Giancaterini, L.; Cantalini, C.; Ottaviano, L. Response to NO2 and other gases of resistive chemically exfoliated MoS2-based gas sensors. *Sensors Actuators, B Chem.* **2015**, *207*, 602–613.

23. Perrozzi, F.; Emamjomeh, S.M.M.; Paolucci, V.; Taglieri, G.; Ottaviano, L.; Cantalini, C. Thermal stability of WS2 flakes and gas sensing properties of WS2/WO3 composite to H2, NH3 and NO2. *Sensors Actuators, B Chem.* **2017**, *243*, 812–822.

24. Nguyen, E.P.; Carey, B.J.; Daeneke, T.; Ou, J.Z.; Latham, K.; Zhuiykov, S.; Kalantar-zadeh, K. Investigation of two-solvent grinding-assisted liquid phase exfoliation of layered MoS2. *Chem. Mater.* **2015**, *27*, 53–59.

25. Carey, B.J.; Daeneke, T.; Nguyen, E.P.; Wang, Y.; Ou, J.Z.; Zhuiykov, S.; Kalantar-zadeh, K.; Zhen Ou, J.; Zhuiykov, S.; Kalantar-zadeh, K. Two solvent grinding sonication method for the synthesis of two-dimensional tungsten disulphide flakes. *Chem. Commun.* **2015**, *51*, 3770–3773.

26. Deepika; Li, L.H.; Glushenkov, A.M.; Hait, S.K.; Hodgson, P.; Chen, Y. High-Efficient Production of Boron Nitride Nanosheets via an Optimized Ball Milling Process for Lubrication in Oil. *Sci. Rep.* **2014**, *4*.

27. Deng, S.; Qi, X.; Zhu, Y.; Zhou, H.; Chen, F.; Fu, Q. A facile way to large-scale production of few-layered graphene via planetary ball mill. *Chinese J. Polym. Sci.* **2016**, *34*, 1270–1280.

28. Grayfer, E.D.; Kozlova, M.N.; Fedorov, V.E. Colloidal 2D nanosheets of {MoS} 2 and other transition metal dichalcogenides through liquid-phase exfoliation. *Adv. Colloid Interface Sci.* **2017**, *245*, 40–61.

29. Ghorai, A.; Midya, A.; Maiti, R.; Ray, S.K. Exfoliation of {WS}2in the semiconducting phase using a group of lithium halides: a new method of Li

intercalation. *Dalt. Trans.* **2016**, *45*, 14979–14987.

30. Xing, T.; Mateti, S.; Li, L.H.; Ma, F.; Du, A.; Gogotsi, Y.; Chen, Y. Gas Protection of Two-Dimensional Nanomaterials from High-Energy Impacts. *Sci. Rep.* **2016**, *6*, 35532.

31. Gutiérrez, H.R.; Perea-López, N.; Elías, A.L.; Berkdemir, A.; Wang, B.; Lv, R.; López-Urías, F.; Crespi, V.H.; Terrones, H.; Terrones, M.; et al. Extraordinary room-temperature photoluminescence in triangular WS 2 monolayers. *Nano Lett.* **2013**, *13*, 3447–3454.

32. Zhou, P.; Xu, Q.; Li, H.; Wang, Y.; Yan, B.; Zhou, Y.; Chen, J.; Zhang, J.; Wang, K. Fabrication of Two-Dimensional Lateral Heterostructures of WS2/WO3·H2O Through Selective Oxidation of Monolayer WS2. *Angew. Chemie - Int. Ed.* **2015**, *54*, 15226–15230.

33. Hong, J.; Hu, Z.; Probert, M.; Li, K.; Lv, D.; Yang, X.; Gu, L.; Mao, N.; Feng, Q.; Xie, L.; et al. Exploring atomic defects in molybdenum disulphide monolayers. *Nat. Commun.* **2015**, *6*, 6293.

34. Di Paola, A.; Palmisano, L.; Venezia, A.M.; Augugliaro, V. Coupled Semiconductor Systems for Photocatalysis. Preparation and Characterization of Polycrystalline Mixed WO 3 /WS 2 Powders. *J. Phys. Chem. B* **1999**, *103*, 8236–8244.

35. Wong, K.C.; Lu, X.; Cotter, J.; Eadie, D.T.; Wong, P.C.; Mitchell, K.A.R. Surface and friction characterization of MoS2 and WS2 third body thin films under simulated wheel/rail rolling-sliding contact. *Wear* **2008**, *264*, 526–534.

36. Feldman, Y.; Frey, G.L.; Homyonfer, M.; Lyakhovitskaya, V.; Margulis, L.; Cohen, H.; Hodes, G.; Hutchison, J.L.; Tenne, R. Bulk Synthesis of Inorganic Fullerene-like $MS_2$ (M = Mo, W) from the Respective Trioxides and the Reaction Mechanism. *J. Am. Chem. Soc.* **1996**, *118*, 5362–5367.

37. Margolin, A.; Rosentsveig, R.; Albu-Yaron, A.; Popovitz-Biro, R.; Tenne, R. Study of the growth mechanism of WS2 nanotubes produced by a fluidized bed reactor. *J. Mater. Chem.* **2004**, *14*, 617–624.

38. Benoist, L.; Gonbeau, D.; Pfister-Guillouzo, G.; Schmidt, E.; Meunier, G.; Levasseur, A. X-ray photoelectron spectroscopy characterization of amorphous molybdenum oxysulfide thin films. *Thin Solid Films* **1995**, *258*, 110–114.

39. Y.Shigesato; A.Murayama; T.Kamimori; K.Matsuhiro Characterization of evaporated amorphous WO3 films by Raman and FTIR spectroscopies. *Appl. Surf. Sci.* **1988**, *34*, 804–811.

# CHAPTER 5.
# $WS_2$ as gas sensor: strengths, weaknesses and improvement of the performances

## ABSTRACT

This chapter reports the experimental results regarding the gas sensing properties of thin films made of $WS_2$ exfoliated flakes. Responses to $NO_2$ and $H_2$ gases have been measured and possible strategies to improve device performances by combination with Graphene Oxide and light activation of the sensors have been explored.

## CONTENTS

## 5.1 Introduction

Prior to discuss the results, it is important to remind the following figures of merit that have been introduced to address these "gas response properties":

- base line resistance (BLR): the resistance in dry air at equilibrium before a gas exposure;

- base line recovery: the ability of the sensor to recover the base line in air after gas exposure;

- relative response (RR): the ratio ($R_G/R_A$) or ($R_A/R_G$) for a given concentration of oxidizing or reducing gas, respectively. $R_A$ and $R_G$ represent the resistance in dry Air and in Gas, respectively;

- adsorption/desorption time (τads/des): the time required to reach 90% of the full response at equilibrium, during both gas adsorption and desorption;

- recovery percentage (RP): the percentage ratio ($\Delta_D/\Delta_A$) × 100, where $\Delta_D$ and $\Delta_A$ are the variations of the electrical resistance during gas adsorption and desorption, respectively, calculated within the time scale of the sensing cycle.

## 5.2 Exfoliated $WS_2$ as gas sensor

It has been reported that TMDs gas sensors operating at room temperature have shown remarkable limitations, largely related to irreversible desorption of the gas molecules, displaying incomplete recovery of the base line at 25°C [1,2]. The selection of the best operating temperature (OT), the one that provides the complete base line recovery, within reasonable response times and acceptable gas relative responses (RR), is limited in TMDs by the intensifying of the oxidation processes with increasing the OT as previously discussed. Base line recovery and response times depend on the adsorption-desorption kinetic of gases with the sensor surface, which eventually improves with increasing the OT. RR is mostly related to microstructure (i.e surface area, grain size), concentration of surface defects (i.e. oxygen or sulfur vacancies) and structure of the reacting surface (crystalline or amorphous). Having already demonstrated the issues related to surface chemistry and oxidation of TMDS, to find the best OT exfoliated $WS_2$ drop casted on $Si_3N_4$ substrates were previously air annealed at 180 °C to stabilize the $WO_3$ content up to ≈58%.

SEM picture of the sensing device shown in Figure 5- 1 highlights a homogeneous distribution of annealed flakes, enabling current percolation paths between adjacent flakes, covering an area of 1.4x0.6 $mm^2$ over 30 µm spaced Pt interdigitated electrodes.

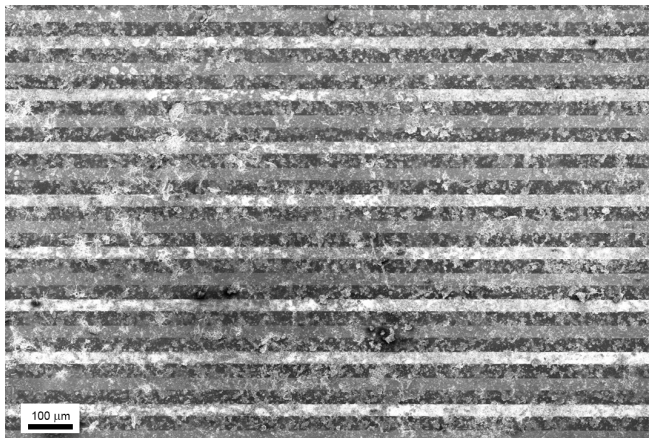


Figure 5- 1. SEM image of sensor obtained by drop casting exfoliated $WS_2$ and annealing at 180 °C on $Si_3N_4$ substrate provided with Pt finger type electrodes (30 microns apart)

Given these premises, in order to find the best Operating Temperature (OT) of the sensor, the response has been measured at different OT as shown in Figure 5- 2. Both at 50°C and 100°C the Relative Response is high but the desorption kinetics of the NO2 are slow. Conversely, at 150°C OT, while the relative response is less than the others, the base line recovery is almost complete, resulting that one the best operating temperature of the sensor.

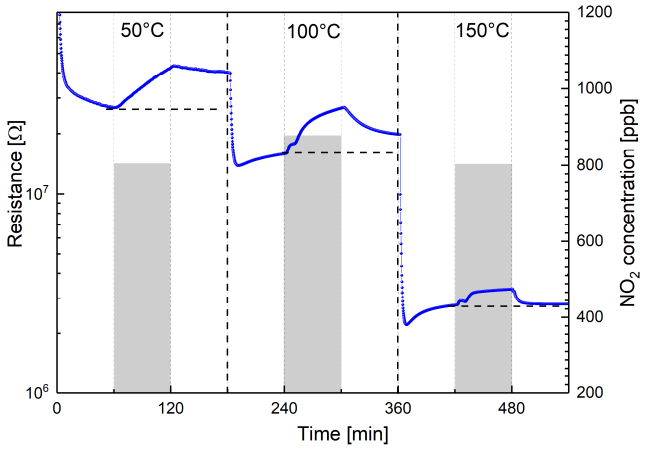


Figure 5- 2. The electrical response of $WS_2$ post-annealed at 180 °C at different operating temperatures and 800 ppb $NO_2$ in dry air. Horizontal black dotted lines mark the base line resistances. $NO_2$ pulses are represented by the grey shaded rectangular plots. The time scale of the experiment consists of 1 hours conditioning in dry air and 1-hour exposure to $NO_2$ gases respectively.

Figure 5- 3a shows the normalized dynamic resistance changes, at 150°C OT of few-layers $WS_2$ thin films to $NO_2$ and $H_2$ in the 100 ppb–5 ppm and 1 ppm–250 ppm gas concentration ranges, respectively. $WS_2$ films respond as *n*-type semiconductors with decreasing/increasing resistance upon exposure to $H_2$/$NO_2$ respectively. Degassing with dry air at 150 °C OT, the base line resistance (BLR), as indicated by the black dotted line in the figure, is almost recovered. $WS_2$ flakes are more sensitive to $NO_2$

than $H_2$ gas, with associated low detection limits (LDL) of 200 ppb and 5 ppm respectively, confirming what has been previously reported in literature.

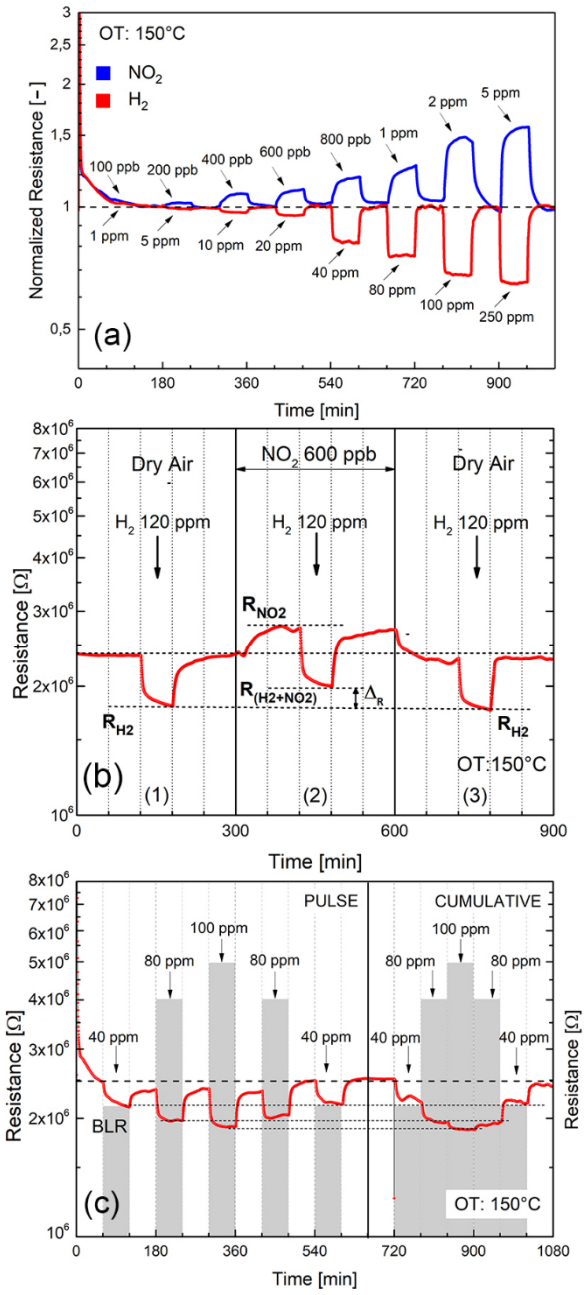


Figure 5- 3. Electrical responses of the exfoliated $WS_2$ post-annealed at 180°C, at 150°C operating temperature in dry air. (a) Comparison of the normalized dynamic response to $NO_2$ (100ppb-5ppm) and $H_2$ (1-250 ppm); (b) $NO_2$ cross sensitivity to $H_2$: first panel the response to 120 ppm $H_2$ in dry air, second panel response to 120 ppm $H_2$ with 600 ppb $NO_2$, third panel response to 120 ppm $H_2$ (as to first panel) for comparison; (c) Reproducibility and base line recovery by exposing the film to both pulse and cumulative $H_2$ concentrations in the range 40–100 ppm. $H_2$ concentrations highlighted in the figure by grey shadowed rectangular plots.

Cross sensitivity which represents the ability of $WS_2$ to detect $H_2$ in the presence of $NO_2$ interfering gas has been shown in Figure 5- 3b. Panel (1) of Figure 5- 3b shows the $WS_2$ response to $H_2$ alone in dry air carrier at 150°C OT. The “cross sensitivity”

produced by interfering $NO_2$ to the measure of $H_2$ is displayed in panel (2) of Figure 5- 3b. By exposing to 600 ppb $NO_2$, sensor resistance initially increases, yielding at equilibrium the resistance value $R_{NO2}$. As soon as 120 ppm $H_2$ is introduced, the resistance decreases yielding the equilibrium value shown as $R_{(H2+NO2)}$. The cross-sensitivity effect is displayed in the picture as (ΔR), to indicate the gap between the electrical resistance to 120 ppm $H_2$ alone (i.e. $R_{H2}$) and that in the presence of 120 ppm $H_2$ and 600 ppb $NO_2$ (i.e. $R_{(H2+NO2)}$). These results imply that the response to 120 ppm $H_2$ is affected by the presence of a small amount (i.e. 600 ppb), of $NO_2$ interfering gas, confirming the stronger affinity of $WS_2$ to detect $NO_2$ as respect to $H_2$.

Reproducibility of the electrical response to pulse (on/off) and cumulative modes $H_2$ gas adsorption is shown in Figure 5- 3c, demonstrating acceptable response characteristics to $H_2$. Under pulsed conditions, the base line resistance (BLR) fully regains its initial value after completion of each desorption cycle in dry air. Under cumulative stepwise adsorption/desorption mode, the $H_2$ gas resistance increases/decreases steadily, matching almost the same $H_2$ resistance values obtained under pulsed conditions (black lines at saturation correspond to 40, 80 and 100 ppm $H_2$).

Long term stability properties of the electrical response of both base line and saturation resistances to 800 ppb $NO_2$ over a period of 12 months (corresponding to approximately 5 months of cumulative operations at 150°C operating temperature) were also recorded. Figure 5- 4a shows base line resistances (lower curve) and saturation resistances corresponding to 800 ppb $NO_2$ (upper curve), randomly collected over a period of 52 weeks. Average resistances with associated standard deviations are calculated over a set of 5 consecutive measurements. Relative responses (RR) taken over the investigated period are also highlighted in the figure. No remarkable fluctuations of both base line and resistances at saturation are detectable, attesting good long-term stability of the electrical properties of the $WS_2$ films. To validate electrical responses shown in Figure 5- 4a, the oxidation state of the sensor surface was also investigated, measuring the $WO_3$ content before and after 52 weeks conditioning. Figure 5- 4b compares the XPS W 4f signal of the as exfoliated $WS_2$ 180°C annealed film before (lower curve) and after 52 weeks long term conditioning to different gases and 150°C OT (upper curve). Beside an increase of the signal noise after long term conditionings, no substantial increase of the $WO_3$ content is detected. These observations imply that exfoliated $WS_2$ films, previously stabilized at 180°C, can satisfactory respond to different gases under sustained conditions at 150°C operating temperature.

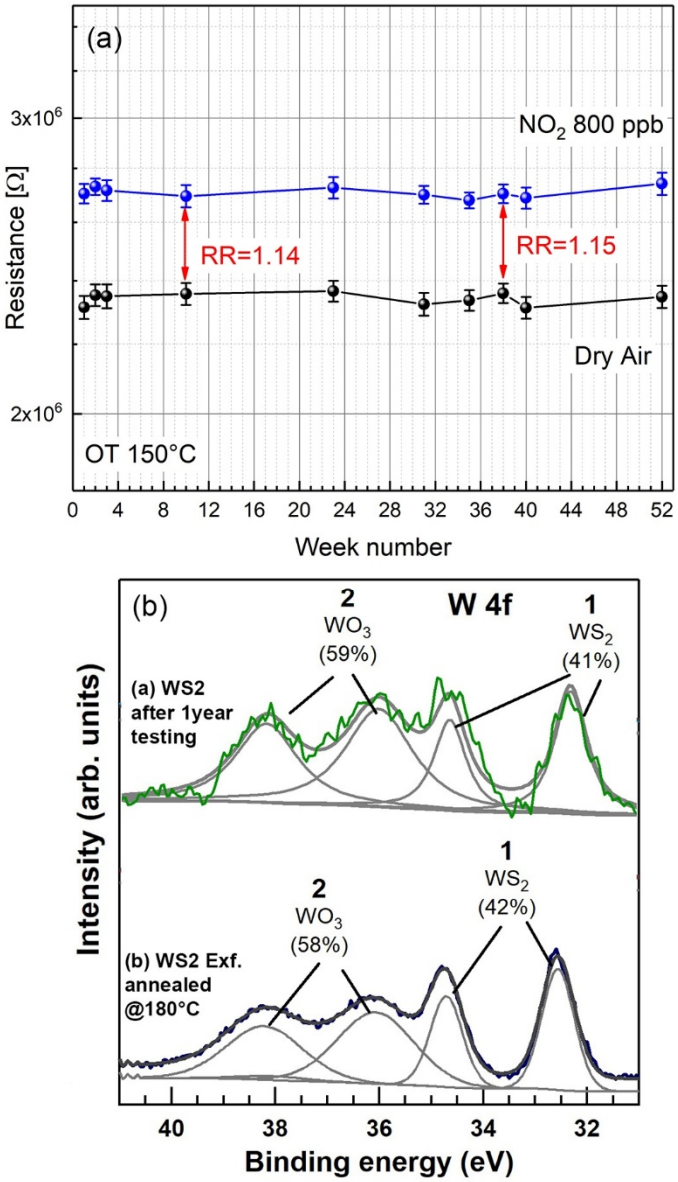


Figure 5- 4. $WS_2$ exfoliated and post-annealed at 180°C. (a) Long term stability properties of the electrical resistances of the base line (lower curve) and 800 ppb $NO_2$ over a period of 12 months (equivalent to approximately 5 months of continuous operation at 150°C operating temperature). Average resistance values with associated standard deviations are calculated over a set of 5 consecutive measurements; (b) Comparison of the XPS signals of the as-exfoliated $WS_2$ annealed at 180°C (lower curve) and the same sample after one-year conditioning to various gases and 150°C operating temperature.

Finally, the influence of humidity on $NO_2$ and $H_2$ gas response at 150°C OT has been also investigated. Figure 5- 5 shows the dynamic response of the films exposed to air with increasing amount of humidity, in the 10% - 80% relative humidity (RH) range. The inset of Figure 5- 5a displays the related sensitivity plot. Considering that at 150°C operating temperature physisorbed water is reasonably evaporated [3], it is unlikely that the decrease of the resistance is induced by a protonic surface charge-transfer mechanism as reported for $WS_2$ humidity sensors operating at room temperature [4].

More reasonably, water vapor at 150°C OT behaves like a reducing gas inducing a steadily resistance decrease in $WS_2$ *n*-type semiconductor, which does not saturate with increasing the RH, as shown in the inset of Figure 5- 5a.

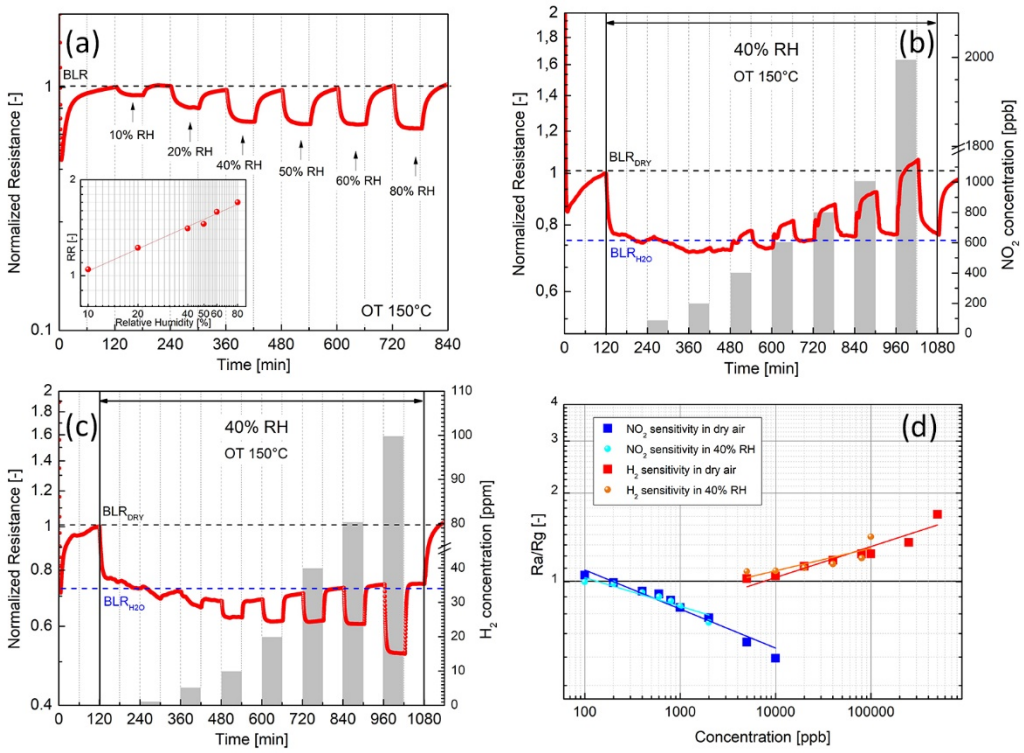


Figure 5- 5. Electrical responses of the exfoliated $WS_2$ post-annealed at 180°C (150°C operating temperature) to different Relative Humidity (RH) conditions. (a) Normalized dynamic response to humidity (10%-80% RH). The inset depicts the corresponding sensitivity plot; (b) Dynamic response to increasing $NO_2$ concentrations in air with 40% RH (c) Dynamic response to increasing $H_2$ concentrations in in air with 40% RH (d) Comparison of the sensitivity plots to $NO_2$ and $H_2$ in dry air and 40% RH respectively.

In order to evaluate the influence of humidity to $NO_2$ and $H_2$ gases response, cross sensitivity tests have been performed. Figure 5- 5b and c show the dynamic responses to different $NO_2$ and $H_2$ concentrations, measured in humid air at 40% RH. As soon as water vapor is introduced, a downshift of the baseline from $BLR_{DRY}$ to $BLR_{H2O}$ is shown. $NO_2$ and $H_2$ dynamic responses in dry and 40% RH are almost similar as shown in Figure 5- 3a and Figure 5- 5b and c. Comparison of the $NO_2$ and $H_2$ gases sensitivities in dry and 40% RH air are shown in Figure 5- 5d. Notably no significant differences are displayed as respect to slopes of the calibrating curves (i.e. sensitivity) and relative responses values (i.e. Ra/Rg), attesting that both $NO_2$ and $H_2$ measurements are not affected by the presence of moisture.

These results, indeed, demonstrate the possibility to produce efficient and reproducible gas sensors, able to detect $NO_2$ and $H_2$ with no significant cross

sensitivity effects induced by humid air in the 10 – 80% RH range and 150°C operating temperature.

### 5.2.1 Gas response mechanism

As previously discussed, by annealing the exfoliated $WS_2$ at 180°C a "surface layer" containing ≈ 58% of amorphous $WO_3$, penetrating at last 10nm from the surface, is formed. It turns out that both structure and chemical composition of the "Surface layer", comprising crystalline $WS_2$ and amorphous $WO_3$, strongly influence the gas response mechanism.

To investigate the contribution of single $WO_3$ on to the electrical properties of $WS_2/WO_3$ pre-annealed composite, we have prepared a fully-oxidized $WS_2$, containing ≈99% amorphous $WO_3$ and tested to $NO_2$. This sample has been prepared by the same exfoliation method by ball milling and drying $WS_2$ powders at 25°C, but setting the sonicating temperature at 60 °C, instead of 25°C for 90 minutes, and finally pre-annealing in dry air at 180°C.

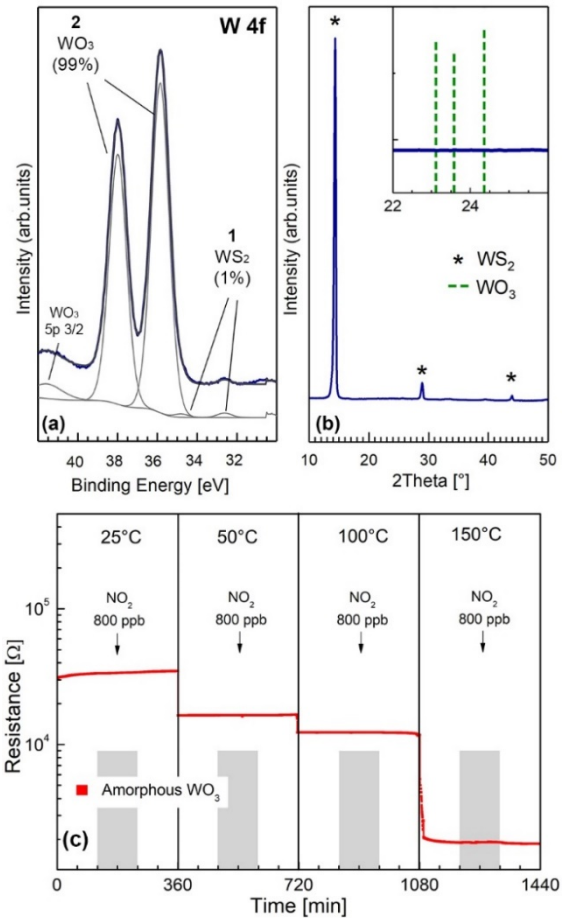


Figure 5- 6. Chemical composition, crystalline structure and microstructural features of a fully oxidized $WO_3$ thin film. (a) W 4f core level XPS spectra; (b) XRD grazing incidence spectra. Top right inset shows the close up of the 2θ region characteristic of crystalline $WO_3$ (corresponding peaks of crystalline $WO_3$, according to ICDS 98-001-7003, are highlighted by dashed green lines); (c) electrical response of the fully oxidized $WO_3$ amorphous film to $NO_2$ and different OTs.

a and b show the XPS and grazing incidence XRD patterns of the fully oxidized film, attesting that the chemical composition of the "surface layer" is ≈ 99% $WO_3$ and that the as formed $WO_3$ is amorphous, as highlighted by the absence of $WO_3$ peaks inside the inset of the XRD pattern of b. It turns out that the fully oxidized region possibly covers the whole surface of the flakes, not extending to the core, which maintain the crystalline structure of pristine exfoliated $WS_2$ (as attested by the presence of $WS_2$ peaks in the XRD pattern of Figure 5- 6). The electrical response of the fully oxidized amorphous $WO_3$ to 800 ppb $NO_2$ and different operating temperatures in dry air is shown in c. According to c, amorphous $WO_3$ is not responsive at all to $NO_2$ gas in dry air, in the operating temperature range 75° - 150°C.

Discussing the gas sensing properties of amorphous $WO_3$ literature reports are very scarce. Some authors found no gas response to NOx of amorphous $WO_3$ deposited by sputtering [5] whereas others demonstrated negligible $NO_2$ response using photochemically produced amorphous $WO_3$ [6]. In most cases the $NO_2$ gas response of amorphous $WO_3$ is smaller as respect to crystalline $WO_3$, frequently associated with base line drift phenomena, with few exceptions mostly related to the preparation conditions. In our case we demonstrated that the interaction of $NO_2$ with amorphous 99% $WO_3$, has no effects altogether.

Having shown in Figure 5- 3a the substantial $NO_2$ and $H_2$ gas response of the $WO_3/WS_2$ composite, we conclude that it is crystalline $WS_2$ which primarily responds to $NO_2$ gas. The predominant gas sensing role played by crystalline $WS_2$ as respect to amorphous $WO_3$, is also supported by the decrease of the electrical resistance with increasing relative Humidity (RH), shown in Figure 5- 5a. Considering that $WO_3$ interacts with humidity by increasing the resistance, due to $WO_3$ lattice oxidation induced by humidity as reported in literature [7], the resistance decrease displayed in Figure 5- 5a rules out any significative contribution of $WO_3$ to the overall humidity response. Moreover, the hypothesis that $WS_2$ is likely to be the responding material, is also supported by our previous research which demonstrated that humidity decreases the sensor resistance in $MoS_2$-based exfoliated [8].

Discussing the contribution of crystalline $WS_2$ to the overall electrical resistance, it was recently demonstrated by first-principles calculations on single $MoS_2$ sulfur-defective layer that $O_2$ irreversibly chemisorbs on sulfur vacancies [9] and that the "heal" of these defects by substitutional O atoms is thermodynamically favorable [10]. Furthermore, in case of direct $NO_2$ molecules interaction with sulfur vacancies, a dissociative adsorption of $NO_2$, leading to O atoms passivating the vacancies, and NO molecules physisorbed on the $MoS_2$ surface, was also proposed [3,11]. Given these premises, we hypothesize that both $O_2$ and $NO_2$ suppress sulfur vacancies, supporting a gas response mechanism based only on physisorption of $NO_2$ and $H_2$ molecules on passivated (i.e. defect free) $WS_2$ surface. This hypothesis is sustained by theoretical studies on the adsorption of $NO_2$, $H_2$, $O_2$, $H_2O$, $NH_3$ and CO gases on defect-free single layer $MoS_2$ and $WS_2$ [12,13]. According to this physisorption model, the size and sign of the resistance changes, when exposing few-flakes of $WS_2$ to oxidizing ($NO_2$) and reducing ($H_2$) gases, depend on the number of exchanged carriers (i.e. electrons) and their direction. $NO_2$ being more electronegative than $H_2$ induces a large electron withdrawal, whereas $H_2$ results in weak electron injection,

explaining the increase/decrease of electrical resistance in *n*-type $WS_2$, as well as the smaller detection limit measured for $NO_2$ (200 ppb) as compared to the one found for $H_2$ (i.e. 5 ppm).

Lastly, a question to be resolved is why both $NO_2$ and $H_2$ sensitivities are not affected by the presence of moisture as shown in Figure 5- 5. This behavior may suggest that water vapor adsorbs on to the $WS_2$ surface with a different and non-competitive mechanism as respect $NO_2$ and $H_2$ gases. Clearly this interaction is a complex issue, and yet to be clarified based on specific theoretical and experimental studies.

## 5.3 $WS_2$/rGO heterostructure for gas sensing enhancement

As previously reported, regarding traditional metal oxide sensors, one of the most important drawbacks is related to their working temperature. Specifically, they need to work at temperature over 250°C to achieve good results, with subsequent issues related to the design of the device and the stability of the material itself.

For this reason, the reported $WS_2$ sensor working at 150°C represents already a good result. However, in need to decrease the operating temperature of the sensing materials, a common drawback of TMDs operating at room temperature, is their slow response and recovery times, or even no recovery when used at low temperatures [8,14,15]. The increase of the operating temperature up to 150 °C greatly improves adsorption/desorption rates and baseline recovery, but causes partial oxidation of TMDs into their metal oxide counterparts, as previously demonstrated for $MoS_2$ and $WS_2$-layered materials [8,16,17]. It turns out that both low and high temperatures hinder the practical use of TMDs due to kinetic (i.e., slow recovery rates) and thermodynamical (i.e., spontaneous oxidation) reasons, respectively. A possible strategy to avoid irreversible adsorption and ageing phenomena, and thus to enhance the long term stability of the sensors, is to operate them at low temperature utilizing light irradiation as an external source of energy, as previously reported for metal oxide sensors [18,19], rGO-Metal Oxide nanocomposite [20], graphene [21], $MoS_2$ [14] and $WS_2$ [22].

Considering the variety of different preparation techniques for producing mono- or few-flake TMDs, consistent with standard electronic processes, some other aspects must be considered. A first issue is the reproducibility of the exfoliation procedure with respect to both microstructure (i.e., number of layers, lateral size, surface area, etc.) and chemical composition (i.e., defects concentration and surface oxidation). A second aspect is the small allowable average lateral size of the TMDs flakes, which may range from 100 to 300 nm, depending on the exfoliation technique [23]. A final issue is the surface coverage of the substrate, needed to create percolation paths for charge carriers between TMDs flakes, bridging metal electrodes. The possibility of using hybrid nanostructures, mostly focused on $MoS_2$/graphene, making use of large-size, conducting-flakes-pathways of Graphene Oxide (GO) or reduced Graphene Oxide (rGO) with dispersed smaller-size, lesser-conductive-flakes of $MoS_2$ has been

recently reported as an effective solution to enhance the fabrication of this new class of gas sensors [1,24,25]. Beside some reports on the utilization of $WS_2$/GO hybrids as electrocatalysts for hydrogen evolution reactions [26,27] and $WS_2$/GO as humidity [28] and $NH_3$ [29] sensors, no applications of $WS_2$/rGO nanocomposite for $NO_2$ gas sensing applications have been reported so far.

The aim of this research has been firstly to demonstrate the reliability of the decoration process leading to the deposition of thin films of well dispersed $WS_2$ flakes over large-size, interconnected rGO flakes, secondly, to demonstrate and discuss the influence of purple blue light ($\lambda$ = 430 nm) to detect $NO_2$ gas in air in the operating temperature range of 25 °C to 50 °C, and lastly, to investigate the influence of water vapor on the $NO_2$ gas response.

### 5.3.1 Synthesis of the $WS_2$-Decorated rGO

GO was prepared via a modified Hummers method [30] starting from graphite flakes of 500 µm maximum size. Monolayers with average sizes of several micrometres and thicknesses of less than 2 nm were obtained and dispersed in water to reach a final concentration of 0.05 mg/mL. Two-dimensional $WS_2$ flakes were prepared as shown in Chapter 4, by two-step exfoliation made of ball milling and sonication techniques. Finally, equal amounts of the two GO/water and $WS_2$/ethanol solutions were mixed together and sonicated for 10 min to homogenize the dispersion and avoid agglomeration.

Thin layers have been prepared by drop casting 8 µL of the water/ethanol dispersed $WS_2$-GO solution on $Si_3N_4$ substrates provided with 30 µm spaced Pt interdigitated electrodes, followed by annealing at 70 °C for 30 min to partially reduce the GO to rGO in order to fix the film resistivity in the range of $10^4$–$10^5$ Ohm.

### 5.3.2 Morphological and Compositional Characterization of the $WS_2$-Decorated rGO

Thin films of $WS_2$-decorated rGO deposited on $Si_3N_4$ substrates provided with Pt finger type electrodes have been characterized. We have firstly deposited by drop deposition the minimum amount of $WS_2$–rGO solution, corresponding to the formation of a continuous percolation path of GO flakes. The development of a continuous percolation path was assessed by recording the electrical resistance of the film corresponding to the onset of an electrical contact between the electrodes (30 microns apart). By further annealing at 70 °C in air for 30 min, the GO flakes have been partially reduced to rGO to yield baseline resistances in air in the range of $10^4$–$10^5$ Ohm.

The $WS_2$-decorated rGO morphology was first characterized by low-resolution TEM, as shown in Figure 5- 7a. $WS_2$ flakes (darker regions) are distributed over a thin, continuous and uniform layer made of interconnected rGO flakes (light-grey background) as revealed by the presence of grey lines attesting the formation of rGO folded edges (yellow arrows in Figure 5- 7). Statistical image analysis carried out on

differently prepared samples over an area of 80 $\mu m^2$, as shown in Figure 5- 7b, exhibits a log-normal $WS_2$ average particle size distribution with an average particle size dimension of 200 nm and an average $WS_2$ flakes coverage percentage of 6%. Notably, the dispersion of the $WS_2$ flakes is homogeneous over the investigated area, meaning that the sonication step after mixing represents an effective strategy to avoid agglomeration of the $WS_2$ flakes.

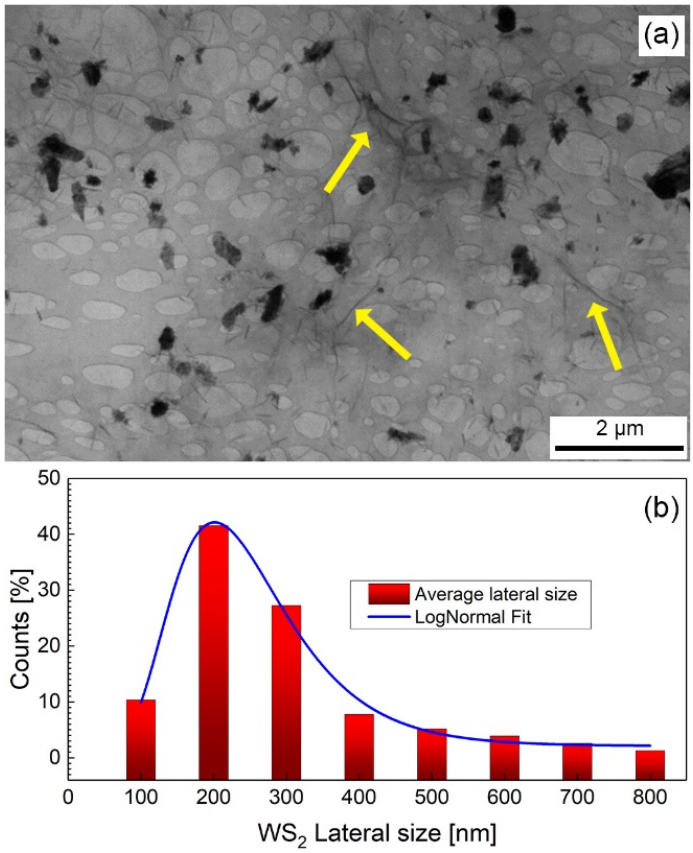


Figure 5- 7. (a) Low-resolution TEM image of $WS_2$-decorated GO deposited on a lacey grid. $WS_2$ flakes (darker regions) distributed over interconnected rGO flakes (light-grey background). The occurrence of grey lines (highlighted by yellow arrows) attest the formation of rGO folded edges; (b) Lateral size distribution of $WS_2$ flakes and corresponding Log Normal fit

The TEM analysis shown in Figure 5- 8a reveals the presence of large (i.e., hundreds of nanometers) transparent, irregularly shaped GO flakes with folded edges (yellow arrow) distributing according to a continuous planar underlying layer. From Figure 5- 8a it is shown that $WS_2$ flakes may also align vertically, as highlighted by the darker needle-shaped formations inside the red circles of Figure 5- 8a. Statistical analysis carried out on the vertically aligned $WS_2$ flakes revealed an average thickness of 15 nm, corresponding approximately to 25 layers. TEM image depicted in Figure 5- 8b illustrates the formation of well-shaped, stacked-few-layers $WS_2$, with edge angles of 120°, deposited over the underlying GO flakes. The crystalline nature of few-flakes $WS_2$ is confirmed by the selected area electron diffraction (SAED) pattern shown in the inset of Figure 2b, which clearly exhibits the formation of $WS_2$ nanosheet with hexagonal atomic arrangements, assigned to $WS_2$ (100) plane [31].

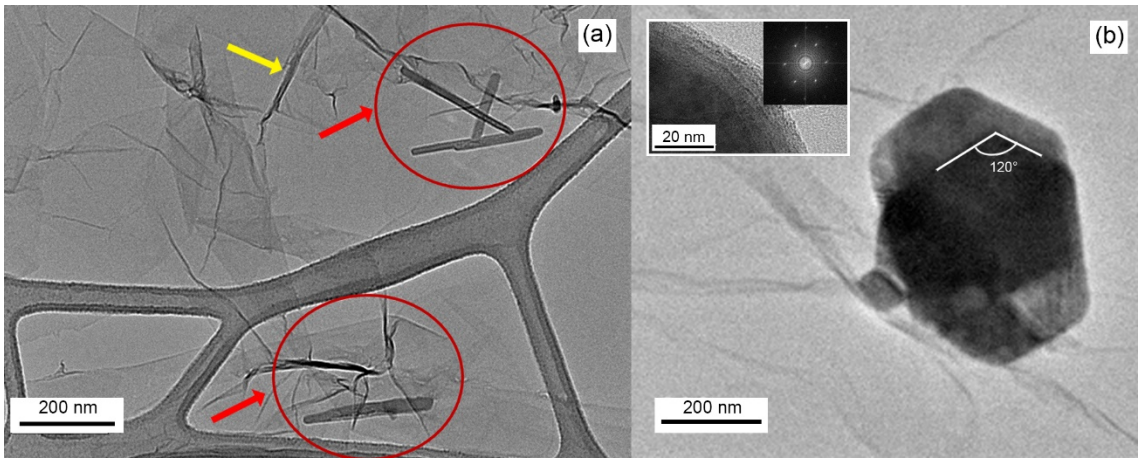


Figure 5- 8. High-resolution TEM of $WS_2$-decorated rGO showing: (**a**) light-grey background of interconnected GO flakes. Darker grey lines (yellow arrow) corresponding to folded GO edges and some $WS_2$ flakes vertically placed on GO flakes (needless inside the red circle); (**b**) a big hexagonal $WS_2$ flake. The inset shows a magnification of the flake's edges with related SAED analysis pattern.

Figure 5- 9 shows the atomic distribution of sulfur (a), tungsten (b), carbon (c) and oxygen (d) elements, as measured by STEM technique, respectively on the sample displayed in Figure 5- 8b. From Figure 5- 9a b, it turns out that the distribution of tungsten and sulfur exactly replicates the shape of the $WS_2$ flake. The carbon signal over the $WS_2$ particles of Figure 5- 9c, may be possibly be attributed to a partial contamination of the sample, whereas the carbon signal deriving from the background, clearly replicates the morphology of the rGO underlying layer. The chromatic signal intensity of oxygen corresponding to the $WS_2$ flake (Figure 5- 9d), is slightly brighter than the background, indicating the occurrence of a higher oxygen concentration over the $WS_2$ flake with respect to the rGO background, suggesting the occurrence of an oxidation process of $WS_2$, as it will be confirmed in the next XPS section.

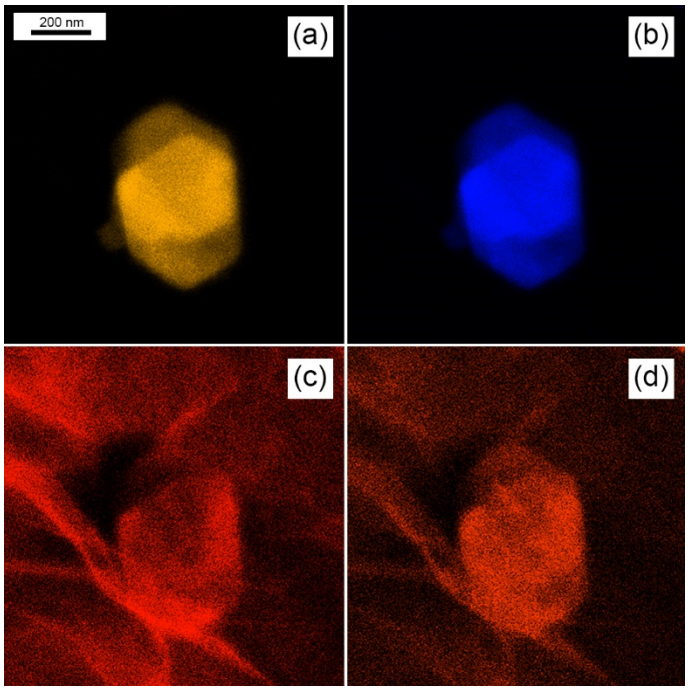


Figure 5- 9. STEM elemental mapping of the flake shown in Figure 2b showing the atomic distribution of: (**a**) sulfur, (**b**) tungsten, (**c**) carbon and (**d**) oxygen.

Figure 5- 10 shows the XPS C1s (a) and W4f (b) core level photoemission spectra of $WS_2$-decorated rGO air-annealed at 70 °C. According to the literature [32,33], the C1s spectrum shown in Figure 5- 10a has been successfully fitted by the sum of five components assigned to C $sp^2$ atoms belonging to aromatic rings and hydrogenated carbon (C=C/C–C 284.7 eV), hydroxyl groups (C–OH, 285.8 eV), epoxy groups (C–O–C, 286.8 eV), carbonyl groups (C=O, 288.0 eV), and carboxyl groups (C=O(OH), 289.2 eV). Upon thermal annealing at 70 °C, the intensity of all the oxygen-containing groups is lowered, with regard to $sp^2$ carbon containing ones (i.e., (C=C/C–C), signifying a loss of oxygen in favor of $sp^2$ carbon.

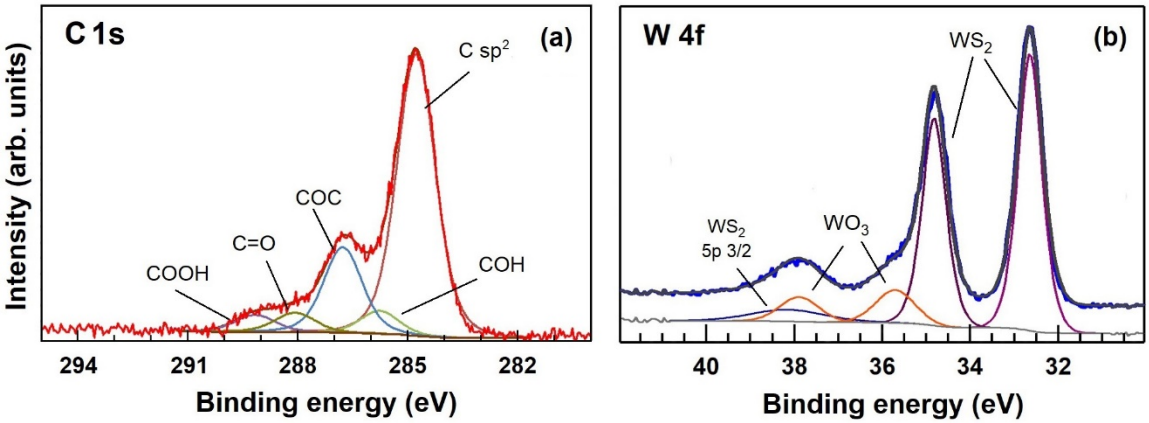


Figure 5- 10. XPS spectra of the $WS_2$-decorated rGO showing (**a**) C1s core level spectrum of rGO flakes and (**b**) W 4f core level spectrum of $WS_2$.

Compared to previous results [34], the XPS spectrum shown in Figure 5- 10a is located halfway between the XPS signals of as deposited GO and the one corresponding to 200 °C UHV-annealed rGO. Regarding the tungsten W4f of Figure 5- 10b, the four peaks fitting the spectrum can be located, according to the literature [35,36], to $WS_2$ and $WO_3$. These results suggest, as previously reported for $MoS_2$ and $WS_2$ [8,16,17], that crystalline $WS_2$ is partially oxidized to $WO_3$ with an associated content of approximately 18%.

Gracing incidence XRD measurements on the $WS_2$-decorated rGO annealed at 70 °C for 30 min, as shown in Figure 5- 11, revealed that the $WO_3$ is amorphous. According to literature [37,38], in fact, the typical $WS_2$ peaks at 2Theta 14.3 and 28.8 represent the (002) and (004) planes and the broad peak in the region 2Theta 20-25 can be attributed to rGO's (002).

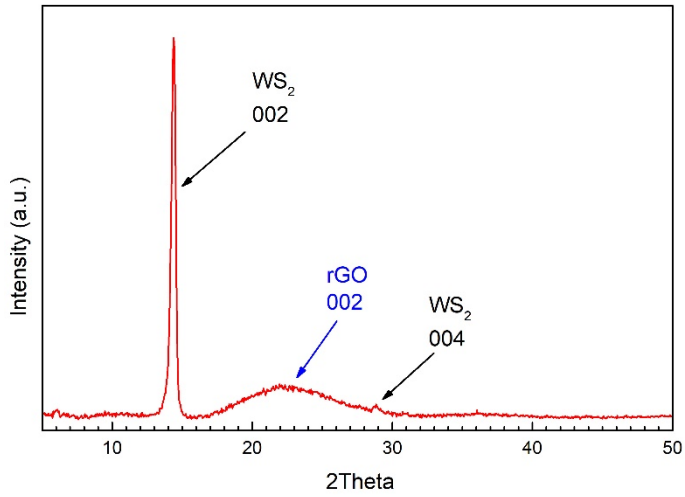


Figure 5- 11. Grazing incidence XRD spectrum of $WS_2$-decorated rGO film

### 5.3.3 $WS_2$/rGO $NO_2$ Gas Response

The reacting surface of the $WS_2$-decorated rGO comprises, as attested by microstructural characterization, a flat underlying layer made of large and interconnected rGO flakes covered with dispersed, partially oxidized, $WS_2$ flakes. Given that $WS_2$ flakes do not form a continuous layer (see Figure 5- 7), it is the rGO layer which mostly determines the baseline resistance of the $WS_2$–rGO hybrid. The $NO_2$ gas responses in dry air of a single rGO film and a $WS_2$-decorated rGO film at 25 °C and 50 °C operating temperatures (OT) are compared in Figure 5- 12.

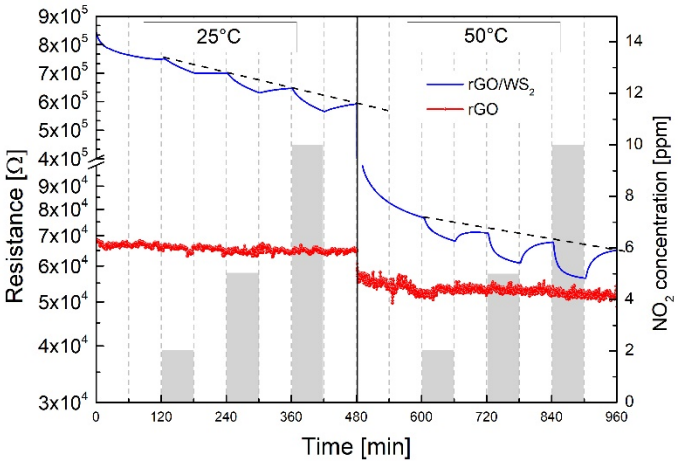


Figure 5- 12. Electrical responses of single rGO (red line) and WS2-decorated rGO films (blue line) in dry air and NO2 concentrations in the range 2–10 ppm at 25 °C and 50 °C operating temperature.

By increasing the OT to 50 °C, the baseline resistance (BLR) of the $WS_2$-decorated rGO (dotted lines in the figure) decreases almost of one decade as compared to rGO, attesting the substantial contribution of the $WS_2$ semiconductor to the overall resistance response. At 25 °C OT, by increasing the $NO_2$ gas concentration, it is noted that: i) the baseline resistance (BLR) is not recovered after gas desorption ii) baseline resistance steadily drifts, decreasing its resistance; iii) the electrical signal never reaches equilibrium under adsorption/desorption conditions within the time schedule of the experiment (i.e., 60 min). Conversely, by increasing the OT to 50 °C, $WS_2$-decorated rGO shows a faster response, improved equilibrium conditions and reduced baseline drift. Besides the positive effects related to the OT, it may be concluded that irreversible adsorption and baseline drift phenomena are still evident at 50 °C OT, representing a serious drawback for the exploitation of near room temperature $WS_2$–rGO hybrids sensors.

According to previous research which demonstrated the positive effect of the combined action of light irradiation and thermal activation on the $NO_2$ response of $WO_3$ and NiO semiconductor sensors [18,19], Figure 5- 13 shows the rGO's and $WS_2$–rGO hybrid's $NO_2$ gas responses at 25 °C in dry air under Purple Blue light (PB $\lambda$ = 430 nm @ 2.88 eV) and different power densities at 270 $\mu W/cm^2$, 468 $\mu W/cm^2$ and 668 $\mu W/cm^2$. Bare rGO exhibits neither significant changes of the electrical response at different power densities (in Figure 5- 13 the response at 668 $\mu W/cm^2$ is shown) nor any appreciable gas response to 1 ppm $NO_2$. $WS_2$-decorated rGO yields relative responses (RR = Ra/Rg at 1ppm $NO_2$) of approximately 1.21, more or less independent of the power density. Response and recovery times, in contrast, improve with increasing the power density.

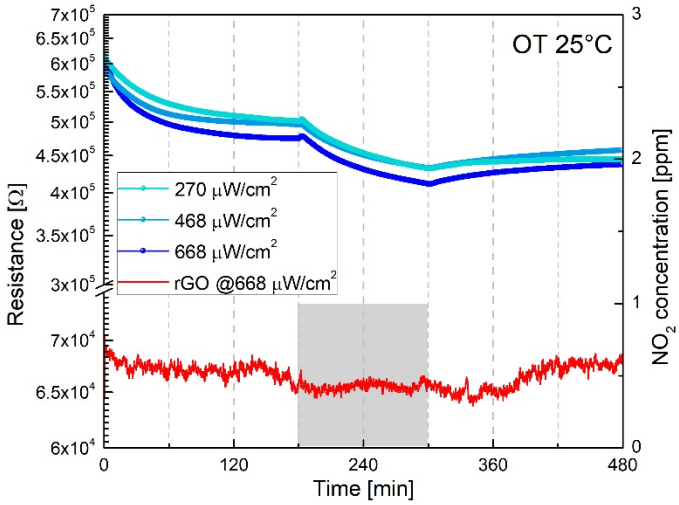


Figure 5- 13. Response to 1 ppm $NO_2$ in dry air of $WS_2$-decorated rGO and bare rGO film (red curve) irradiated by Purple–Blue (λ = 430 nm) light at different power densities (270 μW/cm², 468 μW/cm², 668 μW/cm²).

By selecting the 668 μW/cm² light power density, Figure 5- 14 shows the electrical response of the $WS_2$-decorated rGO to 1 ppm $NO_2$ in dry air under "dark" and "purple–blue" conditions at 25 °C and 50 °C OT respectively.

If we now define the recovery percentage (RP) as the percentage ratio $(\Delta_D/\Delta_A) \times 100$, where $\Delta_D$ and $\Delta_A$ (see Figure 5- 14) are the desorption/adsorption resistances' variations (Δ), measured at the end of each desorption/adsorption cycle (i.e., 60 min), it turns out that light illumination strongly enhances the recovery of the baseline resistance during desorption.

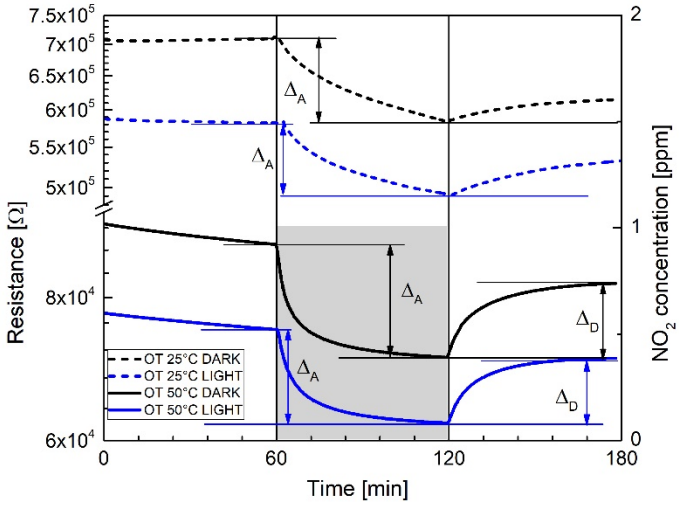


Figure 5- 14. The 1 ppm $NO_2$ gas responses of the $WS_2$-decorated rGO under "dark" and "light" conditions (dotted lines) at 25 °C operating temperatures compared to the "dark" and light" conditions (solid lines) at 50 °C operating temperature.

Table 5-1. Comparison of RR, RP, τads and τdes to to 1 ppm $NO_2$ in dark conditions and PB light illumination (λ = 430 nm at 668 $\mu W/cm^2$) at different OT (25–50 °C). Notably (-) means that no equilibrium conditions have been reached within the time scale of the experiment.

| **RESPONSE TO 1 ppm $NO_2$** | | | | |
|---|---|---|---|---|
| **OPERATING CONDITIONS** | **RR Ra/Rg** | **RP $\Delta_D/\Delta_A$** | **$T_{ads}$** | **$T_{des}$** |
| | **[–]** | **[%]** | **[min]** | **[min]** |
| 25 °C DARK | 1.18 ± 0.02 | 23 | - | - |
| 25 °C LIGHT | 1.21 ± 0.02 | 65 | - | - |
| 50 °C DARK | 1.20 ± 0.02 | 60 | 22 | 26 |
| 50 °C LIGHT | 1.27 ± 0.02 | 70 | 16 | 18 |

As shown in Figure 5- 14 and Table 5-1, recovery percentage (RP) values increase from 23% (dark) to 65% (light) at 25 °C OT, and from 60% (dark) to 70% (light) at 50 °C OT. Moreover, considering features and shapes of the curves displayed in Figure 5- 14, at 25 °C OT regardless of "dark" or "light" exposures, no equilibrium conditions are achieved within the timescale of the experiment (i.e., 60 min). In contrast, as attested by the horizontal slopes of the two bottom curves of Figure 5- 14, equilibrium conditions are achieved under adsorption/desorption conditions when light irradiation is performed and when the OT is increased to 50 °C. Notably, according to Table 5-1, given the associated uncertainty of the measurement (± 0.02), no substantial changes of the relative responses' values are recorded with respect to 25 °C, either by increasing the OT to 50 °C or by illuminating the sensor with purple blue light.

The results shown in Table 5-1 are in line, both in terms of sensitivity, using comparable definitions, and time constants with those reported in literature for hybrid graphene/$MoS_2$ structures for $NO_2$ sensing [1,24] working in dark conditions and at higher operating temperatures (at least 150 °C).

Figure 5- 15 compares the normalized dynamic gas responses of the $WS_2$–rGO sensor at 50 °C OT under dark and light conditions, respectively. By increasing the $NO_2$ concentration from 200 ppb to 1 ppm, purple blue light irradiation promotes full baseline recovery after each $NO_2$ pulse, as demonstrated by the horizontal slope of the dotted line of Figure 5- 15. $WS_2$-decorated rGO exhibits an experimental detection limit of 400 ppb $NO_2$ in dry air. The inset of Figure 5- 15 shows the sensitivity plot of the response under PB illumination, with associated standard deviations.

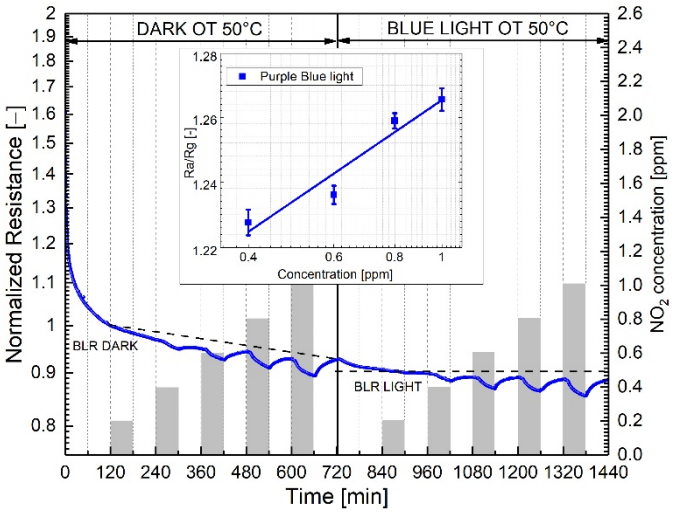


Figure 5- 15. Comparison of $WS_2$-decorated rGO's electrical responses to increasing $NO_2$ concentrations at 50 °C operating temperature under dark and light conditions respectively. The inset shows the sensitivity plot corresponding to light conditions. The bars in the inset represent the standard deviation calculated over a set of five measurements performed for each gas concentration. Dotted lines indicate the baseline resistance in dry air.

Moreover, reproducibility tests of the electrical response under pulse and cumulative $NO_2$ adsorption/desorption exposures, shown in the supporting Figure 5- 16. The $WS_2$-decorated rGO film shows good dynamic and cumulative responses to $NO_2$. Figure 5- 16a displays the electrical signal under forward and backward dynamic pulses to $NO_2$ in the concentration range 5–10 ppm. BLR fully regains its initial value after completion of each cycle. Under cumulative stepwise adsorption/desorption mode, as shown in Figure 5- 16b, the $NO_2$ gas resistance increase/decreases steadily matching almost the same resistances at saturation and in comparison, to panel (a).

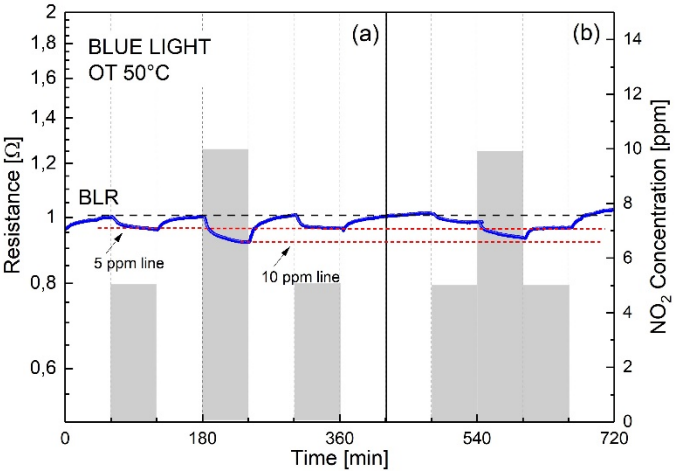


Figure 5- 16. Reproducibility and base line recovery features of the $WS_2$-decorated rGO by exposing the film to both dynamic and cumulative $NO_2$ concentrations (5–10 ppm) under light irradiation (purple blue). Panel (a): dynamic responses to repeated on/off runs; panel (b): cumulative adsorption/desorption runs by stepwise increase and decrease of the $NO_2$ concentration.

Additionally, long-term stability properties of the baseline and saturation resistances to 1 ppm $NO_2$ over a period of 12 months were also recorded. Figure 5- 17 shows baseline resistances (upper curve) and saturation resistances corresponding to 1 ppm (lower curve), randomly collected over a period of 52 weeks, with associated standard deviations calculated over a set of five consecutive measurements. No remarkable fluctuations of both baseline and resistances at saturation are detectable, demonstrating good long-term stability properties of the $WS_2$ films.

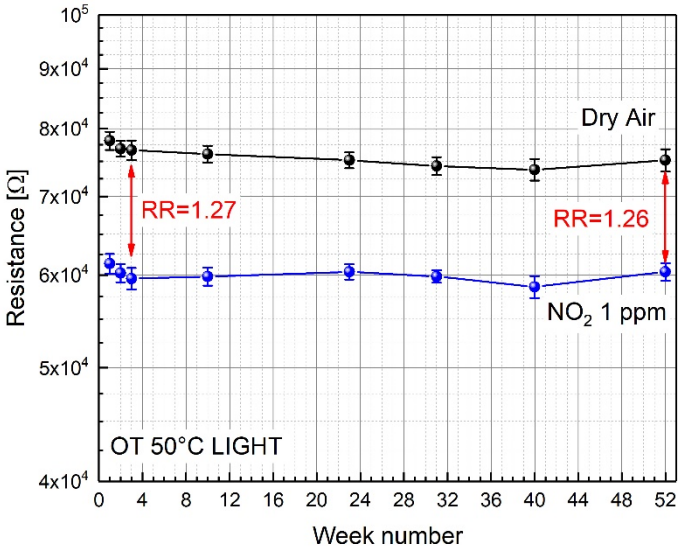


Figure 5- 18. Long term stability properties of the $WS_2$/rGO hybrid sensor. Base line resistances (upper curve) and saturation resistances corresponding to 1 ppm (lower curve), randomly collected over a period of 52 weeks, with associated standard deviations calculated over a set of 5 consecutive measurements are shown. Relative responses (RR) taken over the investigated period are also highlighted.

The effect of 40% relative humidity (RH) to the $NO_2$ response, under dark and light conditions, at 50 °C OT, is shown in Figure 5- 19. Regardless of the illumination: i) the baseline resistance slightly increases from dry to humid (40% RH) conditions; ii) the $NO_2$ relative responses (Ra/Rg) at 40% RH, do not change appreciably neither under dark or light conditions; iii) the baseline resistance is fully recovered after each adsorption/desorption cycle. This behavior demonstrates that humidity, regardless of the illumination conditions, does not appreciably interfere with the $NO_2$ gas adsorption mechanism, suggesting, as it will be discussed in the next paragraph, that $NO_2$ preferentially adsorbs on $WS_2$, since energetically favored as respect to water vapor.

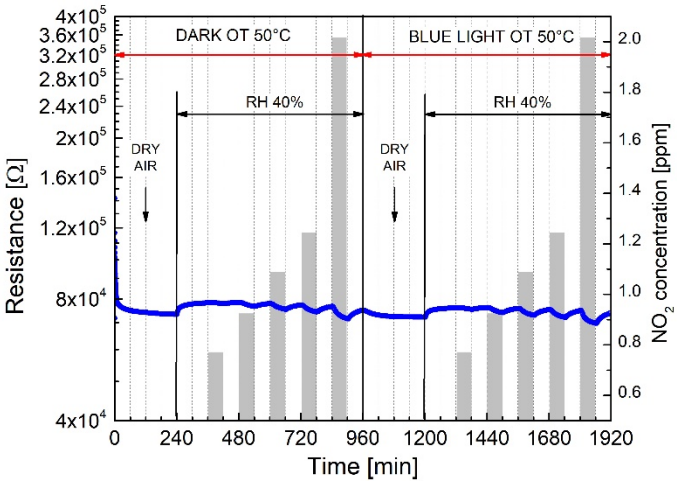


Figure 5- 20. The influence of 40% Relative Humidity (40% RH) on the $NO_2$ response of $WS_2$-decorated rGO under dark and light illumination at 50 °C operating temperature.

### 5.3.4 $WS_2$/rGO Gas Sensing Mechanism

Discussing the gas sensing mechanism of the $WS_2$–rGO hybrid sensor with respect to water vapor and $NO_2$, the single contribution of the rGO and $WS_2$ species and $WS_2$–rGO hybrid to the overall gas response have to be considered.

Regarding the single rGO in a previous work of our group [34] it has been demonstrated that both as-deposited GO and partially reduced rGO (annealed in vacuum at 200 °C) exhibit a *p*-type response to $NO_2$, resulting in a decrease of the resistance in the operating temperature range of 25–150 °C. Considering that the rGO prepared in this work shows a degree of reduction, located halfway between these two extremes, we would have expected a decrease of the resistance in Figure 5- 12, rather than no response when exposing bare rGO film to $NO_2$ gas. The lack of any gas response may not be entirely attributed to the decrease of functional groups induced by the mild reduction process (i.e., air annealed at 70 °C), but mostly to a substantially smaller amount of the deposited rGO, which amounts to approximately 1/10 of the quantity previously utilized [34]. It may be concluded that the deposition procedure adopted here yields an rGO film which does not significantly contribute to the $NO_2$ response, while it guarantees the formation of a continuous, conductive layer "bridging" distant platinum finger-type electrodes.

Regarding single $WS_2$, which is reported to increase its resistance to $NO_2$, exhibiting an *n*-type response [16,22], some considerations apply. According to the XPS section, $WS_2$ flakes deposited on rGO partially oxide to amorphous $WO_3$ (approx 18%). Amorphous $WO_3$, as previously discussed [16,22], acts as a non-conductive phase, eventually inhibiting the charge–carrier transfer mechanism within the flakes. It turns out that the formation of $WO_3$, while not contributing to the overall gas response, has the merely negative effect of partially covering the underlying reacting surface of the $WS_2$ flakes, eventually decreasing the relative gas response.

Regarding crystalline $WS_2$, the variation of the electrical resistance induced by Air–$NO_2$ mixtures, is part of a complex mechanism involving the combined effects physisorption, chemisorption, the role of edges and surface defects and the transduction mechanism. First principle calculations on $MoS_2$ sulfur-vacancy-defective monolayers [9,11] demonstrated that $O_2$ firstly chemisorbs on existing sulfur vacancies, secondly, that sulfur vacancies are passivated (i.e., "healed") by the dissociative chemisorption of $O_2$ molecules, leading to the formation of two Mo-O bonds. In case of direct $NO_2$ molecules interaction with sulfur vacancies, a dissociative chemisorption of $NO_2$ takes place, leading to oxygen atoms passivating the vacancies (i.e., "secondary healing") and NO molecules eventually to be physisorbed on the $MoS_2$ surface. Considering that both $MoS_2$ and $WS_2$, are susceptible to spontaneous oxidation in air [17], the mechanism of sulfur vacancies suppression operated by $O_2$ and $NO_2$ claimed for $MoS_2$, can be reasonably extended to sulfur defective $WS_2$. Under these circumstances, literature reports based on first principle calculations on "healed" $WS_2$ surfaces pointed out that $O_2$, $NO_2$ and $H_2O$ physisorb on defect-free monolayer $WS_2$ surfaces [13,39].

Regarding $WS_2$–rGO hybrids, they decrease their overall resistance when exposed to $NO_2$ (Figure 5- 12), exhibiting, as reported for $MoS_2$/Graphene composites [24,25], an overall *p*-type response. Bearing in mind that the $WS_2$–rGO hybrid's gas response depends on both charge transfer values (positive charge transfer values between adsorbing molecules and the material surface stand for electrons withdrawal from the material) and adsorption energies (negative adsorption energy means that the adsorption process is exothermic and energetically favourable), the following discussion applies.

According to Table 5-2, adsorption of a single $NO_2$ molecule on rGO yields charge transfer values of approximately 0.029e and associated adsorption energies of –0.80 eV [11,13,39]. By contrast, the adsorption of a single $NO_2$ molecule on defect free $WS_2$ indicates that $NO_2$ physisorbs on $WS_2$ yielding charge transfer values of 0.178e and associated adsorption energies of –0.41 eV [13,39].

Table 5-2. Adsorption energy on rGO and $WS_2$ of $O_2$, $NO_2$ and $H_2O$ molecules. Note that negative adsorption energy means that the adsorption process is exothermic and energetically favorable.

| PHYSISORBED MOLECULES | ADSORPTION ENERGY ON RGO [eV] | REFERENCE | ADSORPTION ENERGY ON $WS_2$ [eV] | REFERENCE |
|---|---|---|---|---|
| $O_2$ | -0.16 | [40] | -0.24 | [40] |
| $NO_2$ | -0.80 | [11,13,39] | -0.41 | [13,39] |
| $H_2O$ | -0.04 | [41] | -0.23 | [13] |

Considering that calculated $NO_2$ charge transfer values are 0.029e for rGO and 0.178e for $WS_2$, it turns out that $WS_2$ yields a net charge transfer 6.14 times higher than on of rGO per $NO_2$ physisorbed molecule. Given these premises, the electrical response of $WS_2$-decorated rGO as compared to single rGO shown in Figure 5- 12, accounts for the larger $WS_2$'s charge carrier exchange with respect to rGO.

Figure 5- 21, which is a schematic illustration of the $WS_2$-decorated rGO film, deposited between two platinum electrodes 30 microns apart, highlights that $NO_2$ molecules adsorb on both rGO and $WS_2$ causing electrons to withdraw from both materials. Considering the smaller charge transfer induced by $NO_2$ adsorption on rGO (i.e., 0.029e) with respect to $WS_2$ (i.e., 0.178e), by exposing the $WS_2$–rGO hybrid to $NO_2$ gas, the $NO_2$ gas molecule withdraws electrons mainly from the $WS_2$ surface. As a consequence, electron-depleted *n-type* $WS_2$ flakes drain electrons from the underlying *p-type* rGO, thanks to a rapid electron transport from the highly conducting rGO to the less-conducting $WS_2$ [1,27]. The increase of hole concentration in *p-type* rGO due to physisorption of $NO_2$ molecules on $WS_2$ flakes, explains the decrease of the overall resistance of the *p-type* $WS_2$-decorated rGO shown in Figure 5- 12. It may be concluded that rGO flakes, with excellent transport capability, serve as highly conductive channels bridging distant electrodes, whereas $WS_2$ decoration eventually modulates the $NO_2$ gas response.

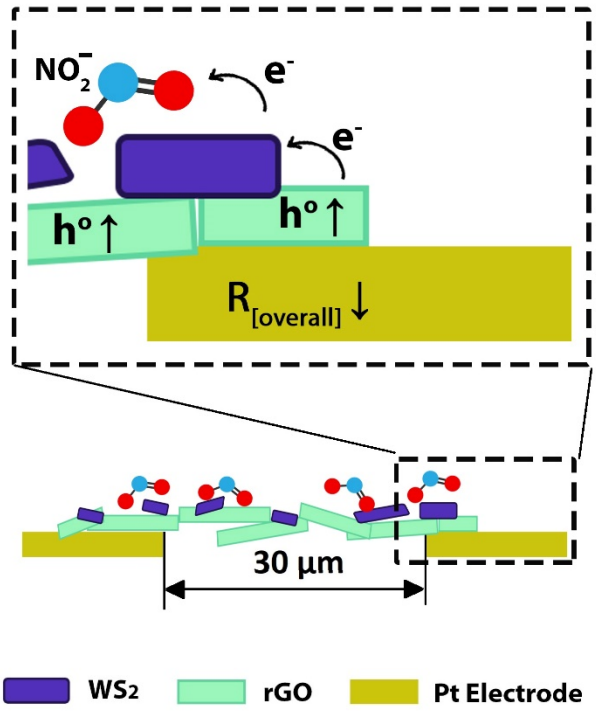


Figure 5- 22. Schematic illustration of the proposed sensing mechanism of $WS_2$-decorated rGO hybrid during $NO_2$ exposure.

Regarding the influence of purple–blue light, it is well known that response and recovery rates depend on the adsorption energy of the adsorbed gas molecules (see

Table 5-2). Light irradiation and thermal activation represent, therefore, two alternative or complementary modes to improve response/recovery rates [19]. By irradiating $WS_2$-decorated rGO with purple–blue light (PB λ = 430 nm) the associated photon energy of 2.88 eV and power density of 668 μW/cm$^2$ provide: i) a large quantity of photo generated electrons/holes; ii) the required energy to desorb physisorbed $O_2$, $NO_2$ and $H_2O$ molecules from both rGO and $WS_2$ flakes. Under $NO_2$ gas and PB light illumination, physisorbed oxygen partially desorbs from its adsorption site (□) according to reaction (5-1) while $NO_2$ physisorbs on free sites (□) left behind from oxygen desorption according to reaction (5-2). At equilibrium the overall reaction is represented by equation (5-3).

$$(O_2^- - \square) + h^+ + e^- \rightleftharpoons\uparrow O_2 + \square + e^- \quad (5\text{-}1)$$

$$NO_2 + \square + e^- \rightleftharpoons (NO_2^- - \square) \quad (5\text{-}2)$$

$$(O_2^- - \square) + h^+ + e^- \rightleftharpoons (NO_2^- - \square) + \uparrow O_2 \quad (5\text{-}3)$$

Considering that $NO_2$ molecules withdraw electrons with an associated charge transfer of 0.178e as compared to that of oxygen of 0.136e [13], under $NO_2$ adsorption, equation (3) is shifted to the right, meaning an excess of holes, which explains the overall resistance decrease of the $WS_2$–rGO hybrid. Moreover, the improved recovery percentages and response times of Figure 5- 14, account for the extra light-photogenerated carriers which speed up the time to reach equilibrium (equation 3) both during gas exposure and recovery.

Regarding water interaction with $WS_2$–rGO hybrid the reason why humidity, regardless of the illumination conditions, does not appreciably interfere with the $NO_2$ gas response, can be tentatively explained (see Table 5-2) evaluating that the adsorption energy of a $NO_2$ molecule on $WS_2$ is approximately twice (–0.41 eV) the corresponding energy of water (–0.23 eV), indicating a stronger attitude of $NO_2$ molecules to adsorb on $WS_2$ compared to water. Finally, the initial resistance increase of the $WS_2$–rGO when exposed to humid air can be explained taking into consideration that water is a reducing agent, which adsorbs on both rGO and $WS_2$ injecting electrons, thus decreasing the hole concentration in rGO and $WS_2$, causing an overall resistance increase of the $WS_2$–rGO hybrid.

## 5.4 Chapter summary and conclusions

In conclusion, it has been demonstrated that by pre-annealing the films at 180°C, reproducible gas sensing responses to $NO_2$ and $H_2$ at 150°C operating temperature are achieved, thus highlighting a possible strategy to control the spontaneous ageing of these devices by thermal induced oxidation.

It has been demonstrated that exfoliated $WS_2/WO_3$ composite films show excellent gas sensing properties to reducing $H_2$ and oxidizing $NO_2$ gases at 150°C OT. In this work, the LDL of 5 ppm to $H_2$, and 200 ppb $NO_2$ in dry air carrier, are found as one of the smallest so far ever measured utilizing $WS_2$ flakes. These outstanding gas sensing properties have been demonstrated by pre-annealing the $WS_2$ films at 180°C, thus precluding the formation of crystalline $WO_3$. The role of the as-formed amorphous $WO_3$ has been evaluated, resulting non-contributing to the gas sensing performances.

Moreover, sensor behavior has been enhanced by the design of a rGO/$WS_2$ heterostructure, which resulted to enhance conductivity and lowering up to quasi-room temperature sensing with the help of light-activated sensing.

## 5.5 Bibliography Chapter 5

[1] Long H, Harley-Trochimczyk A, Pham T, Tang Z, Shi T, Zettl A, Carraro C, Worsley M A and Maboudian R 2016 High Surface Area MoS2/Graphene Hybrid Aerogel for Ultrasensitive NO2Detection *Adv. Funct. Mater.* **26** 5158–65

[2] Long H, Chan L, Harley-Trochimczyk A, Luna L E, Tang Z, Shi T, Zettl A, Carraro C, Worsley M A and Maboudian R 2017 3D $MoS_2$ Aerogel for Ultrasensitive $NO_2$ Detection and Its Tunable Sensing Behavior *Adv. Mater. Interfaces* **4** 1700217

[3] Barsan N and Weimar U 2001 Conduction model of metal oxide gas sensors *J. Electroceramics* **7** 143–67

[4] Jha R K and Guha P K 2016 Liquid exfoliated pristine $WS_2$ nanosheets for ultrasensitive and highly stable chemiresistive humidity sensors *Nanotechnology* **27** 475503

[5] Kim T S, Kim Y B, Yoo K S, Sung G S and Jung H J 2000 Sensing characteristics of dc reactive sputtered WO3 thin films as an NOx gas sensor *Sensors Actuators, B Chem.* **62** 102–8

[6] Chu C W, Deen M J and Hill R H 1998 Sensors for detecting sub-ppm NO2 using photochemically produced amorphous tungsten oxide *J. Electrochem. Soc.* **145** 4219–25

[7] Staerz A, Berthold C, Russ T, Wicker S, Weimar U and Barsan N 2016 The oxidizing effect of humidity on WO3based sensors *Sensors Actuators, B Chem.* **237** 54–8

[8] Donarelli M, Prezioso S, Perrozzi F, Bisti F, Nardone M, Giancaterini L, Cantalini C and Ottaviano L 2015 Response to NO2 and other gases of resistive chemically exfoliated MoS2-based gas sensors *Sensors Actuators, B Chem.* **207** 602–13

[9] Ma D, Wang Q, Li T, He C, Ma B, Tang Y, Lu Z and Yang Z 2016 Repairing sulfur vacancies in the MoS2 monolayer by using CO, NO and NO2 molecules *J. Mater. Chem. C* **4** 7093–101

[10] Kc S, Longo R C, Wallace R M and Cho K 2015 Surface oxidation energetics and kinetics on MoS2 monolayer *J. Appl. Phys.* **117**

[11] Li H, Huang M and Cao G 2016 Markedly different adsorption behaviors of gas molecules on defective monolayer MoS2 : a first-principles study *Phys. Chem. Chem. Phys.* **18** 15110–7

[12] Yue Q, Shao Z, Chang S and Li J 2013 Adsorption of gas molecules on monolayer MoS2 and effect of applied electric field *Nanoscale Res. Lett.* **8** 425

[13] Zhou C, Yang W and Zhu H 2015 Mechanism of charge transfer and its impacts on Fermi-level pinning for gas molecules adsorbed on monolayer WS2 *J. Chem. Phys.* **142** 1–8

[14] Late D J, Huang Y K, Liu B, Acharya J, Shirodkar S N, Luo J, Yan A, Charles D, Waghmare U V., Dravid V P and Rao C N R 2013 Sensing behavior of atomically thin-layered MoS2 transistors *ACS Nano* **7** 4879–91

[15] Cho B, Hahm M G, Choi M, Yoon J, Kim A R, Lee Y-J J, Park S-G G, Kwon J-

D D, Kim C S, Song M, Jeong Y, Nam K-S S, Lee S, Yoo T J, Kang C G, Lee B H, Ko H C, Ajayan P M and Kim D-H H 2015 Charge-transfer-based gas sensing using atomic-layer MoS2 *Sci. Rep.* **5** 8052

[16] Perrozzi F, Emamjomeh S M M, Paolucci V, Taglieri G, Ottaviano L and Cantalini C 2017 Thermal stability of WS2 flakes and gas sensing properties of WS2/WO3 composite to H2, NH3 and NO2 *Sensors Actuators, B Chem.* **243** 812–22

[17] Gao J, Li B, Tan J, Chow P, Lu T-M M and Koratkar N 2016 Aging of Transition Metal Dichalcogenide Monolayers *{ACS} Nano* **10** 2628–35

[18] Giancaterini L, Emamjomeh S M, De Marcellis A, Palange E, Resmini A, Anselmi-Tamburini U and Cantalini C 2016 The influence of thermal and visible light activation modes on the NO2 response of WO3 nanofibers prepared by electrospinning *Sensors Actuators, B Chem.* **229** 387–95

[19] Geng X, Lahem D, Zhang C, Li C-J, Olivier M-G and Debliquy M 2019 Visible light enhanced black NiO sensors for ppb-level NO2 detection at room temperature *Ceram. Int.* **45** 4253–61

[20] Hu J, Zou C, Su Y, Li M, Ye X, Cai B, Kong E S-W, Yang Z and Zhang Y 2018 Light-assisted recovery for a highly-sensitive NO2 sensor based on RGO-CeO2 hybrids *Sensors Actuators, B Chem.* **270** 119–29

[21] Berholts A, Kahro T, Floren A, Alles H and Jaaniso R 2014 Photo-activated oxygen sensitivity of graphene at room temperature *Appl. Phys. Lett.* **105** 163111

[22] Huo N, Yang S, Wei Z, Li S-S, Xia J-B and Li J 2015 Photoresponsive and Gas Sensing Field-Effect Transistors based on Multilayer WS2 Nanoflakes *Sci. Rep.* **4** 5209

[23] Ottaviano L, Palleschi S, Perrozzi F, D'Olimpio G, Priante F, Donarelli M, Benassi P, Nardone M, Gonchigsuren M, Gombosuren M, Lucia A, Moccia G and Cacioppo O A 2017 Mechanical exfoliation and layer number identification of MoS 2 revisited *2D Mater.* **4** 045013

[24] Cho B, Yoon J, Lim S K, Kim A R, Kim D-H, Park S-G, Kwon J-D, Lee Y-J, Lee K-H, Lee B H, Ko H C and Hahm M G 2015 Chemical Sensing of 2D Graphene/MoS 2 Heterostructure device *ACS Appl. Mater. Interfaces* **7** 16775–80

[25] Niu Y, Jiao W C, Wang R G, Ding G M and Huang Y F 2016 Hybrid nanostructures combining graphene-MoS2 quantum dots for gas sensing *J. Mater. Chem. A* **4** 8198–203

[26] Yang J, Voiry D, Ahn S J, Kang D, Kim A Y, Chhowalla M and Shin H S 2013 Two-dimensional hybrid nanosheets of tungsten disulfide and reduced graphene oxide as catalysts for enhanced hydrogen evolution *Angew. Chemie - Int. Ed.* **52** 13751–4

[27] Zhang J, Wang Q, Wang L, Li X and Huang W 2015 Layer-controllable WS2-reduced graphene oxide hybrid nanosheets with high electrocatalytic activity for hydrogen evolution *Nanoscale* **7** 10391–7

[28] Jha R K, Burman D, Santra S and Guha P K 2017 WS2/GO Nanohybrids for Enhanced Relative Humidity Sensing at Room Temperature *IEEE Sens. J.* **17**

1–1

[29] Wang X, Gu D, Li X, Lin S, Zhao S, Rumyantseva M N and Gaskov A M 2019 Reduced graphene oxide hybridized with WS2 nanoflakes based heterojunctions for selective ammonia sensors at room temperature *Sensors Actuators, B Chem.* **282** 290–9

[30] Treossi E, Melucci M, Liscio A, Gazzano M, Samorì P and Palermo V 2009 High-Contrast Visualization of Graphene Oxide on Dye-Sensitized Glass, Quartz, and Silicon by Fluorescence Quenching *J. Am. Chem. Soc.* **131** 15576–7

[31] Mao X, Xu Y, Xue Q, Wang W and Gao D 2013 Ferromagnetism in exfoliated tungsten disulfide nanosheets *Nanoscale Res. Lett.* **8** 1–6

[32] Stankovich S, Dikin D A, Piner R D, Kohlhaas K A, Kleinhammes A, Jia Y, Wu Y, Nguyen S B T and Ruoff R S 2007 Synthesis of graphene-based nanosheets via chemical reduction of exfoliated graphite oxide *Carbon N. Y.*

[33] Park S, Lee K S, Bozoklu G, Cai W, Nguyen S B T and Ruoff R S 2008 Graphene oxide papers modified by divalent ions - Enhancing mechanical properties via chemical cross-linking *ACS Nano*

[34] Prezioso S, Perrozzi F, Giancaterini L, Cantalini C, Treossi E, Palermo V, Nardone M, Santucci S and Ottaviano L 2013 Graphene Oxide as a Practical Solution to High Sensitivity Gas Sensing *J. Phys. Chem. C* **117** 10683–90

[35] Di Paola A, Palmisano L, Venezia A M and Augugliaro V 1999 Coupled Semiconductor Systems for Photocatalysis. Preparation and Characterization of Polycrystalline Mixed WO 3 /WS 2 Powders *J. Phys. Chem. B* **103** 8236–44

[36] Wong K C, Lu X, Cotter J, Eadie D T, Wong P C and Mitchell K A R 2008 Surface and friction characterization of MoS2 and WS2 third body thin films under simulated wheel/rail rolling-sliding contact *Wear* **264** 526–34

[37] THI VU T H, THI TRAN T T, THI LE H N, THI NGUYEN P H, BUI N Q and ESSAYEM N 2015 A new green approach for the reduction of graphene oxide nanosheets using caffeine *Bull. Mater. Sci.* **38** 667–71

[38] Zhang K, Zhang Y and Wang S 2013 Enhancing thermoelectric properties of organic composites through hierarchical nanostructures *Sci. Rep.* **3** 3448

[39] Bui V Q, Pham T T, Le D A, Thi C M and Le H M 2015 A first-principles investigation of various gas (CO, H2O, NO, and O2) absorptions on a WS2monolayer: Stability and electronic properties *J. Phys. Condens. Matter* **27** 305005

[40] Bagsican F R, Winchester A, Ghosh S, Zhang X, Ma L, Wang M, Murakami H, Talapatra S, Vajtai R, Ajayan P M, Kono J, Tonouchi M and Kawayama I 2017 Adsorption energy of oxygen molecules on graphene and two-dimensional tungsten disulfide *Sci. Rep.* **7** 1–10

[41] Guo L, Jiang H, Shao R, Zhang Y and Xie S 2011 Two-beam-laser interference mediated reduction , patterning and nanostructuring of graphene oxide for the production of a flexible humidity sensing device *Carbon N. Y.* **50** 1667–73

# CHAPTER 6
# Understanding nanomaterials and gas sensing: nanoparticles of doped ZnO as $H_2$ and $NO_2$ sensors

The work presented in this chapter is the result of an on-going collaboration with Prof. A. Martucci from Department of Industrial Engineering, University of Padova.

## ABSTRACT

This chapter reports the experimental outcomes achieved with the application of doped ZnO nanoparticles as gas sensors for $H_2$ and $NO_2$ gases. Colloidal synthesis of the doped nanoparticles is described and the results of both chemoresistive and optical gas sensing are reported.

## CONTENTS



## 6.1 Doped-ZnO as gas sensing material

From the variety of gas sensors, semiconducting metal oxide sensors such as ZnO, $SnO_2$, $TiO_2$, $WO_3$, CuO, NiO, $In_2O_3$ have been extensively used. Recently, ZnO nanostructures with variety of morphologies have been widely studied and applied for gas sensing applications as these materials under operating conditions possess high electron mobility, non-toxic nature, high-specific surface area, good chemical, and thermal stability.

Zinc oxide is a nonstoichiometric oxide presenting a slight deficiency of lattice oxygen ions [$ZnO_{1-x}$], which has been traditionally ascribed as the cause to its distinctive n-type behavior [1]. Zinc oxide is one of the most studied semiconductor metal oxides for gas sensing applications because of its chemical sensitivity to many analytes, detects toxic gases and organic vapors, high thermal stability, suitability to doping, nontoxicity, abundance in nature, and low cost [2–4].

Doping has been shown to influence the optical and electrical properties of ZnO, with beneficial e□ects for its catalytic and sensing performances [5,6]. In particular, trivalent cations as substitutional dopants for zinc within ZnO have been extensively studied, mostly for application in transparent conductors. In fact, doping ZnO with trivalent cations such as $Ga^{3+}$ or $Al^{3+}$ (Figure 6- 1) greatly enhances its conductivity without altering the transparency in the visible spectral range, turning highly resistive, undoped ZnO into a transparent conductive oxide (TCO) [7]. These aliovalent dopants are also responsible for the generation of a localized surface plasmon resonance (LSPR) in the near-infrared, arising from the increased free electron concentration. While the main applications of TCOs are in optoelectronic devices including solar cells, touch panel displays, and energy e□cient windows, they have recently proved to be interesting materials also for gas sensing applications: in fact, indium tin oxide (ITO) has already been tested for the detection of hydrogen and volatile organic compound (VOC); gallium- and aluminum-doped zinc oxide (GZO and AZO, respectively) have also been used for electrical sensing of hydrogen, methanol, nitrogen dioxide, and hydrogen sulfide, and optical sensing of hydrogen.

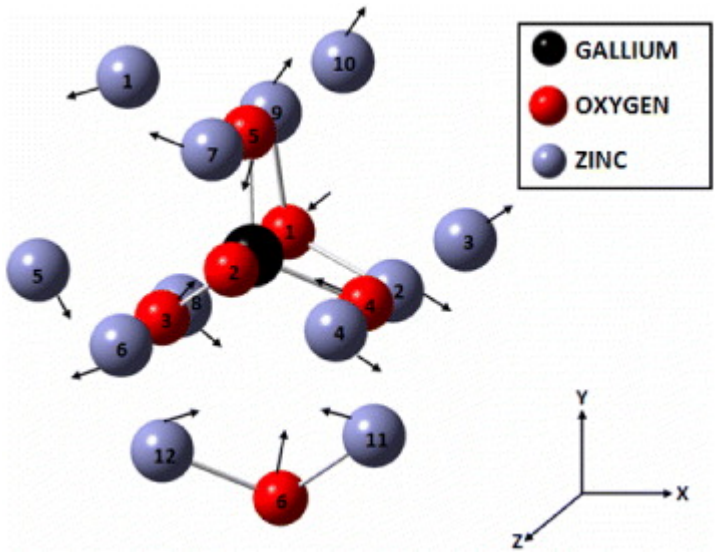


Figure 6- 1. Structure example of Ga-doped Zinc Oxide (GZO) [8]

Regarding gas sensing applications, in addition to the common chemoresistive approach, the presence of LSPR can be used to produce optical gas sensors, in which plasmonic metal nanostructures are generally coupled to a semiconductive matrix (usually a metal oxide), responsible for the reaction with the target analyte, while the metal acts as optical probe, providing an optically detectable signal. In particular, the LSPR peak of highly doped ZnO nanocrystals (NCs) can be used to detect both oxidizing and reducing gases, combining the reactivity of ZnO toward gaseous analytes, and the optical signatures provided by the plasmonic resonance. Previous results on plasmonic semiconductors used for detecting metal ions in water, although through an aggregation-induced shift of the LSPR and not through a modulation due to a change in charge carrier concentration and redox reactions in liquid provided encouraging results for the application of doped semiconductors as plasmonic sensors.

**Gropup III and group IV doped ZnO: syhtnesis**

Zinc oxide NCs were synthesized through heat-up colloidal method [9,10]. In a typical synthesis of undoped ZnO NCs, 1.26 g of Zn stearate (ZnSt2), 3.2 g of 1-dodecanol (1-DDOL), and 1.76 g of oleic acid (OA) were mixed together in a round-bottom flask, using 21 mL of 1-octadecene (ODE) as noncoordinating solvent. To obtain doped nanoparticles, a certain amount of gallium acetylacetonate (Ga(Acac)3) was added (36 and 73 mg to obtain, for example, nominal molar doping levels of 5% and 10%). The round-bottom flask was then connected to a Schlenk line, degassed at room temperature, and maintained under inert (nitrogen) atmosphere for the duration of the whole reaction. The solution was first heated to 130°C, it was maintained at this temperature for 45 min, and eventually it was heated to 240°C under strong stirring with a heating rate of at 10°C/min. After 3 h at 240°C to ensure efficient dopant incorporation, the solution was cooled down to room temperature under nitrogen. The NCs were then collected and purified through redispersion/centrifugation cycles using chloroform or toluene as solvents and acetone as nonsolvent. After purification, the NCs were redispersed in octane or toluene at a concentration of ∼100 mg/mL. Spin-coated films were deposited from these concentrated solutions at 1000 rpm for 30 s and then stabilized on a hot plate at 150 °C for 15 min in air. This procedure was repeated to obtain desired film thickness. Thin films were then treated in a 5% $H_2$–95% Ar gas mixture at 450°C. A visual synthesis of ZnO nanoparticle is reported in Figure 6- 2.

In light to reach optimum gas sensing properties, ZnO nanostructured materials have to be calcined at appropriate temperature. It is a well-known fact that, with increasing annealing or calcination temperature, the crystallinity of the ZnO nanomaterials is improved and the extent of stoichiometric defects in the form of oxygen vacancies is increased. Greater the number of such defects better is the gas sensing response. However, a very high annealing temperature causes the agglomeration of the particles, resulting in increased crystallite size and reduced specific surface which in turn retards the gas response [11].

Moreover, in order to enhance the sensitivity of the nanoparticles to hydrogen, GZO has been doped with Pt nanoparticles [12]. Platinum NPs were synthetized using polyol method. Typically, 67 mg Chloroplatinic acid ($H_2PtCl_6$) and 18.7 mg Sodium chloride (NaCl) were dissolved in 3 mL ethylene glycol, degassed and maintained in nitrogen. In another flask, 150 mg of Sodium nitrate ($NaNO_3$) and 55 mg polyvinylpyrrolidone (PVP) were dissolved in 13 mL ethylene glycol, degassed, and heated to 160 °C in nitrogen. After ~20 min, the first solution was rapidly injected into the second one. Then temperature was kept at 160 °C in inert atmosphere for 30 min and cooled down to room temperature. Particles were precipitated with excess acetone, centrifuged and finally redispersed in ethanol resulting in a 30 mM nominal concentration.

For Aluminum, Silicon and Germanium doping, the same procedure has been carried out, using as a dopant precursor Aluminum acetylacetonate (Al acac), Tetraethylorthosilicate (TEOS) and Germanium isopropoxide (Ge IPO) respectively.

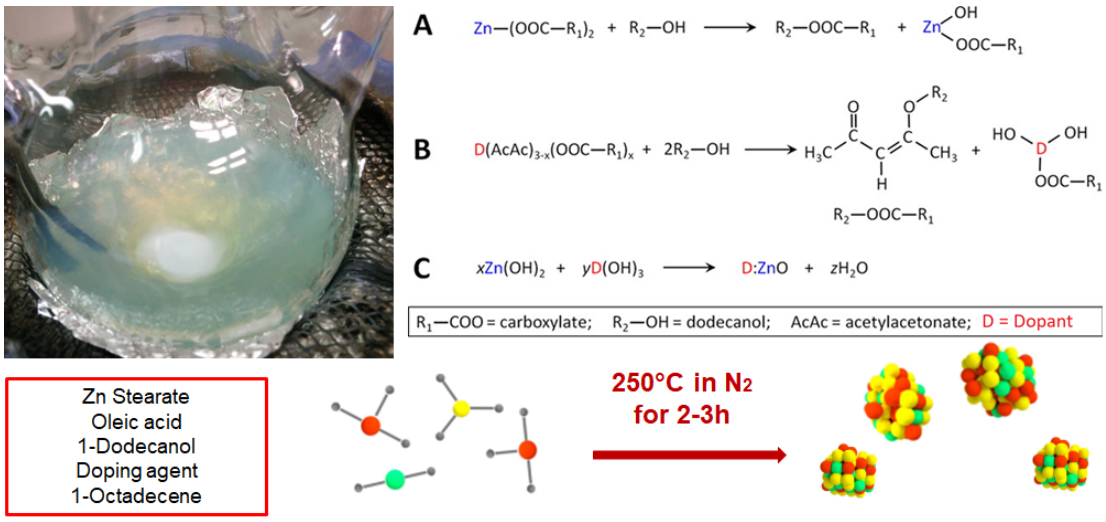


Figure 6- 2. Resume of the non aqueous heat up colloidal synthesis

### 6.1.1 Microstructural characterization of GZO nanoparticles and GZO+Pt nanoparticles

ZnO NCs with different doping levels were synthesized by varying the amount of the gallium precursor in the reaction mixture. As previously demonstrated [9], the presence of the aliovalent dopant within ZnO triggers the formation of a LSPR feature in the near-infrared, as evident from Figure 6- 3. The IR signatures of GZO nanocrystals are strongly dependent on the Ga doping, which also slightly affects the absorption properties in the visible spectrum.

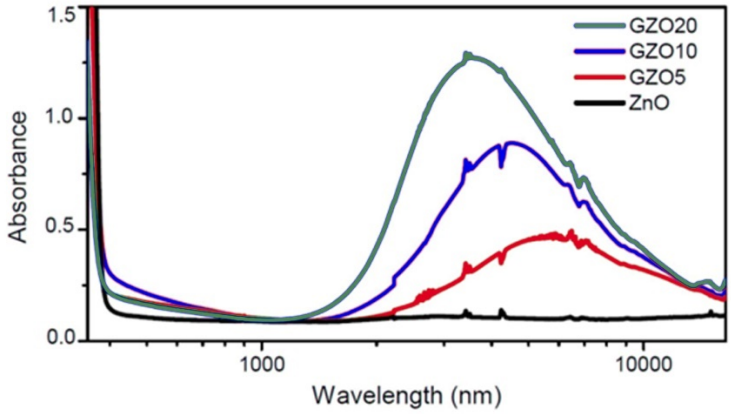


Figure 6- 3. Combined UV-Vis-NIR and FTIR absorption spectra for ZnO, GZO5, GZO10 and GZO20.

The GZO NPs synthesized here are all crystalline in hexagonal wurtzite structure (ICDD No. 36-1451) without any impurities or particular preferred orientation, as shown in Figure 6- 4. Because of the broad diffraction peaks of nanoscale particles, no detectable shift of the peaks between doped and undoped ZnO can be observed.

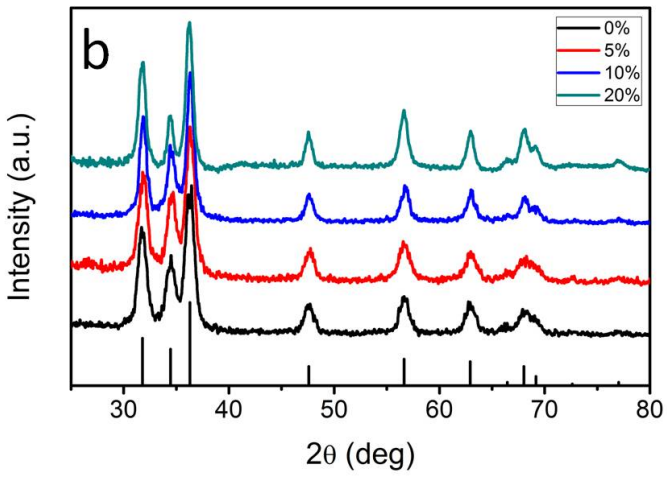


Figure 6- 4. XRD spectra of GZO with different amount of dopant

Finally, SEM pictures of nanoparticles with different amount of Ga are reported in Figure 6- 5. As shown, all deposited films are uniform and homogeneous on a scale of several micrometers and possess a similar morphology regardless of the amount of dopant. The images at high magnification show a transition from spherical particles to slightly elongated and faceted particles at increased Ga doping, which is fairly common for highly doped NCs.

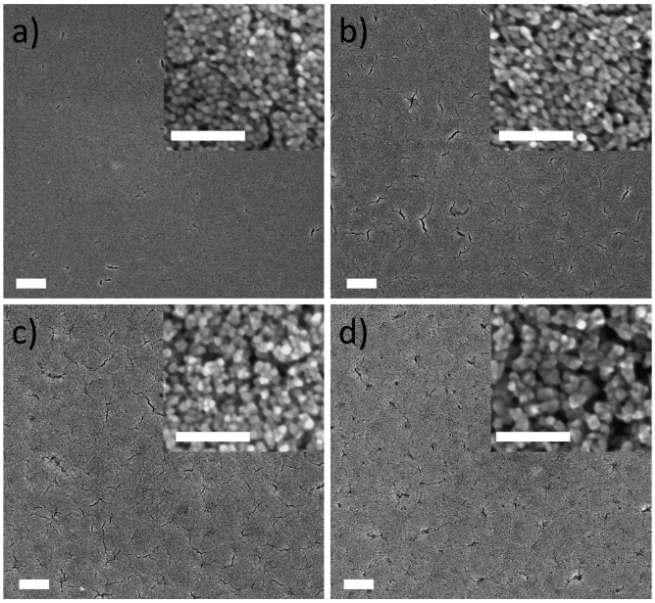


Figure 6- 5. SEM images of (a) ZnO, (b) GZO5, (c) GZO10, and (d) GZO20 thin films. Scale bars for main panels and insets are 1 µm and 100 nm, respectively.

The effect of Pt nanoparticles on material microstructure have also been observed. Figure 6- 6 (a) and (b) confirm the presence of Pt NPs on the film, and XRD patterns for GZO 10% with and without Pt nanoparticles, reveal the appearance of sharp and clear peaks for in the sample with Pt, related to the presence of Pt on the surface.

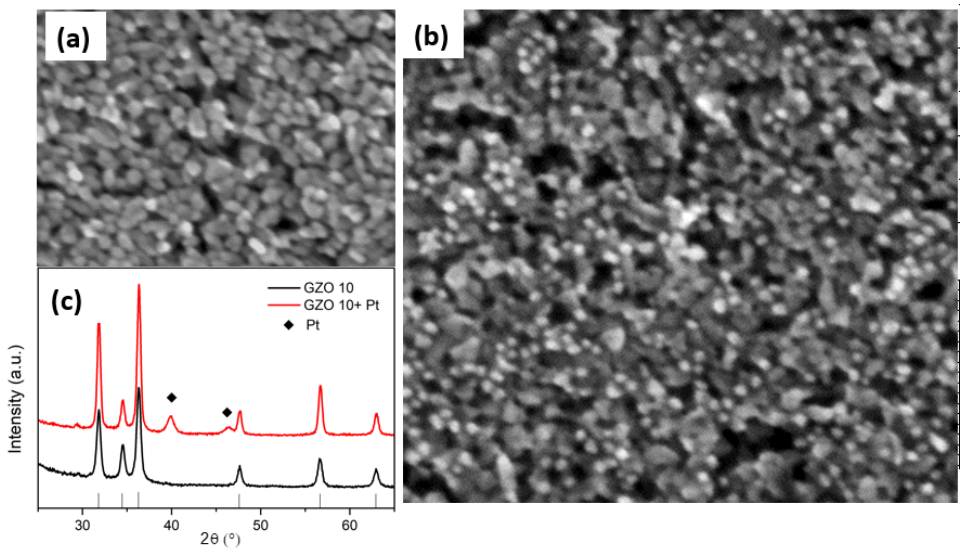


Figure 6- 6. Characterization of Ga-doped ZnO NPs. (a) SEM picture of uncoated GZO film; (b) GZO film coated with Pt NPs; (c) comparison of the XRD spectra of the two films.

## 6.2 Gas sensing characterization of GZO nanoparticles and GZO+Pt nanoparticles

When synthesized as a nanocrystalline material using colloidal techniques, ZnO and Ga-doped ZnO have been demonstrated to show a series of lattice defects including oxygen vacancies, zinc vacancies, interstitial zinc, and substitutional gallium, which are related to the dopant concentration and contribute to some defect- related emission [13].

As demonstrated in Chapter 1, being ZnO a n-type semiconductor, reducing and oxidizing gases promote an injection or a removal of electron in the conduction band, respectively. Besides the obvious effect on the change of the electrical resistance with the gas concentration, which is the main feature of a chemoresistive ZnO gas sensors, variations in carrier density can also affect the optical band gap–for n-type semiconductor like ZnO through a blue-shift for reducing gas and a red-shift for oxidizing gas, through the Burstein–Moss effect [14].

Given these premises, the ZnO doped nanoparticles have been tested both as optical and chemoresistive gas sensing material.

### 6.2.1 Optical gas sensing

Previous works have demonstrated that noble metal particles embedded in the metal oxide matrix can act as optical probes, using their LSPR shifts, caused by carrier density variation, instead of monitoring shifts in the band gap of the metal oxide [15,16]

Plasmonic metal oxides like GZO can open the possibility to obtain the same effect simply exploiting their LSPR features in the infrared, without the need to develop nanocomposite thin films composed of plasmonic NCs embedded within a metal oxide matrix. Moreover, the TCO plasmon resonance can be also easily tuned with dopant concentration, heat treatments, or tailoring grains size and shape and consequently can be exploited at different wavelengths for different sensing purposes. Here, the variation in the LSPR peak for GZO films has been measured by exposing the films to 1% vol $H_2$ and 1000 ppm of $NO_2$ at different operating temperatures in the range 25–150°C and using dry air as carrier gas. Higher temperatures (>200 °C) were found to drastically decrease the plasmonic absorption due to decrease in oxygen vacancies and therefore led to baseline instability. The reference parameter is the “optical absorbance change”, which is defined as the difference between absorbance during gas exposure and absorbance in air ($OAC = Abs_{Gas} - Abs_{Air} = \Delta_{Abs}$). After exposure to hydrogen, the absorbance in the NIR range increases, while upon exposure to $NO_2$ a decrease in optical absorption in the NIR is observed.

Figure 6- 7 shows the optical gas sensing properties of GZO film with 5 and 10% Ga coated with Pt NPs. Due to the catalytic activity of Pt for hydrogen oxidation, the samples showed a strong enhancement of the response and a better dynamic response, for both Ga doping content with respect to pure GZO film. On the contrary, the Pt NPs have very little effect on $NO_2$ optical sensing.

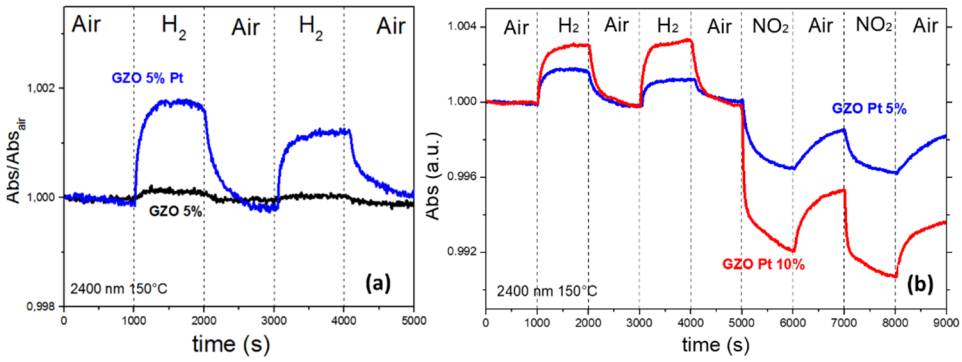


Figure 6- 7. (a) Dynamic absorption changes for two cycles Air/$H_2$ 1% and two cycles Air/$NO_2$ 1000 ppm at 2400 nm and at 150 °C OT for GZO film with 5% Ga uncoated (black line) and coated (red line) with Pt NPs. (b) Dynamic absorption changes for two cycles Air/$H_2$ 1% and two cycles Air/$NO_2$ 1000 ppm at 2400 nm and at 80 °C OT for GZO film with 5% (black line) and 10% (blue line) Ga.

It is widely believed that Pt catalyst enhances reducing gas sensing of metal oxide via spillover mechanism [17]. This interaction is a chemical reaction by which additives assist the redox process of metal oxides. The term spillover refers to the process, illustrated in Figure 6- 8, namely the process where the metal catalysts dissociate the molecule, then the atom can 'spillover' onto the surface of the semiconductor support. At appropriate temperatures, reactants are first adsorbed on to the surface of additive particles and then migrate to the oxide surface to react there with surface oxygen species, affecting the surface conductivity[18].

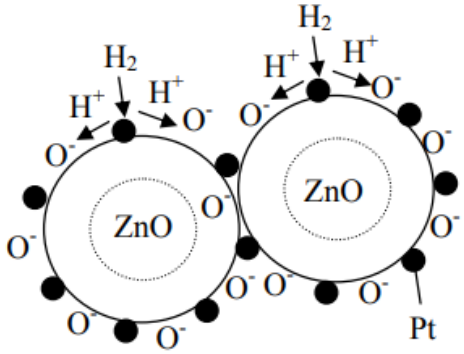


Figure 6- 8. Gas sensing mechanisms based on spillover effect of Pt doped ZnO

## 6.2.2 Chemoresistive gas sensing

The chemoresistive response of the Pt doped GZO films to sub ppm NO2 gas concentration was also investigated and compared with optical gas sensing measurements. Changes of the electrical resistance of ZnO-based metal oxides to $NO_2$ have been extensively reported in the literature by activating the sensor response by thermal, [4] and visible light irradiation [10,19] in order to decrease the operating temperature toward mild (T <100 °C) or even ambient (25 °C) conditions. In this study we explored the effect of both temperature (in the OT range 25–100 °C) and visible light irradiation using purple–blue (PB) LED source (λ = 430 nm and 770 μW/cm$^2$ intensity) on the electrical gas sensing properties of Pt doped GZO films for the detection of $NO_2$ (400 ppb) gas. Figure 6- 9 shows the normalized changes of the electrical resistance of Platinum doped GZO films to 400 ppb $NO_2$ gas concentration activated by thermal (a-d) and purple-blue light irradiation (e-h) modes in a temperature range from 25˚C to 100˚C.

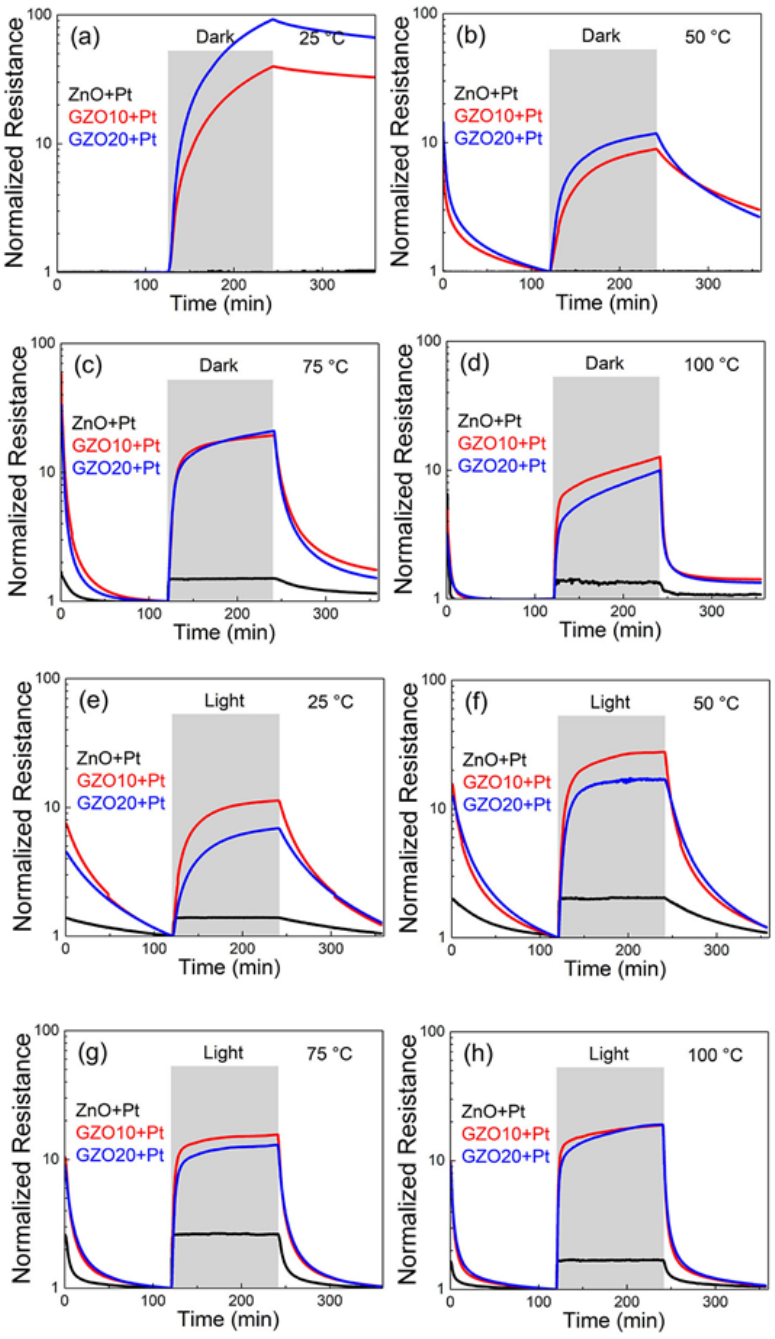


Figure 6- 9. Chemoresistive gas sensing properties of ZnO and GZO film with 10 and 20% Ga doped with Pt NPs. Normalized resistance changes to 400 ppb $NO_2$ exposure (gray shaded box) at different operating temperatures (25 ˚C-100 ˚C) under dark (a–d) and purple–blue light irradiation (e–h) conditions.

From a previous study of our groups [10] has been demonstrated that Ga doping of ZnO films enhances the Relative Responses (RRs), improves the Recovery Percentages of the Baseline (RPs), and slightly increases the response times. By analyzing the electrical responses at different OT and under dark conditions (Figure 6-9 a-d) we observed that addition of Pt to GZO improves the RRs with a maximum at GZO 20+Pt at 75 ˚C operating temperature, see Table 6-1. RRs improvement of Pt

doped films in Dark condition continues up to 75 ˚C and decreases at 100 ˚C. Also, addition of Pt improves the Recovery Percentages (RPs) over the operating temperature from 25 ˚C to 100 ˚C in Dark. It could be noted that under thermal activation mode in dark, addition of Ga and Pt increase both RRs and Recovery Percentages (RPs) indicating a synergistic effect with a maximum value obtained for GZO 20+Pt at operating temperature not exceeding than 75 ˚C, see Figure 6- 9 a-d and Table 6-1.

Irradiation with PB light, as shown in Figure 6- 9 e-h, further enhances RRs in most of sensors and remarkably increases the RPs in all investigated sensors with respect to dark conditions. Given the positive effect of PB light irradiation, reasonable gas sensing features are maintained even at 50 °C OT, yielding for the GZO10+Pt. The best gas sensing response in terms of RR, RP and response time under combined thermal and light illumination condition was obtained for GZO10+Pt at 75 ˚C with values of 15.45, 99.38 and 41 respectively, see table 1. Moreover, Gallium free Pt doped ZnO films activated with PB light show gas response even at room temperature (Figure 6- 9e) as compared to the gallium free Pt doped ZnO in dark (Figure 6- 9a).

Table 6-1. Comparison of RR and RP to 400 ppb NO2 in dark conditions and PB light (λ = 430 nm) illumination at different OT (25–100 °C).

| (°C) | Sample | Relative Response RR=Rg/Ra [-] | | RP=[ΔD/ΔA ]*100 [%] | |
|---|---|---|---|---|---|
| | | Dark | LED | Dark | LED |
| 25 | GZO 0% | 1 | 2.94 | 0 | 90 |
| | GZO 0% + Pt | 1 | 1.36 | 0 | 77.13 |
| | GZO 10% | 3.52 | 2.44 | 0 | 80.66 |
| | GZO 10% + Pt | 39.09 | 11.01 | 18 | 95.95 |
| | GZO 20% | 47.73 | 10.44 | 19.28 | 93.8 |
| | GZO 20% + Pt | 93.82 | 6.72 | 26.68 | 90.28 |
| 50 | GZO 0% | 1 | 2.65 | 0 | 88.15 |
| | GZO 0%+Pt | 1 | 2.03 | 0 | 83.64 |
| | GZO 10% | 1 | 5.31 | 15.77 | 88.74 |
| | GZO 10% + Pt | 8.79 | 27.6 | 74.75 | 98.51 |
| | GZO 20% | 5.8 | 27.5 | 69.62 | 98.01 |
| | GZO 20% + Pt | 12.18 | 16.89 | 83.29 | 98.41 |
| 75 | GZO 0% | 1.18 | 2.03 | 0 | 99,00 |
| | GZO 0%+Pt | 1.49 | 2.63 | 69.4 | 98.59 |
| | GZO 10% | 4.29 | 8.81 | 87.47 | 99.33 |
| | GZO 10% + Pt | 19.2 | 15.45 | 95.85 | 99.38 |
| | GZO 20% | 15.78 | 20.82 | 95.28 | 99.06 |
| | GZO 20% + Pt | 20.7 | 12.72 | 97.43 | 99.32 |
| 100 | GZO 0% | 1.46 | 1.58 | 54.59 | 89.34 |
| | GZO 0%+Pt | 1.35 | 1.68 | 79.19 | 91.23 |
| | GZO 10% | 6.17 | 8.74 | 96.24 | 98.25 |
| | GZO 10% + Pt | 12.58 | 18.87 | 96.41 | 99.35 |
| | GZO 20% | 10.81 | 24.41 | 97.52 | 99.23 |
| | GZO 20% + Pt | 10.02 | 16.03 | 96.11 | 99.01 |

When GZO concentration is increased from 10% to 20%, Pt loading results in depressing the RRs for all the investigated temperatures. Similar to that of RRs, when

GZO concentration is increased from 10% to 20%, Pt loading slightly decrease the RPs for all the investigated temperatures, this phenomenon is less pronounced in the temperature range 75 ˚C-100 ˚C, see Table 6-1. Under combined thermal and blue light activation modes both Ga and Pt addition increases the adsorption and desorption times. Desorption times were always longer than adsorption times. Indeed, the adsorption/desorption times under LED illumination were much faster (given the same OT) with respect to the thermally activated samples. To this extend it is worth to notice that the light activation mode for most of the investigate films trigger the achievement of equilibrium conditions (i.e. most of the not detectable (n.d.) conditions in Table 6-1 have been disappeared and substituted by the respective response time.

## 6.3 Comparison of gas sensing performances of Ga, Al, Si and Ge doped ZnO nanoparticles (GZO, AZO, SZO, GeZO)

This paragraph reports on very preliminar results about ZnO NPs doped by trivalent cations ($Al^{3+}$ and $Ga^{3+}$) or tetravalent cations ($Si^{4+}$ and $Ge^{4+}$).

XRD characterization reported in Figure 6- 10 reveal peak analysis of XRD pattern confirm the mean dimensions estimated by TEM, and the typical Wurtzite crystalline structure (ICDD No. 00-036-145).

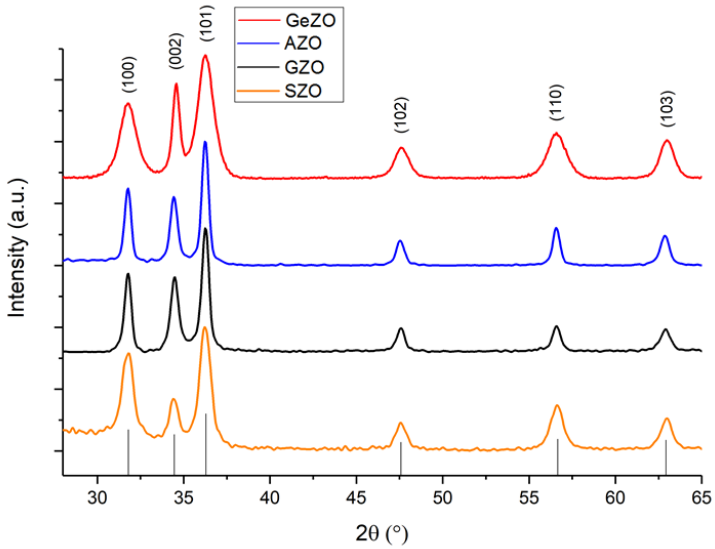


Figure 6- 10. XRD spectra of GZO, AZO, SZO and Ge at 5%.

No other phases corresponding to metal, oxides, or binary dopant-Zn formation are present, confirming a doping effect of cations during synthesis. From SEM-EDS measurements an efficiency of doping ranging from 40% till 70% was verified.

Dopant nature and concentration affected also LSPR absorbance intensity, amplifying the potential useful signal of the sensor. In particular, LSPR intensity becomes higher increasing dopant concentration (verified till 20% of doping) and using gallium as

dopant agent. At same dopant concentration lower LSPR intensity is found respectively in ZnO:Ge, ZnO:Al and ZnO:Si.

### 6.3.1 Optical gas sensing

Gas sensing tests have been performed at 2400 nm, due to instrumental spectrophotometer limit, at different operative temperatures, exposing the sensing material at $NO_2$-air cycles. As expected sensing properties increase with the temperature because oxygen vacancies increase and, as evident in Figure 6- 11, best response in term of signal variation is obtained for ZnO:Ga, but signal drift it is minimized for ZnO:Si.

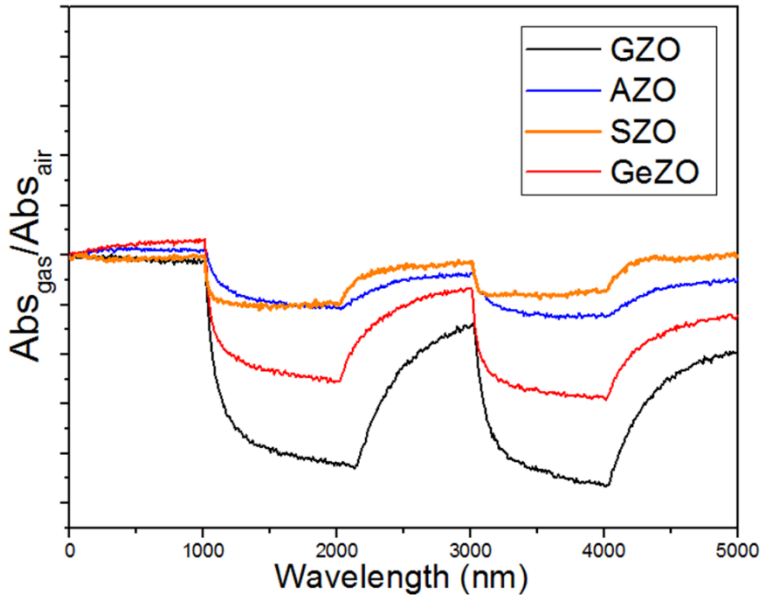


Figure 6- 11. Dynamic absorption changes for two cycles Air/$NO_2$ 1000 ppm at 2400 nm and at 150 °C OT for GZO, AZO, SZO, GeZO films.

### 6.3.2 Chemoresistive gas sensing

The responses of GZO, AZO, SZO and GeZO to 400 ppb $NO_2$ in the temperature range 25-100°C, both in dark and light conditions, are described in Figure 6- 12 in terms of normalized changes in resistance and calculation on Relative Response and Recovery percentage are reported in Table 6-2.

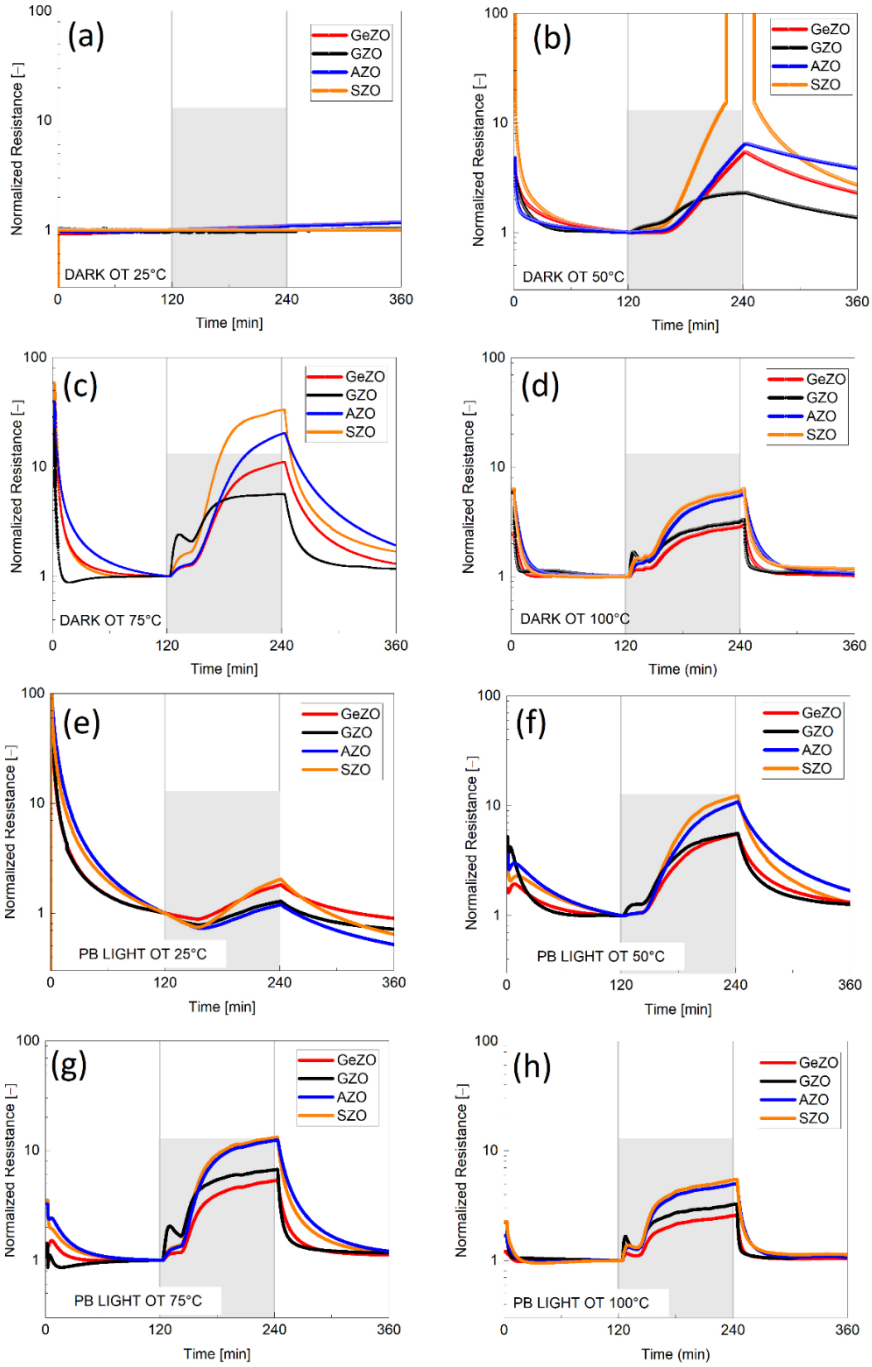


Figure 6- 12. Chemoresistive gas sensing properties of GZO, AZO, SZO and GeZO films 5% doped. Normalized resistance changes to 400 ppb $NO_2$ exposure (gray shaded box) at different operating temperatures (25 ˚C-100 ˚C) under dark (a–d) and purple–blue

As shown in the previous paragraph, both the presence of trivalent and noble metal enhances the chemoresistive response of ZnO. A lot of literature reports on the effect of gallium and aluminum [5,8,10,12], but almost nothing have been reported regarding the effect of tetravalent ions.

Table 6-3. Comparison of RR and RP to 400 ppb $NO_2$ in dark conditions and PB light (λ = 430 nm) illumination at different OT (25–100 °C). Data concerning ZnO undoped are taken from a previous work of our groups [10].

| OT (°C) | Sample | RR=RG/RA [-] | | RP=[ΔD/ΔA ]*100 [%] | |
|---|---|---|---|---|---|
| | | Dark | LED | Dark | LED |
| 25 | ZnO undoped | n.d. | 2.94 | n.d. | n.d |
| | GZO 5% | n.d. | 1.28 | n.d. | n.d. |
| | AZO 5% | n.d. | 1.19 | n.d. | n.d. |
| | SZO 5% | n.d. | 2.02 | n.d. | n.d. |
| | GeZO 5% | n.d. | 1.80 | n.d. | n.d. |
| 50 | ZnO undoped | 1 | 2.65 | 0 | 88.15 |
| | GZO 5% | 2.30 | 5.53 | 71.48 | 94.24 |
| | AZO 5% | 6.13 | 10.58 | 44.43 | 92.88 |
| | SZO 5% | 32.77 | 13.03 | 97.87 | 98.73 |
| | GeZO 5% | 10.93 | 5.30 | 97.01 | 97.3 |
| 75 | ZnO undoped | 1.18 | 2.03 | 0 | 99 |
| | GZO 5% | 5.62 | 6.66 | 96.34 | 97.09 |
| | AZO 5% | 19.88 | 12.33 | 95.18 | 98.18 |
| | SZO 5% | 32.77 | 13.03 | 97.87 | 98.73 |
| | GeZO 5% | 10.93 | 5.30 | 97.01 | 97.3 |
| 100 | ZnO undoped | 1.46 | 1.58 | 54.59 | 89.34 |
| | GZO 5% | 3.16 | 3.23 | 96.55 | 96.83 |
| | AZO 5% | 5.49 | 4.95 | 98.55 | 98.05 |
| | SZO 5% | 6.03 | 5.43 | 96.59 | 97.02 |
| | GeZO 5% | 2.85 | 2.56 | 98.68 | 97.34 |

By analyzing the results in Figure 6- 12 and Table 6-2, a strong improvement given by the presence of dopant is clearly observed. In particular, aluminum doped and silicon doped zinc oxide NPs, gave outstanding results in terms of relative responses for all the investigated temperature range, possibly due to the increase of carrier density.

Moreover, the positive effect given by light activation is confirmed. The main effect of light is observed at low temperatures. At room temperature, while in dark conditions all the samples show no response to 400 ppb NO2, in case of light activation a slight but clear response is measured, even if no equilibrium condition are achieved both in adsorption and in desorption, giving the impossibility to calculate RPs.

Notwithstanding the effect of light to suppress in a certain way sensors' RR, as already observed [10,12], the main advantage of UV-activation is the enhancement in terms

of gas desorption, i.e. base line recovery, after gas exposure. This effect is more pronounced for trivalent dopants as compared to tetravalent ones, and it is really remarkable at 25°C and 50°C. At higher temperatures, thermal induced desorption is actually the predominant phenomenon.

A question to be resolved is the particular influence of the single dopant species in the sensing behavior and this, together with the study of different amounts of doping, represent a future challenge for this particular work.

## 6.4 Chapter summary and conclusion

Doped and undoped Zinc thin films obtained by TCOs colloidal nanoparticles were synthesized and used for gas sensing application. TCO's near infrared LSPR shifts were exploited to detect $H_2$ and $NO_2$ in the optical gas sensing measurements, confirming response to gases increasing with dopant concentration and finding optimal compromising temperature at 150°C. Electrical gas sensing was also performed, obtaining results coherent with optical tests; moreover using blue light irradiation becomes possible to use TCOs like $NO_2$ sensor at room temperature. The role of platinum NPs in increasing sensing performances through Pt catalytic activity, was also investigated.

## 6.5 Bibliography Chapter 6

1. Enke, C.G. Nonstoichiometry, diffusion, and electrical conductivity in binary metal oxides. (Wiley series on the science and technology of materials). P. Kofstad. 160 Abb. 11 Tab. {XI}, 382 S. Ca. 1060 Schrifttumshinweise. Format 15.5 {\texttimes} 23 cm. Wiley Inter. *Mater. Corros. und Korrosion* **1974**, *25*, 801–802.

2. Xu, J.; Pan, Q.; Shun, Y.; Tian, Z. Grain size control and gas sensing properties of ZnO gas sensor. *Sensors Actuators B Chem.* **2000**, *66*, 277–279.

3. Lupan, O.; Chai, G.; Chow, L. Novel hydrogen gas sensor based on single ZnO nanorod. *Microelectron. Eng.* **2008**, *85*, 2220–2225.

4. Resmini, A.; Anselmi-Tamburini, U.; Emamjomeh, S.M.; Paolucci, V.; Tredici, I.G.; Cantalini, C. The influence of the absolute surface area on the NO2 and H2 gas responses of ZnO nanorods prepared by hydrothermal growth. *Thin Solid Films* **2016**, *618*, 246–252.

5. Paraguay D., F.; Miki-Yoshida, M.; Morales, J.; Solis, J.; Estrada L., W. Influence of Al, In, Cu, Fe and Sn dopants on the response of thin film ZnO gas sensor to ethanol vapour. *Thin Solid Films* **2000**.

6. Della Gaspera, E.; Guglielmi, M.; Perotto, G.; Agnoli, S.; Granozzi, G.; Post, M.L.; Martucci, A. CO optical sensing properties of nanocrystalline ZnO-Au films: Effect of doping with transition metal ions. *Sensors Actuators, B Chem.* **2012**.

7. Freeman, A.J.; Poeppelmeier, K.R.; Mason, T.O.; Chang, R.P.H.; Marks, T.J. Chemical and thin-film strategies for new transparent conducting oxides. *MRS Bull.* **2000**.

8. Stashans, A.; Olivos, K.; Rivera, R. Physical and chemical properties of a Ga-doped ZnO crystal. *Phys. Scr.* **2011**, *83*, 065604.

9. Della Gaspera, E.; Chesman, A.S.R.; van Embden, J.; Jasieniak, J.J. Non-injection Synthesis of Doped Zinc Oxide Plasmonic Nanocrystals. *ACS Nano* **2014**, *8*, 9154–9163.

10. Sturaro, M.; Della Gaspera, E.; Michieli, N.; Cantalini, C.; Emamjomeh, S.M.S.M.; Guglielmi, M.; Martucci, A. Degenerately Doped Metal Oxide Nanocrystals as Plasmonic and Chemoresistive Gas Sensors. *ACS Appl. Mater. Interfaces* **2016**, *8*, 30440–30448.

11. D. Shinde, S.; Patil, G.E.; Kajale, D.D.; Wagh, V.G.; Gaikwad, V.B.; Jain, G.H. Effect of Annealing On Gas Sensing Performance of Nanostructured ZnO Thick Film Resistors. *Int. J. Smart Sens. Intell. Syst.* **2012**, *5*, 277–294.

12. Rigon, M.; Paolucci, V.; Sturaro, M.; Emamjomeh, S.M.; Cantalini, C.; Martucci, A. Effect of Pt Nanoparticles on the Plasmonic and Chemoresistive Gas Sensing Properties of ZnO:Ga Film. *Proceedings* **2018**.

13. Zhu, W.; Kitamura, S.; Boffelli, M.; Marin, E.; Gaspera, E. Della; Sturaro, M.; Martucci, A.; Pezzotti, G. Analysis of defect luminescence in Ga-doped ZnO nanoparticles. *Phys. Chem. Chem. Phys.* **2016**.

14. Lee, G.H.; Yamamoto, Y.; Kourogi, M.; Ohtsu, M. Blue shift in room temperature photoluminescence from photo-chemical vapor deposited ZnO films. *Thin Solid Films* **2001**.

15. Gaspera, E. Della; Buso, D.; Martucci, A. Gold nanoparticles to boost the gas sensing performance of porous sol-gel thin films. *J. Sol-Gel Sci. Technol.* **2011**.

16. Jain, P.K.; Manthiram, K.; Engel, J.H.; White, S.L.; Faucheaux, J.A.; Alivisatos, A.P. Doped nanocrystals as plasmonic probes of redox chemistry. *Angew. Chemie - Int. Ed.* **2013**.

17. Morrison, S.R. Selectivity in semiconductor gas sensors. *Sensors and Actuators* **1987**, *12*, 425–440.

18. Tamaekong, N.; Liewhiran, C.; Wisitsoraat, A.; Phanichphant, S. Sensing characteristics of flame-spray-made Pt/ZnO thick films as H2 gas sensor. *Sensors* **2009**, *9*, 6652–6669.

19. Geng, Q.; He, Z.; Chen, X.; Dai, W.; Wang, X. Gas sensing property of ZnO under visible light irradiation at room temperature. *Sensors Actuators, B Chem.* **2013**.